

Analysis of cell to module losses and UV radiation hardness for passivated emitter and rear cells and modules

Von der Fakultät für Mathematik und Physik
der Gottfried Wilhelm Leibniz Universität Hannover

zur Erlangung des akademischen Grades

Doktor der Naturwissenschaften

Dr. rer. nat.

genehmigte Dissertation von

M.Sc. Robert Witteck

geboren am 03.10.1986 in Eberswalde-Finow

Erscheinungsjahr 2019

Referent: Prof. Dr. Rolf Brendel
Korreferenten: Prof. Dr. Giso Hahn
Prof. Dr. Friedrich Dinkelacker
Tag der Promotion: 12.03.2019

Abstract

This work presents an experimental analysis and analytical modeling of cell to module losses for passivated emitter and rear cells (PERC), which enables to build a PERC solar module with a record efficiency of 20.2%. Further, it examines the ultraviolet radiation hardness of solar modules employing crystalline silicon (c-Si) solar cells featuring dielectric passivation layers.

Today, PERC are on the transition to mass production and expected to become the dominating c-Si solar cell technology in terms of market share in the next few years. Thus, it is of major importance to implement these high efficiency PERC into high efficiency solar modules. When transferring solar cells into a solar module additional recombination, optical, and resistive losses reduce the power of the solar module compared to the power of the solar cell, termed cell to module losses. In this work we study the individual recombination, optical, and resistive characteristics of various cell and module test samples. Based on our experimental results we develop an analytical model that allows to simulate the cell to module losses and reproduces the measurement results of test modules within the measurement uncertainty. We show that a reduction of the cell to module losses requires an adaptation of both, the solar cell as well as the solar module components. We employ the analytical model to improve the cell's front metalization, cell interconnection, light harvesting and cell spacing to reduce the cell to module losses for passivated emitter and rear cells and build an industrial like 60-cell sized solar module with a record power conversion efficiency of 20.2% in 2017.

Besides the efficiency, the long-term reliability of solar modules is crucial and a performance degradation of new promising technologies can impair their importance for the industry. The application of new metalization pastes that enable to contact lowly doped emitters, increases the spectral response of a PERC in the UV wavelength range. This requires the application of new encapsulation materials with enhanced UV transmittance for PERC solar modules. Thus, we investigate the effect of ultra violet (UV) radiation on PERC modules in this work. In general, accelerated UV aging tests on solar modules focus on testing the polymer materials of the module, but neglect effects on the cell level. However, previous studies also showed that UV radiation affects the silicon nitride passivation of diffused silicon wafers.

We report on the UV radiation hardness of solar modules featuring PERC with various silicon nitride passivation layers and employing different encapsulation polymers. Our results reveal that employing polymers with increased UV transparency results in a solar module power loss of 6% after a UV dose of 497 kW h m^{-2} . We show that the degradation in module power is due to a reduction of the module's open circuit

voltage. This loss is related to an increased charge carrier recombination in the cell, which we ascribe to a degradation of the amorphous silicon nitride (SiN_y) surface passivation. With ray tracing simulations we determine for the first time the critical photon flux reaching the SiN_y /silicon interface. We develop a novel analytical model to describe the effect of high energetic photons on the solar module performance. The modeling of the experimental results reveals that all photons with energies above 3.5 eV deteriorate the surface passivation.

We test our physical model for another crystalline silicon cell technology employing dielectric passivation layers, a Passivated Emitter and Rear Totally-diffused (PERT) cell. We process solar modules with bifacial n-type silicon PERT cells that are embedded in an encapsulation polymer with increased UV transparency. Modules with front junction cells featuring an aluminum oxide (AlO_x) surface passivation at the illuminated side are stable for a UV dose of 598 kW h m^{-2} . In contrast, irradiating modules with back junction cells featuring a SiN_y passivation layer at the illuminated side reduces the output power by 15%. Modeling the measured external quantum efficiency of the solar modules with numerical device simulations shows that high energetic photons increase the surface saturation current density by a factor of 18. Modeling the same solar module with the physical analytical model reveals a similar increase of the surface saturation current density by a factor of 17.

Key words: passivated emitter and rear solar cells, solar modules, UV degradation

Zusammenfassung

Diese Arbeit präsentiert eine Analyse und analytische Modellierung von Zell-zu-Modul-Verlusten von Passivated Emitter and Rear Cell (PERC) Solarzellen, welche ein Solarmodul mit einem Rekordwirkungsgrad von 20.2 % ermöglichen. Ferner wird ein physikalisches Modell für die Modellierung der Leistungsverluste in einem Solarmodul mit kristalline Silizium (c-Si) Solarzellen und dielektrischen Passivierschichten durch ultraviolette (UV) Strahlung präsentiert.

Die Solarindustrie ist gegenwärtig dabei, das Konzept der PERC-Solarzelle in die Massenproduktion zu überführen. Es ist zu erwarten, dass diese Zelltechnologie den Markt für c-Si Solarzellen in den kommenden Jahren dominieren wird. Daher ist es besonders wichtig, diese hocheffizienten PERC Zellen in hocheffiziente Solarmodule zu integrieren. Beim Transfer von Solarzellen in ein Solarmodul reduzieren zusätzliche optische, Rekombinations-, und Widerstandsverluste die Leistung des Solarmoduls im Vergleich zur Leistung der Solarzelle, Zell-zu-Modul-Verluste genannt. In dieser Arbeit untersuchen wir die jeweiligen Zell-zu-Modul-Verluste und zeigen, dass die Reduzierung dieser Verluste eine Anpassung sowohl von der Solarzelle als auch des Moduls erfordert. Wir stellen verschiedene Probenkörper aus PERC Solarzellen, Solarmodule und einzelnen Modulkomponenten her, um sowohl deren Rekombination als auch die elektrischen und optischen Eigenschaften zu charakterisieren. Wir entwickeln ein analytisches Modell basierend auf den experimentellen Ergebnissen und modellieren die Zell-zu-Modul-Verluste der Probenkörper innerhalb der Messgenauigkeit. Wir optimieren die Zellmetallisierung, die Zellverschaltung, das Lichtmanagement und die Zellabstände und stellen ein industrietypisches 60-Zellen-Solarmodul her, mit einem Rekordwirkungsgrad von 20.2 %.

Neben dem Wirkungsgrad ist auch die Langzeitstabilität von Solarmodulen essenziell und eine Leistungsdegradation von neuen, vielversprechenden Technologien kann deren industrielle Relevanz beeinträchtigen. Wir untersuchen die Beständigkeit von PERC Solarmodulen mit verschiedenen Siliziumnitrid (SiN) Passivierschichten und unterschiedlichen Einkapselungsmaterialien unter dem Einfluss von Ultraviolettstrahlung (UV-Strahlung). Unsere Ergebnisse zeigen, dass UV-lichtdurchlässige Polymere nach einer UV-Dosis von 497 kWh m^{-2} zu einer Reduzierung der Modulleistung von bis zu 6 % führen. Wir zeigen, dass die Minderung der Modulleistung durch eine Reduzierung der Leerlaufspannung bedingt ist. Diese Reduzierung ist auf eine erhöhte Rekombination in der Solarzelle zurückzuführen, welche wir durch eine Erhöhung der Grenzflächenzustandsdichte zwischen der amorphen Siliziumnitrid (SiN_y) Oberflächenpassivierung und dem n^+ -Typ Silizium (Si) erklären. Wir bestimmen mittels optischer Simulationen den kritischen Photonenfluss, welcher die

SiN_y/Silizium Grenzfläche erreicht. Darauf basierend entwickeln wir ein neues physikalisches Modell, um den Einfluss von hoch energetischen Photonen auf die Leistung des Solarmoduls zu beschreiben. Die Modellierung der experimentellen Ergebnisse zeigt, dass Photonen mit einer Energie von mehr als 3.5 eV die Grenzfläche zwischen der Oberflächenpassivierung und dem Siliziums verschlechtern.

Wir überprüfen unser Modell mit einer weiteren kristallinen Silizium Zelltechnologie, der Passivated Emitter and Rear Totally-diffused (PERT) Solarzelle. Wir stellen bifaziale n-Typ PERT Solarzellen her und machen aus diesen Solarmodule mit UV durchlässigem Einkapselungsmaterial. Die Module mit pn-Übergang auf der Zellvorderseite und Aluminiumoxid (AlO_x)/p⁺-Typ Silizium Oberflächenpassivierung sind stabil nach der Bestrahlung mit UV Licht und einer UV-Dosis von 598 kW h m⁻². Im Gegensatz dazu, führt die Beleuchtung von Modulen mit pn-Übergang auf der Zellrückseite und SiN_y/n⁺-Typ Silizium Oberflächenpassivierung zu einer Verschlechterung der Modulleistung von 15 %. Die Modellierung der Quanteneffizienzmessungen mittels numerischer Simulationen zeigt, dass hochenergetische Photonen die Oberflächenrekombination um einen Faktor von 18 erhöhen. Mit dem physikalischen Modell erhalten wir ein ähnliches Ergebnis, welches eine Erhöhung der Oberflächenrekombination um einen Faktor von 17 zeigt.

Stichwörter: Solarzellen, Solarmodule, UV Degradation

Contents

1	Introduction	1
2	State of the art industrial cells and modules	4
2.1	Passivated emitter and rear cells	4
2.2	Role of the amorphous silicon nitride (SiN_y) layer	5
2.2.1	The SiN_y anti-reflection coating	6
2.2.2	The SiN_y surface passivation layer	9
2.2.3	Modeling recombination	10
2.3	The passivated emitter and rear cell (PERC) front and rear metalization	11
2.4	Recombination below metal contacts	12
2.5	Current density and voltage characteristics of a solar cell and a solar module	13
2.6	General structure of a solar module	15
2.7	Cell interconnection wires	17
2.8	Cell to module losses	17
2.8.1	Resistive cell to module losses	19
2.8.2	Optical cell to module losses	19
2.9	Accelerated aging with ultraviolet (UV) light	20
3	Sample preparation and characterization techniques	24
3.1	PERC baseline process	24
3.2	PERT cell process	26
3.2.1	Variation of the silicon nitride layer	27
3.2.2	Adaptations of the front and rear metalization	27
3.2.3	Sample preparation and determination of optical finger and busbar properties	28
3.3	Test module baseline process	29
3.3.1	Samples for optical interconnector properties	30
3.3.2	Samples for the optical characterization of the encapsulation polymers	31
3.3.3	Test modules for the verification of the analytical cell to module loss model	31
3.3.4	Test modules for accelerated UV testing	32
3.4	Characterization techniques	34
3.4.1	Variable angle spectroscopic ellipsometry	34
3.4.2	Reflection and transmission measurement	35
3.4.3	Quasi steady state photoconductance decay measurements	36

3.4.4	Determination of the specific finger, busbar and cell interconnector resistances	36
3.4.5	Determination of the contact resistance	37
3.4.6	Determining cell and minimodule current-voltage characteristics	39
3.4.7	Quantum efficiency and reflection measurements	41
3.4.8	Light beam induced current measurements	42
3.5	Accelerated aging with ultraviolet light	42
4	Determining the cell and module model parameters from the experimental results for the modeling of cell to module losses	44
4.1	Current voltage analysis of the passivated emitter and rear cells	44
4.2	Optical properties of cell interconnectors	45
4.2.1	Results of the measurement of the optical properties of the cell interconnectors	45
4.2.2	Discussion of the optical properties of the cell interconnectors	48
4.3	Geometrical and optical properties of front metal fingers	49
4.3.1	Results of the finger geometry measurements	49
4.3.2	Results of the measurement of the optical properties of the front metal fingers	51
4.3.3	Modeling the effective optical finger width in a module	52
4.3.4	Discussion of the cell to module losses for the front metal fingers	53
4.4	Finger-emitter contact resistance	55
4.4.1	Results of the finger-emitter contact resistance measurements	55
4.4.2	Discussion of the finger-emitter contact resistance measurements	55
4.5	Optical properties of the backsheet within a solar module	56
4.5.1	Modeling the effect of the backsheet reflection on the module current	56
4.5.2	Discussion of the current enhancement by the backsheet	57
4.6	Parameters from literature	58
4.7	Parameter overview	59
5	Modeling cell to module losses	61
5.1	Analytical series resistance model	61
5.1.1	Comparing the analytical series resistance model to finite element simulations	70
5.1.2	Applying the optical factors	71
5.1.3	Recombination losses for varying front metalization	71
5.1.4	Applying the analytical model to experimental test modules	71
5.1.5	Discussion of the analytical model presented in this work	73
5.2	Modeling the module power output for variations of the front metalization and cell interconnection	74
5.2.1	Influence of the number of front fingers	75
5.2.2	Influence of the number of cell interconnectors	76
5.2.3	Module power output for various module configurations	76
5.2.4	Effect of the cell spacing	78
5.2.5	Discussion of the simulated finger number, CI number and CI width	79
5.3	Application of the analytical model to full-sized modules	80
5.3.1	Building a high power module	80
5.3.2	Breakdown of the cell to module losses	81

5.3.3	Building a high efficiency module	82
5.3.4	Discussion of the application of the analytical model to full-sized modules	83
6	Accelerated aging with ultraviolet light	85
6.1	Measurement results of test samples and modules	86
6.1.1	Results of the ellipsometer measurements on planar test samples with varying passivation layer	86
6.1.2	Results of the transmittance measurement of test samples with varying encapsulation materials	87
6.1.3	Results of the electrochemical capacitance voltage measurement	88
6.1.4	Results of the current-voltage measurement of test modules .	89
6.1.5	Discussion of optical and current-voltage measurement results	90
6.2	UV degradation of solar modules featuring passivated emitter and rear cells	90
6.2.1	Results of UV degradation of PERC test modules with varying encapsulation material	90
6.2.2	Results of UV degradation of PERC test modules with varying SiN _y refractive index	92
6.2.3	Discussion of UV aging experiments of PERC test modules .	93
6.3	Analytical modeling of UV degradation	94
6.4	UV aging of test modules featuring PERT cells	99
6.4.1	Results of UV aging experiments	99
6.4.2	Discussion of UV aging experiments	101
6.5	Numerical modeling the UV degradation of the external quantum efficiency	101
6.6	Modeling variations of the fixed charge	102
6.7	Improved UV stability of silicon nitride passivation layers	104
6.7.1	Results of quasi-steady state measurements on silicon oxide and silicon nitride passivation stacks	104
6.7.2	Discussion of the quasi-steady state measurements	105
7	Summary	107
7.1	Analysis and reduction of cell to module losses	107
7.2	Ultraviolet radiation hardness of solar modules	108
A	Appendix A	111
A.1	Contact resistance	111
A.2	Half cell contact firing	112
	Bibliography	114
	List of publications	132
	Acknowledgments	136

List of Abbreviations

$I(V)$	current-voltage characteristics
$J(V)$	current density-voltage characteristics
3D	three dimensional
a-Si	amorphous silicon
Ag	silver
Al	aluminum
AlO_x	aluminum oxide
ARC	anti-reflection coating
BSF	back surface field
c-Si	crystalline silicon
CI	cell interconnector
CIR	cell interconnection ribbon
CIW	cell interconnection wire
CTM	cell to module
Cz	Czochralski
DDM	double-diode model
ECV	electrochemical capacitance voltage
EMA	ethylene-methyl acrylate copolymer
EQE	external quantum efficiency
EVA	poly ethylene-vinyl acetate
FEM	finite element method
FZ	float-zone
HF	hydrofluoric acid
IBC	interdigitated back contact solar cells
IEC	International Electrotechnical Commission
IMR	intermediate reflector
IR	near infra red
ISFH	Institute for Solar Energy Research Hamelin
KOH	potassium hydroxide
LBIC	light beam induced current
LCO	laser contact opening
LCOE	levelized cost of electricity
MIS	metal insulator semiconductor
MPP	maximum power point
PECVD	plasma enhanced chemical vapour deposition
PERC	passivated emitter and rear cell
PERT	passivated emitter, rear totally-diffused
PET	poly ethylene terephthalate

List of Abbreviations

PO	polyolefin
PU	polyurethane
PV	photovoltaic
PVB	polyvinyl butyral
PVDF	polyvinylidene fluoride
PVF	polyvinyl fluoride
QSSPC	quasi-steady-state photoconductance
QWOT	quarter-wave optical thickness
RCA	Radio Corporation of America
RCE	rotating-compensator ellipsometer
SALD	spatial atomic layer deposition
SEM	scanning electron microscope
Si	silicon
SiN _y	amorphous silicon nitride
SiO ₂	silicon dioxide
SiO _x	silicon oxide
SIR	string interconnection ribbon
SRH	Shockley-Read-Hall
SRV	surface recombination velocity
SSR	sum of squared residuals
STC	standard testing conditions
TEM	transmission electron microscope
TiO ₂	titanium dioxide
TLM	transmission line method
UV	ultraviolet
VASE	variable angle spectroscopic ellispometry

List of symbols

Symbol	Description	Unit
$A_{\text{act,ci}}$	active cell area adjacent to a cell interconnection ribbon	m^2
$A_{\text{act,f}}$	active cell area adjacent to a finger	m^2
A_{act}	active cell area	m^2
A_{cell}	cell area	m^2
A_{ciw}	cross section area of a cell interconnection wire	m^2
A_{ci}	cell area covered with cell interconnection ribbon	m^2
A_{dev}	device area	m^2
A_{f}	cross section area of front metal finger	m^2
A_{perc}	absorption for a PERC	-
A_{tcci}	total cell interconnector cross section area	m^2
D_{it}	interface state density	m^{-2}
D_{uv}	UV dose	kW h m^{-2}
EQE_{cell}	EQE of a cell	-
E_{e}	Irradiance per area	W m^{-2}
E_{g}	bandgap energy	eV
E_{t}	defect state energy	eV
E_{uv}	irradiance of UV light source	W m^{-2}
FF	fill factor	%
I	current	A
$I_{\text{act,ci}}$	current of area consisting of active and cell interconnection ribbon area	A
I_{act}	current of active area	A
I_{i}	intensity of incident light	W m^{-2}
I_{mpp}	current at maximum power point	A
I_{r}	intensity of reflected light	W m^{-2}
I_{sc}	short circuit current	A
I_{t}	intensity of transmitted light	W m^{-2}
J	current density	A m^{-2}
J_{01}	first diode saturation current density	A m^{-2}
J_{02}	second diode saturation current density	A m^{-2}
J_{0b}	base saturation current density	A m^{-2}
$J_{0e,\text{met}}$	metalized emitter saturation current density	A m^{-2}
$J_{0e,\text{pass}}$	passivated emitter saturation current density	A m^{-2}
J_{0i}	saturation current density prior UV degradation	A m^{-2}
$J_{0r,\text{bsf}}$	rear BSF saturation current density	A m^{-2}
$J_{0r,\text{pass}}$	passivated rear saturation current density	A m^{-2}

Symbol	Description	Unit
$J_{0s,met}$	saturation current density for metalized surface	$A m^{-2}$
$J_{0s,pass}$	saturation current density for passivated surface	$A m^{-2}$
J_{0s}	surface saturation current density	$A m^{-2}$
J_0	saturation current density	$A m^{-2}$
J_{mpp}	current density at maximum power point	$A m^{-2}$
$J_{sc,act}$	short circuit current density of active area	$A m^{-2}$
J_{sc}	short circuit current density	$A m^{-2}$
$J_{sc}(V_{oc})$	$J_{sc}(V_{oc})$ characteristics	$A m^{-2}$
L_t	transfer length	m
N_{ci}	number of cell interconnector	-
N_{cpm}	number of cells per module	-
N_{cps}	number of cells per string	-
N_f	number of front metal fingers	-
N_{it}	number of interface states per area	m^{-2}
N_{ph}	number of photons	$m^{-2} s$
N_{sp}	number of solder pads	-
N_{uci}	number of unit cells	-
P_{cell}	power output of a solar cell	W
P_{cell}	power output of a solar module	W
P_{mpp}	power at maximum power point	W
Q_f	fixed charge density	m^{-2}
R	reflectance	-
R_{Ag}	reflectance of a front metal fingers	-
$R_{c,f}$	finger contact resistance	Ω
R_{cell}	reflectance of a cell	-
R_c	contact resistance	Ω
R_{int}	reflectance of a cell area without fingers	-
R_m	measured resistance	Ω
R_p	specific shunt resistance	Ωm^2
R_{sh}	sheet resistance	$\Omega \square^{-1}$
R_s	specific series resistance	Ωm^2
S_{n0}	surface recombination velocity of electrons	$m s^{-1}$
S_{p0}	surface recombination velocity of holes	$m s^{-1}$
T	transmittance	-
V	voltage	V
V_{mpp}	voltage at maximum power point	V
V_{oc}	open circuit voltage	V
Δn	average excess charge carrier concentration	m^{-3}
A	Lambertian factor	-
Φ	photon flux	m^{-2}
Φ_b	bond breaking photon flux	m^{-2}
η	energy conversion efficiency	%
η_{perc}	PERC collection efficiency	$m^{-2} s$
\hat{n}	complex refractive index	-
λ_0	wavelength of reflectance minimum	m
λ_b	critical wavelength of bond breaking photons	m
λ_c	cut-off wavelength	m
\mathcal{I}	amplitude of the electric vector of the incident field	-
ρ_{bb}	line resistance of a busbar	Ωm^{-1}

Symbol	Description	Unit
ρ_b	specific base resistance	$\Omega \text{ m}$
$\rho_{c,\text{rear}}$	line resistance of the aluminum (Al) rear side	$\Omega \text{ m}^{-1}$
ρ_c	specific contact resistance	$\Omega \text{ m}^{-1}$
ρ_f	line resistance of a finger	$\Omega \text{ m}^{-1}$
ρ_{rear}	line resistance of the Al rear side	$\Omega \text{ m}^{-1}$
σ_n	electron capture cross section area	m^2
σ_p	hole capture cross section area	m^2
σ_{uv}	UV photon capture cross section area	m^2
τ_{eff}	effective charge carrier lifetime	s
θ_i	angle of incidence	$^\circ$
θ_r	angle of reflection	$^\circ$
θ_t	angle of refraction	$^\circ$
c	speed of light in vacuum	m s^{-1}
d_{bb}	distance between busbars	m
d_{c2c}	cell to cell distance	m
d_{ciw}	cell interconnection wire diameter	m
d_c	contact distance	m
d_f	distance between two fingers	m
d_{s2s}	string to string distance	m
$f_{e,\text{met}}$	front metal area fraction	-
$f_{\text{met,opt}}$	effective optical front metal area fraction	-
$f_{r,\text{met}}$	rear metal area fraction	-
h	Planck constant	J s
h_{cell}	height of a cell	m
h_{uc}	height of a unit cell	m
k	extinction coefficient	-
k_{bb}	optical factor for a busbar	-
k_{bs}	optical enhancement factor of the backsheet	-
k_{ci}	optical factor for cell interconnector	-
$k_{f,\text{cell}}$	optical factor for front metal finger of a cell	-
$k_{f,\text{mod}}$	optical factor for front metal finger in a module	-
k_{red}	reduction of module's current due to glass and EVA	-
l_f	length of a front metal finger	m
n	refractive index	-
n_1	parameter in SRH recombination equation	m^{-3}
n_i	intrinsic carrier concentration	m^{-3}
n_s	surface electron concentration	m^{-2}
p_1	parameter in SRH recombination equation	m^{-3}
p_f	finger pitch	m
p_s	surface hole concentration	m^{-3}
r_{bb}	specific resistance of a busbar	$\Omega \text{ m}$
r_c	reflection coefficient	-
r_f	specific resistance of a finger	$\Omega \text{ m}$
r_{mat}	specific resistance of a material	$\Omega \text{ m}$
t_{SiN}	thickness of the SiN_y layer	m
t_{bb}	thickness of a busbar	m
t_{cell}	cell thickness	m
t_{cir}	cell interconnection ribbon thickness	m
t_c	transmission coefficient	-

Symbol	Description	Unit
t_{eva}	thickness of the EVA	m
t_f	thickness of a front metal finger	m
t_{glass}	thickness of the glass	m
t_{sir}	string interconnection ribbon thickness	m
t_{uv}	UV exposure time	s
v_{th}	thermal velocity	$m s^{-1}$
w_{bb}	width of a busbar	m
w_{cell}	width of a cell	m
$w_{ci,eff}$	effective optical width of cell interconnector	m
w_{cir}	cell interconnection ribbon width	m
w_{ci}	cell interconnector width	m
$w_{f,eff}$	effective optical width of a finger	m
w_f	width of a front metal finger	m
w_{sir}	string interconnection ribbon width	m
w_{uc}	width of a unit cell	m

CHAPTER 1

Introduction

In 2017 the Kaneka company presented a record-breaking crystalline silicon (c-Si) solar cell with a power conversion efficiency of 26.6% [1]. This further closed the gap to the theoretical maximum efficiency limit of 29.4% for single junction c-Si solar cells [2]. The same company also holds the efficiency record for photovoltaic (PV) modules with 24.4% [3], which indicates the higher potential for the improvement of modules compared to cells. Both records were achieved utilizing laboratory scale production equipment.

Employing mass production techniques the modules with the highest efficiencies that are commercially available are produced by SunPower with an efficiency of about 22.8% [4]. However, these modules use interdigitated back contact solar cells (IBC), which are more expensive than aluminum (Al) back surface field (BSF) solar cells. Figure 1.1 (a) shows the average PV-system price per installed capacity in the United States for six solar module manufacturers. The data is taken from Ref. [5]. Here, we advice the reader that the data in Fig. 1.1 (a) needs to be regarded with care, since the PV modules make up only a fraction of about 30% of the total system price and components like the mounting system, installation, cables etc. scale with the size of the PV system [7]. We consider only the years from 2012 to 2016 and filter the top six c-Si solar module manufacturers according to the number of installed PV systems. The dark bars represent data for manufacturers producing solar modules with Al-BSF solar cells. The orange bar denotes the data for SunPower's modules employing high efficiency IBC. For the solar modules from REC Solar, the average system price per watt is 3.8 \$/W. In contrast, utilizing SunPower's modules increases the PV system price by about 35%.

However, besides the solar module's efficiency the module prize is of major importance for the costumer. Thus, in 2017 the majority of solar modules comprise of Al-BSF c-Si solar cells, covering a market share of over 70% [8]. This cell type has been optimized in the last decades and cell efficiencies of 20.3% with industrial production equipment have been reported [9]. Interconnecting and encapsulating the cells in a solar module further reduces their efficiency due to optical, recombination, and resistive cell to module (CTM) losses. Thus, the solar modules featuring Al-BSF cells with the highest module efficiency have an efficiency of about 18.4% [10], a loss in efficiency of 1.9%_{abs} compared to the solar cell. Obviously, there is a huge gap between state of the art low cost industrial manufactured solar cells and modules. Thus, a reduction of the CTM losses is highly attractive for solar module manufacturers.

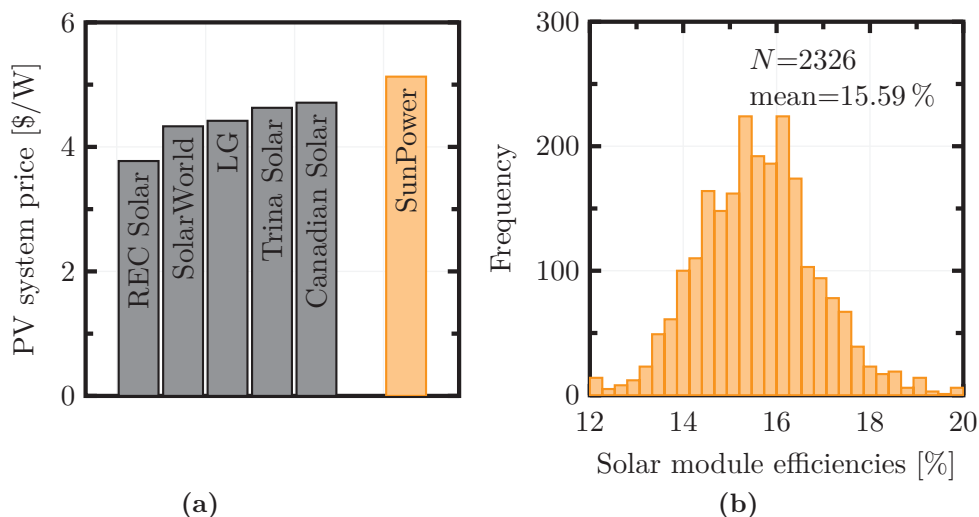


Figure 1.1: (a) Price for PV systems in the U.S. between 2012 and 2016 employing solar modules from various manufacturers. The data has been taken from Ref. [5]. (b) Frequency of the efficiency from 2326 commercially available solar modules featuring c-Si cells. The mean module efficiency is 15.59%. The data was taken from Ref. [6]

Due to the cell architecture the efficiency of Al-BSF cells is limited to about 20% [11]. Considering fluctuations in the production processes, the average module efficiency is even lower. Figure 1.1 (b) shows a histogram of 2326 commercial available c-Si PV modules. For the plot we take the data from Ref. [6] and filter all solar modules with 60 c-Si solar cells. The average module conversion efficiency of the 2326 modules is 15.6%. Thus, besides a reduction of CTM losses further developed cell technologies are required for high efficiency modules.

An interesting alternative with similar production costs as the Al-BSF cell is the passivated emitter and rear cell (PERC). Many studies predict that the PERC technology has the potential for solar cells with conversion efficiencies of over 24% [12, 13] and solar modules with 22% [12]. Hence, the PERC technology may lead to a new era of industrial high efficiency solar cells and modules. At the beginning of this work there have been only a few reports regarding CTM losses for this cell type. Before this work the highest reported efficiency for an industrial type solar module with 60 PERC was 19.5%, with an independently confirmed module power of 294 W [14]. Despite this outstanding result the authors report a CTM loss in module power of 2%.

The purpose of this work is to further investigate the CTM losses for PERC modules, with focus on understanding the coupling of the losses on the cell and module level. This requires to study the optical, recombination, and resistive losses of the solar cell as well as the solar module in carefully designed experiments. Based on the experimental results we develop an analytical model to simulate and reduce the CTM losses on the cell and module level. The optimizations on the cell and module level allow to build a high efficiency PERC module with a conversion efficiency over 20%.

Besides a high module efficiency and low production costs, the solar module's reliability is of major importance for the manufacturers and customers. The materials for solar modules are precious and therefore solar modules should produce a constant

power output for a long service life under various weather conditions. Thus, introducing a cutting-edge technology into mass production may fail if it lacks long-term stability. Industrial solar modules have to pass various accelerated aging tests to allow manufacturers to issue a product warranty that guarantees a constant module power output for many years of outdoor exposure [15, 16, 17, 18, 19]. Further, the modules need to pass these tests to fulfill various standards and get certificated for their installation. There are many accelerated test methods to stress the cell and module components, which are well established procedures for module manufacturers, e.g. humidity freeze cycles, damp heat tests or mechanical loading (see Refs. [15, 16, 17, 18, 19]).

A test that generally mainly focuses on the reliability of the module's encapsulation materials is the accelerated aging with ultraviolet (UV) light. Several publications imply that UV light may influence the dielectric passivation layers at the cell's surface. The PERC cell architecture and the development of new metalization pastes increase the spectral response of PERC in the UV wavelength range. Thus, module manufacturers increasingly apply encapsulation polymers with enhanced UV transparency to exploit this improved spectral response in PERC solar modules. This increases the power output of the solar module and the annual yield. However, there are few reports regarding the UV stability of PERC modules in the literature. Thus, we also examine the UV radiation hardness of PERC solar modules in this work.

In chapter 2, we introduce the PERC solar cell and module concepts as well as the theoretical background for the modeling of the CTM losses and the degradation mechanisms due to UV radiation.

Chapter 3 describes the experimental test structures and characterization techniques to determine the material properties as input parameters for the CTM and the UV aging model. Furthermore, we build experimental test modules to verify the simulation results.

In chapter 4 and 5 we analyse the optical, recombination, and resistive CTM losses for PERC solar modules. We present an analytical model based on our experimental results to simulate these CTM losses. We verify the model by comparing the simulation with experimental results of six test modules. After verification, we apply the model to simulate the effect of changes in the front metalization, cell interconnection and cell spacing on the optical, recombination, and resistive CTM losses for a PERC module. We employ the analytical model to optimize the cell front metalization and the cell interconnection to build two modules, one aiming for an enhanced power output and one aiming for an improved module efficiency.

In chapter 6, we examine the UV radiation hardness of solar modules featuring PERC. From the literature it is known that UV light may affect the cell's surface passivation layers [20]. However, an analysis of the UV stability of PERC in a solar module is missing. Moreover, there exist only phenomenological models and a physical model to describe and understand the degradation mechanism due to UV radiation is missing. Hence, we investigate the UV radiation hardness of various PERC. Additionally, we examine the UV radiation hardness of passivated emitter, rear totally-diffused (PERT) cells and develop a physical model to understand the UV light induced degradation mechanisms.

Finally, chapter 7 summarizes all the results of this work.

CHAPTER 2

State of the art industrial cells and modules

In this chapter we introduce the passivated emitter and rear cell (PERC) as the central cell technology of this work and highlight the differences to the currently market-dominating Al-BSF cell. We focus on the silicon nitride layer and the front metalization, since their influence on the optics, the recombination and resistive properties of the solar cell is vital for this thesis. The second part of the chapter introduces the solar module structure and gives an overview of the cell to modules losses as well as UV aging processes for solar cells and modules.

2.1 Passivated emitter and rear cells

In 1972 Mandelkorn et al. [21] presented a c-Si solar cell concept with a full area aluminum (Al) rear contact. They reported unusual high voltages due to an electric field at the rear side of the cell, created by the Al-silicon eutectic alloy that forms within a rapid thermal process step. This electric back surface field (BSF) was the patron for the name of this cell concept that is nowadays known as full area Al-BSF solar cell. In 2017, this cell type is dominating the solar cell industry with a market share of over 70 % [8].

Figure 2.1 (a) schematically shows the cross section scheme of an Al-BSF cell. It consists of a p-type base with an n⁺-type front emitter. An amorphous silicon nitride (a-SiN_y:H abbreviated with SiN_y in this work) layer covers the front side of the emitter. At the front side silver (Ag) fingers and busbars contact the n⁺-type emitter to extract the cell's current. On the rear side, an Al layer covers the p-type base. The thin Al-silicon (Si) eutectic alloy forms the p⁺ BSF region. This BSF reduces the recombination of charge carriers at the rear surface and enables the formation of an Ohmic contact between the Si and the Al metal layer [21, 22]. However, the absorption of near infra red (IR) light in the Al is detrimental and realizing rear saturation current densities below 200 fA cm⁻² is challenging [23, 11]. This limits the efficiency of Al-BSF cells to about 20 %, which is far below the theoretical limit for single junction c-Si solar cells of 29.4 % [2].

In 1989 Blakers et al. [24] presented a cell concept with a conversion efficiency of 22.8 %. Besides the dielectric layer at the front, they also applied a dielectric layer at

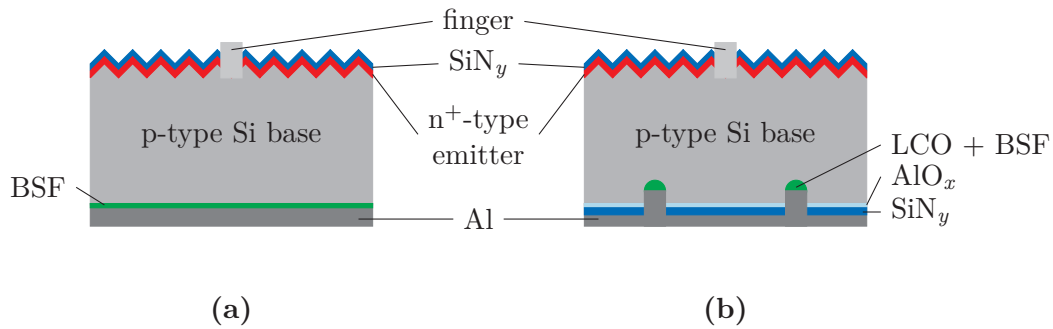


Figure 2.1: (a) Scheme of an Al-BSF cell. (b) Scheme of a PERC.

the rear side. This layer overcomes the drawbacks of the Al-BSF cell by increasing the reflection of light at the cell's rear side. Further, the dielectric layers reduce the recombination of charge carriers at the cell's surfaces, termed passivation. Hence, Blakers et al. named this cell concept a passivated emitter and rear cell (PERC). Three decades later, PERCs are on the transition to industrial mass production and predicted to be the successor of the Al-BSF cell concept in terms of market share [8, 25]. In the literature record efficiencies for industrial like mono c-Si PERC of 22.6% have been reported [26].

Figure 2.1 (b) schematically depicts the cross section of a PERC. It consists of a p-type base with an n^+ -type front emitter. At the front side Ag fingers and busbars contact the n^+ -type emitter to extract the cell's current. As for the Al-BSF, a SiN_y layer covers the front side of the emitter. On the rear side, a stack of aluminum oxide (AlO_x) and SiN_y covers the rear side of the base. On the rear side laser contact openings (LCOs) in the $\text{AlO}_x/\text{SiN}_y$ stack enable the local contact formation of the full area Al rear metalization with the base. The contact formation is realized in a rapid thermal firing process, where the Al also creates a local BSF within the LCOs.

2.2 Role of the SiN_y layer

The requirements for the dielectric amorphous silicon nitride (SiN_y) layer of a PERC are threefold. On the front side it acts as an anti-reflection coating (ARC), while on the rear side it increases the reflection of light back into the cell. Further, it acts as a passivation layer that reduces the recombination of charge carriers at the cell's surfaces. In 1981 Hezel et al. [20] first reported about the passivation capabilities and one year later Sexton [27] reported about the ARC properties of SiN_y for solar cells.

Other conceivable dielectric passivation layers for solar cells are, e.g. aluminum oxide (AlO_x), amorphous silicon (a-Si), silicon dioxide (SiO_2) or titanium dioxide (TiO_2). However, for an industrial PERC a passivation layer also has to meet additional requirements regarding costs, processing steps and long term stability.

For the primordial PERC Blakers et al. applied a silicon dioxide (SiO_2) layer at the PERC's front and rear side. For a long time the highest reported efficiencies for single junction silicon solar cells had been achieved with a thermal SiO_2 [28, 29].

A drawback of thermal oxides is the high deposition temperature of about 1000 °C, which is cost intensive for industrial mass production. Plasma enhanced chemical vapour deposition (PECVD) is a deposition technique that reduces the production costs. However, PECVD deposited SiO₂ lacks thermal stability within the high temperature contact firing step, when it is coated with an Al layer, which is required for industrial PERC [30, 31, 32, 33]. Similar problems regarding firing stability have been reported for amorphous silicon (a-Si), since it starts to crystallize at high temperatures [30, 34]. Furthermore, such passivation layers suffer from parasitic absorption [35]. The ARC properties of titanium dioxide (TiO₂) were already known from its application in the glass industry and first concepts for solar cells have been reported in the 1970's [36, 37]. Yet, the passivation quality of a single layer is not satisfying for the application in solar cells [38]. AlO_x provides excellent passivation qualities, but generally only for p-type silicon and may also suffer from thermal stability problems, when deposited as a single layer [39, 40].

SiN_y meets all these requirements for an anti-reflection coating (ARC) and a passivation layer. In the mass production as well as in this work it is deposited in a PECVD process at low temperatures of 350 °C to 400 °C. Furthermore, it creates a surface passivation that is stable after the contact firing step [41, 42]. This enables the application of screen-printing technology for printing the metal contacts and employing metal pastes with glass frits that etch through the dielectric layer during the fast firing step for the contact formation.

Covering an AlO_x with a SiN_y layer also results in a thermal stable passivation layer stack [39, 40]. For this combination of SiN_y and AlO_x the best passivation qualities on p-type silicon have been reported with effective surface recombination velocities below 10 cm s⁻¹ [43, 44, 39].

Due to the excellent passivation quality, low temperature deposition and an over a wide range adjustable refractive index, SiN_y is commonly used for the application in industrial PERC manufacturing [45, 38, 46, 47].

2.2.1 The SiN_y anti-reflection coating

There are several approaches to reduce the unintended reflection properties of surfaces, but the most widely used is the application of a quarter-wave optical thickness (QWOT) layer. The principle is based on destructive interference, which minimizes the reflectivity of a surface for a certain wavelength and angle of incidence. Bare silicon reflects on average 35 % of the incident light in the wavelength range of 300 nm to 1200 nm [27]. On a planar surface an anti-reflection coating potentially reduces this reflection loss to 11 % [27]. A textured cell surface further improves the light trapping, resulting in an average reflection below 3 % with an ARC [48, 49].

The key parameters for an optimal ARC are the complex refractive index \hat{n} and the thickness t_{SiN} . The complex refractive index is defined as

$$\hat{n} = n + ik, \tag{2.1}$$

where the real part n is the refractive index and the imaginary part k the extinction coefficient. Both, n and k vary with the wavelength of the light [50, 51]. Within this work we always report n and k for a wavelength of 633 nm.

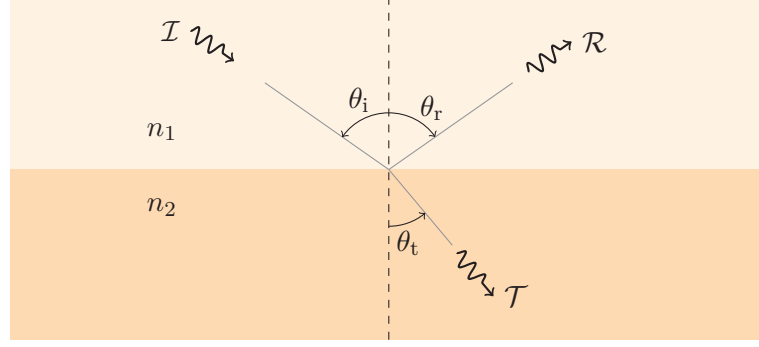


Figure 2.2: Two media layer systems illustrating Snell's law. Media 1 has a refractive index n_1 and media 2 has a refractive index n_2 .

Figure 2.2 schematically shows a light ray with complex amplitude \mathcal{I} incident on the interface of two media under the angle θ_i . The light ray splits into a part that is transmitted \mathcal{T} with angle θ_t into the second media and a part \mathcal{R} that is reflected with angle θ_r . The characteristic angles relate according to Snell's law to [50, 51]

$$\theta_t = \theta_i \arcsin\left(\frac{n_1}{n_2}\right). \quad (2.2)$$

The ratio of the reflected complex amplitude \mathcal{R} and the transmitted complex amplitude \mathcal{T} to the incident complex amplitude \mathcal{I} is termed the reflection coefficient r_c and the transmission coefficient t_c [50]:

$$r_c = \frac{\mathcal{R}}{\mathcal{I}} \quad \text{and} \quad t_c = \frac{\mathcal{T}}{\mathcal{I}}. \quad (2.3)$$

The complex amplitude of the incident wave consists of two independent components that are parallel (\parallel) and perpendicular (\perp) to the plane of incidence. Solving Maxwell's equations for both components results in the well known Fresnel equations for the corresponding r_c and t_c [50]:

$$\left. \begin{aligned} r_{c\parallel} &= \frac{n_2 \cos \theta_i - n_1 \cos \theta_t}{n_2 \cos \theta_i + n_1 \cos \theta_t}, \\ r_{c\perp} &= \frac{n_1 \cos \theta_i - n_2 \cos \theta_t}{n_1 \cos \theta_i + n_2 \cos \theta_t} \end{aligned} \right\} \quad (2.4)$$

$$\left. \begin{aligned} t_{c\parallel} &= \frac{2n_1 \cos \theta_i}{n_2 \cos \theta_i + n_1 \cos \theta_t}, \\ t_{c\perp} &= \frac{2n_1 \cos \theta_i}{n_1 \cos \theta_i + n_2 \cos \theta_t} \end{aligned} \right\} \quad (2.5)$$

These equations are crucial for the later ray tracing simulations and the optical measurements.

We define the reflectance R and transmittance T as the ratio of the reflected I_r and transmitted intensity I_t to the incident intensity I_i of the light

$$R = \frac{I_r}{I_i} = \frac{|\mathcal{R}|^2}{|\mathcal{I}|^2} = |r_c|^2 \quad \text{and} \quad T = \frac{I_t}{I_i} = \frac{|\mathcal{T}|^2}{|\mathcal{I}|^2} = \frac{n_2 \cos \theta_t}{n_1 \cos \theta_i} |t_c|^2. \quad (2.6)$$

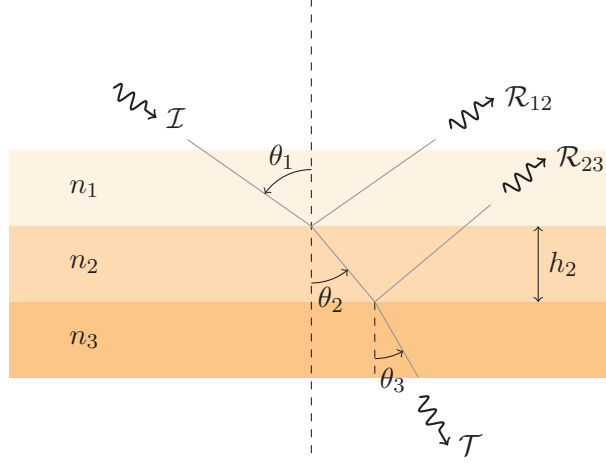


Figure 2.3: A dielectric layer with refractive index n_2 and thickness h_2 situated between two media with refractive index n_1 and n_3 . One part of the incident light ray \mathcal{I} is reflected at the interfaces resulting in reflections \mathcal{R}_{12} and \mathcal{R}_{23} , while the other part is transmitted resulting in a light ray \mathcal{T} .

By the law of conservation of energy $R+T=1$, if there is no absorption in the media.

Figure 2.3 shows a homogeneous dielectric layer with refractive index n_2 and thickness h_2 , situated between two homogeneous media with refractive index n_1 and n_3 . This is generally the case for a solar cell, where media 1 may represent the atmosphere or the encapsulation polymer, the dielectric layer the ARC and media 3 the silicon. The angles θ_1 , θ_2 , and θ_3 indicate the angle between the light ray and the surface normal of each layer. A part of the incident light ray \mathcal{I} is reflected at the interfaces of the layers, resulting in reflections \mathcal{R}_{12} and \mathcal{R}_{23} , while the other part is transmitted resulting in a light ray \mathcal{T} .

In the special case of normal incident light, $\theta_i=0$ and the reflectance relates to [51, 52]

$$R = \left(\frac{n_1 n_3 - n_2^2}{n_1 n_3 + n_2^2} \right)^2. \quad (2.7)$$

For a minimum in reflectance of the dielectric layer the refractive index relates to

$$n_2 = \sqrt{n_1 n_3}. \quad (2.8)$$

This relation is crucial for optimizing the optics of the solar cell's anti-reflection coating for a measurement in a cell tester or within a solar module. As an example, considering a c-Si solar cell with $n_3=3.87$ in air with $n_1=1$, the reflectance will be a minimum for an ARC with $n_2 \approx 1.97$, while for a solar cell encapsulated in a polymer with $n_1=1.5$, an $n_2 \approx 2.41$ reduces the reflection.

The position of the reflection minimum as a function of the wavelength depends on the thickness of the ARC. The optimal thickness of the ARC for a certain wavelength λ_0 is obtained by [51]

$$t_{\text{ARC}} = \frac{\lambda_0}{4n_2}. \quad (2.9)$$

The refractive index of SiN_y is adjustable within a range of 1.85 to 2.62 [47]. Varying the SiH₄/NH₃/H₂ gas flow in the PECVD tool changes the stoichiometry and consequently, the refractive index of the SiN_y layer. Therefore, SiN_y is suitable as an ARC for solar cells in air as well as for solar cells within a module.

However, changing the stoichiometry and increasing the silicon fraction also increases the imaginary part of the complex refractive index and thus, the absorption of the ARC [47, 53]. Hence, an optimization of the anti-reflection coating requires a careful balancing of \hat{n} and t_{SiN} .

2.2.2 The SiN_y surface passivation layer

Besides reducing the reflection of incident light, SiN_y also acts as a surface passivation layer on silicon. Illuminating a solar cell generates excess charge carriers. These photo-generated excess charge carriers decay after their lifetime by a process termed recombination. We distinguish between three fundamental recombination processes: (i) radiative recombination, (ii) Auger recombination, and (iii) recombination via defect states, also termed Shockley-Read-Hall (SRH) recombination [54, 55]. The latter describes the recombination via defect states in the band gap of the semiconductor. The surface of the solar cell is an abrupt termination of the silicon crystal lattice resulting in defects due to unsaturated dangling bonds. These defects act as recombination states in the band gap and thus, cause SRH recombination.

A passivation layer reduces the recombination of electrons and holes at the surface. Numerous studies showed that SiN_y provides excellent passivation qualities [20, 56, 46, 38, 57, 45]. The origin of the passivation by SiN_y is twofold: (i) It reduces the number of dangling bonds and thus, the density of recombination active interface trap states D_{it} at the silicon surface, termed chemical passivation. (ii) It reduces the concentration of minority charge carriers at the surface due to a fixed charge density Q_{f} , termed field effect passivation. A recombination process requires the presence of both, electrons and holes, and thus, reducing the number of one charge carrier type reduces the surface recombination.

The chemical passivation is attributed to the large amount of hydrogen in the SiN_y layer, which passivates the dangling bonds [58]. The fixed charge density is a result of dangling bonds in the SiN_y layer known as K-centers. These K-centers act as traps for holes and create a positive fixed charge in the SiN_y layer [59, 60, 61, 62, 63]. In phosphorous doped silicon, holes are the minority charge carriers and in boron doped silicon, electrons are the minority charge carriers. When depositing SiN_y on a phosphorous doped n-type emitter the positive charge induces an accumulation layer. On boron doped p-type silicon the positive charge creates an inversion layer. Both layers reduce the concentration of minority charge carriers near the surface and hence, reduce the surface recombination [20]. However, for PERC various research groups showed that an accumulation layer passivates the boron doped base more efficacious than a SiN_y inversion layer [44, 43, 64]. Thus, AlO_x with a negative fixed charge is applied to the p-type surfaces and SiN_y with the positive fixed charge is applied to the n-type surfaces of a PERC .

2.2.3 Modeling recombination

The modeling of the recombination of charge carriers in silicon has been extensively studied in transistors and solar cells since the 1950's [65, 66, 67, 68, 69, 70, 71, 72, 73, 74, 75, 76, 77]. In the following, we will focus on the surface recombination of the phosphorous emitter.

For a single trap or defect state at energy level E_t , charge carriers recombine at the surface according to the SRH recombination theory with the rate [65]

$$U_s = \frac{p_s n_s - n_i^2}{\frac{1}{v_{th} D_{it}} \left(\frac{p_s + p_1}{\sigma_n} + \frac{n_s + n_1}{\sigma_p} \right)}, \quad (2.10)$$

where v_{th} is the thermal velocity, n_i is the effective intrinsic carrier concentration, σ_n and σ_p are the electron and hole capture cross section coefficients, and n_s and p_s are the surface carrier concentrations of electrons and holes, respectively. The parameters n_1 and p_1 incorporate the thermal emission of charge carriers from a defect state and D_{it} is the density of defects states whose Fermi level coincides with E_t [54, 78, 79]. Upon integration over the whole band gap E_g , we calculate the total recombination rate as

$$U_s = \int_0^{E_g} \frac{p_s n_s - n_i^2}{\frac{1}{v_{th} D_{it}(E)} \left(\frac{p_s + p_1(E)}{\sigma_n(E)} + \frac{n_s + n_1(E)}{\sigma_p(E)} \right)} dE. \quad (2.11)$$

Close to the band edges the recombination through defects is negligible [80, 81, 82, 83, 84] and thus, n_1 and p_1 are negligible in Eq. 2.11. Assuming low level-injection and a heavily doped emitter, i.e. $n_s \gg p_s$, further simplifies Eq. 2.11 and the surface recombination rate is given by [71, 85, 72, 83]

$$U_s = \frac{p_s n_s - n_i^2}{n_s} \int_0^{E_g} v_{th} D_{it} \sigma_p dE. \quad (2.12)$$

Vice versa, for a p-type surface this assumption results in a surface recombination rate of

$$U_s = \frac{p_s n_s - n_i^2}{p_s} \int_0^{E_g} v_{th} D_{it} \sigma_n dE. \quad (2.13)$$

The integrals denote the surface recombination velocities for electrons and holes S_{n0} and S_{p0} that follow the relation

$$\left. \begin{aligned} S_{p0} &= \int_0^{E_g} \sigma_p v_{th} D_{it} dE \\ S_{n0} &= \int_0^{E_g} \sigma_n v_{th} D_{it} dE. \end{aligned} \right\} \quad (2.14)$$

Following the approach of Del Alamo et al. [85], we can express the recombination rate of a PERC with an n-type emitter as a surface saturation current density J_{0s}

$$J_{0s} = \frac{qU_s}{\frac{p_s n_s}{n_i^2} - 1} = \frac{q n_i^2 S_{p0}}{n_s}. \quad (2.15)$$

Since the saturation current density affects the open circuit voltage of a solar cell (see Eq. 2.19), Eq. 2.15 allows to relate effects on the surface passivation to the current-voltage characteristics of the solar cell.

2.3 The PERC front and rear metalization

Figure 2.4 (a) shows a typical state of the art front side and (b) a rear side metalization grid of a pseudo-squared PERC. The front side consists of three vertical Ag busbars and 88 horizontal Ag fingers. These fingers have to provide a low contact resistance to the emitter and a high conductivity to transport the current to the busbars. At the same time the shading of the active cell area by the fingers has to be small, which requires a high aspect ratio (height to width ratio). The busbars collect the current from the fingers and are important for the subsequent cell interconnection as well as the measurement of the cell's current-voltage $I(V)$ characteristic. We distinguish between two cell shapes: (i) a pseudo-square shape, a square with rounded corners as depicted in Fig. 2.4 and (ii) a full-square shape. Monocrystalline cells often have a pseudo-square shape due to the cylindrical form of the ingot from the pulling in the Czochralski (Cz) process. Multi crystalline cells often have a full-square shape [86].

There are many techniques to form the metal contacts for a solar cell like stencil-printing, pad-printing, ink-jet printing, dispensing, laser micro-sintering, evaporation or plating. Reference [87] provides an overview for the processes and application of the various techniques. All have their drawbacks when it comes to costs, production throughput rate, reliability, process complexity and finger aspect ratio.

In this work, we focus on the single screen-printing technology, since it is an industrially established metalization technique for the mass production of solar cells [8]. The width and the uniformity of the front fingers and busbars depend on the printing screen, the mesh and the Ag paste. A single screen-printing process creates the fingers and busbars in one printing step. This restricts this printing technique to the application of one metalization paste for fingers and busbars. Typical finger widths for single print go down to 45 μm .

The cell's rear side in Fig. 2.4 (b) features a full area Al layer with three rows of Ag solder pads. Each row consists of ten equidistantly spaced solder pads. These are crucial for the subsequent cell interconnection, since Al is not solderable due to the formation of a native oxide [88]. The bright horizontal lines in Fig. 2.4 (b) indicate the laser contact openings (LCOs) of the rear dielectric.

For the contact formation we perform a fast firing step in a conveyor belt furnace. The furnace comprises various zones of different temperature and during the firing process the cells reach a peak temperature of about 900 $^{\circ}\text{C}$. During the fast firing step the Al layer at the rear side liquefies at lower temperatures than the silicon. In

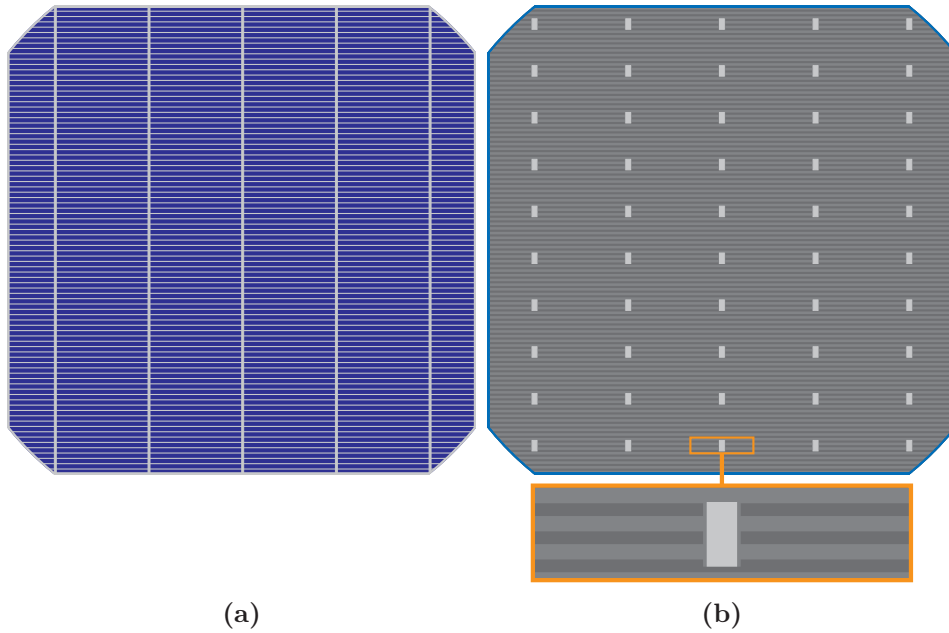


Figure 2.4: Scheme of the front and rear metalization of a pseudo-squared PERC. (a) Front metalization of a solar cell with three Ag busbars (vertical) and 88 Ag fingers (horizontal). The blue color indicates the SiN_y surface. (b) Al rear metalization of a PERC with three rows of Ag solder pads. Each row consists of ten solder pads. The horizontal lines in the magnification indicate the LCOs.

areas with LCOs, where the Al is in direct contact to the silicon, the solid silicon dissolves into the liquid Al. After the peak temperature point the liquid solidifies again and forms an eutectic layer that creates the local BSF in the LCOs [89]. In areas without LCOs the SiN_y layer blocks the liquid Al from the silicon and no alloy is formed [90]. For the front side the Ag paste contains lead borosilicate glass frits that enable the contact formation. During the fast firing step the glass frits etch through the SiN_y layer and allow the Ag particles to form a contact with the emitter [91]. In case of single screen-printing technology the busbars employ the same Ag paste and also contact the emitter.

2.4 Recombination below metal contacts

On the one hand, the contact formation is essential to extract and transport charge carriers from the cell to the terminals. On the other hand, the metal also creates defect states for recombination processes (pp. 10). Thus, it is necessary to distinguish between passivated and metalized surfaces. We assign each passivated and metalized surface a saturation current density $J_{0s,pass}$ and $J_{0s,met}$, respectively. For a PERC we distinguish the passivated surface saturation current densities for the emitter $J_{0e,pass}$ and rear side $J_{0r,pass}$ as well as the metalized surface saturation current densities for the metalized emitter $J_{0e,met}$ and the metalized rear side $J_{0r,bsf}$ [92]. We also assign a saturation current density J_{0b} for the base. Adding all saturation current densities

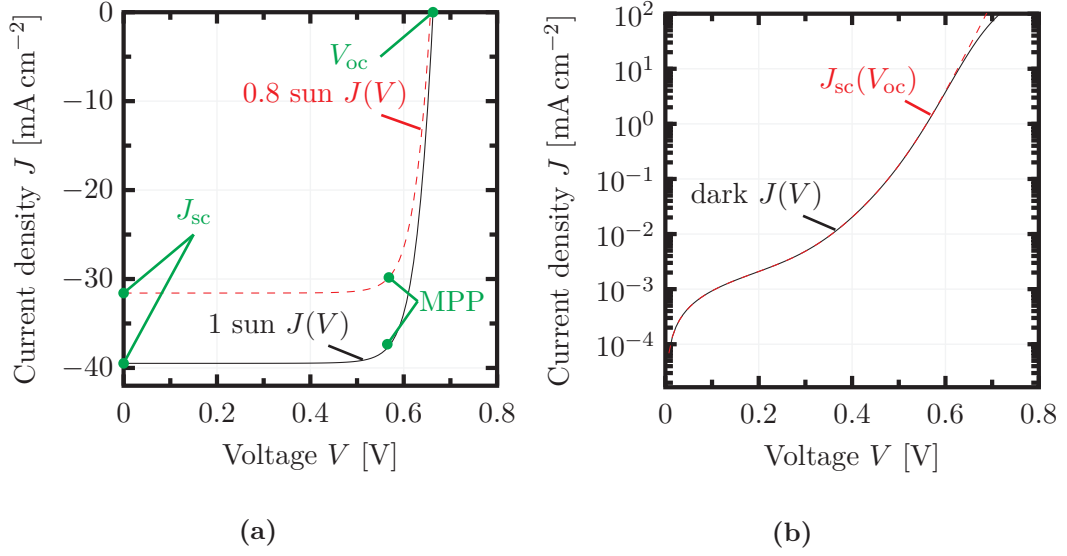


Figure 2.5: (a) Illuminated $J(V)$ characteristics for different illumination intensities of 0.8 and 1 sun. The green circles indicate the characteristic operation points of a solar cell. (b) Dark $J(V)$ and $J_{sc}(V_{oc})$ characteristics.

we obtain the saturation current density for the cell [93]

$$\begin{aligned}
 J_{01} &= J_{0s,pass} + J_{0s,met} + J_{0b} \\
 &= J_{0e,pass} (1 - f_{e,met}) \\
 &\quad + J_{0r,pass} (1 - f_{r,met}) \\
 &\quad + J_{0e,met} f_{e,met} + J_{0r,bsf} f_{r,met} + J_{0b},
 \end{aligned} \tag{2.16}$$

where $f_{e,met}$ and $f_{r,met}$ are the metal area fractions of the front and rear side, respectively.

At the rear side the Al contacts the base only in the vicinity of the LCOs of the rear dielectric and contributes to $f_{r,met}$ [94]. All saturation current densities affect the $J(V)$ characteristics of the solar cell. Thus, varying the metalization, bulk material or passivation layer of the solar cell influences the $J(V)$ characteristics of the solar module.

2.5 Current density and voltage characteristics of a solar cell and a solar module

Figure 2.5 shows the current density J as a function of the voltage V of a solar cell and a solar module, respectively. For the $J(V)$ characteristic, we measure the current I as a function of V and normalize the current to the device area A_{dev} , which is either the solar cell or the solar module area, to obtain the current density

$$J(V) = \frac{I(V)}{A_{dev}}. \tag{2.17}$$

This allows a comparison of the current-voltage characteristics for devices of different size, e.g. solar cells and solar modules.

Figure 2.5 shows the four $J(V)$ characteristics that are important for this work. Figure 2.5 (a) shows the $J(V)$ characteristics for two different illumination intensities of 1 sun and 0.8 sun. The terminology 1 sun denotes an illumination intensity of 1000 W m^{-2} with an AM1.5G spectrum [95]. The three characteristic operation points are the maximum power point (MPP), the short circuit current density J_{sc} and the open circuit voltage V_{oc} . At the MPP we denote the current density with J_{mpp} and the voltage with V_{mpp} . Likewise, we denote the power output of the solar cell or the solar module at this point with P_{mpp} . The P_{mpp} is calculated by

$$P_{mpp} = V_{mpp} J_{mpp} A_{dev} = V_{mpp} I_{mpp}, \quad (2.18)$$

where I_{mpp} is the current of the device at the MPP.

Figure 2.5 (b) shows the dark $J(V)$ and the $J_{sc}(V_{oc})$ characteristics. The dark $J(V)$ characteristic is measured without any illumination. For the $J_{sc}(V_{oc})$ characteristic the J_{sc} and V_{oc} are measured for various illumination intensities. Both characteristics are similar except for the high voltage range above 0.6 V. Here, the specific series resistance R_s influences the dark $J(V)$ characteristic, while there is no influence on the $J_{sc}(V_{oc})$ characteristics.

For the modeling of the $J(V)$ characteristics of a solar cell or module we employ the two-diode or double-diode model (DDM) [96, 97, 98, 99]. According to this model the current density relates to

$$J = J_{01} \left[\exp \left(\frac{q(V - JR_s)}{kT} \right) - 1 \right] + J_{02} \left[\exp \left(\frac{q(V - JR_s)}{2kT} \right) - 1 \right] + \frac{V - JR_s}{R_p} - J_{sc}, \quad (2.19)$$

where J_{01} and J_{02} are saturation current densities, R_s is a lumped series resistance and R_p is a lumped parallel resistance [100]. J_{02} describes the recombination within the depletion region [98, 99]. The shunt resistance originates from an unintended current flow between emitter and base and is ideally infinitely high to avoid any additional currents than the current flow to the terminals. The series resistance consists of contributions by the cell interconnection, metalization, emitter and base and thus, is of major importance when optimizing the solar cell interconnection or metalization. Ideally R_s is zero allowing for optimal current transport to the terminals of the solar cell or module.

Varying the illumination intensity affects the current generation in the cell and the J_{sc} scales linearly with the illumination intensity. Thus, illuminating the solar cell or module with different illumination intensities results in different voltage drops at the series resistance and in turn, affects the V_{mpp} . Thus, measuring the $J(V)$ characteristics for various illumination intensities allows to determine the R_s of a solar cell or module [100]. The ratio between the product of current density and voltage at MPP and the product of J_{sc} and V_{oc}

$$FF = \frac{J_{mpp} V_{mpp}}{J_{sc} V_{oc}} \quad (2.20)$$

is termed fill factor. At V_{oc} , when no current flows and J_{sc} , when there is no potential difference between the terminals, the cell is unaffected by any series resistance. Hence, a deterioration of either the R_s or the R_p always results in a reduction of the FF .

The conversion efficiency η relates the P_{mpp} to the illumination intensity E_e and the device area:

$$\eta = \frac{P_{\text{mpp}}}{E_e A_{\text{dev}}}. \quad (2.21)$$

2.6 General structure of a solar module

Figure 2.6 schematically shows the top view of a section of two strings of a solar module. The inset indicates the cross sectional view at the position of the red rectangle.

In the top view four cell interconnection ribbons (CIRs) connect two PERCs in series in each string. w_{cell} and h_{cell} indicate the width and height of a PERC, respectively. At the end of the string a string interconnection ribbon (SIR) of width w_{sir} creates the connection between adjacent strings. Between the cells of a string is a gap of distance d_{c2c} . The distance between strings is denoted as d_{s2s} . At the edge, a metal frame borders the solar module.

The cross sectional view at the bottom of Fig. 2.6 indicates the encapsulation by two layers of poly ethylene-vinyl acetate (EVA) of thickness t_{eva} , one covering the front and the other covering the rear side of the cells. The thickness of the cell is denoted with t_{cell} . A white colored backsheet covers the rear EVA, while the front poly ethylene-vinyl acetate (EVA) is covered with a glass of thickness t_{glass} .

Today, the majority of solar modules consist of 60 cells in series connection [8]. Cell interconnectors (CIs) typically connect ten cells that form a string. Most of the module manufacturers employ cell interconnection ribbons (CIRs) as CI. Soldering the CIRs to the busbars at the front side of one cell and to the rear Ag pads of the adjacent cell creates the series interconnection. This interconnection creates an unavoidable gap between two cells d_{c2c} , which is in the range from 3 mm to 4 mm for industrial manufactured solar modules. A string interconnection ribbon (SIR) interconnects the end joints of each string.

After establishing the cell interconnection, the panel of cells is embedded between two polymer layers. Most module manufacturers employ EVA as encapsulation polymer. Alternative materials are silicone, polyolefin (PO), polyvinyl butyral (PVB) or polyurethane (PU). Regarding long term stability and optical parameters some are superior to EVA [101]. However, the costs of EVA are much lower compared to the other materials and thus, it is predicted to dominate the market in the next decades [8].

A low iron glass covers the front side EVA. Most glass manufacturers also apply an anti-reflection coating to the glass. On the rear side a backsheet is applied to rear EVA layer. Such backsheets consist of a mixture of various polymer layers, e.g. polyvinyl fluoride (PVF), poly ethylene terephthalate (PET), polyvinylidene fluoride (PVDF), and ethylene-methyl acrylate copolymer (EMA) [102]. When targeting a high module power, a white colored backsheet is a natural choice to increase reflections. Other backsheet colors are generally used due to aesthetic aspects, e.g. for building integrated PV.

A lamination process joins all compounds together to form the module. For this process the lamination chamber is evacuated to prevent any trapped air in between

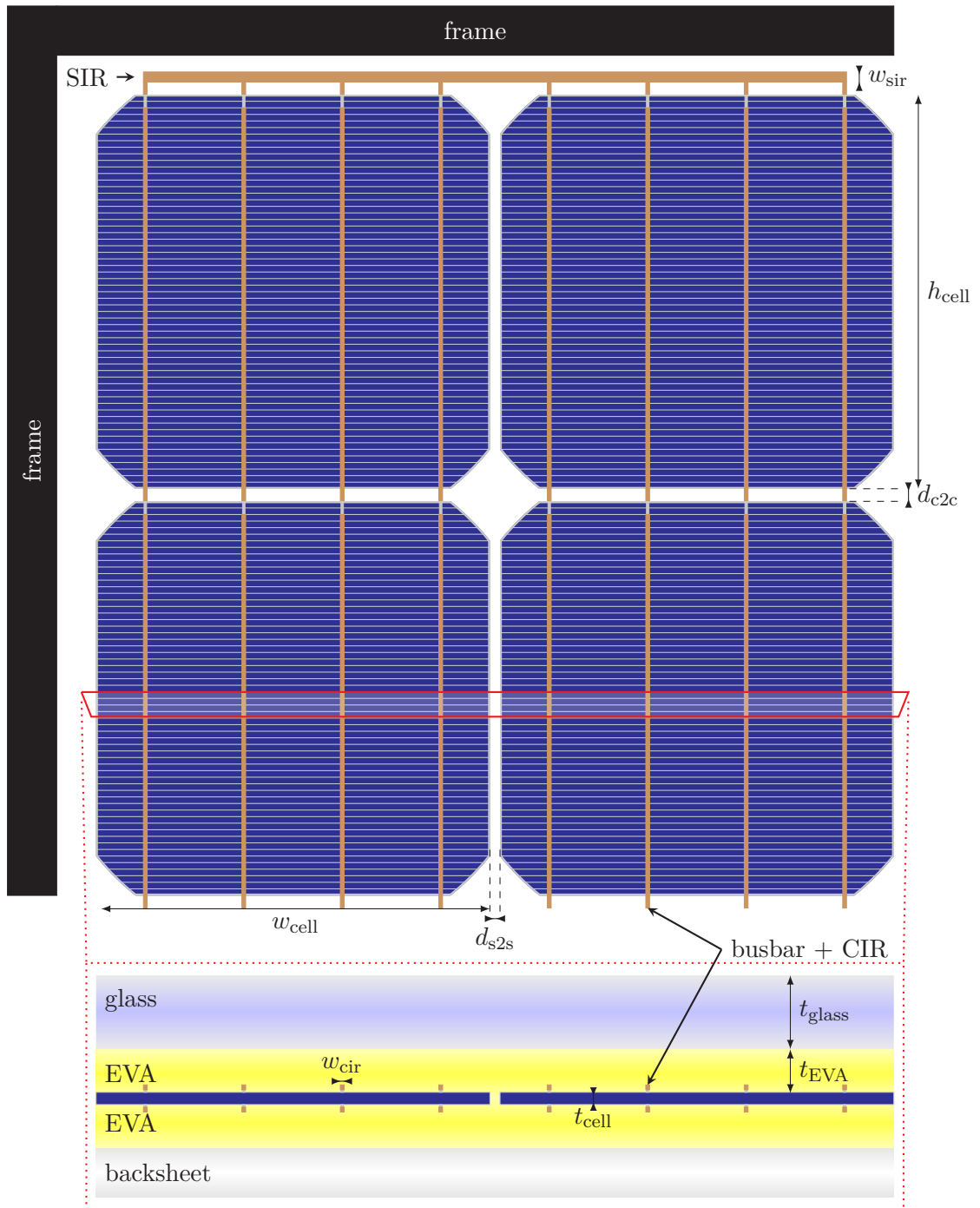


Figure 2.6: Scheme of a solar module showing a section of two strings. Each string contains two PERCs interconnected with four cell interconnection ribbons (CIRs). At the end of the string the CIRs are soldered to a string interconnection ribbon (SIR), which creates the interconnection between two adjacent strings. The inset at the bottom indicates the cross sectional view at the position of the red rectangle. On the illuminated side the front glass and the top EVA layer cover the cells and on the rear side the bottom EVA and the backsheet cover the cells.

the polymers. A heating step melts the EVA that then bonds with the front glass and the rear backsheet. Afterwards the EVA cross-linking starts to join all components together [103].

A frame made out of Al or stainless steel borders the solar module and serves for the protection against mechanical loads, handling, storage, mounting or grounding of the module.

2.7 Cell interconnection wires

Soldering cell interconnection ribbons (CIRs) to the cell's busbars has been investigated since the 1970's and thus, is a well established process in solar module manufacturing [104]. However, recently another type of cell interconnector (CI) became of great interest. It completely omits the busbars and applies a dense mesh of cell interconnection wires (CIWs) that directly contact the front metal fingers. For the contact formation two approaches are currently pursued: (i) Employing wires with a low melting point alloy coating and embedding the wires in a transparent polymer with an adhesive layer to form the contact within the lamination process [105]. (ii) Soldering the wires to the fingers employing infrared soldering technology [106, 107]. These concepts are known as smart wire or multi busbar technology [105, 108, 109, 110, 106, 107]. A typical mesh of CIWs consists of 12 to 40 wires with a diameter of 100 μm to 400 μm . The advantage of the smart wire technology is that it combines the soldering of the cell interconnection and the lamination process in one step. A disadvantage of the smart wire approach is the additional polymer, which absorbs light and thus, reduces the module current. The soldering of all wires to each front metal finger makes the multi busbar approach more elaborate than the standard cell interconnection process.

2.8 Cell to module losses

There are three major loss channels for solar cells and modules: optical, recombination, and resistive losses. All loss channels are coupled with each other and affect the $I(V)$ characteristics of a solar cell and a solar module. Encapsulating a solar cell into a solar module changes the quantity of these three loss channels for the cell, i.e. the same solar cell measured in air shows different optical, recombination, and resistive losses within a solar module. The relative change of the cell's power output P_{cell} measured in air and within a module P_{cell} is termed cell to module (CTM) factor. The CTM factor is defined as

$$CTM = \frac{P_{\text{mod}}}{\sum_{i=1}^{N_{\text{cpm}}} P_{\text{cell},i}}, \quad (2.22)$$

where N_{cpm} is the number of cells per solar module and $P_{\text{cell},i}$ is the power of the i -th cell in the module.

An increased recombination mainly manifests in a reduction of the open circuit voltage. Resistive power losses originate from the various series resistances of the solar cell and the solar module. Each current conducting path to the terminals

contributes to the lumped series resistance of the solar module and reduces the fill factor. Optical losses are due to the reflection and absorption of the front glass, EVAs, cell, metalization, cell interconnection and backsheet. These losses manifest in a reduction of the J_{sc} .

In the past, many authors focused on resistive and optical cell to module loss analysis. Blakers [111] gave special attention to the optics of the front metalization. He presented analytical calculations and measurements of the effective optical width of plated front metal fingers. For the measurement they coupled a quartz glass with 2-propanol to the cell and measured an effective shading of 0.7 for the fingers in air and 0.4 for the fingers under the glass-propanol stack. Krauter et al. [112] focused on the encapsulation material and optimized it for the annual yield to gain 3% additional daily energy output. McIntosh et al. [101] compared EVA and various silicones for the PV module encapsulation within ray tracing simulations. They found that silicone outperforms EVA by up to 1.2% in I_{sc} and concluded that silicone is most preferable to EVA. However, they considered an EVA with a rather high absorption for wavelengths below 400 nm, which is not the case for all types of EVA (see section 6.1.2, pp. 87). J. Schneider et al. [113] presented detailed analysis of the effect of light harvesting, anti-reflection coating, thin glass, and encapsulation materials with enhanced UV transparency. They showed that a combined improvement of these components results in a gain in I_{sc} and η of 5%. Further, they determined the effective optical width of standard and structured cell interconnection ribbons with light beam induced current measurements. I. Peters et al. [114] presented a detailed analysis of optical losses due to module components as well as optical losses of the cell within the module.

In contrast, Caballero et al. [115] presented an analytical series resistance model including the emitter, base, finger, busbar, and cell interconnects. They validated their model by experimental series resistance measurements. Their model allows to optimize the series resistance of screen-printed cells within a solar module. Guo et al. [116] presented a detailed theoretical and experimental analysis of series resistance losses for half cells within a solar module. Jung et al. [117] investigated CTM losses due to the series resistance of the cell interconnection and the cell mismatch.

Detailed investigation of combined optical and resistive losses were carried out by Haedrich et al. [118]. They considered optical properties of the glass, encapsulation polymers, backsheet and account for the cell spacing in the module. Further, their model includes series resistance losses of the cell interconnection.

The mentioned studies allow to optimize the solar module power output due to reduced individual optical, recombination, and resistive CTM losses. However, all three loss channels are coupled. For instance, reducing the absorption in the front encapsulation results in a higher J_{sc} that requires an increased number of front metal fingers to transport the current without additional series resistance losses. This increase in front metalization fraction in turn increases the cell's recombination saturation current density. Hence, reducing the cell to module losses requires to address all loss mechanisms and optimize the cell as well as the module components.

In our model we account for the combined optical, recombination, and resistive CTM losses. For the modeling of the CTM losses we utilize the double diode model. Therefore, we employ Eq. 2.16 to account for the recombination parameter J_{01} . J_{02}

we extract from the cell measurements. The consideration of the resistive and optical losses are described in the following.

2.8.1 Resistive cell to module losses

Charge carriers experience various series resistances on the path from the origin of generation within the cell to the terminals. Thus, the series resistance we obtain from the $I(V)$ characteristics is a lumped series resistance. The symmetry of the front metalization allows to split the cell into various unit cells, an approach first presented by Wolf et al. [100]. Many authors adopted and extended this approach [119, 120, 121, 122, 123, 124, 87]. It is based on the calculation of the Joule power loss for each unit cell. Accumulating the Joule power losses of the whole solar cell P_{loss} allows to determine the solar cell's specific series resistance R_s with [125]

$$R_s = \frac{P_{\text{loss}}}{I_L^2} A_{\text{cell}}, \quad (2.23)$$

where A_{cell} is the cell area and I_L is the light generated current.

We distinguish the series resistance of the cell and the module. For the cell we consider contributions of the front metal fingers, busbars, emitter, base and rear metalization. At the module level we additionally take the contributions of the cell interconnector and string interconnection ribbon into account for the series resistance calculation. For the calculation of the Joule power loss within each unit cell we adopt the approach of Deb et al. [123]. They split the emitter area in various triangles and squares, which allows an analytical calculation of the series resistance. Mäckel et al. [125] already demonstrated the applicability of the model for the emitter and fingers and extended it for selective emitters. In this work we will apply the approach of Deb et al. and extend it to a simple analytical model to calculate the series resistance losses of a PERC module.

2.8.2 Optical cell to module losses

Optical cell to module losses originate from the additional reflection and absorption of the front glass, EVAs, and cell interconnection. Tracing a photon incident to a solar module with a structure according to Fig. 2.6, the photon has to pass the glass ARC, glass, encapsulation polymer, cell interconnection, and front metalization to eventually reach the cell surface. Further, the encapsulation changes the optic of the cell due to the difference in the refractive index between air and the module encapsulation. On the other hand, according to Eq. 2.2 total internal reflection at the module's glass-air interface may occur and reflect the light back and forth within the module, increasing the probability that it is absorbed by the cell. Thus, the encapsulation environment also creates optical gains. Various authors applied analytical models to investigate optical cell to module losses [111, 112, 126, 118]. However, analytical modeling of a complete module including all encapsulation materials, cell interconnection and cell gaps, down to the cell texture and ARC with the light ray reflected back and forth in the materials is cumbersome.

In this work we utilize two approaches to consider the optical cell to module losses: (i) We employ the ray tracing software *Daidalos* [127]. (ii) We measure the J_{sc} of the

cell before and after encapsulation and determine empirical optical reduction and enhancement factors.

Simulating a solar cell in a complete module is challenging due to the large scale size differences between cell and module structures. For instance, the size of the pyramid texture is in the micrometer range, while the dimensions of the module are in the meter range. Tracing a light ray incident to a module, thus is time consuming and demands rather high computation resources. *Daidalos* circumvents these issues combining a multi-domain approach with Monte-Carlo based particle tracing [128]. We split the module and cell components into various unit cells exploiting the symmetries of the cell interconnection, metalization and cell texture. Each unit cell corresponds to a simulation domain. The ray tracing tool generates photons of random wavelength and angle of incidents and calculates the interaction of the photons with the elements of each simulation domain. By shifting the photon between the various simulation domains *Daidalos* bypasses the large scale differences of cell and module domains. This allows for fast simulations that agree well with measurement results [129, 128, 130, 131].

From the ray tracing simulation we determine the wavelength dependent absorption of a PERC module $A_{\text{perc}}(\lambda)$. Multiplying the absorption with the photon flux of the spectrum Φ and the collection efficiency of a PERC η_{perc} and integrating for all wavelengths yields the J_{sc}

$$J_{\text{sc}} = q \int A_{\text{perc}}(\lambda) \Phi(\lambda) \eta_{\text{perc}}(\lambda) d\lambda. \quad (2.24)$$

2.9 Accelerated aging with UV light

Solar modules may suffer from various power degradation mechanisms due to exposure to harsh environmental conditions, which decreases the energy yield of the PV system. Investigating the degradation under real circumstances is time consuming. Accelerated aging is a possibility to investigate degradation mechanisms within a couple of months. There are several accelerated aging setups, e.g. humidity freeze, damp heat or intense exposure to UV light. The International Electrotechnical Commission (IEC) regulates the settings and requirements each test sequence has to fulfill [16].

In this work we will focus on the degradation induced by exposing the solar module to UV light. The stability of PV modules exposed to UV radiation has been extensively investigated back in the 90s, especially for modules encapsulated with poly ethylene-vinyl acetate (EVA) [132, 133, 134, 135]. These studies showed that UV light was responsible for a discoloration of the polymer. UV radiation can also result in an embrittlement of the PET coated backsheets material, which may result in less weathering resistant solar modules [136, 137]. Today, the UV stability of EVA and other polymers has been remarkably improved by adding UV absorbing agents to the polymers [134, 138, 139, 140]. EVA is used by the vast majority of solar module manufacturers and it is predicted to stay the dominating encapsulation material in the next years [8]. Thus, we consider EVA as the reference encapsulation polymers in our UV experiments.

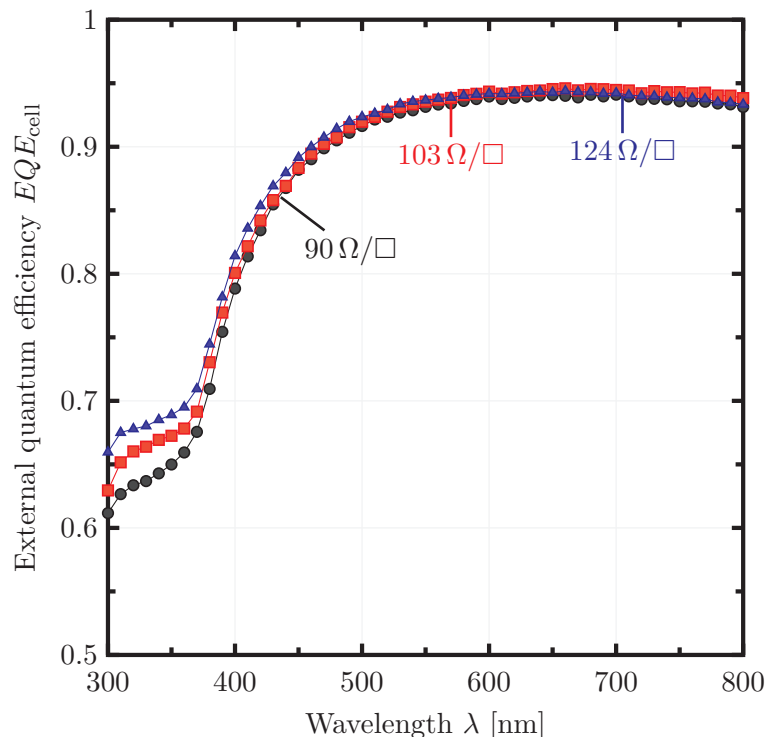


Figure 2.7: External quantum efficiency of three PERC with a varying emitter sheet resistance of $90 \Omega/\square$, $103 \Omega/\square$ and $124 \Omega/\square$.

During the last decade, the progress in development of metalization pastes improved the formation of the Ohmic contact. This allows to decrease the doping concentration of the cell's emitter, which increases the emitter sheet resistance. Figure 2.7 shows the external quantum efficiency (EQE) of three PERC with an emitter sheet resistance of $90 \Omega/\square$, $103 \Omega/\square$ and $124 \Omega/\square$. With increasing emitter sheet resistance the EQE in the wavelength range from 300 nm to 380 nm increases, termed blue response in the following. Hence, a lower emitter doping increases the blue response and in turn improves the energy conversion efficiency of the solar cell.

The exploitation of this enhancement in blue response requires encapsulation materials with an increased UV transparency for a solar module. Vogt et al. [131] showed that UV transparent EVA results in a gain in J_{sc} of up to 1.9 % for a location in Germany.

However, several studies showed that the UV radiation affects the SiN_y passivation layer. References [141, 62, 142] showed that a thermal treatment and UV light changes the fixed charge Q_f and decreases the surface passivation. However, this effect was only observed for photons with energies above 4.9 eV, which are unlikely to pass the glass and polymer encapsulation. Spectroscopic investigations with H-terminated Si-surfaces showed a wavelength-dependent photo desorption of surface hydrogen by UV light [143]. Hence, the origin of UV degradation may be related to the chemical passivation attitudes of SiN_y .

Gruenbaum et al. [144] reported stability problems for point concentrator cells with SiO_2/Si interface. They observed that the degradation is due to the absorption of UV light with sufficient energy to inject electrons from the Si conduction band

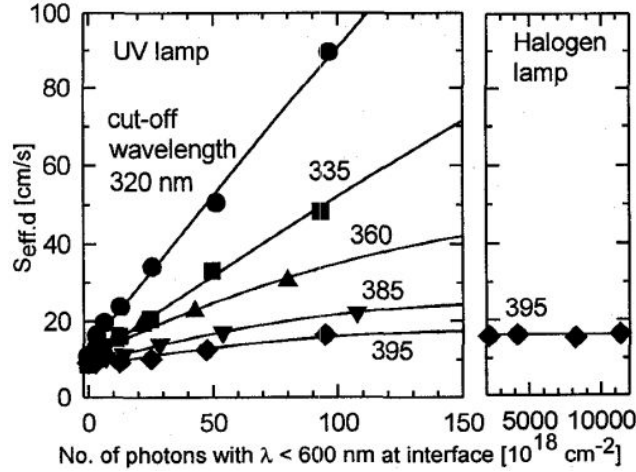


Figure 2.8: Measured differential SRV $S_{\text{eff,d}}$ of SiN_y /p-type Si passivations as a function of the number of UV photons reaching the Si/ SiN_y interface and the UV cut-off wavelength. Graphic taken from Ref. [46]

into the SiO_2 . However, Black et al. [145] showed that this effect is unlikely for non-concentrator cells.

Jager et al. [146] and Blumenstock et al. [147] showed for metal insulator semiconductor (MIS) inversion layer solar cells that UV light generates states at the SiN_y /p-type Si interface. This significantly reduced the V_{oc} as well as the I_{sc} within 3 h of UV illumination with a 200 W mercury lamp. They applied optical filters with varying UV cut-off wavelength to MIS solar cells. From the experimental results they derived that the interface states are formed due to the breaking of Si-H or Si-OH bonds by photons with energies above 3.7 eV [56, 146, 147, 148].

Lauinger et al. [46] performed similar experiments by illuminating SiN_y on p-type Si lifetime samples with a 400 W metal halide UV lamp for 120 h and applying optical filters with varying UV cut-off wavelength. Their results showed that light with wavelengths below 400 nm increases the surface recombination velocity (SRV) of the lifetime samples [46, 149]. Figure 2.8 shows their measured effective SRV as a function of UV photons reaching the SiN_y /p-type Si interface. Their results indicate that the degradation rate increases with increasing photon energy and that the degradation process is still not finished after 120 h UV exposure.

Blumenstock et al. [147] indicated that the plasma damage during the PECVD deposition creates interface states, that are initially passivated by hydrogen. During the UV illumination these hydrogen bonds break, which increased the SRV for the MIS cells. Kamioka et al. [150] and Tachibana et al. [151] also reported similar results for SiN_y on non-fired n^+ -type Si surfaces, which degrade under UV light due to plasma induced surface damage during the PECVD deposition of the SiN_y . Lauinger [152] showed that employing a remote plasma may circumvent this problem and presented UV stable solar cells with SiN_y on an n^+ -type emitter. However, applying the same passivation layer for lifetime samples showed a degradation after UV exposure. Hence, he assumed that for solar cells the recombination below the metal contacts was the dominant recombination loss, which prevented the measurement of UV induced losses for the solar cells.

Although UV degradation has been studied for many years, a detailed analysis of the effect of UV radiation on solar modules with varying encapsulation material and containing solar cells with varying passivation layer is missing. The majority of the reported publications either investigated SiN_y /p-type Si interfaces or non-fired lifetime samples. This is not representative for industrial type PERC with an SiN_y /n⁺-type Si interface. Furthermore, the contact firing (see section 3.1, pp. 24) changes the properties of the SiN_y passivation layer and hence, affects the passivation quality [153, 154]. The results of Lauinger [152] suggest that for solar cells with improved metalization pastes and less recombination below the the contacts a degradation of the surface passivation due to UV light is conceivable. Thus, we investigate the effect of UV radiation on cell and module level in this work and present a new model to describe the UV degradation of the solar module performance.

CHAPTER 3

Sample preparation and characterization techniques

In the first part of this chapter we describe the process flow for the various samples, solar cells and modules we investigate in this work. The second part introduces the characterization techniques and methods. Figure 3.1 shows a flow chart with the PERC baseline process as the center branch. The upper part shows the cell and the lower part the module processes. We describe all samples that vary from this baseline process in the branches next to it.

The branch on the left hand side shows the processes for the n-type PERT cells that is similar to the PERC baseline process. In this branch we only indicate processes that distinguish significantly from the PERC baseline. The major differences are the n-type base material, the doping process by ion implantation, and the stencil-printing of the bifacial front and rear metalization. Those cells serve as a reference for the UV aging experiments (see section 3.2, pp. 26).

The branch on the right hand side indicates the variations of the PERC baseline process. Here, we vary the refractive index and thickness of the front SiN_y layer (see section 3.2.1, pp. 27) as well as the front and rear metalization (see section 3.2.2, pp. 27 and section 3.2.3, pp. 28) of the PERC. Until the point of the variation in the branch, these samples will always follow the PERC baseline process.

On the module level we produce test modules employing various cell interconnections (see section 4.2, pp. 45) and prepare samples for the optical characterization of various encapsulation polymers (see section 3.3.2, pp. 31).

A detailed description of all processes is given in the following sections.

3.1 PERC baseline process

In this work, we process all PERCs according to an industrial like process flow as presented in Fig. 3.1 [155]. The base material is a boron-doped, (100)-oriented Cz-grown mono crystalline (156×156) mm² silicon wafer with a specific resistance ρ_b of $2 \Omega \text{ cm}$. First, we remove the saw damage in a potassium hydroxide (KOH) etch and perform an RCA (Radio Corporation of America) cleaning step [156]. For the pyramidal-texturing and the diffusion process we coat the rear side with a protection

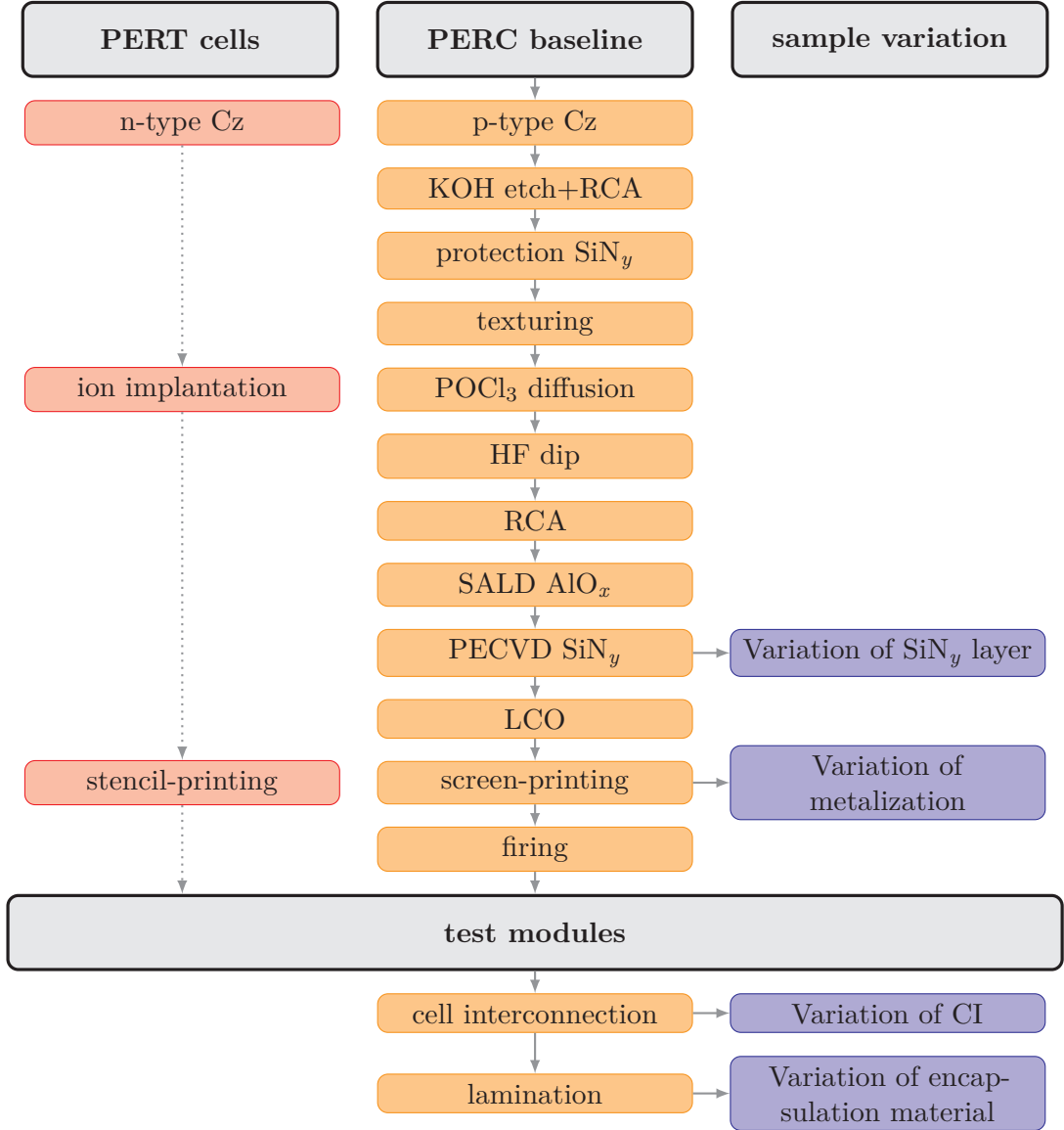


Figure 3.1: Process flow for the various samples in the experimental section.

SiN_y layer. The average wafer thickness after texturing is 170 μm. We create the phosphorous-doped front emitter with a POCl₃ diffusion, resulting in an average sheet resistance of 87 Ω/□ and a surface doping concentration of $2.2 \times 10^{20} \text{ cm}^{-3}$. We remove the protection SiN_y layer and the phosphorous silicate glass from the diffusion in a hydrofluoric acid (HF) dip and clean the wafer in an RCA step. For the passivation of the rear side we deposit a 5 nm thick AlO_x layer employing spatial atomic layer deposition (SALD). Subsequently, we deposit a SiN_y layer in a PECVD tool with a thickness of 100 nm at the front side and 200 nm at the rear side, measured on a planar surface. For the contact formation we locally ablate the rear side AlO_x/SiN_y stack with a picosecond pulsed laser. The laser contact openings (LCOs) extend as parallel lines along the wafer with a pitch of a few hundred micrometer. We realize the front and rear metalization employing single print screen-printing technology. In the baseline process we print 3 busbars and 88 front metal fingers. The rear side consists of 3 rows with 10 equidistantly spaced

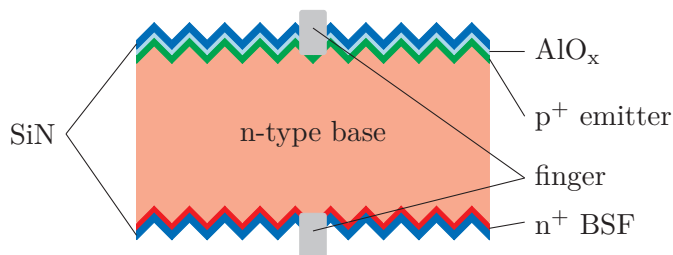


Figure 3.2: Scheme of a bifacial PERT solar cell.

solder pads for each row. The cell process ends with a belt-firing process with a peak firing temperature of 800 °C to 900 °C.

3.2 PERT cell process

Another cell technology employing dielectric passivation layers is the passivated emitter, rear totally-diffused (PERT) solar cell. Figure 3.2 shows a scheme of a bifacial PERT cell. For the n-type base we process $(156 \times 156) \text{ mm}^2$ pseudo-square textured Cz grown silicon wafers to bifacial PERT solar cells following the process flow reported in Ref. [157]. After cleaning and texturing we form the p⁺-type emitter at the front and the n⁺-type back surface field (BSF) layer at the rear side employing ion implantation and subsequent anneal. The implant dose is $2.00 \times 10^{15} \text{ cm}^{-3}$ for the boron-doped emitter and $1.25 \times 10^{15} \text{ cm}^{-3}$ for the phosphorous-doped BSF layer. Subsequently, we deposit a stack of $\text{AlO}_x/\text{SiN}_y$ on the p⁺-type emitter and a SiN_y layer on the n⁺-type BSF layer for the surface passivation. We deposit the 10 nm thick AlO_x layer by SALD. Both SiN_y layers are 100 nm thick (measured on a planar reference) and deposited by plasma enhanced chemical vapor deposition. We employ stencil printing technology for the front and rear side metalization, applying a Ag paste for the n⁺-type BSF and a Ag/Al paste for p⁺-type emitter. Subsequently, we form the contacts in a fast firing process in a conveyor belt furnace.

In this work, the average PERT cell efficiency is 20.7% when illuminating the p⁺-type emitter side with an AM1.5G spectrum at 1000 W m^{-2} and when measured at 25 °C on a reflective and conductive brass chuck. The bifacial factor is the ratio of the conversion efficiencies of the cell's front side to the rear side. These cells have bifacial factors of up to 99% [158]. This allows to investigate the properties of the SiN_y and $\text{AlO}_x/\text{SiN}_y$ passivation layers for equivalent processed cells with similar $I(V)$ characteristics. Thus, this cell concept is not the main focus of this work, but serves as reference for the UV degradation experiments, when illuminating the SiN_y or $\text{AlO}_x/\text{SiN}_y$ side of a cell.

3.2.1 Variation of the silicon nitride layer

We process a batch of 20 solar cells according to the baseline process in section 3.1 (pp. 24). In the PECVD tool we vary the gas flow rates of Si:N:H to obtain SiN_y layers with various refractive indexes. For each SiN_y variation we process five PERC and a float-zone (FZ) silicon sample. The FZ silicon samples are without texture and diffusion. These samples serve for the optical characterization of the SiN_y layer. We adjust the deposition time to obtain coatings with equal optical thicknesses and thus have the minimum reflectance at similar wavelengths (see Eq. 2.9, p. 8). Subsequently, the FZ silicon samples skip all the remaining processing steps of the baseline process except the fast firing step in the conveyor belt furnace. For the measurement of the thickness and refractive index we employ an ellipsometer with a He:Ne gas laser with a center wavelength of 633 nm. In the following we denote these samples with SiN_n , where the index indicates the corresponding refractive index n at 633 nm. Table 3.1 lists the four groups with the various SiN_y layers.

Table 3.1: Variation of the SiN_y layers. For each group we process a planar FZ wafer for the optical characterization of the SiN_y and five PERC.

group	refractive index n	SiN_y thickness t_{SiN} [nm]
$\text{SiN}_{1.99}$	1.99	94.8
$\text{SiN}_{2.07}$	2.07	91.4
$\text{SiN}_{2.29}$	2.29	81.6
$\text{SiN}_{2.53}$	2.53	76.5

3.2.2 Adaptations of the front and rear metalization

Besides full cells, we also investigate half cells. Therefor, we adjust the single screen-printing step in the baseline process and interrupt the busbars in the center of the cell. Figure 3.3 indicates these adaptations. For symmetry reasons and to prevent cell cracks when soldering a cell interconnection ribbon to the busbar, the front metal grid has a gap of 1 mm in the center of the solar cell. We adjust the ends of the busbars in the center to be equal to the busbar's end at the cell edges (see inset in Fig. 3.3). This reduces the risk of crack formation due to thermo mechanical stress during the soldering process [159, 160].

We modify the number and location of the rear solder pads to equidistantly distribute them on the half cell's rear side. Instead of 10 solder pads we print 6. We apply a laser process to create a notch and break the cell into two halves.

We also vary the number of front metal fingers and busbars. Besides 3 busbars, we process 4 and 5 busbar cells and vary the number of front metal fingers between 88 and 120. The width of the busbars varies from 0.8 mm to 1.3 mm.

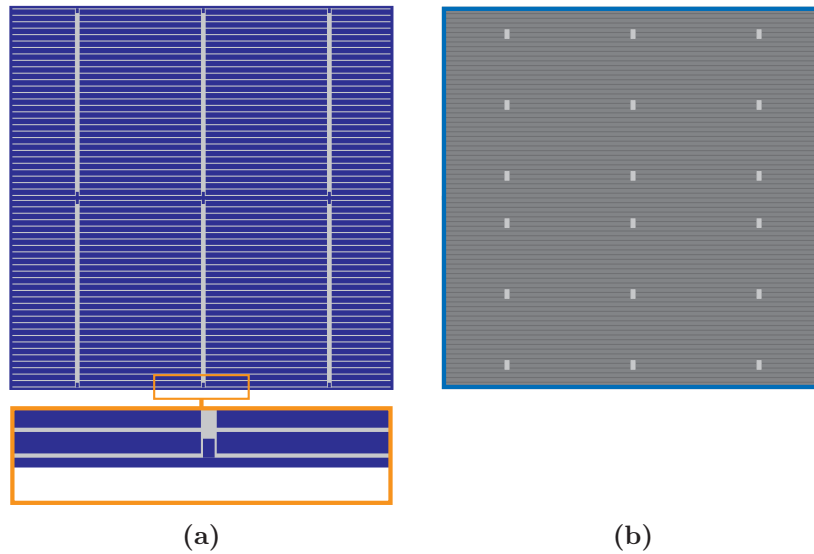


Figure 3.3: (a) Front metalization of a half PERC with three Ag busbars (vertical) and 88 Ag fingers (horizontal). The interruption of the metalization in the center of the cell is for the half cell laser cutting. (b) Al rear metalization of a half PERC with three rows of Ag solder pads. In comparison to Fig. 2.4 we adjust the number and the spacing of the solder pads.

3.2.3 Sample preparation and determination of optical finger and busbar properties

We process a PERC corresponding to the process flow in section 3.1 (pp. 24) and vary the front metalization. The cell features 104 front metal fingers and 4 busbars. We also print a $(21 \times 21) \text{ mm}^2$ square of the Ag paste in between two busbars. With the printed square we determine the reflectance of the Ag paste. For the determination of the busbar and finger geometries we employ an optical microscope. We capture images of 934 fingers and 20 busbars. We cut the cell perpendicular to the fingers and prepare samples for the scanning electron microscope (SEM) to measure the cross section area and shape of the fingers.

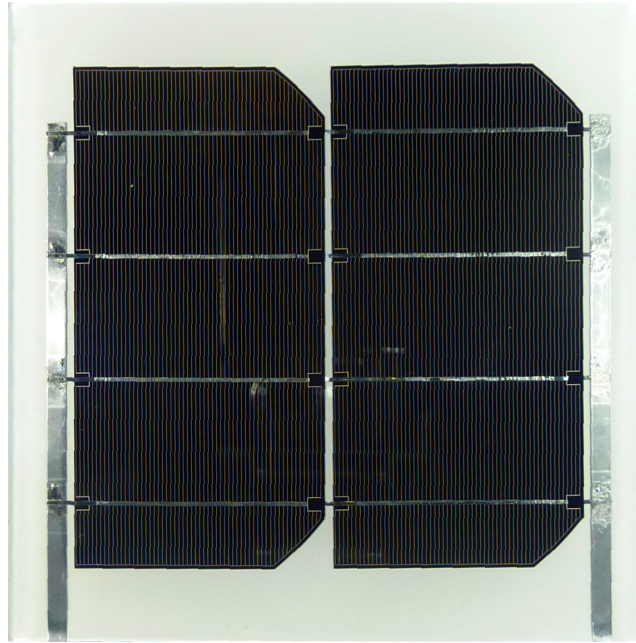


Figure 3.4: Test module containing two half PERCs connected in series. For the cell interconnection we solder 4 standard cell interconnection ribbons (CIRs) onto the busbars. We establish the series interconnection by connecting the busbars from the cell on the right hand side to the solder pads at rear side of the cell on the left hand side. At the end of the string we solder string interconnection ribbons (SIRs) to the CIRs to contact the cell with crocodile clips. We laminate the cells between two layers of EVA with a low iron soda lime glass at the front and a white colored backsheet at the rear side.

3.3 Test module baseline process

The number of cells in a test module varies between 1 and 5 cells and is different compared to a typical industrial 60-cell solar module. However, the structure of the test modules is identical to that of a typical industrial solar module as described in section 2.6 (see pp. 15). Thus, the experimental results are comparable to a full 60 cell industrial solar module, but require less resources and allow the application of more characterization tools since a 60 cell module is too large for many measuring devices, e.g. *LOANA* (see section 3.4.6, pp. 39). Figure 3.4 shows a photography of a test module with two half cells. We interconnect the cells employing 4 cell interconnection ribbons (CIRs). At the end of each CIR we apply a string interconnection ribbon (SIR) for the $I(V)$ measurements.

We manually solder CIRs onto the busbars of the one cell and onto the solder pads at the rear side of the adjacent cell. The CIR is a copper ribbon with a SnPbAg alloy, which we denote as the standard CIR in the following. The gap between two cells is 3 mm. For the soldering we place the cell on a 5 mm thick silicone sheet on a hot plate. The temperature of the hot plate is set to 110 °C. This setup reduces the thermal stress of the cell within the soldering process since it decreases the temperature difference to the soldering tip. Prior the soldering process, we dip the CIR into soldering flux to remove metal oxides [161]. For the soldering process we employ a soldering iron with a tip temperature of 300 °C. At the end of the string we solder an SIR to contact the module with crocodile clips.

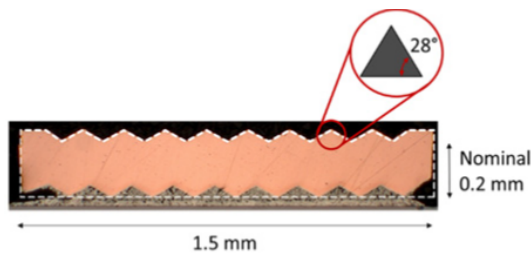


Figure 3.5: Microscope cross section image of a groove-structured cell interconnection ribbon [130].

For the encapsulation process we place the cells between two layers of EVA, each with a thickness t_{eva} of $450\ \mu\text{m}$. We cover the top EVA with a low iron soda lime glass of thickness $t_{\text{glass}} = 3.2\ \text{mm}$ and the rear EVA with a white colored backsheet. We laminate all test modules with a laboratory laminator for 10 minutes and a peak lamination temperature of $155\ ^\circ\text{C}$.

3.3.1 Samples for optical interconnector properties

We produce six one-cell test modules and apply various cell interconnectors (CIs) to the PERCs. We denote these modules as M-StdCIR, M-Lasertext, M-Col, M-CIW, M-LRF, and M-LHS. For the modules M-StdCIR, M-Lasertext, M-Col, and M-LRF we solder standard cell interconnection ribbons (CIRs) onto the four busbars. The width w_{cir} of these CIRs varies for each busbar between 1 mm, 1.3 mm, 1.5 mm and 2 mm.

M-StdCIR is the reference module employing only the standard CIR. In module M-Lasertext we texture the CIR surface after the soldering process with a laser. For the module M-Col we apply a white colored film on each CIR. The module M-CIW features cell interconnection wires (CIWs) instead of CIRs. For module M-LRF we apply a film with an Al coated groove structure onto the standard CIR. For test module M-LHS we solder a groove-structured CIR with Ag coating onto the busbars. Figure 3.5 shows a microscope cross section images of such a groove-structured CIR. The geometrical width of the CIR in the test modules M-LRF and M-LHS varies between 1 mm, 1.5 mm and 2.5 mm. The thickness of all CIR t_{cir} as well as the diameter of the CIW is $200\ \mu\text{m}$, since thicker CIs result in mechanical stability problems [162]. Table 3.2 lists all test modules and differences of the CIs.

Table 3.2: Overview of the six one-cell test modules with PERCs and varying cell interconnectors.

module	CI width [mm]	CI surface
M-StdCIR	1, 1.3, 1.5, 2	standard CIR
M-Lasertext	1, 1.3, 1.5, 2	laser texture
M-Col	1, 1.3, 1.5, 2	white colored film
M-CIW	0.2	round wires
M-LRF	1, 1.5, 2.5	groove-structured Al foil
M-LHS	1, 1.5, 2.5	groove-structured CIR

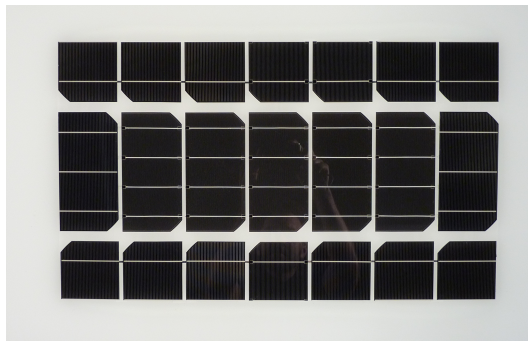


Figure 3.6: The photograph shows the test module M6. The module consists of five half PERCs. Only the five cells in the middle contribute to the performance of the module. A passepartout of inactive cells surrounds the active string to create conditions similar to a 60 cell solar module.

3.3.2 Samples for the optical characterization of the encapsulation polymers

We prepare glass-polymer-glass samples with silicone and poly ethylene-vinyl acetate (EVA) encapsulation materials. Here, we chose two different silicones termed SIL and SIL_{UV} as well as two different EVAs termed EVA and EVA_{UV}. The index UV indicates that the materials have an enhanced transmittance in the UV wavelength range. All polymers have a thickness of 450 μm . We laminate each encapsulation polymer between two glasses in a laboratory laminator. The lamination process is equal to the lamination process of a solar module and takes 10 minutes with a peak lamination temperature of 155 $^{\circ}\text{C}$.

3.3.3 Test modules for the verification of the analytical cell to module loss model

We produce six test modules M1 through M6 with various optical and electrical properties. Each test module consists of a string with five half PERCs. We surround these five PERCs with a passepartout of electrically isolated quarter cells to create conditions as in a 60 cell solar module. Only the central string consisting of the five half PERCs contributes the module performance. Figure 3.6 shows a photograph of test module M6.

The modules M1 through M6 vary in the cell to cell distance d_{c2c} as well as the string to string distance d_{s2s} and employ various cell interconnection ribbons (CIRs). Test module M1 has a cell to cell d_{c2c} and string to string spacing d_{s2s} of 2 mm and standard CIRs. Test module M2 has the same cell spacing as test module M1, but instead of the standard CIRs we apply white colored CIRs. For test module M3 through M6 we increase the cell spacing to examine the current enhancement by the backsheet. Test module M3 features an unequal cell spacing of $d_{c2c} = 2$ mm and $d_{s2s} = 40$ mm.

For the test modules M4 and M5 we increase the cell to cell and string to string distance to $d_{c2c} = d_{s2s} = 40$ mm. Besides the standard backsheet we apply an intermediate reflector (IMR) between the two EVA layers for test module M5 to avoid

reflections below the cell, as shown in Fig. 4.8 (see p. 57). This IMR is a thin white colored foil, which we apply to the rear EVA.

For M6 we apply the same IMR, but consider an unequal cell spacing of $d_{c2c} = 5$ mm and $d_{s2s} = 13$ mm. These distances are the maximum of the available module laminator for a 120 half cells module. Table 3.3 gives an overview of the fabricated test modules.

Table 3.3: Overview of the 5x1 test modules with various CIR and cell spacing. IMR indicates the application of an intermediate reflector.

module	d_{c2c} [mm]	d_{s2s} [mm]	CIR	IMR
M1	2	2	Std.	-
M2	2	2	White	-
M3	2	40	White	-
M4	40	40	White	-
M5	40	40	White	✓
M6	5	13	White	✓

3.3.4 Test modules for accelerated UV testing

From the batch of PERC with varying SiN_y (see section 3.2.1, pp. 27) and the PERT cells, we build ten one-cell test modules. In all test modules with PERC cells, the n^+ -type emitter side with the SiN_y passivation layer faces the illuminated side. All PERC test modules are covered with a low iron soda lime glass on the top and a white colored backsheet on the rear side. For the bifacial PERT cells we also employ a low iron soda lime glass on the top but a black colored backsheet on the rear side. Each test module is laminated in a laboratory laminator for 10 minutes and a peak lamination temperature of 155 °C. Table 3.4 gives an overview of the test modules.

The test module M-Ref is our reference module with a PERC featuring the reference SiN_y coating with refractive index $n = 2.07$. Here we encapsulate the PERC with two layers of a typical industrial EVA. In section 6.1.2 (pp. 87), we determine the cut-off wavelength λ_c of the encapsulation polymers according to Ref. [163], where the transmittance of the encapsulation polymer is equal to 10 %. The cut-off wavelength of the EVA in test module M-Ref is $\lambda_c = 364$ nm

For the test modules M-UVEVA, M-UVSIL, and M-SIL we vary the material of the encapsulation polymer. We encapsulate PERCs with the reference SiN_y coating with $n = 2.07$ between the various polymers from section 3.3.2. For test module M-UVEVA we employ the EVA with an enhanced UV transparency and a cut-off wavelength of $\lambda_c = 320$ nm, denoted as EVA_{UV} . For the other two test modules we use two different silicones. For test module M-UVSIL we utilize a silicone with enhanced UV transparency and a cut-off wavelength of $\lambda_c = 312$ nm, denoted as SIL_{UV} . For M-SIL we employ a silicone with cut-off wavelength of $\lambda_c = 368$ nm, denoted as SIL.

For the test modules M-SIN_{1.99}, M-SIN_{2.07}, M-SIN_{2.29}, and M-SIN_{2.53} we encapsulate PERCs with varying refractive index of the SiN_y layer between two layers of EVA_{UV} .

For test module M-SIN_{1.99} we employ a PERC with $n = 1.99$, for test module M-SIN_{2.07} we utilize a PERC with $n = 2.07$, for test module M-SIN_{2.29} we encapsulate a PERC with $n = 2.29$, and for test module M-SIN_{2.53} we employ a PERC with $n = 2.53$.

For the test modules M-PERT_{AIO} and M-PERT_{SiN} we encapsulate the bifacial PERT cells with the EVA_{UV} and vary the orientation of the cells. In test module M-PERT_{AIO} the p⁺-type emitter side with the AlO_x/SiN_y passivation layer faces the illuminated side. In test module M-PERT_{SiN} the cell's n⁺-type BSF side with the SiN_y passivation layer faces the illuminated side. Note that in the latter case the cell is in a back junction configuration.

Table 3.4 shows an overview of all test modules indicating the SiN_y refractive index, cell orientation and the encapsulation polymer with the corresponding cut-off wavelength.

Table 3.4: Overview of the test modules for the UV aging test.

test module	SiN _y n	illuminated passivation interface	encapsulation material	encapsulation λ_c [nm]
M-Ref	2.07	SiN _y /n ⁺ -type emitter	EVA	364
M-UVEVA	2.07	SiN _y /n ⁺ -type emitter	EVA _{UV}	320
M-SIL	2.07	SiN _y /n ⁺ -type emitter	SIL	368
M-UVSIL	2.07	SiN _y /n ⁺ -type emitter	SIL _{UV}	312
M-SIN _{1.99}	1.99	SiN _y /n ⁺ -type emitter	EVA _{UV}	320
M-SIN _{2.07}	2.07	SiN _y /n ⁺ -type emitter	EVA _{UV}	320
M-SIN _{2.29}	2.29	SiN _y /n ⁺ -type emitter	EVA _{UV}	320
M-SIN _{2.53}	2.53	SiN _y /n ⁺ -type emitter	EVA _{UV}	320
M-PERT _{SiN}	2.07	SiN _y /n ⁺ -type BSF	EVA _{UV}	320
M-PERT _{AIO}	-	AlO _x /p ⁺ -type emitter	EVA _{UV}	320

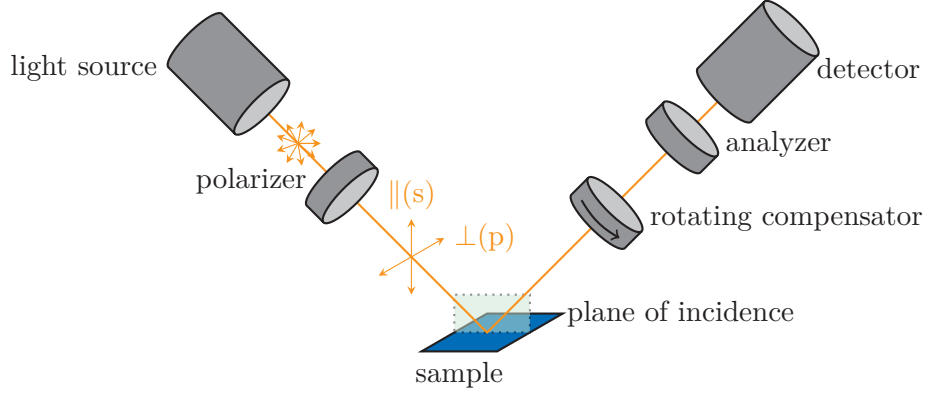


Figure 3.7: Principle of spectroscopic ellipsometry. A light source generates a light beam that is directed through a linear polarizer to the sample. The sample reflects the light that passes a rotating compensator and an analyzer before it hits the detector.

3.4 Characterization techniques

3.4.1 Variable angle spectroscopic ellipsometry

Variable angle spectroscopic ellipsometry (VASE) measures the change in the polarization state of light due to a reflection at the sample surface and allows to determine the complex refractive index and the thickness of a dielectric layer on a Si sample [164]. In this work we employ a *Woollam M-2000UI* rotating-compensator ellipsometer (RCE) [165]. Figure 3.7 depicts the principal of a VASE measurement.

A xenon lamp generates a light beam that is directed through a linear polarizer to the sample. The polarization state of the incident light can be decomposed in a component that is parallel $\parallel(p)$ and perpendicular $\perp(s)$ to the plane of incidence. The sample reflects the light that passes a rotating compensator and an analyzer before it hits the detector, which measures the polarization state of the reflected light. In particular it measures the phase difference

$$\Delta = \delta_i - \delta_r \quad (3.1)$$

and the ratio of the Fresnel reflection coefficients (see Eq. 2.4, p. 7)[164]

$$\tan \Psi = \frac{|r_{c\parallel}|}{|r_{c\perp}|}, \quad (3.2)$$

where δ_i is the phase difference before and δ_r the phase difference after the reflection.

The quantities Δ and Ψ yield the fundamental equation of ellipsometry [166, 167, 164]

$$\rho_r = \frac{r_{\parallel}}{r_{\perp}} = \tan \Psi \exp(i\Delta). \quad (3.3)$$

For a detailed description of the principle of ellipsometry measurements we refer to Ref. [164].

The employed ellipsometer measures Δ and Ψ as a function of the wavelength for various angles of incidence θ_i . We measure the reflection close to the pseudo

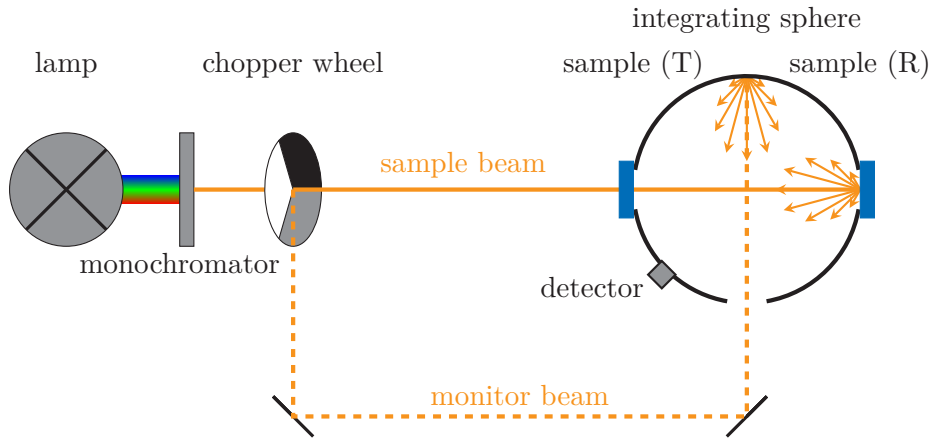


Figure 3.8: Scheme of the reflection and transmission measurement. A lamp in combination with a monochromator creates monochromatic light that is split by a chopper wheel into a sample and monitor beam. Both beams enter an integrating sphere with a detector. The sample is mounted at the entrance port of the sphere for a transmission measurement (sample T) and at the exit port for a reflection measurement (sample R).

Brewster angle for the substrate in air ($\approx 75^\circ$ for Si) at 50° , 55° , 60° , 65° and 75° in a wavelength range from 240 nm to 1700 nm. A measurement with various angles increases the amount of measurement data, which improves the modeling of the data [165]. The software *Wvase32* controls the measurement device, models the acquired data and determines the complex refractive index \hat{n} . For the fit of the optical model to the data a Levenberg-Marquardt regression algorithm is implemented in the software [166].

3.4.2 Reflection and transmission measurement

We conduct reflection and transmission measurements with a *Varian Cary 5000* two-channel spectrophotometer [168]. Figure 3.8 shows a schematic of the measurement principle of the two-channel spectrophotometer. A deuterium (185 nm to 350 nm) and a halogen lamp (350 nm to 3300 nm) in combination with a monochromator create monochromatic light that is either blocked, passed or reflected by a chopper wheel to create a sample or monitor beam. The chopper wheel rotates with a frequency of 30 Hz. If the chopper wheel blocks the light, the internal dark signal is measured. The monitor beam is coupled to the pre-amplifier of the detector's A/D converter and adjusts the signal at the A/D converter's input channel to compensate variations in the irradiance. The sample beam directs the monochromatic light to the sample that is placed at the entrance of the integrating sphere for the transmission measurement (sample T) or at the exit of the integrating sphere for the reflection measurement (sample R). The integrating sphere collects all the transmitted and reflected light that is then measured by a photomultiplier or a PbS detector. The photomultiplier is sensitive in the wavelength range from 185 nm to 900 nm and the PbS detector is sensitive in the wavelength range from 900 nm to 3000 nm.

The transmission and reflection measurements base on a relative measurement principle. The transmission measurement requires a signal without sample in the sample beam S_{100} , which serves as a 100% baseline. For the evaluation of the

sample's transmission, we compare the measurement signal with a sample in the sample beam S_{sample} to the 100 % measurement signal according to

$$T(\lambda) = \frac{S_{\text{sample}}(\lambda)}{S_{100}(\lambda)}. \quad (3.4)$$

For the reflection measurement the signal of a reference calibration standard S_{100} with a known reflection R_{ref} serves as the 100 % baseline. Further, a signal with open ports of the integrating sphere S_0 serves as a 0 % baseline. This correction is necessary, since a part of the light entering the integrating sphere is reflected from the edge of the sample port, which depends on the measurement setup [169]. The sample's reflection is calculated according to

$$R(\lambda) = R_{\text{ref}}(\lambda) \frac{S_{\text{sample}}(\lambda) - S_0(\lambda)}{S_{100}(\lambda) - S_0(\lambda)}. \quad (3.5)$$

3.4.3 Quasi steady state photoconductance decay measurements

The quasi-steady-state photoconductance (QSSPC) decay measurement technique is a contactless and fast method to measure the effective charge carrier lifetime τ_{eff} in a semiconductor for a varying excess charge carrier concentration Δn [170, 171]. In this work we employ a *Sinton Instruments WCT-120* lifetime tester for the QSSPC measurements. For the measurement a sample is placed on a temperature controlled stage. A coil operating in a resonant circuit induces eddy-currents into the sample to measure the conductance. A flash pulse of light generates excess charge carriers in the sample, which increases the sample's conductivity. The light intensity is measured with a reference cell to derive the generated charge carriers in the sample. Due to the recombination of charge carriers according to their effective lifetime, the conductivity of the sample reduces. The effective lifetime can be determined from the time dependent conductivity and the decay of the charge carriers, respectively.

For a diffused sample with different recombination rates in the emitter and base the method of Kane et al. [172] allows to determine the surface saturation current density J_{0s} from the slope of a fit to the Auger corrected $1/\tau_{\text{eff}}(\Delta n)$ function. For all samples we evaluate the slope according to the method of Kane et al. [172] for an excess carrier concentration Δn of $7 \times 10^{15} \text{ cm}^{-3}$.

3.4.4 Determination of the specific finger, busbar and cell interconnector resistances

We employ four point probe measurements to determine the specific resistances of fingers, busbars and cell interconnectors (CIs).

We contact the busbars of a PERC with a frame consisting of bars, each holding 19 spring-loaded pogo pins (see Fig. 3.10, p 39). For each busbar the frame has one bar. Applying a constant current we measure the voltage drop between two busbars to determine the resistance for all fingers between the two busbars R_m . The line

resistance of a front metal finger ρ_f depends on the number of front metal fingers N_f and the distance d_{bb} between the two busbars and is given by

$$\rho_f = \frac{R_m n_f}{d_{bb}}. \quad (3.6)$$

For the measurement of the specific resistance of a busbar we laser cut a 1 cm cell stripe out of a PERC with a busbar in the center of the stripe. We contact the busbar with needle point probes and measure the resistance for various distances between the probes.

Similar we determine the specific resistance of the cell interconnection ribbon (CIR) and the cell interconnection wire (CIW). We contact each CI with four crocodile clips and measure the resistance while varying the distance between the clips.

3.4.5 Determination of the contact resistance

For the determination of contact resistances we employ the transmission line method (TLM) [173, 174, 175]. Figure 3.9 (a) shows a test structure to determine the finger to emitter contact resistance $R_{c,f}$. We cut a PERC into 9 stripes of equal width employing a laser. The width W_c of each stripe is 1 cm. A measurement head with 16 spring-loaded pogo pins contacts eight fingers simultaneously and measures the potential difference for a constant current. Then the measurement head moves to the next eight fingers and the measurement procedure is repeated.

Similarly, we determine the contact resistance between CIR and busbar as well as CIW and finger. Figure 3.9 (b) shows a scheme of the test structure for the measurement of the contact resistance of a CIR to the busbar. We laser cut a stripe with a width of 1 cm out of a PERC with a busbar in the center of the stripe. The width of the busbar is W_c . Subsequently, we solder CIRs to the busbar with a distance $d_c = 1$ cm and laminate the stripe according to the module process between a stack of glass, EVA and a backsheet. We measure the voltage drop between two CIRs applying a constant current. Figure 3.9 (b) depicts the way we apply the current and voltage probes.

Figure 3.9(c) shows data for a TLM measurement of a sample with front metal fingers as in Fig. 3.9 (a). The measured resistance R_m increases linearly with the contact distance d_c , which is for this sample the finger distance d_f . We fit the measurement data with a linear regression model

$$R_m = 2R_{c,f} + \frac{R_{sh}}{W_c} d_f, \quad (3.7)$$

where R_c is the contact resistance and R_{sh} the emitter sheet resistance. We fit the model to the data with a least-square Levenberg-Marquardt fit algorithm. The slope of the linear model contains information regarding the sheet resistance of the emitter. The current has to flow through two contacts. Thus, the intercept with the ordinate axis is twice the contact resistance R_c . Analogously, we evaluate the contact resistance for the cell interconnectors in Fig. 3.9 (b).

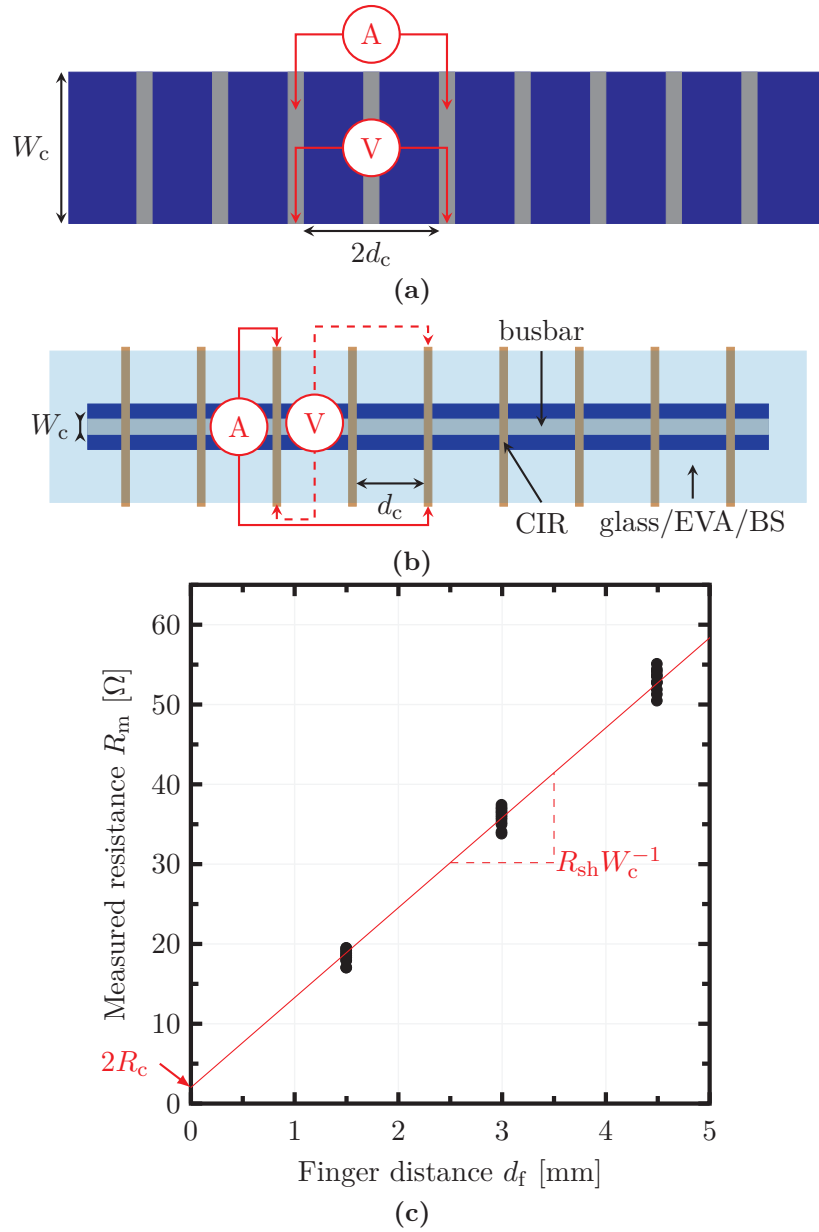


Figure 3.9: (a) and (b) schematically show sample structures for the measurement of the contact resistance according to the transmission line method (TLM). W_c is the width of the contact area and d_c the distance between two contacts. We measure the potential difference for a defined current to calculate the corresponding resistance between two contacts. Permuting between all possible contacts we measure the resistance R_m between various contact combinations of multiple distances d_c . (a) schematically shows a sample for the finger contact resistance. We contact the fingers with pogo pins. (b) schematically shows a sample for cell interconnection ribbons (CIRs). We solder CIRs to the busbar in the center of a cell stripe. Subsequently, we laminate the cell stripe with glass, EVA and a transparent backsheets (BS) as in a module. We extend the CIRs outside of the encapsulation and contact them with crocodile clips to measure the resistance for various contacts distances d_c . (c) shows example TLM measurement data for 4 front metal fingers of a sample as in (a). The black dots represent the measurement data and the red line represents the linear regression to the data. The slope of the linear regression line contains information about the sheet resistance R_{sh} . The intercept with the ordinate axis is twice the contact resistance R_c [173]

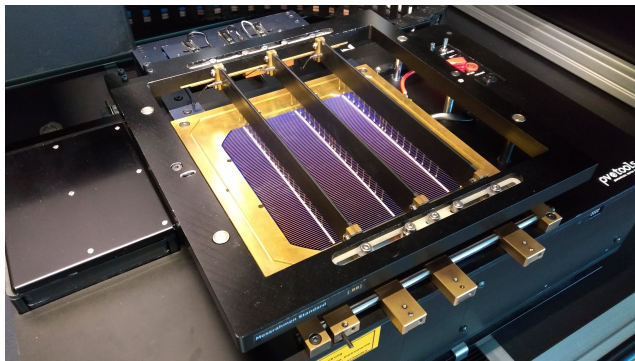


Figure 3.10: Measurement setup for the various $I(V)$ characteristics of a solar cell. A PERC is placed on a temperature controlled brass chuck that contacts the cell's rear side. On the front side a contact frame with three pin-bars, each containing 19 spring-loaded pogo pins contacts the busbars of the cell.

For the determination of the specific contact resistance ρ_c of a front metal finger with width w_f we employ [174]

$$R_{c,f} = \frac{\rho_c}{W_c L_t} \coth\left(\frac{w_f}{2L_t}\right), \quad (3.8)$$

with the transfer length

$$L_t = \sqrt{\frac{\rho_c}{\rho s h}}. \quad (3.9)$$

We apply Newton's method to solve the transcendental equation Eq. 3.8 and extract ρ_c .

3.4.6 Determining cell and minimodule current-voltage characteristics

We employ a *PVtools LOANA* solar cell analysis system to determine the $I(V)$ characteristics of solar cells and one-cell test modules [176]. We measure the dark $I(V)$, $I_{sc}(V_{oc})$, and illuminated $I(V)$ characteristics according to the standard testing conditions (STC). The STC demand a cell temperature of 25 °C and an irradiation intensity corresponding to 1000 W m^{-2} under an air mass of AM1.5G [177]. Figure 3.10 shows the measurements setup. The solar cell is placed on the brass chuck. This temperature controlled chuck contains a PT1000 temperature sensor and a sense pin in the center. A contact frame containing three pin-bars contacts the busbars at the cell's front side with 19 spring-loaded pogo pins for the current and voltage measurement.

In a first step, we determine the I_{sc} of the sample cell at an illumination intensity of 1000 W m^{-2} . The measurement system contains a calibrated reference cell with known I_{sc} at 1000 W m^{-2} . A filtered Xenon arc lamp simultaneously flashes the reference and sample cell to measure the I_{sc} . In a second step an LED array illuminates the sample cell with an intensity that is necessary to reach the I_{sc} . We apply a voltage sweep from -0.50 V to 0.68 V and measure the current I to determine the illuminated $I(V)$ characteristics of the cell. We also measure the illuminated $I(V)$ characteristics for an intensity of 800 W m^{-2} . For the $I_{sc}(V_{oc})$ characteristics we vary the intensity

of the LED array and measure the I_{sc} and V_{oc} for various illumination intensities. For the dark $I(V)$ we perform voltage sweep from -0.5 V to 0.7 V and measure the current without illumination [176]. With the cell area we calculate the $J(V)$ from the $I(V)$ characteristic.

For the extraction of the characteristic cell properties we perform a first order and a second order interpolation to determine J_{sc} and V_{oc} , respectively. We fit the measurement data with Eq. 2.19 according to the double-diode model (DDM). However, Eq. 2.19 is a transcendental equation and difficult to evaluate. Considering the $J_{sc}(V_{oc})$ characteristic, we only measure V_{oc} and J_{sc} for varying illumination, which simplifies Eq. 2.19. The assumption that $V=V_{oc}$ implies $J=0$ and Eq. 2.19 simplifies to

$$J_{sc} = J_{01} \exp\left(\frac{qV_{oc}}{kT}\right) + J_{02} \exp\left(\frac{qV_{oc}}{2kT}\right) + \frac{V_{oc}}{R_p}. \quad (3.10)$$

Thus, we first fit Eq. 3.10 to the $J_{sc}(V_{oc})$ and extract the first and second diode saturation current densities J_{01} and J_{02} . The shunt resistance R_p we obtain from the dark $J(V)$ measurements. Subsequently, we fit the illuminated $J(V)$ with Eq. 2.19 to determine the P_{mpp} . We extract the series resistance from the two illuminated $J(V)$ characteristics with varying intensities of 800 W m⁻² and 1000 W m⁻² [100].

Modules containing more than one solar cell do not fit into the *LOANA* system. Here, we employ a *halm* module flasher to determine the illuminated $I(V)$ characteristics. The module flasher employs an 80 ms light flash instead of an LED for the illumination. A drawback of this transient measurement technique is that capacitance induced hysteresis effects may occur. We reduce this effect by measuring the $I(V)$ characteristics from I_{sc} to V_{oc} (forward) and V_{oc} to I_{sc} (backward) [178]. Another drawback of the module flasher is that it can not measure the dark $I(V)$ and $I_{sc}(V_{oc})$ characteristics.

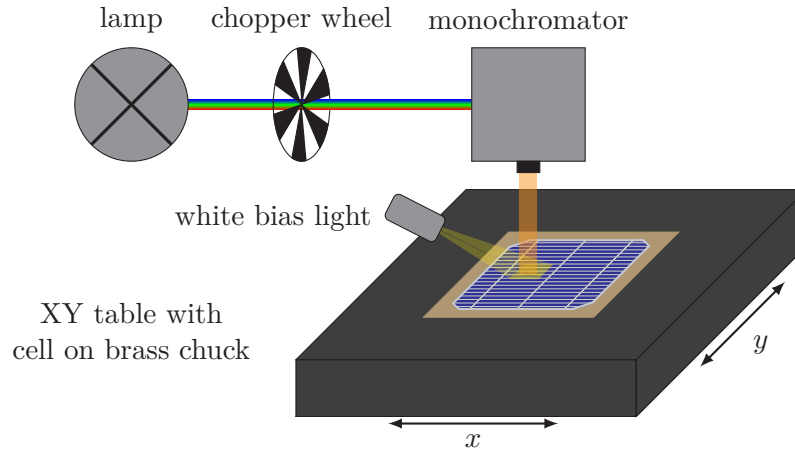


Figure 3.11: Scheme of the EQE measurement. A lamp generates a light beam that enters via a chopper wheel a grating monochromator. The monochromatic light is focused on the sample placed on a brass chuck. The brass chuck is mounted on a XY table that can move in the x and y direction. A white bias light superimposes the monochromatic light.

3.4.7 Quantum efficiency and reflection measurements

Figure 3.11 shows the measurement principle of the external quantum efficiency (EQE) measurement. A tungsten halogen and a xenon arc lamp generate a light beam that enters via a chopper wheel a grating monochromator. We illuminate an area of $(20 \times 20) \text{ cm}^2$ with monochromatic light. The EQE is a small signal measurement method and the intensity of the monochromatic light is too weak to establish an injection level similar to the operation conditions of a solar cell. Thus, we superimpose the monochromatic light with a white bias light. We measure the I_{sc} of the solar cell with needle point probes. For modules we contact the string interconnection ribbons with four crocodile clips. Modulating the monochromatic light with a chopper wheel and filtering the current signal in a lock-in amplifier allows to separately measure the spectral short circuit current of the cell [176, 179].

The EQE is the ratio of the J_{sc} to incident photon flux per wavelength

$$EQE(\lambda) = \frac{1}{q} \frac{J_{\text{sc}}(\lambda)}{\Phi(\lambda)}. \quad (3.11)$$

With the same setup we also measure the reflection of the cell by placing an integrating sphere in the monochromatic beam. The measurement principle is similar to the Cary measurement in section 3.4.2 (see pp. 35). The monochromatic light beam passes an integrating sphere under an angle of 8° to the samples surface. The integrating sphere is coated with diffuse reflecting BaSO_4 . Light reflected by the sample surface reenters the sphere, where it is reflected back and forth and eventually detected by a silicon and a germanium detector [176].

3.4.8 Light beam induced current measurements

The minimal spot size of $(1 \times 3) \text{ mm}^2$ limits the resolution of the EQE measurement. For high resolution mappings we employ light beam induced current (LBIC) measurements with six diode lasers with a wavelength of 405 nm, 532 nm, 670 nm, 830 nm, 925 nm and 980 nm. The spot diameter of the lasers varies from $60 \mu\text{m}$ to $100 \mu\text{m}$. We place the cell on a brass chuck and contact the cell's busbars with needle point probes to measure the I_{sc} . For module measurements we contact the string interconnection ribbon with crocodile clips. Modulating the six diode lasers at different frequencies allows to simultaneously evaluate the current signal for all six laser wavelengths [176]. Thus, we can measure the local spectral short circuit current of the cell and module with a lateral resolution of a few hundred micrometer.

3.5 Accelerated aging with ultraviolet light

Before the accelerated ultraviolet (UV) aging test, all PERC are illuminated for 96 h by halogen lamps with an intensity of 1-sun to stabilize the cells regarding light induced degradation [180]. For the accelerated UV aging test we illuminate the samples with mercury lamps. We employ *Hoerle UVASpot* lamps with a broad spectral irradiance from 300 nm to 450 nm and *Philips TL20W/01 UVB313* with a peak in the spectral irradiance at 313 nm. We measure the spectrum of the light sources with an *Avantes AvaSpec-2048* fiber optic spectrometer [181]. Figure 3.12 shows the normalized spectral irradiance E_{uv} of the UVASpot and UVB313 UV lamps in the center of the UV chamber.

For the UVASpot lamps the illumination intensity at the module surface is $(331 \pm 15) \text{ W m}^{-2}$ in the UV wavelength range from 300 nm to 400 nm [182]. At the same location in the UV chamber we measure the UV intensity with a *Kipp und Zonen CUV3* UV radiometer [183]. The metal plate that holds the test samples in the UV chamber has a controlled temperature of 40°C . We subdivide the metal plate into squares, each with an area of $(10 \times 10) \text{ cm}^2$ and measure the average distributed illumination intensity with the CUV3 UV radiometer at the test samples locations. This procedure we repeat every time when we take the test samples out of the UV chamber for their characterization. This light source we employ for the accelerated aging test according to IEC61345 [19] for all experimental test modules.

For the UVB313 lamps the illumination intensity at the module surface is $(83 \pm 6) \text{ W m}^{-2}$ in the UV wavelength range from 300 nm to 400 nm. For the measurement of the illumination intensity we employ an *Opsytec Dr. Goebel Radiometer* [184]. This light source we employ for the accelerated aging tests of the samples for the QSSPC measurements.

For a better comparison to outdoor irradiance data we report the time t_{uv} the samples are in the UV chamber in terms of a UV dose, which is calculated by

$$D_{\text{uv}} = \int_{300 \text{ nm}}^{400 \text{ nm}} E_{\text{uv}}(\lambda) t_{\text{uv}} d\lambda = \int_{300 \text{ nm}}^{400 \text{ nm}} \Phi(\lambda) t_{\text{uv}} \frac{hc}{\lambda} d\lambda, \quad (3.12)$$

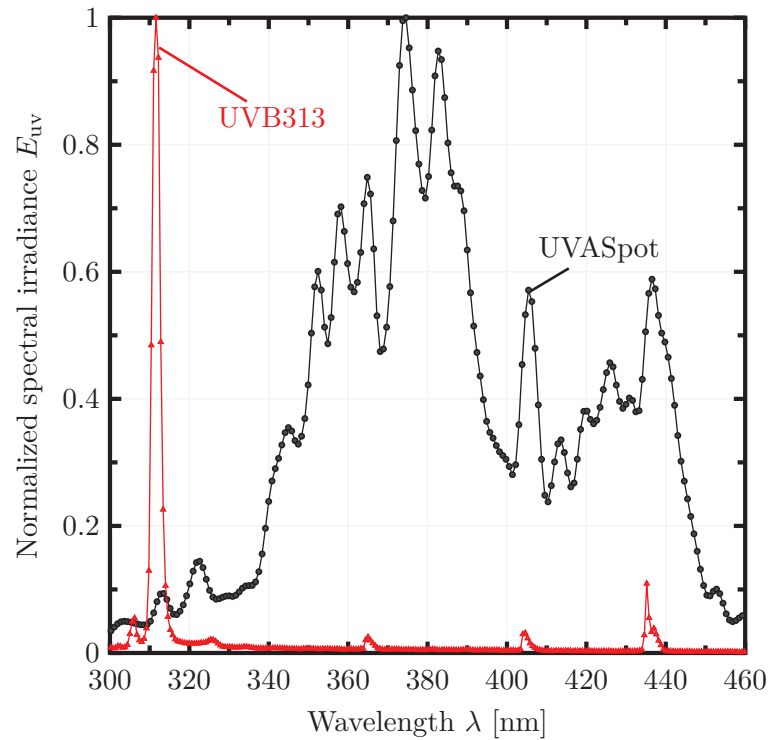


Figure 3.12: Normalized spectral irradiance $E_{uv}(\lambda)$ of the UVASpot and UVB313 light sources. The lines are a guide to the eye.

where Φ is the photon flux at the module surface, h is Planck's constant and c the speed of light. For the UVASpot lamps, a UV exposure time t_{uv} of 1500 h equals a UV dose of about 500 kW h m^{-2} . This D_{uv} corresponds to approximately 14.7 years outdoor exposure for a moderate climate (Potsdam, Germany, $34 \text{ kW h m}^{-2} \text{ a}^{-1}$ [185]) and 5.3 years for desert climate (Arizona, USA, $93 \text{ kW h m}^{-2} \text{ a}^{-1}$ [186]).

CHAPTER 4

Determining the cell and module model parameters from the experimental results for the modeling of cell to module losses

In this chapter we analyse test samples from the previous chapter to extract the parameters for the analytical model of the cell to module losses. At the end we summarize all results in a table.

4.1 Current voltage analysis of the passivated emitter and rear cells

For the determination of the characteristic $J(V)$ parameters we employ the cells of the PERC batch from section 3.1. We measure the $J(V)$ characteristics with the *LOANA* solar cell analysis system and extract the cell efficiency η , short circuit current density J_{sc} , open circuit voltage V_{oc} , fill factor FF , first diode saturation current density J_{01} , and second diode saturation current density J_{02} (see section 3.4.6, pp. 39). Table 4.1 lists the average values and the standard deviation of 272 PERCs.

Table 4.1: Characteristic $J(V)$ parameters of a PERC batch showing the average values and the standard deviation.

η [%]	J_{sc} [mA cm ⁻²]	V_{oc} [V]	FF [%]	J_{01} [fA cm ⁻²]	J_{02} [nA cm ⁻²]
20.6±0.3	39.4±0.25	660±0.3	79.2±0.8	242±32	11±5

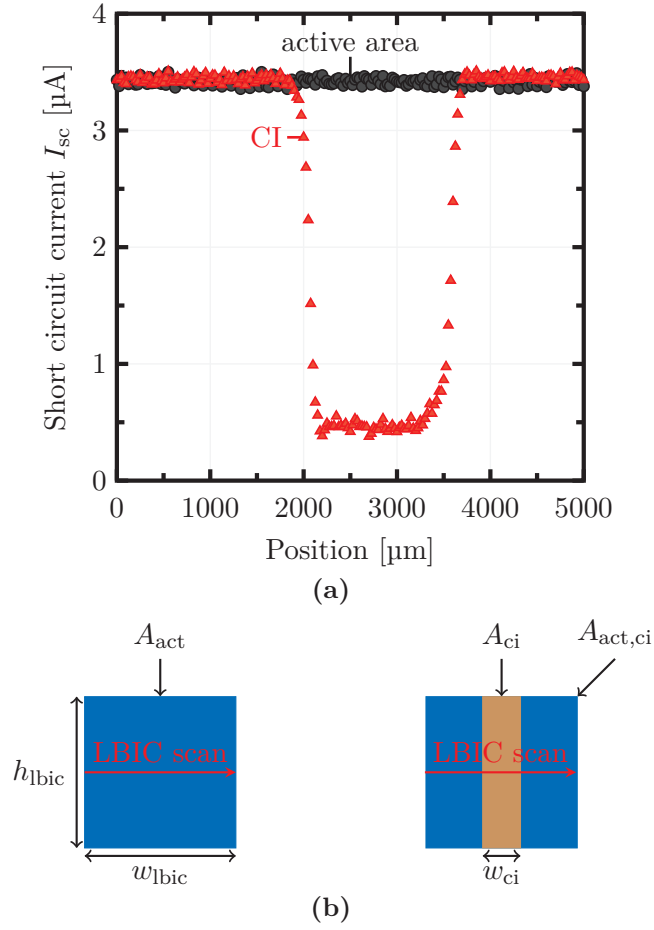


Figure 4.1: (a) LBIC measurement with a 980 nm laser for test module M-StdCIR with a cell interconnector (CI) width w_{ci} of 1.5 mm. The black circles (●) show a measurement for the active cell area and the red triangles (▲) show a measurement across the CI, which is a cell interconnection ribbon (CIR) for test module M-StdCIR. (b) Scheme of an LBIC scan for the determination of the k_{ci} value. The area on the left hand side incorporating only active module areas A_{act} is equal to the sum of the area $A_{act,ci}$ adjacent to the CI and the area covered with CI A_{ci} on the right hand side. The red arrow indicates the direction of the LBIC measurement

4.2 Optical properties of cell interconnectors

4.2.1 Results of the measurement of the optical properties of the cell interconnectors

We conduct light beam induced current (LBIC) measurements on the test modules M-StdCIR, M-Lasertext, M-Col, M-CIW, M-LRF, and M-LHS from section 3.3.1 (pp. 30) and compare areas with and without a cell interconnector (CI). Figure 4.1 (a) shows the LBIC current I_{sc} as a function of the laser position for the test module M-StdCIR. The measurement in Fig. 4.1 (a) is for the 980 nm laser. The black data represents a measurement on the active cell area for the test module. The red data shows the measurement for a position with cell interconnector. At the position of the CI the I_{sc} is reduced due the shading of the active cell area by the CI. The geometrical width w_{ci} of the cell interconnector for this test module is 1.5 mm.

Figure 4.1 (b) schematically shows two such LBIC measurements. Both LBIC measurements cover the same area of width w_{lbic} and height h_{lbic} . The scheme on the left hand side depicts an area consisting of only active area A_{act} . The scheme on the right hand side depicts an area consisting of an active area with size $A_{\text{act,ci}}$ and an area covered with a CI with area A_{ci} . This can be any kind of cell interconnector, either a cell interconnection ribbon or a cell interconnection wire. Since the areas of the LBIC measurements are equal, we obtain the relation

$$\begin{aligned} A_{\text{act}} &= A_{\text{act,ci}} + A_{\text{ci}}, \\ A_{\text{act}} &= A_{\text{tot,ci}}, \\ h_{\text{lbic}} w_{\text{lbic}} &= h_{\text{lbic}} w_{\text{lbic}}. \end{aligned} \tag{4.1}$$

From the LBIC measurement, we obtain a current I_{act} for the area on the left hand side, and $I_{\text{act,ci}}$ for the area on the right hand side. Assuming that only the active areas generate a current during the LBIC scan and that the current densities for both active areas are equal we obtain the relation

$$\begin{aligned} \frac{I_{\text{act}}}{A_{\text{act}}} &= \frac{I_{\text{act,ci}}}{A_{\text{act,ci}}}, \\ \frac{I_{\text{act}}}{A_{\text{act}}} &= \frac{I_{\text{act,ci}}}{A_{\text{tot,ci}} - A_{\text{ci}}}, \\ A_{\text{ci}} &= A_{\text{act}} \left(1 - \frac{I_{\text{act,ci}}}{I_{\text{act}}} \right), \\ w_{\text{ci,eff}} &= w_{\text{lbic}} \left(1 - \frac{I_{\text{act,ci}}}{I_{\text{act}}} \right), \end{aligned} \tag{4.2}$$

where $w_{\text{ci,eff}}$ is the effective optical width of the CI.

Similar, we determine $w_{\text{ci,eff}}$ of the cell interconnectors in the test modules M-StdCIR, M-Lasertext, M-Col, M-CIW, M-LRF, and M-LHS. We define the optical factor k_{ci} as the ratio of the effective optical width $w_{\text{ci,eff}}$ to the geometrical width w_{ci} to compare the various cell interconnectors

$$k_{\text{ci}} = \frac{w_{\text{ci,eff}}}{w_{\text{ci}}}. \tag{4.3}$$

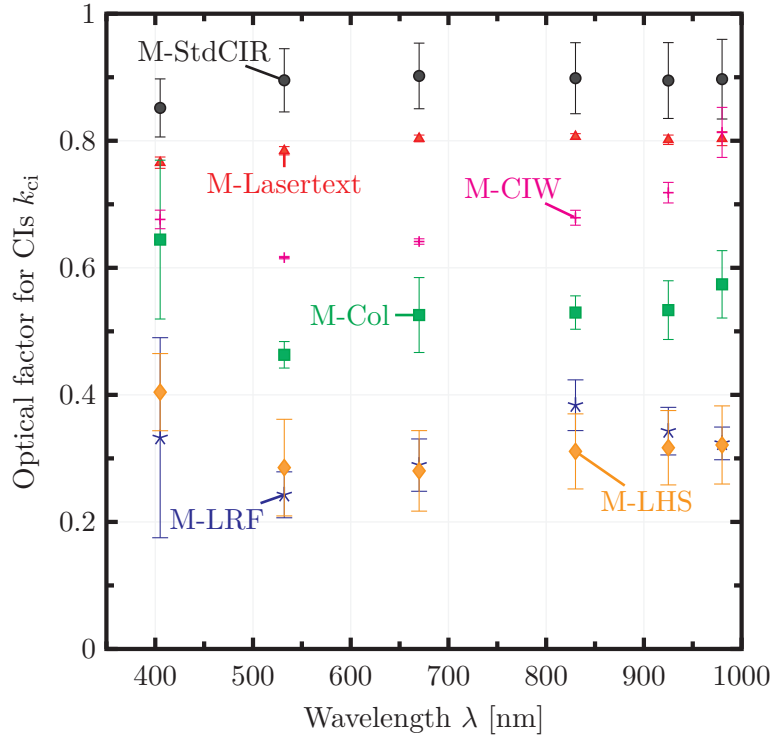


Figure 4.2: Optical factor k_{ci} for the various CI optics. We measure $w_{ci,eff}$ with six different lasers and determine k_{ci} for each wavelength λ . The symbols represent the average k_{ci} values and the error bars represent the standard deviation.

Figure 4.2 shows k_{ci} for the various cell interconnectors in the test modules M-StdCIR, M-Lasertext, M-Col, M-CIW, M-LRF, and M-LHS as function of the six LBIC laser wavelengths. The symbols indicate the mean k_{ci} and the error bars indicate the standard deviation of 40 LBIC scans for each of the various CIs with a width varying from 1 mm to 2.5 mm.

We measure the highest k_{ci} values of 0.89 for the test module M-StdCIR employing the standard cell interconnection ribbon (CIR). Texturing the surface of the standard CIR decreases k_{ci} in test module M-Lasertext by 0.1. Employing a cell interconnection wire (CIW) further decreases the optical ratio as well as applying a white color to the CIR surface. Here, we also observe spectral dependencies. The k_{ci} of the test module M-CIW increases with increasing wavelength. For both test modules M-Col and M-CIW k_{ci} increases at 405 nm. We measure the lowest k_{ci} values for the test modules M-LRF and M-LHS with the structured CIs. The k_{ci} for the test module M-LRF is slightly lower in the range from 405 nm to 532 nm, while it is higher from 830 nm to 925 nm.

We calculate an average k_{ci} value for each CI considering the AM1.5G spectrum. Table 4.2 summarizes these spectral weighted k_{ci} values.

Table 4.2: Spectral weighted k_{ci} values for the various CIs.

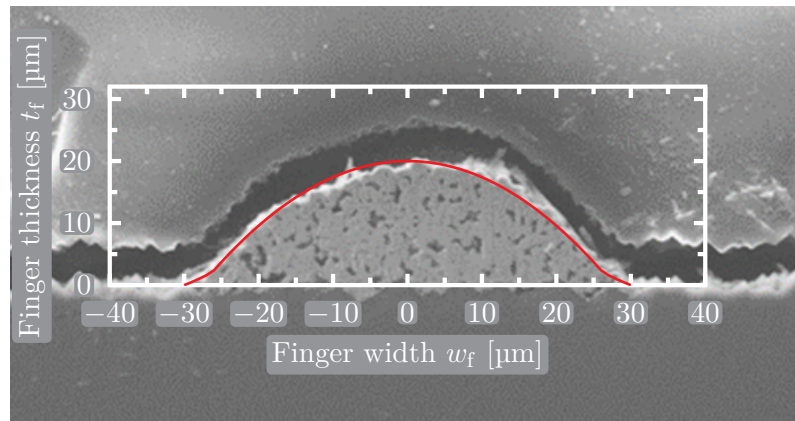
CI	M-StdCIR	M-Lasertext	M-Col	M-LHS	M-LRF	M-CIW
k_{ci}	0.89 ± 0.05	0.79 ± 0.01	0.54 ± 0.05	0.32 ± 0.06	0.31 ± 0.06	0.67 ± 0.01

4.2.2 Discussion of the optical properties of the cell interconnectors

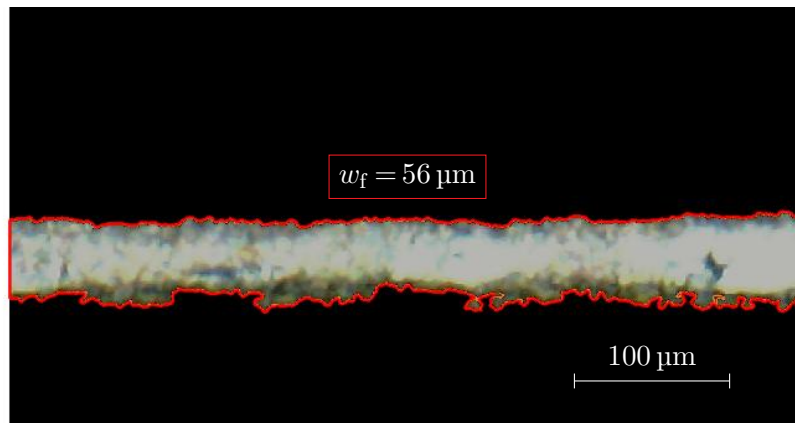
We measure the highest optical factor for the test module M-StdCIR with the standard cell interconnection ribbon (CIR). Here, the specular reflecting and flat rectangular shaped cross section of the CIR are detrimental since they reflect most of the light out of the module and less light under the critical angle for total internal reflection. Increasing the surface roughness or applying white colored CIRs increases the fraction of diffuse reflections. Here, the effect of total internal reflection is beneficial for the cell interconnector (CI) and reduces the geometrical width by 50 % in the test module M-Col. This is in agreement with values extracted from EQE measurements in Ref. [187]. Applying a groove-structure to the CIR as for test module M-LHS and M-LRF, further increases the amount of total internal reflected light and reduces the geometrical CIR width by 70 %. This agrees with values in Ref.[113], although they neglected spectral effects by employing only one laser with a wavelength of 980 nm. The round shape of the cell interconnection wire (CIW) has a similar effect and reduces the geometrical width of the CIW by 33 %.

We also observe spectral variations for k_{ci} in Fig. 4.2. The EVA absorbs light with wavelengths below 410 nm. Thus, for the laser with a central wavelength of 405 nm, k_{ci} increases for the modules M-Col, M-LHS and M-LRF since their reflection characteristics increase the path of light in the EVA. Further, the k_{ci} for test module M-LRF employing the Al coated grooves is significantly higher at 830 nm compared to test module M-LHS with the Ag coated grooves. We attribute this increase in k_{ci} to an absorption peak of Al centered at 833 nm [88].

The average k_{ci} values in Table 4.2 are in good agreement with values from the literature, where values of $k_{ci} = 0.97$ for a standard CIR, $k_{ci} = 0.55$ for a white colored CIR, $k_{ci} = 0.25$ for structured CIR, and $k_{ci} = 0.6$ to 0.7 for a CIW have been reported [188, 189, 187, 113, 190].



(a)



(b)

Figure 4.3: (a) SEM image of a cross section of a front metal finger with a magnification factor of 1000. The red line in the superimposed graph indicates an approximation to the finger shape, which is a combination of a Gaussian and a second order polynomial function. (b) Top view micrograph of a front metal finger with a magnification factor of 100. We employ our image processing tool to extract the area of the finger. The red line indicates the perimeter of the extracted area. From the area we calculate the average finger width w_f of the front metal fingers.

4.3 Geometrical and optical properties of front metal fingers

4.3.1 Results of the finger geometry measurements

Figure 4.3 (a) shows the SEM image of a cross section of a front metal finger with a magnification factor of 1000. The red line in the superimposed graph indicates an approximation to the finger shape. We approximate the shape of the finger by a combination of a Gaussian and a second order polynomial function

$$t_f(w_f) = \begin{cases} a \exp\left(-\frac{w_f^2}{2b^2}\right) & \text{for } |w_f| \geq 54 \mu\text{m}, \\ \frac{c^2 - w_f^2}{d} & \text{for } |w_f| < 54 \mu\text{m}, \end{cases} \quad (4.4)$$

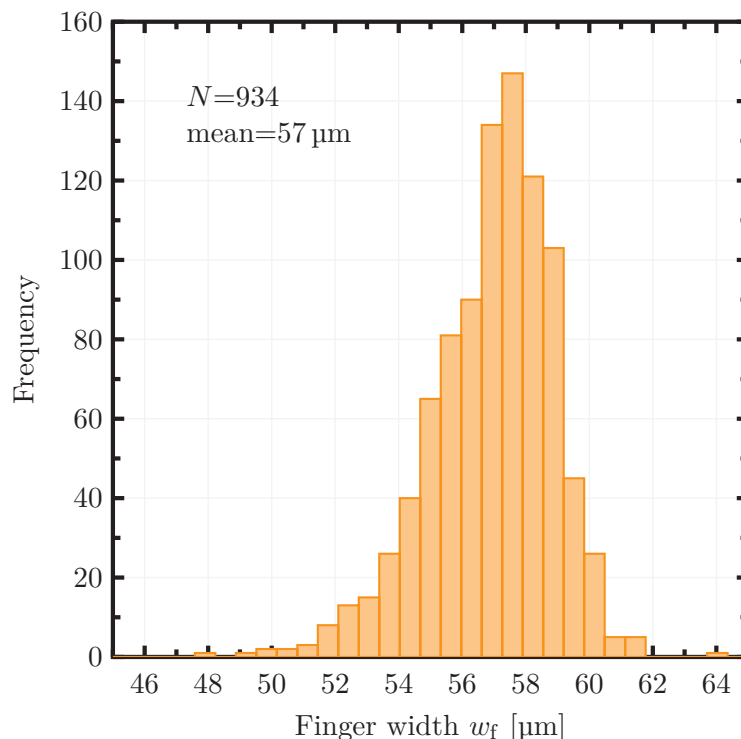


Figure 4.4: Frequency of finger widths w_f for a PERC. We measure a number of 934 fingers and determine a mean finger width of $(57 \pm 2) \mu\text{m}$.

where t_f is the thickness of the finger, w_f is the width of the finger, and a , b , c and d are free fit parameters. Using $a = 70 \mu\text{m}$, $b = 15 \mu\text{m}$, $c = 30 \mu\text{m}$ and $d = 14 \mu\text{m}$ fits our experimental data.

The micrograph in Fig. 4.3 (b) shows the top view of a front metal finger with a magnification factor of 100. Our image processing tool increases the contrast and creates a binary image to extract the finger area. For the binary image we convert the darkest 30% of all pixels to 0 and the remaining pixels to 1 in each image. In this way, we distinguish the finger from the background. A finger always extends across the total width of a micrograph. Integrating the area of all pixels and dividing by the width of the micrograph image, we obtain the mean width of a finger. The red contour line surrounding the finger in Fig. 4.3 (b) indicates the perimeter of such an extracted area. The average width of the finger w_f in Fig. 4.3 (b) is $56 \mu\text{m}$.

Figure 4.4 shows a histogram of the width for 934 finger measurements on a PERC (see section 3.2.3, pp. 3.2.3). The mean finger width is $57 \mu\text{m}$ with a standard deviation of $2 \mu\text{m}$.

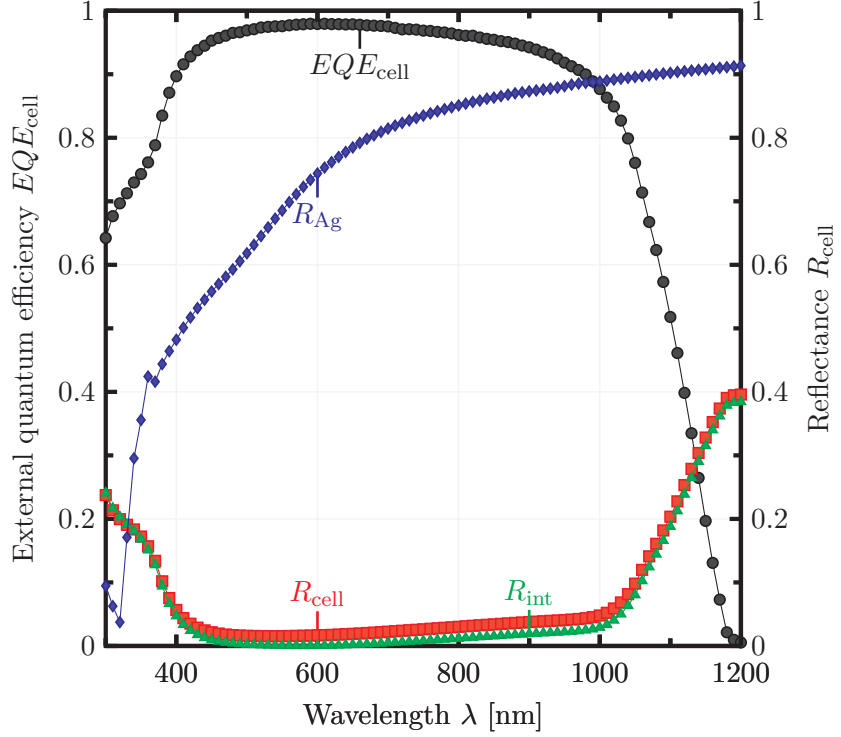


Figure 4.5: The black circles (\bullet) show the EQE_{cell} and the red squares (\blacksquare) the reflection R_{cell} measurement data for a $(2 \times 2) \text{ cm}^2$ area between two busbars, containing only front metal fingers. The green triangles (\blacktriangle) show the reflection of the intermediate cell area between the front metal fingers R_{int} as determined by Eq. 4.5. The blue diamonds (\blacklozenge) show the reflection measurement R_{Ag} for a $(2.1 \times 2.1) \text{ cm}^2$ area consisting of the Ag paste of the fingers.

4.3.2 Results of the measurement of the optical properties of the front metal fingers

Figure 4.5 shows the external quantum efficiency EQE_{cell} and reflectance R_{cell} of a PERC measured on a $(2 \times 2) \text{ cm}^2$ area between two busbars, containing only front metal fingers. Figure 4.5 also shows the reflectance R_{Ag} of an $(2.1 \times 2.1) \text{ cm}^2$ square consisting only of the Ag paste for the front metal fingers. From the reflectance of the silver paste and the cell we determine the effective optical width $w_{f,\text{eff}}$ of the fingers according to a method presented in Refs. [191, 192]. The reflectance of the cell

$$R_{\text{cell}}(\lambda) = f_{\text{met,opt}} R_{\text{Ag}}(\lambda) + (1 - f_{\text{met,opt}}) R_{\text{int}}(\lambda), \quad (4.5)$$

comprises the reflectance of the front metal fingers R_{Ag} as well as the reflectance of the silicon and the anti-reflection coating (ARC) from areas in between the fingers R_{int} . The effective optical fraction of the front metalization is denoted $f_{\text{met,opt}}$. Recalling Eq. 2.9 (see section 2.2.1, pp. 8) the reflectance from areas in between the fingers R_{int} is approximately zero for a certain wavelength λ_0 due to the ARC. Thus, we can attribute the remaining reflectance to the front side metalization and determine $f_{\text{met,opt}}$. Assuming that $f_{\text{met,opt}}$ is independent of the spectrum, Eq. 4.5 allows to determine R_{int} for all wavelengths. We iterate this procedure until $f_{\text{met,opt}}$ converges, since the minimum of R_{cell} and R_{int} are not necessarily found for the same

λ_0 due to the spectral dependence of R_{Ag} . Solving the minimization problem we determine the corrected reflectance R_{int} and $f_{met,opt}$ of the fingers.

From the reflection measurement in Fig. 4.5 and the deduced fraction of the front metalization $f_{met,opt}$, we determine the effective optical width of a front metal finger $w_{f,eff}$ for a cell in air. We introduce an optical factor $k_{f,cell}$ as the ratio between the effective optical width for a finger on a cell in air and the geometrical width of the finger

$$k_{f,cell} = \frac{w_{f,eff}}{w_f} = f_{met,opt} \frac{p_f}{w_f}, \quad (4.6)$$

where p_f is the pitch of the fingers. We measure optical factors for the front metal fingers of a cell in air from 0.87 to 0.91.

4.3.3 Modeling the effective optical finger width in a module

In section 4.3.2 we deduced the optical factor of a front metal finger for a cell in air $k_{f,cell}$ from reflection measurements. However, measuring the optical factor for a finger within a module is challenging, since not all the light of the measurement spot is reflected back into the integrating sphere due to total internal reflection at the glass-air interface (see section 3.4.7, pp. 41). Thus, we employ the ray tracing program *Daidalos* to determine an optical factor for the fingers of a cell within a module $k_{f,mod}$ [127].

We apply the same method from section 4.2 for the LBIC measurement to determine the optical factor from the simulations. First, we simulate a cell in air. The simulation domain extends over an area A_{act} that is equal in length to the length of the finger and equal in width to the pitch of the front metal fingers of the measured cell. This simulation only comprises the cell without any front metalization.

Then we perform a second simulation of the same area, but including one front metal finger, denoted as $A_{act,f}$. For the finger shape we apply the function of the profile in Fig. 4.3 (a) and assume a uniform spatial expansion of the profile in the length dimension of the simulation domain.

We introduce a Lambertian factor Λ to account for a specular or diffuse reflecting finger. $\Lambda=0$ represents a specular reflecting finger and $\Lambda=1$ assumes a perfect diffuse Lambertian reflector. Values between 0 and 1 comprise fractions of specular and diffuse reflection.

Simulating the current for an area with finger $I_{act,f}$ and the current for an area without a finger I_{act} , we calculate the effective optical finger width $w_{f,eff}$ according to the method in section 4.2 (pp. 45) with

$$w_{f,eff} = w_{act} \left(1 - \frac{I_{act,f}}{I_{act}} \right). \quad (4.7)$$

Applying Eq. 4.6 we determine the optical factor for the finger $k_{f,cell}$ from the simulated $w_{f,eff}$. Then we perform the same simulations for a cell in a module and likewise determine the optical factor $k_{f,mod}$.

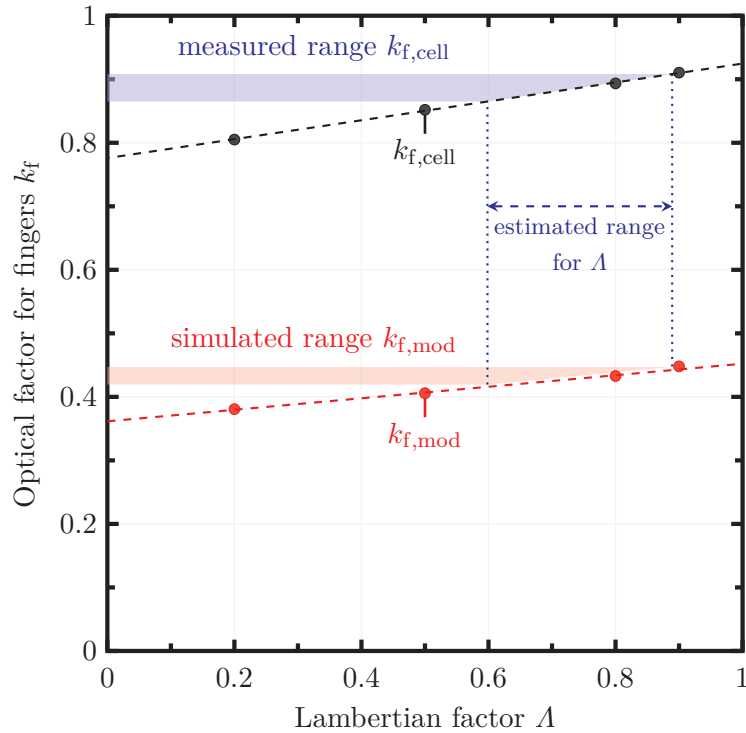


Figure 4.6: Simulated optical factor for the front metal fingers for different Lambertian factors. We distinguish between fingers for a cell in air $k_{f,cell}$ and in a module $k_{f,mod}$. The dashed lines represent the linear regression. The blue area marks the range for $k_{f,cell}$ from the measurement. The dotted lines indicate the range of the corresponding Lambertian factor for this range and the red area marks the range for $k_{f,mod}$.

Figure 4.6 shows the simulation results for $k_{f,cell}$ and $k_{f,mod}$ for various Lambertian factors Λ . The dashed lines represent a linear regression fit. The blue areas indicate the range of the measured optical factor for a cell in air from section 4.3.2 (pp. 51). From the measurement results we deduce the range of Λ . For a Λ from 0.6 to 0.89 the $k_{f,cell}$ from the simulation is similar to the experimental determined values. We assume that Λ does not change due to the transition of a cell from air into a module and determine the red area indicating the range for the optical factor for the fingers within a module $k_{f,mod}$. The range for $k_{f,mod}$ is between 0.42 and 0.45.

4.3.4 Discussion of the cell to module losses for the front metal fingers

We deduce a homogeneous finger width of $57\mu\text{m}$ across the cell with a standard deviation of only $2\mu\text{m}$ from the measurements of the front metal finger width. Thus, we conclude that using a single finger shape with a profile as in Fig 4.3 (a) in the ray tracing simulation domain is representative for all front metal fingers of the whole cell.

We approximate the profile of the finger with a combination of a Gaussian and a second order polynomial function in Eq. 4.4. Two functions are necessary since after the screen-printing, when the Ag paste is still wet, the fingers tend to smear at the edges. For the finger in Fig. 4.3 (a) this transition is visible at $54\mu\text{m}$. With both functions we achieve reasonable approximations of the finger shape. Describing

the wetting properties with a physical model is rather complex and requires the determination of additional attributes of the Ag paste (e.g. viscosity, liquid-solid interfacial tensions) and is out of the scope of this work [193].

The micrographs in Fig. 4.3 (a) and (b) show that the fingers have a surface roughness. Measuring the optical factors for the fingers of a cell in air reveals that $k_{f,cell}$ varies from 0.87 to 0.91. Thus, we conclude that these variations are due to inhomogeneities of the individual finger shape and surface roughness. Our values are higher than the value measured by Blakers [111] of 0.7 for plated fingers. Blakers [111] indicated that the plated fingers reflect specular, which reduces the effective optical width of the fingers according to our results from the ray tracing simulations and explains the different values for $k_{f,cell}$.

In the ray tracing simulations we account for the inhomogeneities of the individual finger shape and surface roughness by introducing a Lambertian factor. This allows to determine the optical factor of the front metal fingers for a cell in a module, since determining $k_{f,mod}$ from reflection measurements is challenging due to the total internal reflection. Recalling Snell's law (see section 2.2, pp. 7), under a certain angle total internal reflection can occur for light on the transition from one media to another. In fact, this is the case for the glass/air interface in a module due to the higher refractive index of glass compared to air. Thus, only a fraction of the light from the measurement spot is reflected back into the integrating sphere.

However, this effect is beneficial for the cells operating in a module, since it increases the probability of absorption for the light reflected back and forth between the cell and the glass/air interface. We find that encapsulating a cell into a module reduces the effective optical width of a front metal finger, resulting in optical factors $k_{f,mod}$ from 0.42 to 0.45. Hence, a finger with a geometrical width of $60\ \mu\text{m}$ reduces to an effective optical width of $25\ \mu\text{m}$ within a module. A reduction of the effective optical width decreases the optical shading by the fingers and improves the module current. Our values are lower than the values for screen-printed fingers presented in Ref. [194] of 0.52 for $k_{f,mod}$. They examined fingers with a geometrical width of $125\ \mu\text{m}$, which might explain the difference to the values in this work due to different finger profile.

Figure 4.6 shows that decreasing the Lambertian factor results in a reduction of the optical factor. If the Lambertian factor decreases, the fraction of the specular reflection by the finger increases. Due to the parabola like shape of the finger, a specular reflecting finger increases the fraction of total internal reflected light. If the Lambertian factor increases the fraction of diffuse reflections increases and more light is scattered out of the module. Thus, for a cell in a module environment, specular reflecting front metal fingers with a parabola like shape and low surface roughness are beneficial. This explains the lower values of 0.36 to 0.38 for the plated fingers of Blakers and Stuckings [111]. Applying stencil printing allows fingers with a rather high aspect ratio but a rectangular like shape, which increases the optical factor within the module for this fingers.

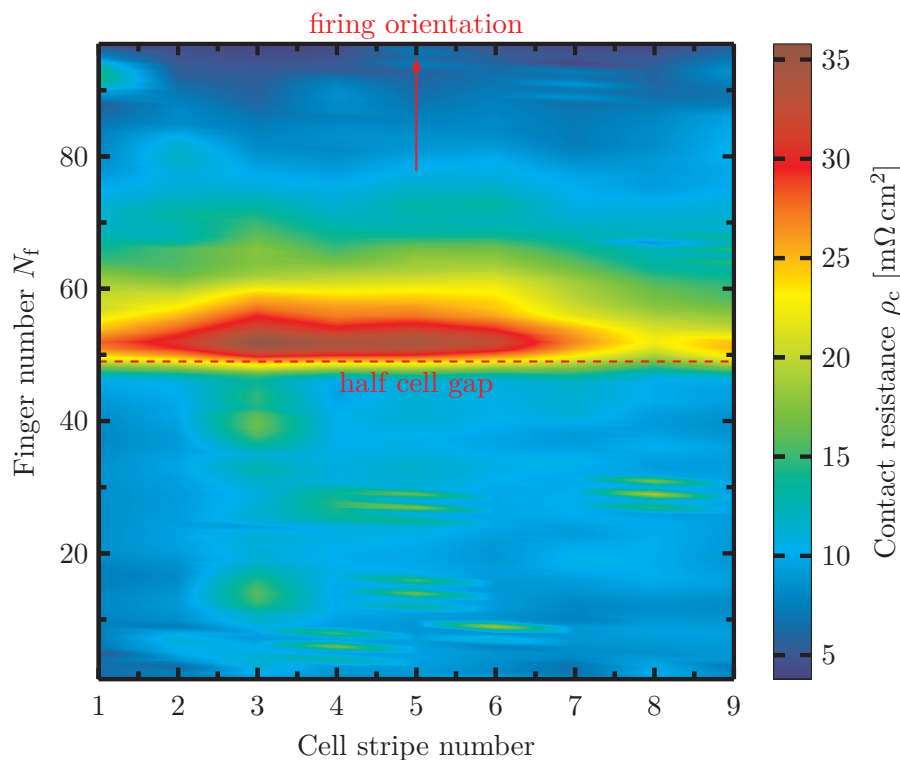


Figure 4.7: Specific finger - emitter contact resistance ρ_c measured on 9 cell stripes of 1 cm width from a PERC with half cell grid. Each cell stripe contains 104 front metal fingers. For the representation in the figure the data in between the measurement points is interpolated. We measure a mean ρ_c of $(12 \pm 6) \text{ m}\Omega \text{ cm}^2$. The dashed line indicates the half cell gap of the metal grid and the red arrow the orientation in the conveyor belt furnace for the contact firing.

4.4 Finger-emitter contact resistance

4.4.1 Results of the finger-emitter contact resistance measurements

Figure 4.7 shows a surface plot of the specific contact resistance ρ_c for nine cell stripes from a PERC with half cell metalization grid (see section. 3.4.5, pp. 37). Each cell stripe contains 104 front metal fingers. The data in between the measurement points is interpolated. The horizontal dashed line in the center of the graph indicates the gap for the half cell metalization grid. The red arrow at the top points in the moving direction of the cell in the conveyor belt furnace during the contact firing.

We measure a mean ρ_c of $12 \text{ m}\Omega \text{ cm}^2$ with a standard deviation of $6 \text{ m}\Omega \text{ cm}^2$ for the complete cell. We observe an increase in ρ_c from the top side to the center of the PERC. On the average of all stripes ρ_c increases from $8 \text{ m}\Omega \text{ cm}^2$ for finger 97 to $25 \text{ m}\Omega \text{ cm}^2$ for finger 52.

4.4.2 Discussion of the finger-emitter contact resistance measurements

In contrast to the finger width the contact resistance of the fingers to the emitter is inhomogeneous across the cell. This is evident due to the average ρ_c of $12 \text{ m}\Omega \text{ cm}^2$

and the rather high standard deviation of $6 \text{ m}\Omega \text{ cm}^2$. The surface plot in Fig. 4.7 indicates a peak in the center of the cell, exactly above the gap for the half cell metalization grid. In this region the contact resistance is three times higher than the cell's average. Considering only the lower half of the cell, the average contact resistance is $10 \text{ m}\Omega \text{ cm}^2$, while for the upper half it is $14 \text{ m}\Omega \text{ cm}^2$.

We find correlations between regions with increased contact resistance and the cell orientation in the conveyor belt furnace (see Appendix A.2). The cell side first entering the furnace always shows an increased contact resistance. A hypothesis is that the interruption of the metal grid suppresses the exchange of heat or charge between the two halves. Rotating the cell 90° , such that the cell edge perpendicular to the front metal fingers enters the furnace first, also results in a deterioration of the contact resistance close to the cell edge first entering the furnace. This we ascribe to the lower conductivity of the front metal fingers that have a 15-20 times smaller cross section area than the busbars. Further, applying a conductive connection to the half cell metal grid interruption by manually printing Ag paste with a tiny brush to the gap between the busbars in the center of the cell, shows no local increase in contact resistance at the metal grid interruption after the contact firing.

A work around to solve this issue is to dry the screen-printing paste in a furnace at 200°C , cut the cells with the laser and then perform the contact firing step. Initially, we introduced this gap for symmetry reasons when cutting the cells into halves and to prevent cell cracks when soldering a cell interconnection ribbon to the busbar.

4.5 Optical properties of the backsheet within a solar module

4.5.1 Modeling the effect of the backsheet reflection on the module current

We simulate a module with *Daidalos* and vary the cell spacing in the simulation to evaluate the contribution by total internal reflections from the backsheet to the module's short circuit current. The module simulation domain incorporates a center cell with periodic boundary conditions. For the simulation we consider a white colored backsheet. We vary the cell spacing d_{c2c} as well as the string spacing d_{s2s} and calculate the J_{sc} . For all variations we set d_{c2c} equal to d_{s2s} . In addition to the white backsheet, we simulate an intermediate reflector (IMR). This IMR is a white foil located on top of the rear EVA and at the same level as the cell (see Fig 4.8). Further, we simulate a half cell. We introduce an optical enhancement factor k_{bs} for the backsheet as

$$k_{bs} = \frac{J_{sc,d}}{J_{sc,0}}, \quad (4.8)$$

where $J_{sc,d}$ is the simulated short circuit current density for a module with varying cell and string spacing and $J_{sc,0}$ is the simulated short circuit current density for a module with no gaps between the cells.

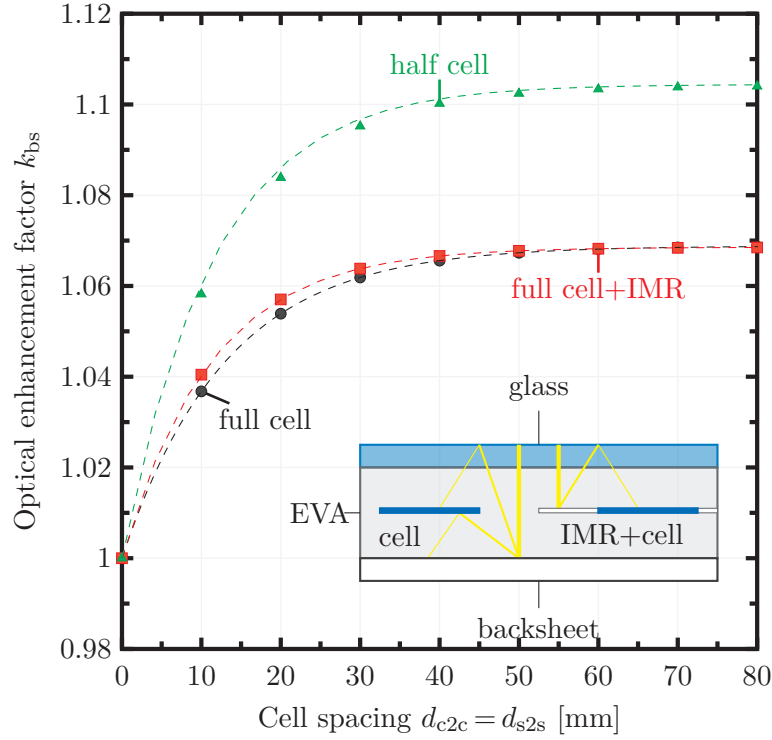


Figure 4.8: Simulated backsheet enhancement factor k_{bs} for a module containing a center cell with periodic boundary conditions. Symbols indicate the data from the ray tracing simulations. Dashed lines indicate an exponential fit according to Eq. 4.9. We simulate a module with full cells and a white backsheet, with full cells and an IMR, and with half cells and a white backsheets. The inset indicates the principle of the IMR.

Figure 4.8 shows the simulated k_{bs} as a function of the cell spacing. The dashed lines indicate an exponential fit to the simulation data

$$k_{bs} = a \exp\left(-\frac{d_{c2c} + d_{s2s}}{b}\right) + c, \quad (4.9)$$

where a, b and c are free fit parameters.

The k_{bs} increases for all cells with increasing cell spacing and saturates at 50 mm. Applying an IMR at cell level results in slightly higher k_{bs} in the range from 0 mm to 30 mm. The k_{bs} of both full cell modules saturate at 50 mm at a $k_{bs} = 1.07$. Employing half cells results in higher k_{bs} that saturate at 50 mm with $k_{bs} = 1.1$.

4.5.2 Discussion of the current enhancement by the backsheet

Figure 4.8 shows that increasing the cell distance, increases the current and in turn the power output of the module. The backsheet reflects light below the cell, where it is absorbed by the cell's rear metalization. Thus an intermediate reflector increases the current enhancement compared to a backsheet by a maximum of 0.4% especially for small cell distances.

Fitting k_{bs} with Eq. 4.9 is useful for the modeling of cell to module losses. Determining the optical enhancement factor for a specific backsheet with ray tracing simulations

and fitting with Eq. 4.9 once, enables to determine k_{bs} for any cell and string spacing. This allows the simple implementation of the optical enhancement factors in an analytical model.

Half cells result in higher k_{bs} and thus, increase the module current with increasing cell gap. In Ref. [195] the authors report an experimentally determined increase of the module current by 3%, when employing half cells. Applying the simulated k_{bs} to their cell distances we calculate a current enhancement of 2.8% for a module consisting of half instead of full cells. The values are in good agreement, considering tolerances of the cell spacing and different optical properties of the backsheet and encapsulation materials. Employing half cells increases the fraction of the backsheet area compared to the fraction of the cell area in a module. In fact, this effect is the reason for the increased current enhancement by the backsheet when employing half cells.

Similar as for the white colored cell interconnection ribbon (CIR), the total internal reflection governs the current enhancement by diffuse reflections from the backsheet and the intermediate reflector (IMR). Thus, a natural choice is to replace the diffuse reflecting IMR with the groove-structured foil we applied to the CIR in test module M-LRF. The measurements of the optical factor of the CIR for the test module M-LRF reveal a k_{ci} of 0.31. This implies that the groove-structured foil reflects about 70% of the light impinging on the CIR onto the cell. Considering the same effect when applying the groove-structured foil in the cell gaps, the optical enhancement factor k_{bs} is equivalent to $1-k_{ci}$. This increases the k_{bs} in a half cells module with a 2 mm cell spacing from a k_{bs} of 1.0167 for a white backsheet to a k_{bs} of 1.027 for a groove-structured foil in the cell gaps, which increases the module current by 1%. In Ref [130], we show with ray tracing simulations that this gain is also achieved for different global locations considering realistic irradiation conditions.

4.6 Parameters from literature

Measuring all required cell and module parameters to model the cell to module losses, is beyond the scope of this work. Hence, we also adopt parameters from the literature. Most of the data was published by the Institute for Solar Energy Research Hamelin (ISFH) for similar cell processes as in this work.

For the contact resistance for the rear side of a PERC, we adopt $\rho_{c, rear}$ values provided in reference [196].

A method to measure the surface recombination at the metal contacts was proposed by Fellmeth et al. [93]. They measured the J_{0s} for cells with various metalization fractions. Hannebauer et al. [197] performed similar measurements for passivated emitter and rear cell. In this work we apply values from Hannebauer et al. since they measured the saturation current densities for similar cells and metalization pastes as in this work.

Vogt investigated the complex refractive index of various front glasses and encapsulation polymers for solar modules [198, 199]. We use his optical data for the low iron soda lime glass, the conventional EVA as well as the EVA with enhanced UV transmittance for the optical simulation.

The evaluation of the ray tracing results requires the collection efficiency η_{perc} of the PERC according to Eq. 2.24 (see pp. 20). We use η_{perc} as determined in Ref. [131].

We consider a reduction of the short circuit current density J_{sc} due to the front glass and EVA of $k_{\text{red}} = 3\%$ to 4% as determined in Refs. [49, 118]. All parameters are listed in Table 4.3 and Table 4.4.

4.7 Parameter overview

Table 4.3 lists all PERC and Table 4.4 lists all module parameters for the simulation of the PERC cell to module losses in this work.

Table 4.4: Summarized module simulation parameters. Parameters marked with an Asterisk have been measured within this work.

parameter	symbol	value	unit	source
SCR thickness	t_{sir}	200	μm	*
SCR width	w_{sir}	6	mm	*
number of CIR	N_{ci}	3-7		*
number of CIW	N_{ci}	10-55		*
CIR thickness	t_{cir}	200	μm	*
CIR width	w_{cir}	1-2.5	μm	*
CIW diameter	d_{ciw}	200	μm	*
line resistance CIR	ρ_{cir}	0.56-0.57	$\text{m}\Omega \text{cm}^{-1}$	*
line resistance SCR	ρ_{SIR}	0.14	$\text{m}\Omega \text{cm}^{-1}$	*
line resistance CIW	ρ_{ciw}	5.33-5.44	$\text{m}\Omega \text{cm}^{-1}$	*
distance between cells	d_{c2c}	1.9-2.1	mm	*
distance between strings	d_{s2s}	1.9-2.1	mm	*
EVA thickness	t_{eva}	440-460	μm	*
glass thickness	t_{glass}	3.1-3.3	mm	*
opt. factor finger (module)	$k_{\text{f,mod}}$	0.42-0.45		*
optical factor CIR	k_{ci}	0.84-0.94		*
opt. fact. white CIR	k_{ci}	0.49-0.59		*
opt. fact. LHS CIR	k_{ci}	0.26-0.38		*
opt. fact. LRS CIR	k_{ci}	0.25-0.37		*
opt. fact. CIW	k_{wire}	0.60-0.71		*,[190]
current reduction glass/EVA	k_{red}	0.03-0.04		[49],[118]

Table 4.3: Summarized range of the cell parameters for this work. Parameters marked with an Asterisk have been measured within this work.

parameter	symbol	value	unit	source
cell area	A_{cell}	240.5	cm^2	*
base resistance	ρ_{b}	1.5-2.5	$\Omega \text{ cm}$	*
cell thickness	t_{cell}	160-170	μm	*
emitter sheet resistance	R_{sh}	83-90	Ω/\square	*
cell efficiency	η	20.3-20.9	%	*
current density non-metalized area	$J_{\text{sc,act}}$	40.75-41.0	mA cm^{-2}	*
shunt resistance	R_{p}	25-242	$\text{k}\Omega \text{ cm}^2$	*
second diode saturation current density	J_{02}	8.5-15	nA cm^{-2}	*
first diode ideality factor	n_{01}	1		*
second diode ideality factor	n_{02}	2		*
base and rear contribution	$J_{0\text{b}}$	100-200	fA cm^{-2}	*
emitter contribution	$J_{0\text{e,pass}}$	80-120	fA cm^{-2}	[197]
metal contribution	$J_{0\text{e,met}}$	350-550	fA cm^{-2}	[197]
number of fingers	N_{f}	80-130		*
finger width (single print)	w_{f}	55-59	μm	*
finger thickness	t_{f}	15-20	μm	*
optical factor finger (cell)	$k_{\text{f,cell}}$	0.87-0.91		*
optical factor busbar	$k_{\text{f,cell}}$	0.97-0.99		*
line resistance finger	ρ_{f}	3.1-4.1	$\text{m}\Omega \text{ cm}^{-1}$	*
busbar thickness	t_{bb}	10-15	μm	*
busbar width	w_{bb}	0.8-1.3	mm	*
line resistance busbar	ρ_{bb}	23-40	$\text{m}\Omega \text{ cm}^{-1}$	*
line resistance metal rear side	ρ_{rear}	34-43	$\text{m}\Omega \text{ cm}^{-1}$	*
contact resistance front	ρ_{c}	6-18	$\text{m}\Omega \text{ cm}^2$	*
contact resistance back	$\rho_{\text{c,rear}}$	8	$\text{m}\Omega \text{ cm}^2$	[196]
soldering joints	N_{sp}	6		*

CHAPTER 5

Modeling cell to module losses

Within this chapter we present an analytical model to simulate the optical, recombination and resistive cell to module (CTM) losses based on our experimental results. For the resistive losses we extend an existing model for the the cell and string interconnection in a solar module. After verification of the model we optimize the cell's front metalization and the cell interconnection to build two modules, one aiming for an enhanced power output and one aiming for an improved module efficiency.

5.1 Analytical series resistance model

The symmetry of the front metalization allows to split the cell into various unit cells. We distinguish contributions of the emitter, base, front metal fingers, busbars, rear metalization, cell interconnector (CI), and string interconnection ribbon (SIR). Figure 5.1 depicts the partition of a PERC into three unit cells.

Unit cell 1 represents the area adjacent to a front metal finger. Thus, it comprises the contribution of the finger, busbar, and emitter to the series resistance of the solar cell. Unit cell 2 represents the area next to the CI that collects the current from the busbar and rear metalization. Unit cell 3 represents a solar cell within a module, which takes the base and the SIR into account. We apply the convention to normalize all resistive power losses to the area of a solar cell, e.g. for a solar cell unit cell 1 occurs two times for each cell interconnector and once per finger.

In this work, we apply the two dimensional analytical series resistance model of Deb et al. and extend the model for the cell and string interconnection with cell interconnection ribbons and cell interconnection wires. With the analytical model we calculate the series resistance of the solar cell and module, which we will derive in more detail in the following.

The resistive power loss P_{loss} given in units of W due to a constant current I traversing a material of length l_{mat} and cross section area A_{mat} follows the relation

$$P_{\text{loss}} = I^2 \frac{r_{\text{mat}} l_{\text{mat}}}{A_{\text{mat}}}, \quad (5.1)$$

where r_{mat} is the specific resistance of the material. We assign a resistive power loss to each unit cell $P_{\text{loss,uci}}$, where the index i indicates the considered unit cell

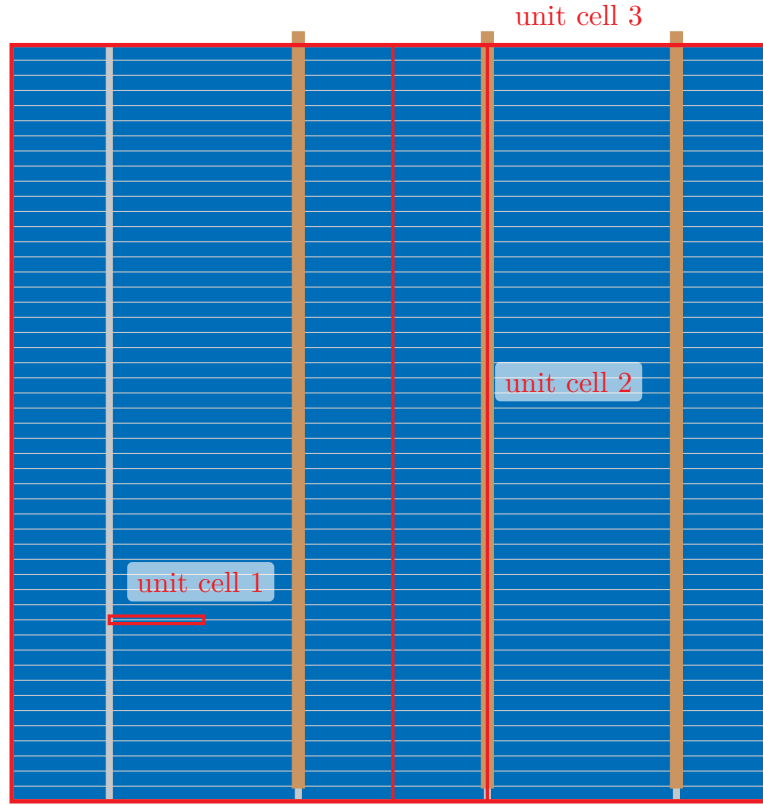


Figure 5.1: Unit cell approach to determine the cell to module power losses. Unit cell 1 accounts for the finger domain. Unit cell 2 contains the cell interconnector for the cell interconnection unit cell 3 represents a solar cell within a module.

in Fig. 5.1. The total resistive power loss P_{tot} for the whole cell is the sum of the resistive power losses of all unit cells 1 through 3

$$P_{\text{tot}} = \sum_{i=1}^3 N_{\text{uci}} P_{\text{loss,uci}}, \quad (5.2)$$

where N_{uci} is the number and $P_{\text{loss,uci}}$ is the resistive power loss of each unit cell per solar cell in a module. From the total resistive power loss we calculate the specific series resistance R_s of the solar cell by

$$R_s = \frac{P_{\text{tot}}}{I_L^2} A_{\text{cell}}, \quad (5.3)$$

where I_L is the light generated current and A_{cell} the cell area.

Unit cell 1

The number of unit cells 1 is determined by the number of front metal fingers N_f and the number of cell interconnectors N_{ci} of the cell and given by

$$N_{\text{uc1}} = 2N_{\text{ci}}N_f. \quad (5.4)$$

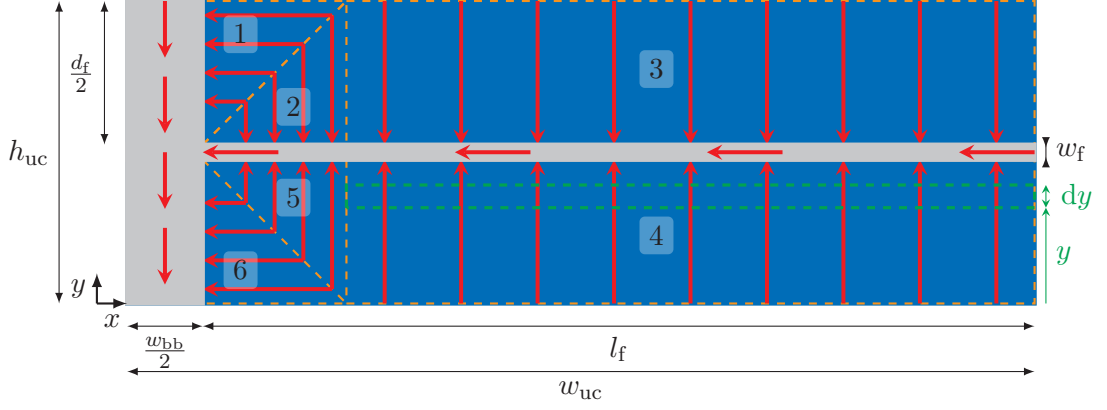


Figure 5.2: Unit cell 1 comprising a finger of length l_f and width w_f as well as half a busbar of width w_{bb} . The height of the unit cell h_{uc} is equal to the finger pitch and the width w_{uc} is equal to half the busbar pitch. The distance between two fingers is d_f . The red arrows indicate the current direction in the emitter, finger and busbar.

A solar cell generates current in all active areas (blue areas in Fig. 5.1) and the current in the emitter region increases incrementally on the path to the metal contacts. We assume a spatially homogeneous emitter sheet resistance R_{sh} , spatially homogeneous generation of charge carriers, and that the current flows perpendicular into the metal components.

Figure 5.2 shows a magnification of unit cell 1. It comprises a finger of length l_f and half a busbar of width w_{bb} . The height of the unit cell h_{uc} is equal to the finger pitch and the width w_{uc} is equal to half the busbar pitch. The distance between two fingers d_f contains only the active cell area and the emitter, respectively. The red arrows indicate the direction of the current flow.

For the cell interconnection we distinguish between a cell interconnection ribbon (CIR) and a cell interconnection wire (CIW). For the CIR we split the emitter into two rectangular (3 and 4) and four triangular (1, 2, 5, and 6) areas. The current flows from the rectangles 3 and 4 as well as the adjacent triangles 2 and 5 into the finger. From the triangles 1 and 6 the current flows into the busbar. From the finger and the busbars the current flows into the CIR.

For the green rectangle in Fig. 5.2 with the width of rectangle 4 and height dy , the differential sheet resistance is [200]

$$dR_{sh,rect4} = \frac{R_{sh}}{\left(l_f - \frac{d_f}{2}\right)} dy. \quad (5.5)$$

Within rectangle 4 the current flows perpendicular into the metal finger. For the green rectangle the current increases incrementally in the y direction with

$$I_{rect4}(y) = \int_0^y J \left(l_f - \frac{d_f}{2}\right) d\hat{y} = J \left(l_f - \frac{d_f}{2}\right) y, \quad (5.6)$$

where J is the current density per area. We select \hat{y} as integration variable to avoid labeling the integration boundary with the same symbol.

According to Eq. 5.1 the incremental resistive power loss for the green rectangle is

$$dP_{e,\text{rect}4} = I_{\text{rect}4}(y)^2 dR_{\text{sh},\text{rect}4} = J^2 R_{\text{sh}} \left(l_f - \frac{d_f}{2} \right) y^2 dy. \quad (5.7)$$

The total resistive power loss for the rectangle 4 is

$$P_{e,\text{rect}} = \int_0^{\frac{d_f}{2}} I_{\text{rect}4}^2 dR_{\text{sh},\text{rect}4} = \frac{J^2 R_{\text{sh}}}{48} d_f^3 (2l_f - d_f). \quad (5.8)$$

Due to the symmetry $P_{e,\text{rect}}$ is also the resistive power loss for rectangle 3.

In the triangular areas the sheet resistance and the current depend on x and y . Here, we utilize that all triangles are equal sided triangles and consider $x = y$. For triangle 5 the differential sheet resistance is given by

$$dR_{\text{sh},\text{tri}5} = \frac{R_{\text{sh}}}{y} dy, \quad (5.9)$$

For the current we integrate with respect to the x and the y direction

$$I_{\text{tri}5} = \int_0^y \int_0^x J d\hat{x} d\hat{y} = \frac{Jy^2}{2}. \quad (5.10)$$

Combining Eqs. 5.9 and 5.10 yields the resistive power loss in the triangle

$$P_{e,\text{tri}} = \int_0^{\frac{d_f}{2}} I_{\text{tri}5}^2 dR_{\text{sh},\text{tri}5} = J^2 R_{\text{sh}} \frac{d_f^4}{256}. \quad (5.11)$$

Likewise, we calculate the resistive power dissipation in the triangles 1,2, and 6.

The total resistive power loss in the emitter sheet for unit cell 1 is

$$P_e = 4P_{e,\text{tri}} + 2P_{e,\text{rect}} = J^2 R_{\text{sh}} \frac{d_f^3 (16l_f - 5d_f)}{192}. \quad (5.12)$$

Similar we calculate the resistive power loss for a finger with a specific resistance r_f and cross section area A_f . We intersect the finger in a segment adjacent to the rectangular and the triangular areas. The rectangular area can be either rectangle 3 or 4 and the triangular area can be either triangle 2 or 5 in Fig. 5.2. The resistive power loss in a finger segment adjacent to a rectangular area is

$$P_{f,\text{rect}} = J^2 r_f \frac{d_f^2 (2l_f - d_f)^3}{48A_f}. \quad (5.13)$$

For the finger segment adjacent to triangle 2 it is necessary to consider the current from rectangle 3 as well. Likewise, the finger segment adjacent to triangle 5 carries

the current from rectangle 4. Therefore, the power dissipation in the finger segment adjacent to a triangle is

$$P_{f,\text{tri}} = J^2 r_f \frac{d_f^3 (7d_f^2 - 40d_f l_f + 60l_f^2)}{240A_f}. \quad (5.14)$$

The total resistive power loss for a finger is

$$P_f = 2P_{f,\text{tri}} + 2P_{f,\text{rect}}. \quad (5.15)$$

For the resistive power loss in a busbar we take into account that the current increases from the start to the end of the busbar and the busbar collects the current from each finger. Considering the j -th unit cell 1 of a busbar, the index j runs from 1 to the number of front metal fingers N_f .

For the upper busbar segment before the j th finger in Fig. 5.2, we take the current of the adjacent triangular area 1 and the sum of the currents from the previous $(j - 1)$ unit cells 1 into account. Thus, the resistive power loss in all upper busbar segments is

$$P_{\text{ubb}} = \frac{J^2 r_{\text{bb}} N_f d_f^3}{120 t_{\text{bb}} w_{\text{bb}}} \left(d_f^2 + 10d_f l_f N_f - 10d_f l_f + 40l_f^2 N_f^2 - 60l_f^2 N_f + 20l_f^2 \right), \quad (5.16)$$

where r_{bb} denotes the specific resistance, w_{bb} the width, and t_{bb} the thickness of the busbar. Here, we utilize [201]

$$\sum_{k=1}^n k^2 = \frac{n(n+1)(2n+1)}{6} \quad (5.17)$$

for the series expansion of the sum in Eq. 5.16.

The lower busbar segment after the j th finger in Fig. 5.2 collects the current from the adjacent triangle 6, the j -th finger, the upper busbar segment and the sum of the currents from the previous $(j - 1)$ unit cells 1. Therefore, the resistive power loss of all lower busbar segments is

$$P_{\text{lbb}} = \frac{d_f^3 J^2 N_f r_{\text{bb}}}{960 t_{\text{bb}} w_{\text{bb}}} \left[3d_f^2 - 40d_f l_f (N_f + 1) + l_f^2 (320N_f^2 + 480N_f + 160) \right]. \quad (5.18)$$

Note that P_{ubb} and P_{lbb} already take the number of front metal fingers into account. Thus, the total resistive power loss in the busbar for the whole solar cell is

$$P_{\text{bb}} = 2N_{\text{ci}}(P_{\text{ubb}} + P_{\text{lbb}}). \quad (5.19)$$

The total power loss of a solar cell with single screen-print metalization for all unit cells 1 is

$$P_{\text{loss,uc1}} = N_{\text{uc1}}(P_e + P_f) + P_{\text{bb}}. \quad (5.20)$$

A cell interconnection wire (CIW) only contacts the finger but not the emitter. In this case we omit all triangular areas in Fig. 5.2 and consider only the rectangular

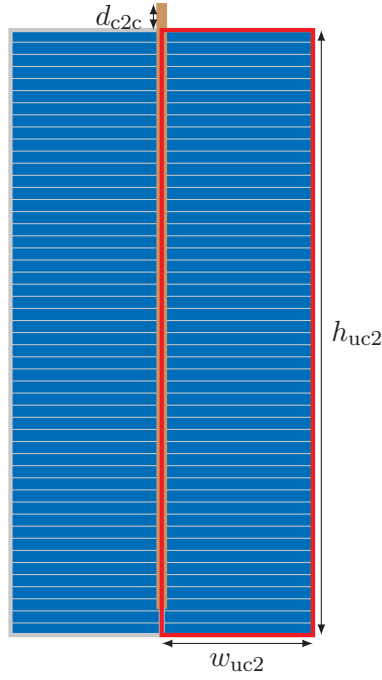


Figure 5.3: Scheme of unit cell 2 with a cell interconnector in the center. The width of the unit cell is w_{uc2} and the height is h_{uc2} . At the end of the cell the CI extends to the next cell over the cell spacing d_{c2c} .

areas. Then rectangles 3 and 4 in Fig. 5.2 extend over the entire finger length l_f and the current flows only from the emitter into the front metal finger. Therefore, we obtain for the resistive power loss in the emitter

$$P_{e,ciw} = J^2 R_{sh} \frac{d_f^3 l_f}{12} \quad (5.21)$$

and in the finger

$$P_{f,ciw} = J^2 r_f \frac{d_f^2 l_f^3}{3A_f}. \quad (5.22)$$

Note that Eqs. 5.21 and 5.22 are equivalent to the formulas in Green [200] and Serreze [122]

The total power loss for unit cell 1 with a CIW is

$$P_{loss,uc1} = N_{uc1} (P_{e,ciw} + P_{f,ciw}). \quad (5.23)$$

Unit cell 2

Figure 5.3 schematically shows unit cell 2 that represents the area next to a cell interconnector (CI). The CI collects the current over the height of unit cell 2 h_{uc2} . The width of unit cell 2 is w_{uc2} . At the ends of a cell the CI extends to the next cell over the cell to cell distance d_{c2c} . The number of unit cells 2 is determined by the number of CIs N_{ci} and given by

$$N_{uc2} = 2N_{ci}. \quad (5.24)$$

Concerning the CI, we distinguish between cell interconnection ribbon (CIR) and cell interconnection wire (CIW). As described in section 2.6 a CIR is soldered onto the busbar. We assume that the CIR contacts the busbar over its full length and thus, the specific resistance of the busbar r_{bb} in Eq. 5.16 and Eq. 5.18 is replaced by a parallel specific resistance of the busbar and the CIR

$$r_{bb\parallel\text{cir}} = \frac{r_{bb}r_{\text{cir}}(t_{bb} + t_{\text{cir}})w_{\text{cir}}}{r_{\text{cir}}t_{bb}w_{bb} + r_{bb}t_{\text{cir}}w_{\text{cir}}}, \quad (5.25)$$

where we set the length of the busbar equal to the length of the CIR. The width of the parallel connection of busbar and CIR we set equal to the width of the CIR.

A cell interconnection wire (CIW) only contacts the finger and thus, collects the current only from the fingers. For the CIW segment before the j -th finger we have to consider the sum of the current of the $(j - 1)$ fingers. Thus, for this CIW segment the resistive power loss reads

$$P_{\text{uciw}} = J^2 r_{\text{ciw}} \frac{N_f d_f^3 l_f^2 (2N_f^2 - 3N_f + 1)}{6A_{\text{ciw}}}, \quad (5.26)$$

where A_{ciw} is the cross section area and r_{ciw} the specific resistance of the cell interconnection wire.

For the CIW segment after the j -th finger, we consider the sum of the currents of all $(j - 1)$ fingers and the current of the j -th finger. Thus, the resistive power loss for this CIW segment is

$$P_{\text{lciw}} = J^2 r_{\text{ciw}} \frac{N_f d_f^3 l_f^2 (2N_f^2 + 3N_f + 1)}{6A_{\text{ciw}}}. \quad (5.27)$$

Combining Eqs. 5.26 and 5.27 yields the resistive power loss in the cell interconnection wire

$$P_{\text{ciw}} = J^2 r_{\text{ciw}} \frac{N_f d_f^3 l_f^2 (2N_f^2 + 1)}{3A_{\text{ciw}}}. \quad (5.28)$$

Note that this equation is equivalent to the relation found by A. R. Burgers [202] for a CIR with multiple solder joints.

For the rear side we assume that each cell interconnector (CI) contacts the Al rear metalization at every point and collects the current. The series resistance contribution of a rear CI then is

$$P_{\text{rear}} = \frac{2}{3} J^2 \frac{r_{\text{ci}}}{A_{\text{ci}}} h_{\text{uc}2}^3 w_{\text{uc}2}^2, \quad (5.29)$$

where r_{ci} is the specific resistance and A_{ci} the cross section area of the CI. Note that in this case a CI is either a cell interconnection ribbon (CIR) or a cell interconnection wire (CIW).

In between two cells a CI conducts the current to the next cell over the distance d_{c2c} . Similarly, at the ends of each string the CI conducts the current to the string interconnection ribbon (SIR). The resistive power loss in the CI extension is

$$P_{c2c} = 2J^2 \frac{r_{\text{ci}}}{A_{\text{ci}}} w_{\text{uc}2}^2 h_{\text{uc}2}^2 d_{c2c}. \quad (5.30)$$

The total power loss for unit cell 2 with CIRs is

$$P_{\text{loss,uc2}} = N_{\text{uc2}} (P_{\text{rear}} + P_{c2c}) \quad (5.31)$$

and with CIWs

$$P_{\text{loss,uc2}} = N_{\text{uc2}} (P_{\text{rear}} + P_{c2c} + P_{\text{ciw}}). \quad (5.32)$$

Unit cell 3

Unit cell 3 occurs once per cell. We assume that the current flow through the wafer of thickness t_{cell} and with base resistance ρ_b is normal to the rear Al. Then, the resistive power loss contribution of the base is

$$P_{\text{base}} = J^2 \rho_b A_{\text{uc3}} t_w. \quad (5.33)$$

At the end of each cell string of the solar module, the string interconnection ribbon (SIR) collects the current from the CI. Thus, the current in the SIR increases with the j -th CI, with j running from the 1 to the number of CI N_{ci} . The power loss in the SIR of all $(j - 1)$ segments is

$$\begin{aligned} P_{\text{sir1}} &= \sum_{j=1}^{N_{\text{ci}}} (J 2 w_{\text{uc2}} h_{\text{uc2}} (j - 1))^2 \frac{r_{\text{sir}}}{t_{\text{sir}} w_{\text{sir}}} w_{\text{uc2}} \\ &= \frac{2}{3} J^2 \frac{r_{\text{sir}}}{t_{\text{sir}} w_{\text{sir}}} w_{\text{uc2}}^3 h_{\text{uc2}}^2 N_{\text{ci}} (2N_{\text{ci}}^2 - 3N_{\text{ci}} + 1), \end{aligned} \quad (5.34)$$

where w_{uc2} is the width of unit cell 2, r_{sir} is the specific resistance, w_{sir} the width and t_{sir} the thickness of the SIR. For the series expansion in Eq. 5.34 we utilize [201]

$$\sum_{k=1}^n k^2 = \frac{n(n+1)(2n+1)}{6}. \quad (5.35)$$

Analogously, the power loss in the SIR of the j -th segment is

$$P_{\text{sir2}} = \frac{2}{3} J^2 \frac{r_{\text{sir}}}{t_{\text{sir}} w_{\text{sir}}} w_{\text{uc2}}^3 h_{\text{uc2}}^2 N_{\text{ci}} (2N_{\text{ci}}^2 + 3N_{\text{ci}} + 1). \quad (5.36)$$

Further we have to consider the contribution of the connection between two strings by an SIR over the distance d_{s2s} to the resistive power loss, which is given by

$$P_{\text{sir3}} = J^2 \frac{r_{\text{sir}}}{t_{\text{sir}} w_{\text{sir}}} 4N_{\text{ci}}^2 w_{\text{uc2}}^2 h_{\text{uc2}}^2 d_{s2s}. \quad (5.37)$$

Therefore, the total resistive power loss in the SIR for a single solar cell is

$$P_{\text{sir}} = \frac{4}{3N_{\text{cps}}} \frac{r_{\text{sir}}}{t_{\text{sir}} w_{\text{sir}}} J^2 h_{\text{uc2}}^2 w_{\text{uc2}}^2 N_{\text{ci}} (3d_{s2s} N_{\text{ci}} + w_{\text{uc2}} + 2N_{\text{ci}}^2 w_{\text{uc2}}), \quad (5.38)$$

where N_{cps} is the number of cells per string.

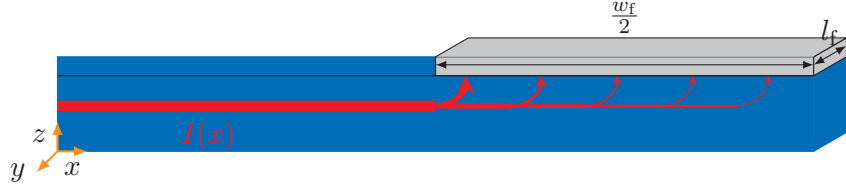


Figure 5.4: Schematic current flow (red) from the emitter (blue) into a front metal finger.

The total power loss for unit cell 3 with CIRs or CIWs is

$$P_{\text{loss,uc3}} = P_{\text{base}} + P_{\text{sir}}. \quad (5.39)$$

Calculating the total resistive power loss according to Eq. 5.2 we can determine the series resistance for the solar cell in the module with Eq. 5.3.

Contact resistance

The resistive power loss due to the contact between the front metal finger and the emitter depends on the specific contact resistance ρ_c of the finger to the emitter, the emitter sheet resistance R_{sh} and the contact area. The same holds for the busbar to emitter contact in case of single screen-printing. We determine their contribution to the resistive power loss of a solar cell according to the model of Berger [174].

Figure 5.4 shows the current I flowing from the emitter into half a finger of width w_f and length l_f . The current flow is perpendicular to l_f and reduces below the finger in the x direction with

$$\frac{dI}{dx} = \frac{V(x)l_f}{\rho_c}. \quad (5.40)$$

In the emitter, the voltage drop due to the emitter sheet resistance below the finger is

$$\frac{dV}{dx} = \frac{I(x)R_{\text{sh}}}{l_f}. \quad (5.41)$$

Combining Eq. 5.40 and 5.41 and rearranging results in

$$\frac{d^2I}{dx^2} = I(x)\frac{R_{\text{sh}}}{\rho_c}. \quad (5.42)$$

Solving the second order differential equation yields the contribution of the finger-emitter contact to the series resistance

$$r_c = l_f d_f \frac{\rho_c}{2l_f L_t} \coth\left(\frac{w_f}{2L_t}\right), \quad (5.43)$$

with the transfer length

$$L_t = \sqrt{\frac{\rho_c}{R_{\text{sh}}}}. \quad (5.44)$$

A detailed solution of Eq. 5.42 is in the appendix (see A.1).

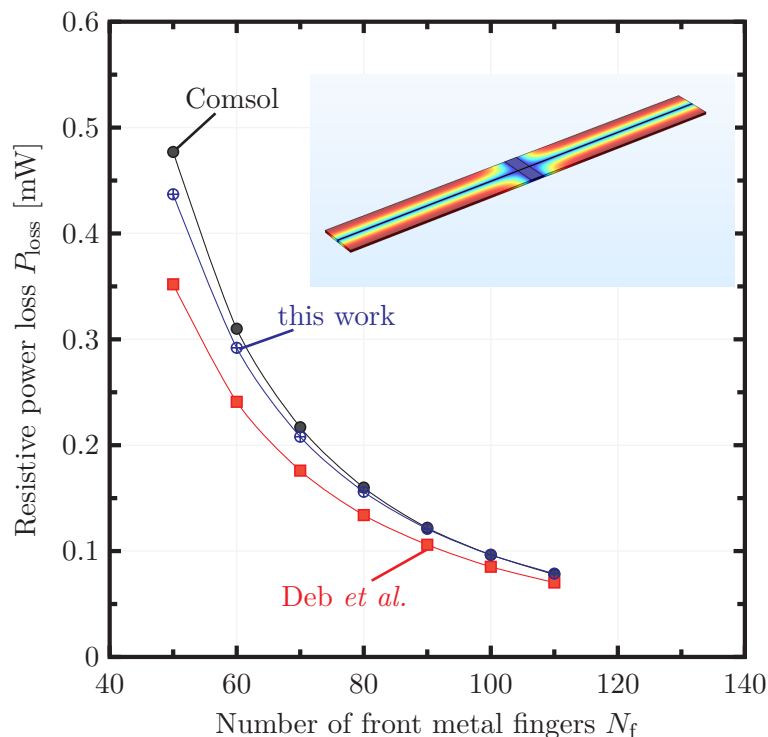


Figure 5.5: Resistive power loss in the emitter, finger and busbar for a varying finger number of front metal fingers N_f according to the analytical model of Deb et al., the analytical model derived in this work and numerical FEM simulations. The inset shows the electric potential distribution of the simulation domain of the FEM model indicating one front metal finger and a busbar.

5.1.1 Comparing the analytical series resistance model to finite element simulations

We conduct three dimensional (3D) numerical simulations based on the finite element method (FEM) employing *Comsol Multiphysics* [203] and compare the results to the analytical model of Deb et al. [123] and the extended model in this work. In all simulations we employ the parameters given in Table 4.3 and Table 4.4. We simulate a unit cell consisting of a finger and a busbar segment as indicated in the inset in Fig. 5.5 and vary the number of front metal fingers N_f .

Figure 5.5 shows the total resistive power loss P_{loss} in the emitter, fingers and busbar calculated according to the model of Deb et al., the numerical FEM simulations and the analytical model in this work for a varying finger number N_f . We vary N_f from 50 to 110 front metal fingers. At $N_f = 110$, the finger pitch is the smallest for all simulation parameters, which reduces the current path in the busbar segment and thus, series resistance losses in the finger and emitter region dominate. Here, the deviations between the three models are small and only $8 \mu\text{W}$. Decreasing N_f increases the finger pitch and thus, the power loss in the busbar segment dominates. Figure 5.5 shows that with decreasing N_f the model of Deb et al. deviates by $125 \mu\text{W}$ for $N_f = 50$ from the FEM simulations. The extended analytical model in this work shows a three times better agreement with the FEM simulations than the model of Deb et al., with a maximum deviation of $40 \mu\text{W}$.

5.1.2 Applying the optical factors

For a solar cell in air only the front metal fingers and the busbars shade the active cell area. This reduces the short circuit current density of the solar cell by

$$J_{sc} = J_{sc,act} \left(1 - \frac{N_f w_f k_{f,cell} w_{cell} - N_{bb} w_{bb} k_{bb} h_{cell}}{A_{cell}} \right), \quad (5.45)$$

where $J_{sc,act}$ is the short circuit current density of the active cell area, N_f is the number of the front metal fingers, w_f the geometrical width of the front metal fingers, $k_{f,cell}$ is the optical factor for a finger on a cell in air, N_{bb} is the number of busbars, w_{bb} the geometrical width of the busbars, k_{bb} the optical factor for a busbar, w_{cell} the width and h_{cell} the height of the solar cell.

For a solar cell in a solar module we consider the current reduction by the glass and encapsulation k_{red} , the current reduction by the shading of the cell interconnector k_{ci} and the current enhancement by the backsheet k_{bs}

$$J_{sc} = k_{bs} J_{sc,act} \left(1 - \frac{N_f w_f k_{f,mod} w_{cell} - N_{ci} w_{ci} k_{ci} h_{cell}}{A_{cell}} - k_{red} \right), \quad (5.46)$$

where $k_{f,mod}$ is the optical factor for a front metal finger for a solar cell in a solar module, N_{ci} the number of cell interconnectors and w_{ci} the geometrical width of the cell interconnector. The cell interconnector is either a cell interconnection ribbon or a cell interconnection wire.

5.1.3 Recombination losses for varying front metalization

For the loss due to recombination of the front metalization we employ Eq. 2.16. We combine the saturation current densities for the base and rear in a lumped J_{0b} and assume that the influence of transferring the cell into the module and changes of the front metalization on J_{0b} is negligible [93]. Thus, J_{01} is given by

$$J_{01} = J_{0e,pass} (1 - f_{e,met}) + J_{0e,met} f_{e,met} + J_{0b}, \quad (5.47)$$

where $J_{0e,pass}$ and $J_{0e,met}$ are the passivated and metalized emitter saturation current density, respectively. The metalization fraction of the emitter is

$$f_{e,met} = \frac{N_f w_f w_{cell} + N_{bb} w_{bb} (h_{cell} - N_f w_f)}{A_{cell}}. \quad (5.48)$$

Note that in case of CIWs the number of busbars is $N_{bb} = 0$ in Eq. 5.48. We assume that the influence of the front metalization on J_{02} is negligible and smaller than the deviation in J_{02} for the PERC batch in Table 4.1. This agrees with measurements of J_{02} in Ref. [204] for a varying front metalization fraction on a similar emitter as in this work.

5.1.4 Applying the analytical model to experimental test modules

For the full analytical model describing the cell to module (CTM) losses we combine the unit cell approach for the series resistance, the saturation current densities and the

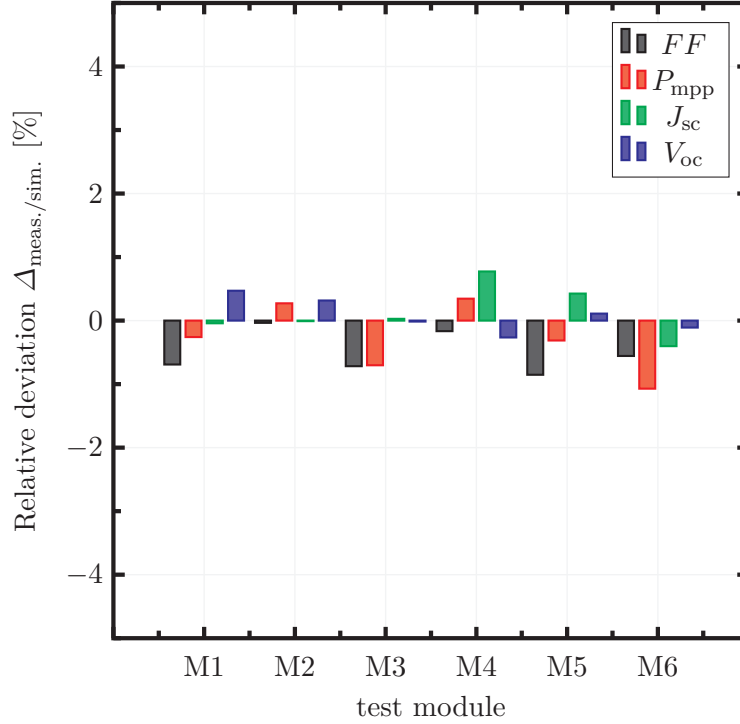


Figure 5.6: Relative deviation of the simulation and measurement of the experimental modules (see Table 5.1).

optical factors with the double-diode model (DDM) (see section 2.5, pp. 13). When modeling experimental results of one-cell test modules we first simulate a PERC with the parameters from Table 4.3 and adjust the $J_{sc,act}$ until the simulated J_{sc} matches the measured J_{sc} of the cell. Subsequently, we vary the parameters in Table 4.3 confined to their measured ranges until the simulated cell's $I(V)$ characteristic fits the measurement data. For the transfer of the cell into the module we account for the optical and resistive losses employing the parameters listed in Table 4.4.

When connecting multiple solar cells in series we have to account for the different operating points of each cell. We express the voltage of the individual cell $I(V)$ characteristics as a function of the current $V(I)$ and add up the voltage values for equal current values to obtain the $I(V)$ characteristics of the module. This requires extrapolating the $I(V)$ characteristics of cells with different J_{sc} in the reverse direction. The cell with the lowest J_{sc} dominates the $I(V)$ characteristics of the module.

Following this approach we simulate modules with input parameters equal to the experimental test modules in section 3.3.3 to verify the model with the measurement results. Table 5.1 represents an overview of the fabricated modules and their measured $I(V)$ characteristics.

Figure 5.6 shows the relative deviation between the simulation and the measurement data of the modules M1 through M6 for the P_{mpp} , FF , J_{sc} and V_{oc} . A negative deviation indicates that the simulation overestimates the measurement data. For all parameters the deviation between simulation and measurement is less than 1.1%. The V_{oc} shows the smallest deviations of all parameters and is less than 0.5%. For a small cell spacing of $d_{c2c} = 2$ mm the J_{sc} deviates marginally and discrepancies are

Table 5.1: Overview of the most relevant measured $I(V)$ parameters for the six 5×1 experimental test modules with various CIR and cell spacing. IMR denotes the intermediate reflector.

module	d_{c2c} [mm]	d_{s2s} [mm]	CIR	IMR	P_{mpp} [W]	FF [%]	I_{sc} [A]	V_{oc} [V]
M1	2	2	Std.	-	11.85	76.82	4.68	3.30
M2	2	2	White	-	12.03	77.27	4.72	3.30
M3	2	40	White	-	12.22	76.18	4.87	3.29
M4	40	40	White	-	12.90	74.90	5.21	3.30
M5	40	40	White	✓	12.84	74.42	5.23	3.30
M6	5	13	White	✓	12.29	76.24	4.89	3.30

below 0.5%. When increasing the cell spacing we observe higher deviations of up to 0.8% for a cell gap of 40 mm. For the FF the simulation generally overestimates the measurement due to the negative deviation between -0.1% and -0.8% and for the power between 0.3% and 1.1%.

5.1.5 Discussion of the analytical model presented in this work

We extended Deb’s model considering the cell and the string interconnection to calculate the series resistance losses of a solar module. The comparison of Deb’s analytical series resistance model with 3D numerical FEM simulations shows that with increasing finger pitch, deviations between both models increase from 10% to 26%. We ascribe these discrepancies to different series resistance losses in the busbar segments, since the current path increases in these parts with increasing finger pitch. In contrast, the analytical series resistance model derived in this work shows a three times better agreement with the 3D FEM simulations, showing a maximum deviation of 8% for the largest simulated finger pitch. This is in agreement with the results in Ref. [205], where the analytical model of this work is compared to FEM simulations of solar modules employing five cell interconnection ribbons and cell interconnection wires.

The analytical model for the simulation of cell to module (CTM) losses considers the influence of cell as well as module components on the optical, recombination, and resistive losses. Both, the cell and the module are coupled and an optimization of the module power requires an adaptation of the cell, e.g. the front metalization. Hence, the simple analytical model and the direct implementation of measurement data allow a reduction of the CTM losses, while also considering changes of the cell’s front metalization. This distinguishes the model from existing CTM models, which focus on the analysis of CTM losses for fixed cell parameters, considering optical and resistive losses [118, 206].

We demonstrate that the analytical model enables to describe the experimental data of PERC that are interconnected and encapsulated into a module. The six experimental test modules vary by up to 8% in measured P_{mpp} , which is higher than the maximum deviation between model and experiment of 1.1% for the P_{mpp} . With increasing cell spacing the deviations between model and experiment increase

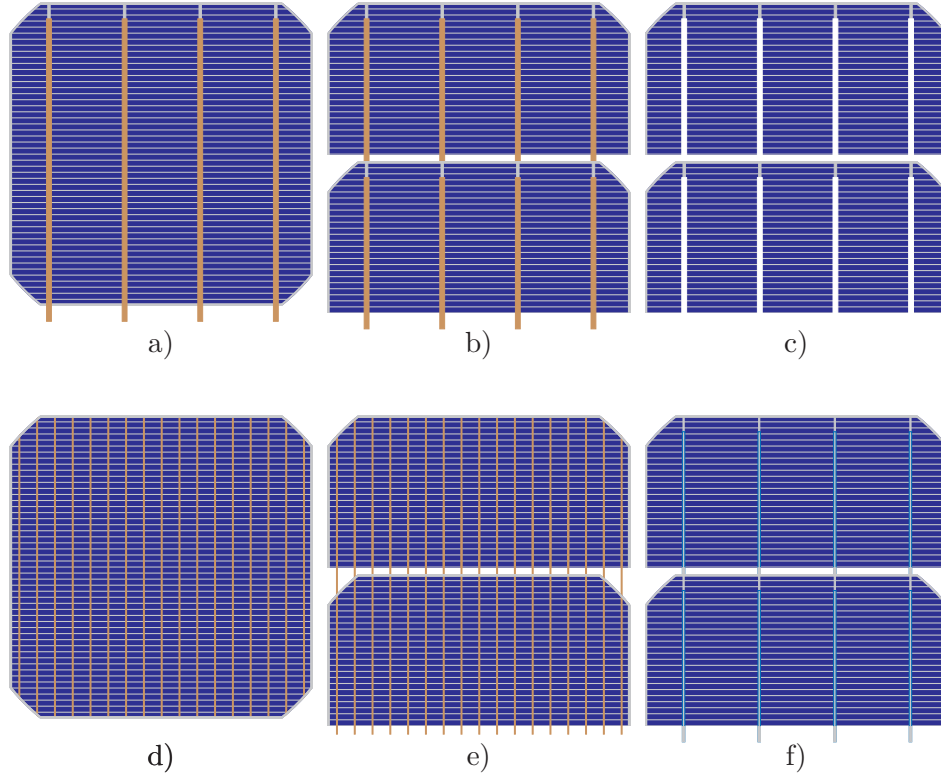


Figure 5.7: Investigated module configurations in this work. For a) we consider std. CIR and full cells. In b) we employ the same CIR with half cells. In c) we apply white-colored CIR to half cells. In configuration d) and e) we apply CIW instead of CIR, while employing full cells in d) and half cells in e). In f) we apply the groove-structured CIR to half cells.

especially in the J_{sc} . If the cell spacing grows, the fraction of backsheets covered area in the module increases and measurement uncertainties of the material properties have a bigger effect. Reflections from the backsheets to the cell may also result in inhomogeneous illumination conditions, which increases the effect of a distributed series resistance and thus, affects the FF . Nonetheless, all deviations are within the uncertainty of our module flasher of 4.2% for P_{mpp} and thus, the analytical model is sufficient for the purpose of this work.

5.2 Modeling the module power output for variations of the front metalization and cell interconnection

In this section we apply the model to simulate the effect of variations of the front metalization and the cell interconnection on the module power output P_{mpp} to determine the optimum parameters for the high power and the high efficiency module.

We simulate a PERC module consisting of 60 (156×156) mm² cells. In all simulations we employ the parameters listed in Table 4.3 and Table 4.4. For the simulation we consider six module configurations. Figure 5.7 schematically shows the six state of the art cell interconnection configurations that we model in this work. For module a)

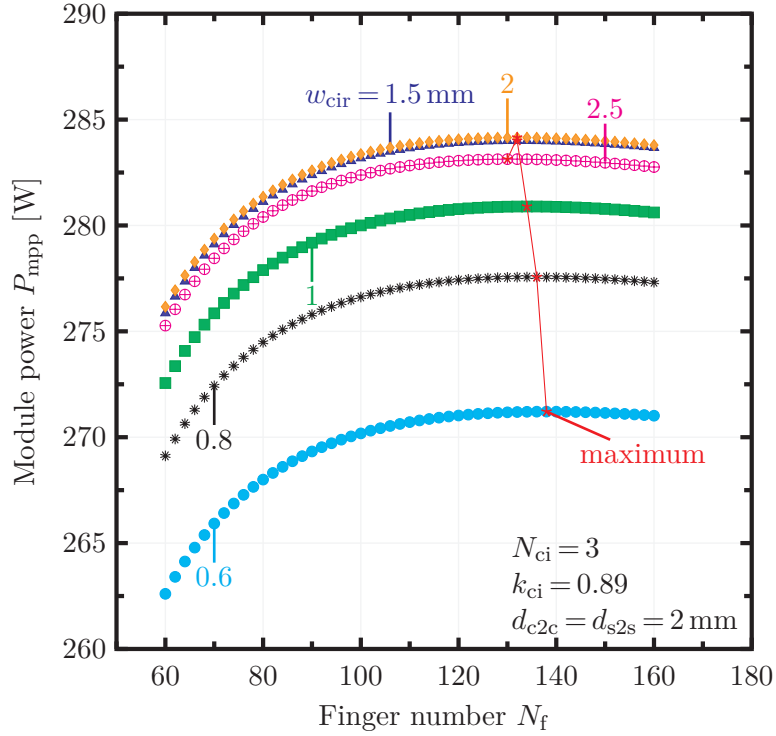


Figure 5.8: Simulated module power output P_{mpp} as function of the number of front metal fingers N_f for a varying CIR widths w_{cir} . We simulate module (a) with full pseudo squared cells featuring three standard CIRs with $k_{\text{ci}} = 0.89$. The CIR width varies from 0.6 mm to 2.5 mm. The red stars ($\text{---}\star\text{---}$) indicate the maximum for each w_{cir} .

we consider the standard cell interconnection ribbons (CIRs) and full cells as our reference module configuration. In b) we employ the same CIRs with half cells. In c) we apply white colored CIRs to half cells. In configurations d) and e) we apply cell interconnection wires (CIWs) to full and half cells. In f) we apply the optical enhanced groove-structured CIRs to half cells.

5.2.1 Influence of the number of front fingers

Figure 5.8 shows the simulated maximum power output P_{mpp} as a function of the number of front metal finger N_f for a varying CIR width w_{cir} . In all simulations we consider full cells and a number of $N_{\text{ci}} = 3$ CIRs with an optical factor $k_{\text{ci}} = 0.89$. The cell to cell d_{c2c} and string to string d_{s2s} spacing is 2 mm in all directions. For each number of fingers we vary the width w_{cir} of the CIRs from 0.6 mm to 2.5 mm. The red stars in Figure 5.8 indicate the maximum P_{mpp} for each CIR width.

We observe that the module power enhances with increasing w_{cir} ranging from 0.6 mm to 2 mm. For the range from 2 mm to 2.5 mm P_{mpp} starts to decrease with increasing w_{cir} . Narrower CIRs require more front metal fingers to achieve the maximum module power output. For instance the maximum for $w_{\text{cir}} = 0.6$ mm is at $N_f = 138$ and for $w_{\text{cir}} = 1.5$ mm it is at $N_f = 132$. We calculate the highest module power output for $w_{\text{cir}} = 2$ mm and $N_f = 132$.

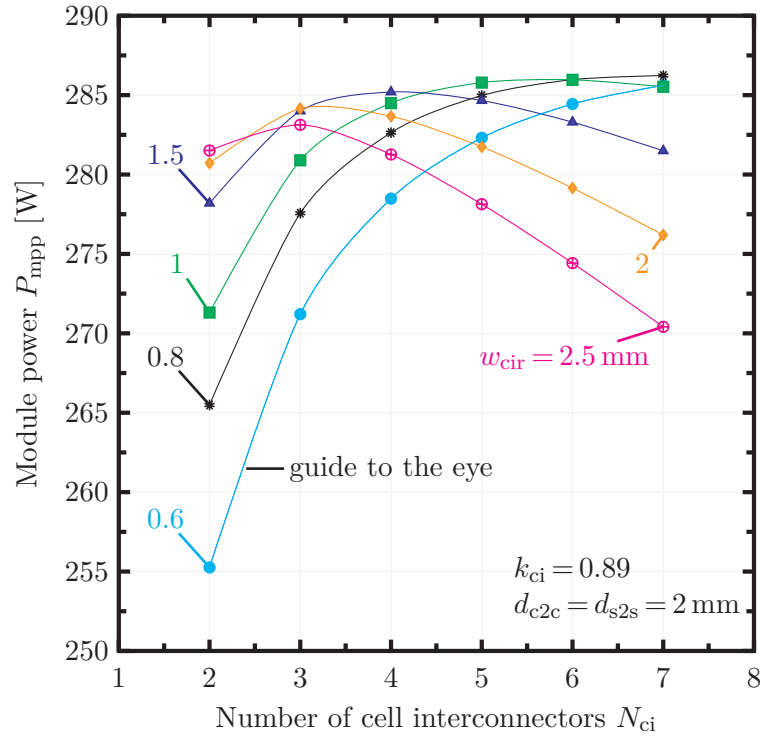


Figure 5.9: Simulated module power output P_{mpp} as function of the number of cell interconnectors N_{ci} . We simulate module a) with standard cell interconnection ribbons (CIRs) and an optical factor k_{ci} of 0.89. We vary the CIR widths w_{cir} from 0.6 mm to 2.5 mm. In each simulation we optimize the number of front metal fingers N_f for a maximum module power output.

5.2.2 Influence of the number of cell interconnectors

Figure 5.9 shows the maximum module power as a function of the number of the cell interconnectors N_{ci} . We simulate module a) with full cells and standard CIRs with an optical factor $k_{ci} = 0.89$. Most state of the art stringers are limited to five CIRs. Assuming further progress in technology in the next years we consider up to seven CIRs in our simulations. We vary the width w_{cir} of the CIR from 0.6 mm to 2.5 mm. In each simulation we optimize the number of front metal fingers for a maximum module power output.

In Fig. 5.9 the module power increases with increasing CIR number to reach a maximum and decrease again. With increasing CIR width it requires less CIRs to achieve this maximum. For instance, when employing $w_{cir} = 2.5$ mm the maximum output power is achieved for 3 CIRs, while it requires 6 CIRs for $w_{cir} = 1$ mm. Our simulations show an optimum for a module with 7 CIRs and $w_{cir} = 0.8$ mm with a power output of 286.2 W.

5.2.3 Module power output for various module configurations

Figure 5.10 shows the module power output for the various module configurations a) through f) from Fig. 5.7. In each simulation we consider a cell spacing of 2 mm and vary the number of the cell interconnector (CI)s N_{ci} . We adjust the number of front

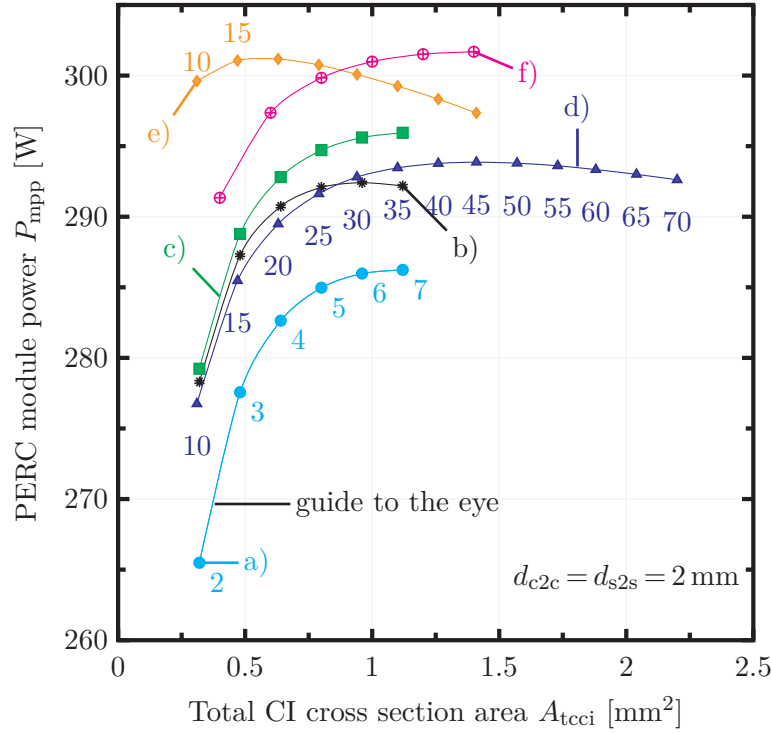


Figure 5.10: Simulated maximum module power output for the various module configuration in Fig 5.7. The cell spacing is 2 mm. For each module we optimize the CIR width for a maximum module power output. In all simulations we adjust the number of front metal fingers for a maximum module power output. The total CI cross sectional area A_{tcci} equals the number of CI times the individual CI cross section area.

metal fingers and the width of the CIR with regard to a maximum module power output. The thickness of the CIRs is fixed to 200 μm since thicker CIRs increase the probability for mechanical issues and cell cracks [207]. Thus, we also limit the diameter of the cell interconnection wires (CIWs) d_{ciw} to 200 μm .

In Fig. 5.10 we report the simulated P_{mpp} as a function of the total cross section area A_{tcci} of all cell interconnectors (CIs). This area equals the number of CI times their individual cross section area and allows to compare the different CI techniques with each other. Figure 5.10 shows the data for the CIRs width w_{cir} that results in the highest power output for each module configuration a) through f). For instance, module a) generates the highest module power with seven CIRs and $w_{cir} = 0.8$ mm. Thus, Fig. 5.10 shows the power output for module a) as function of the total cross section area for 2 to 7 CIRs of widths $w_{cir} = 0.8$ mm. The numbers in Fig. 5.10 for module a) denote the number of CIRs, which is equal for modules b), c), and f). The numbers for module d) and e) denote the number of CIWs.

According to our simulations, module a) with full cells and standard CIRs generates the lowest module power output of 286 W. Module b) uses half cells and the standard CIRs, which increases the P_{mpp} by 6 W compared to module a). For module d) with full cells and CIWs we calculate a gain of 8 W. Combining half cells with white colored CIRs in module c) results in an increase in module power by 10 W. The highest module power we calculate for modules e) using half cells with CIWs and f) using half cells with groove-structured CIRs. For both modules we simulate a

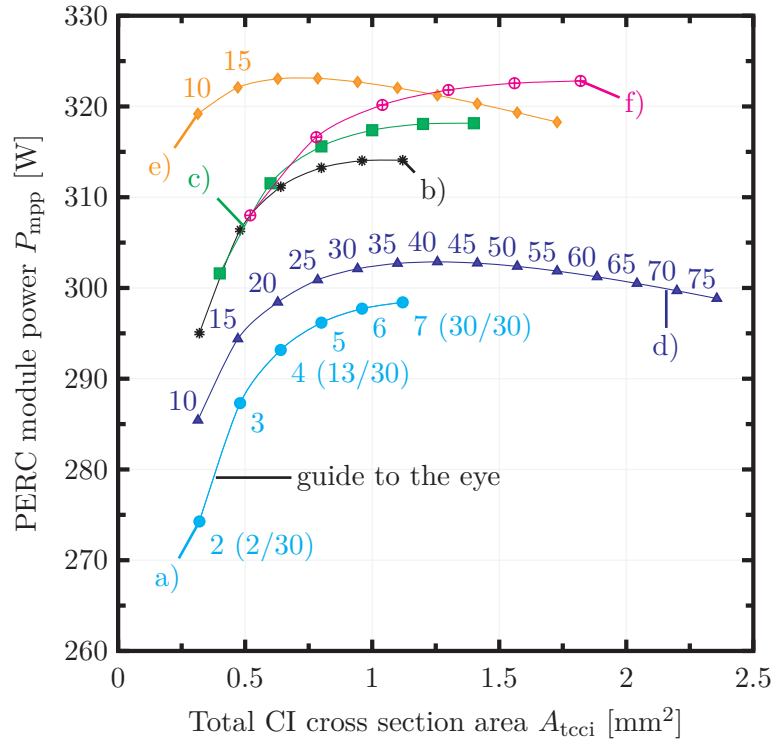


Figure 5.11: Simulated maximum module power output for different interconnection technologies. The number of front metal fingers is optimized to reach maximum module power output while the cell spacing is limited to 30 mm. The numbers in parentheses for module a) indicate the cell to cell and the string to string distances (d_{c2c}/d_{s2s}). All other modules b) through f) exploit the maximum cell spacing of 30 mm.

maximum module power of 301 W, which is a gain of 15 W compared to reference module a).

5.2.4 Effect of the cell spacing

Figure 5.11 shows the module power output for the various module configurations a) through f) as a function of the total cross section area A_{tcci} with a varying cell spacing. We vary the gap between the cells d_{c2c} and the strings d_{s2s} in our simulations and consider 30 mm as an upper limit, since for larger cell gaps the current enhancement by the backsheets increases only marginally according to Fig. 4.8. In each simulation we optimize N_f , w_{cir} and the cell spacing d_{c2c} as well as the string spacing d_{s2s} for a maximum power output. The numbers in parentheses for module a) indicate the cell to cell and the string to string distances (d_{c2c}/d_{s2s}). For all other modules b) through f) the maximum module power is achieved for the maximum cell spacing of 30 mm.

We simulate an increased module power for all modules a) through f). As in Fig 5.10 module a) consisting of full cells featuring the standard CIRs produces the lowest power output. However, the maximum module power for module a) is 298 W, which is an increase of 12 W compared to Fig. 5.10. In contrast to Fig. 5.10, module d) with full cells and CIWs has a lower maximum module power than module b) with

half cells and CIRs. For modules e) and f) we calculate an equal maximum P_{mpp} of 323 W, which is the highest module power for this scenario.

5.2.5 Discussion of the simulated finger number, CI number and CI width

At the beginning of this work, the state of the art front metal grid at our research institution employed 88 front metal fingers and 3 busbars. A reduction of the effective optical finger width allows more fingers for an encapsulated cell compared to a cell in air. Thus, the optimum for the number of front metal fingers shifts in Fig. 5.8 from 88 to more than 132, depending on the cell interconnector width. Our computations reveal a broad maximum and a deviation from the optimum finger number has only a marginal impact on the module power output. For instance, for the simulation of the module with a CIRs width of 1 mm, a deviation of 10 fingers from the optimum at 134 fingers results in a loss in module power output of less than 0.1 %. The red stars indicate that the number of fingers for a maximum module power is slightly different for the various cell interconnection ribbon widths.

Figure 5.9 shows that increasing the number and reducing the width of the CIs increases the module power output. Increasing the number of CIs reduces the current path in the fingers. According to Eq. 5.13 and Eq. 5.22 the resistive power loss in the finger scales with the length of the finger to the power of 3. Thus, increasing the number of CIs significantly reduces the series resistance losses and improves the module power output.

Reducing the series resistance losses in the front metal fingers allows to reduce the number of front metal fingers, which reduces the silver consumption and the recombination below the metal contacts.

Figure 5.10 shows that employing full cells and 10 to 70 CIWs in module d) increases the module power by about 6 W compared to the reference module a) with 3 to 7 CIRs. Due to the mesh of CIWs the current path in the fingers is reduced. The round shape of the CIWs decreases their geometrical width in a module by 33 %.

Utilizing half cells reduces series resistance losses since the cell current scales linearly with the cell area and resistive power losses depend on the current squared (see Eq. 5.1, p. 61) [208, 209]. This results in a similar increase in P_{mpp} for module b) and module d) of about 6 W.

Module e) employing cell interconnection wires with half cells results in a module power output of about 301 W with 18 CIWs. The same P_{mpp} we obtain for the module with half cells and groove-structured CIRs. This shows that reducing the effective optical width due to the groove-structured CIRs and employing half cells to reduce series resistance losses leads to similar module powers as with CIWs.

Fig. 5.10 shows that the current enhancement by the backsheets increases the module power by approximately 12 W for module a). The increased cell to cell spacing increases the CI length and internal reflections by the backsheets. This increases the resistive power losses, which results in a larger total cell interconnector cross section area for all modules in Fig. 5.10.

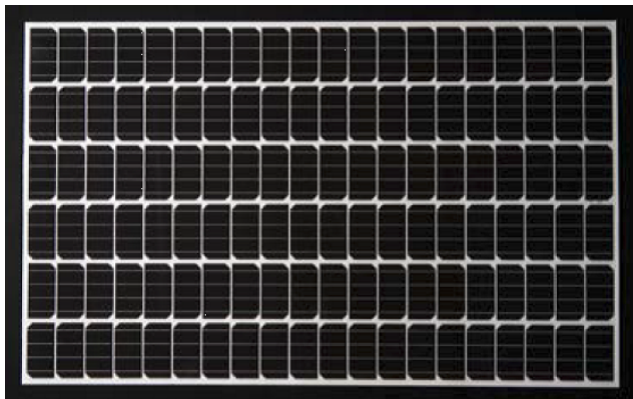


Figure 5.12: Photography of the 294.8 W high power module.

In contrast to Fig. 5.10 CIWs in module d) are inferior to the half cells with CIRs in modules b) and c). Due to the threshold of $200\ \mu\text{m}$ for the wire diameter, the CIWs can not compensate the enhanced module current.

Combining CIWs or the groove-structured CIRs and half cells delivers the highest module performance with a maximum power output of about 323 W. Both approaches, utilizing the dense mesh of CIWs or improving the optics with the groove-structured CIRs, are suitable to enhance the module power output.

5.3 Application of the analytical model to full-sized modules

In this section we apply the analytical model to optimize the front metalization, cell interconnection and cell spacing of a 60 full cell PERC module. The PV industry currently pursues two approaches: (i) Manufacturing solar modules with a maximum power output since the price of a solar module is sold per Watt peak. (ii) Manufacturing solar modules with a maximum module efficiency, since the leveled cost of electricity (LCOE) scale with the size of the PV-system [210]. We consider both approaches and build a high power module as well as a high efficiency module in the following. Our production equipment constrains both modules to a maximum size of $(175 \times 105)\ \text{cm}^2$ and the application of 4 CIRs with a width ranging from 0.8 mm to 2.5 mm and a thickness of $200\ \mu\text{m}$.

5.3.1 Building a high power module

We produce a batch of PERCs according to the baseline process in section 3.1 and vary the front metalization in order to produce a high power module. We adjust the number of front metal fingers and the number of busbars. Instead of 3 busbars and 88 front metal fingers the cells have 4 busbars and 120 fingers as a result of the simulations with the analytical model. For the module process we employ 60 PERC and halve the cells with a laser process. We apply the white colored cell interconnection ribbons to the busbars for the cell interconnection and encapsulate the cells with the EVA_{UV} with an enhanced UV transparency. We increase the cell spacing of the module to increase the amount of internal reflected light by the

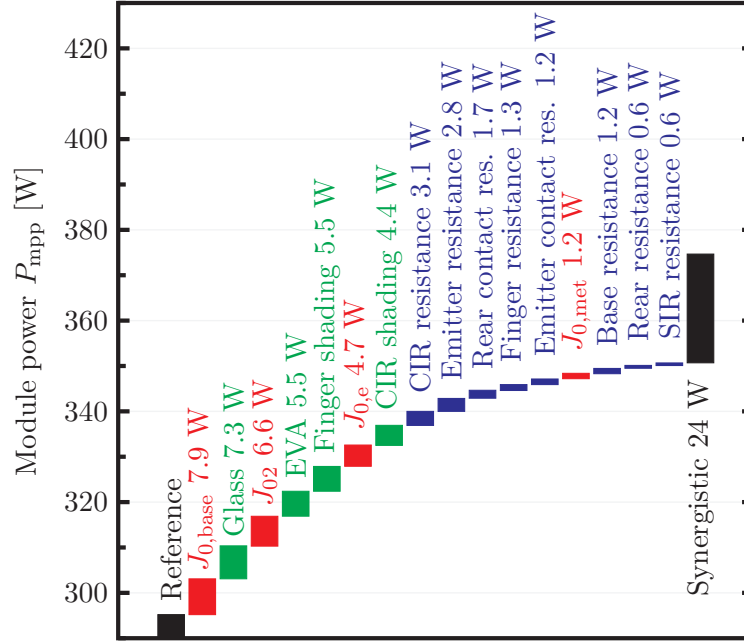


Figure 5.13: Breakdown of the potential gain mechanisms of the 295 W module. We use green bars for optical, red bars for recombination and blue bars for resistive module power gains.

backsheet. Table 5.2 gives an overview of the optimized cell and module parameters compared to the baseline process.

Figure 5.12 shows a photography of the high power module. We measure a module power of 294.8 W, which is a cell to module gain of 5.1 W.

5.3.2 Breakdown of the cell to module losses

We perform a synergistic gain analysis [211, 212] with the analytical model to determine the limiting parameters that restrict a further improved module power output. Figure 5.13 shows the simulation results of this synergistic gain analysis. The green bars denote optical, red bars recombination and blue bars resistive power gains.

We start with the simulation of the experimental test module from section 5.3.1. It produces an output power of 295.2 W and is represented by the left black bar in Fig. 5.13. The module suffers from various optical, recombination, and resistive losses. This is our reference simulation. Then we disable one loss channel at a time in the simulation and calculate the corresponding module power enhancement. The gain in power compared to the reference is then added as a new bar in Fig. 5.13. For the next step this loss mechanism is enabled again and another loss mechanism is disabled. As an example, avoiding the extrinsic contribution of the base recombination and the rear side J_{0b} in the simulation, enhances the simulated power of the reference case by the length of the first red bar (7.9 W) in Fig. 5.13. For the next bar in Fig. 5.13 we re-enable these base and rear recombination losses and disable the reflection and absorption losses in the front glass cover.

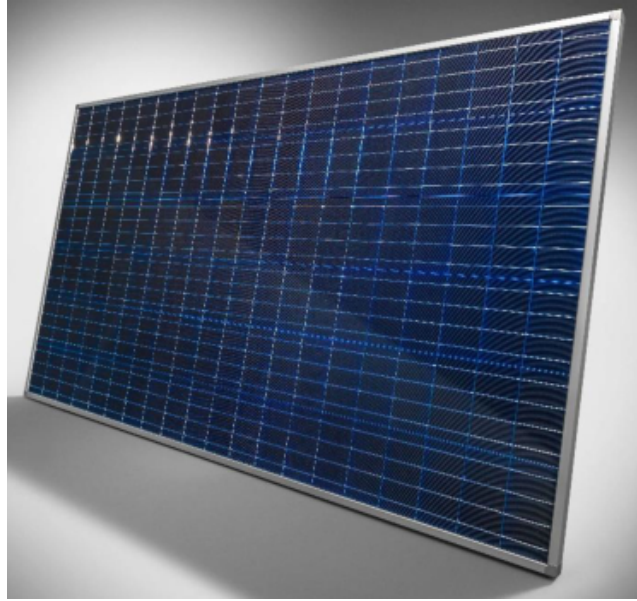


Figure 5.14: Photography of the high efficiency module.

Following this procedure we stepwise disable the various loss mechanisms and sort them by the size of their gains. Accumulating all individual power gains results in a maximum module power of 350.1 W. This power corresponds to a module efficiency of 20.2 % instead of 17.1 % for the reference case. Note that we have not changed the cell spacing in the simulation and hence, the module area is fixed. If we disable all power loss mechanisms simultaneously we obtain a maximum module power output of 374.1 W due to additional synergistic effects.

5.3.3 Building a high efficiency module

We produce a batch of PERCs according to the baseline process in section 3.1 and vary the front metalization in order to produce a high efficiency module. Instead of 3 busbars and 88 front metal fingers the cells have 4 busbars and 104 fingers. We apply a half cell grid for the screen printing of the front and rear metalization. After the contact firing we halve the cells in a laser process. The average cell efficiency of the 120 half cells is 20.8 %.

For the module process we apply groove-structured cell interconnection ribbons (CIRs) for the cell interconnection. We decrease the cell to cell spacing to 1.5 mm and the string to string distance to 1 mm to reduce the module's aperture area. Additionally, we move the string interconnection ribbons at the end of each string below the last cell to increase the fraction of active cell area in the module. Further, we apply the EVA_{UV} with an enhanced UV transparency. In the cell gaps between the two layers of EVA we place the groove-structured foil on top of the rear EVA. Figure 5.14 shows a photograph of the high efficiency module.

Table 5.2 gives an overview of the adjusted cell and module parameters for the high power module and the high efficiency module compared to the standard module.

Table 5.2: Changes in cell and module design after optimization according to the analytical model.

changes	standard module	high power module	high efficiency module
number of fingers	88	120	104
number of CIR	3	4	4
cell area	$(156 \times 156) \text{ mm}^2$	$(78 \times 156) \text{ mm}^2$	$(78 \times 156) \text{ mm}^2$
cell to cell distance	3 mm	4.7 mm	1.5 mm
string to string distance	3 mm	12.8 mm	1 mm
Encapsulation	EVA	EVA _{UV}	EVA _{UV}
CIR	std. CIR	colored CIR	structured CIR
cell gap reflector	std. backsheet	IMR	structured foil

We measure a module power output of 303 W, which corresponds to a CTM factor of 1 and a solar module efficiency of 20.2%. Table 5.3 lists all measured cell and module $I(V)$ characteristics. The rows two to four also show simulation results to analyze the CTM losses. Row two shows the simulated module without any optical and resistive losses, representing the module $I(V)$ characteristic of all interconnected cells. In row three we take only resistive losses due to the cell interconnection into account and in row four we also include optical losses in the simulation.

Table 5.3: The first and the last row show the measured cell and module $I(V)$ characteristics. Rows in between show the simulated $I(V)$ characteristics to analyze the CTM losses.

Device	V_{oc}	I_{sc}	FF	P_{mpp}	η
measured cells	79.4 ^Σ	4.80 [∅]	79.6 [∅]	303 ^Σ	20.8 [∅]
cells interconnected (no losses)	79.4	4.78	79.9	303	
cells interconnected (el. losses)	79.4	4.78	78.7	299	
cells interconnected (opt.&el. losses)	79.4	4.86	78.7	304	
measured module	79.1*	4.86*	79.1*	303*	20.2

*independently confirmed by TÜV Rheinland, Cologne, Germany.

5.3.4 Discussion of the application of the analytical model to full-sized modules

We apply the analytical model to improve the cell's front metalization as well as the cell interconnection to produce a high power module with a power output of 295 W. The gain analysis reveals that the biggest potential for an improved module power output is a reduction of the recombination in the base and the rear side. For the module components the largest improvement is from reducing the reflection and

absorption in the glass. This is in agreement with results from Haedrich et al. [118]. The series resistance losses of 2.8 W (blue bar, emitter resist.) play only a minor role due to the improved front metalization. The total internal reflection of light within the module allows to apply more fingers to the cell without significantly reducing the module power due to optical shading.

With the high efficiency module we demonstrate a record in PERC module efficiency of 20.2% in 2017 and an independently confirmed module power of 303 W. This improves the previous record efficiency for a 60-cell PERC module by 0.7% [23]. Additionally, we obtain a CTM factor of 1, i.e. the sum of the cell powers is equal to the module power in Table 5.3. Compared to the standard and the high power module, we reduced the cell spacing, which reduced the module area by 2.6% compared to a standard module. The smaller cell spacing reduces the module's current and requires less front metal fingers, which in turn reduces recombination losses. Further, the smaller cell gaps decrease series resistance losses due to shorter cell interconnection ribbons. The application of the groove-structured CIR enables to use wider CIRs, which results in a FF loss of only 0.5%_{abs} compared to the average FF of the cells in Table 5.3.

The major driving force for the improvement in module efficiency is the application of the groove-structured cell interconnection ribbon and the groove-structured foil in the cell gaps for the high efficiency module. This further decreases the optical losses and even overcompensates the losses due to absorption in the encapsulation, which results in a current gain of 60 mA compared to the cell's average. In Holst et al. [130] we also demonstrated in simulations and experiments that this will improve the annual yield of the module.

CHAPTER 6

Accelerated aging with ultraviolet light

In this chapter we investigate the ultraviolet (UV) radiation hardness of solar modules featuring solar cells with dielectric passivation layers. At first, we determine the optical characteristics of the dielectric passivation layers and the module materials. Then we expose experimental test modules employing different encapsulation polymers and containing solar cells with varying passivation layers to UV light and measure their $I(V)$ characteristics. In the end we present a model to describe the degradation of the solar module's $I(V)$ characteristic after the UV aging test.

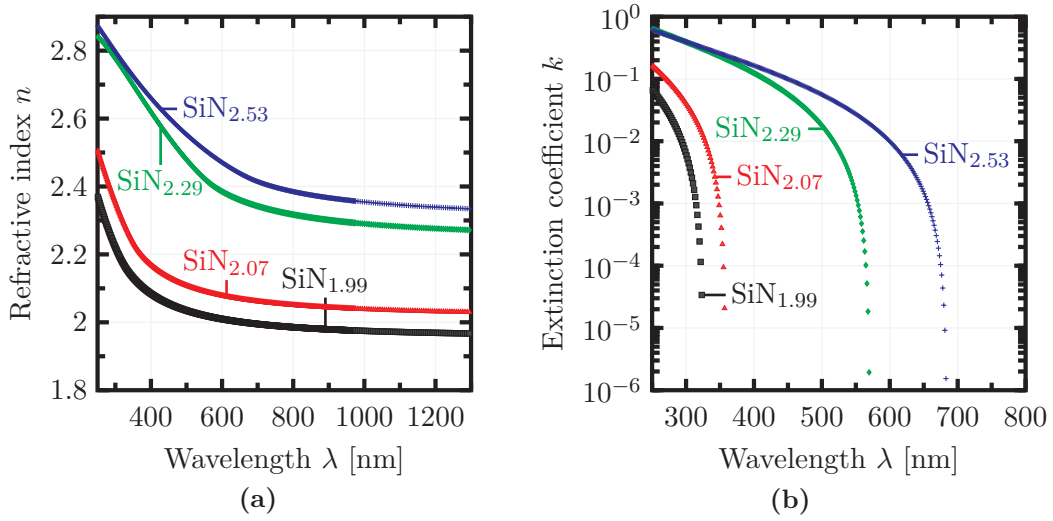


Figure 6.1: Extracted refractive index n and extinction coefficient k from the VASE measurement of the FZ samples with varying SiN _{y} layer.

6.1 Measurement results of test samples and modules

6.1.1 Results of the ellipsometer measurements on planar test samples with varying passivation layer

We fit the Ψ and Δ data from the variable angle spectroscopic ellipsometry measurement of the various SiN _{y} layers on the FZ samples. For the fit we chose a Tauc-Lorentz oscillator model [213]. As initial fitting parameter for the thickness we adopt the values from the He:Ne laser ellipsometer measurements.

Figure 6.1 (a) shows the extracted refractive index n and Fig. 6.1 (b) shows the extinction coefficient k for the various SiN _{y} samples. For all samples k decreases with increasing wavelength. Further, the extinction coefficient increases with increasing refractive index. The ellipsometer is sensitive to k values above 1×10^{-6} . Sample SiN_{1.99} shows the lowest k values that approach 0 for a wavelength of 326 nm. For the other samples k approaches zero at 358 nm for the sample SiN_{2.07}, 571 nm for the sample SiN_{2.29}, and 684 nm for the sample SiN_{2.53}.

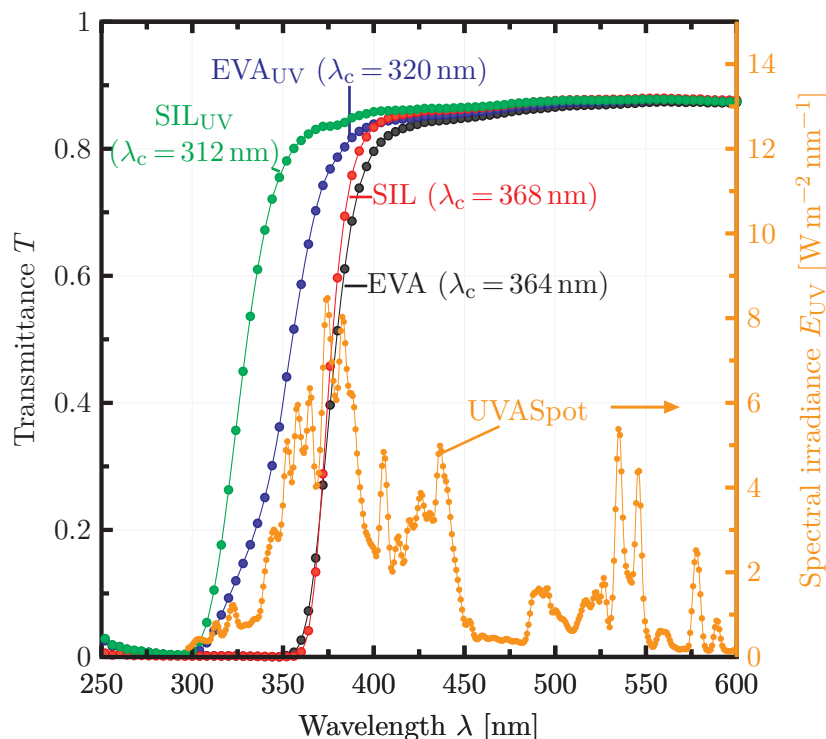


Figure 6.2: Transmittance of the four encapsulation materials laminated between two glasses and the spectral irradiance E_{UV} of the UVASpot UV light source. The lines are a guide to the eye. Each λ_c value in the parentheses denotes the cut-off wavelength at a transmittance equal to 10% [163].

6.1.2 Results of the transmittance measurement of test samples with varying encapsulation materials

Figure 6.2 shows the measured transmittance of the glass-polymer-glass samples with the different encapsulation materials. The sample with the silicone with enhanced UV transparency SIL_{UV} shows the highest transmittance in the UV wavelength range, starting with the transition from absorbing to transmitting at 300 nm. We define the cut-off wavelength λ_c as the longest wavelength in the UV range (below 400 nm), where the transmittance is equal to 10% [163]. For SIL_{UV} we measure a $\lambda_c = 312$ nm. The transmittance of the EVA with enhanced UV transparency EVA_{UV} is lower with a $\lambda_c = 320$ nm. For the samples EVA and SIL we observe cut-off wavelengths of $\lambda_c = 364$ nm and $\lambda_c = 368$ nm, respectively.

Figure 6.2 also shows the measured spectral irradiance E_{UV} of the UVASpot lamps for the accelerated UV aging test (see section 3.5, pp. 42), indicating that the sample SIL_{UV} is transparent for most photons of the spectrum. In the samples EVA and SIL a significant amount of UV light is absorbed in the encapsulation materials.

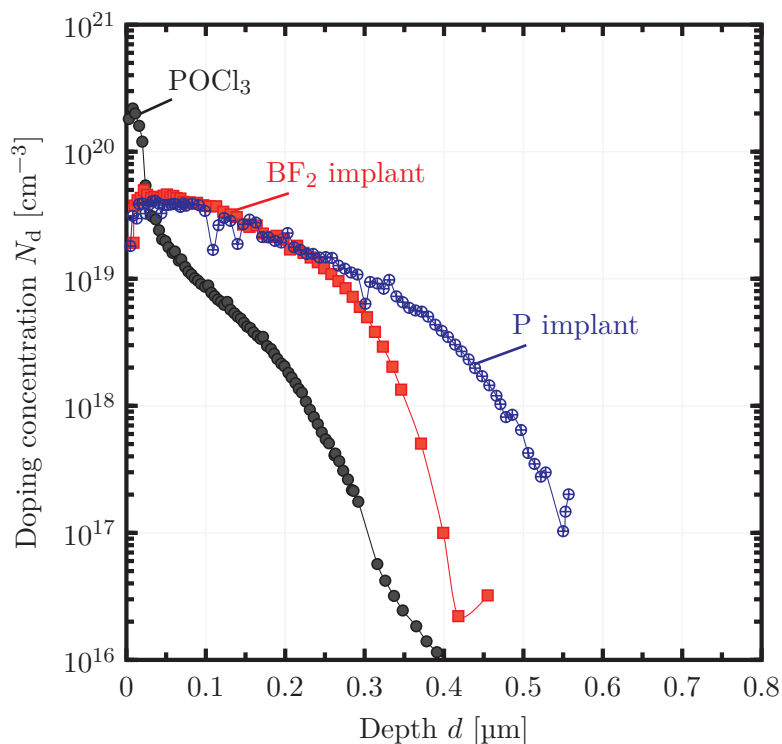


Figure 6.3: Doping concentration as a function of the depth from the surface measured with electrochemical capacitance voltage measurements. The black data (—●—) is for the POCl_3 diffusion of the PERC emitter. The red (—■—) and blue (—○—) function are for the BF_2 and P implanted PERT cells, reprinted with permission of Kiefer [157].

6.1.3 Results of the electrochemical capacitance voltage measurement

Electrochemical capacitance voltage (ECV) measurement is a technique to determine the doping profile within a semiconductor. For further details regarding ECV profiling we refer to Ref. [170]. Figure 6.3 shows the doping concentration N_d as a function of the depth d from the surface for the two ion implanted PERT cells, reprinted with permission from Kiefer [157]. As a comparison Fig. 6.3 also shows the phosphorous emitter profile of the PERC from the POCl_3 diffusion. Figure 6.3 shows, that the doping concentration of the phosphorous emitter of the PERC has a high surface concentration of $2.2 \times 10^{20} \text{ cm}^{-3}$. In comparison the surface concentration for the boron and phosphorous implanted sides of the PERT cells is about one order of magnitude lower.

6.1.4 Results of the current-voltage measurement of test modules

Table 6.1 summarizes the open circuit voltage V_{oc} , short circuit current I_{sc} , and power output P_{mpp} from the $I(V)$ measurements of the test modules for the UV aging experiments.

Table 6.1: PERC test modules employing the reference refractive index of $n = 2.07$ and different materials for the encapsulation polymer (1-4), various refractive indexes n and thicknesses t_{SiN} for the front side SiN_y layer with EVA_{UV} (5-8), and PERT cell test modules with EVA_{UV} prior UV exposure (9-10). The characteristic $I(V)$ parameters are extracted from illuminated $I(V)$ measurements.

row	test module	V_{oc}	I_{sc}	P_{mpp}
1	M-Ref	1.296	4.65	4.60
2	M- EVA_{UV}	1.304	4.73	4.70
3	M-SIL	1.300	4.47	4.40
4	M- SIL_{UV}	1.306	4.65	4.61
5	M- $SiN_{2.53}$	0.646	9.20	4.16
6	M- $SiN_{2.29}$	0.649	9.44	4.30
7	M- $SiN_{2.07}$	0.650	9.53	4.37
8	M- $SiN_{1.99}$	0.645	9.44	4.32
9	M- $PERT_{SiN}$	0.657	9.746	4.70
10	M- $PERT_{AlO}$	0.658	10.085	4.83

For the variations of the encapsulation material in rows 1 through 4 we employ two half cells in one test module, while for the test modules in rows 5 through 10 we employ full cells. Thus, the current for the test modules in rows 1 through 4 is about half the current compared to the test modules in rows 5 through 10. Due to the reduced series resistance losses for half cells, the P_{mpp} of these test modules is higher than for the full cell test modules.

Applying EVA instead of silicone results in higher module currents. We observe an increase in I_{sc} for the test modules M- SIL_{UV} and M- EVA_{UV} employing the UV transparent silicone and EVA compared to the test modules M-SIL and M-Ref with the UV blocking silicone and EVA.

For the test modules with PERC and varying SiN_y layer, test module M- $SiN_{2.07}$ with the reference SiN_y of $n = 2.07$ shows the highest P_{mpp} , as well as I_{sc} and V_{oc} . Increasing the refractive index to 2.29 and 2.53 results in a deterioration of all $I(V)$ parameters with increasing n . Reducing n to 1.99 also results in a deterioration of all $I(V)$ parameters.

We measure the highest module powers for the test modules with bifacial PERT cells. Here, we observe a strong increase in I_{sc} of about 6% when comparing the test modules M- $PERT_{SiN}$ and M- $SiN_{2.07}$ with equal front glass, encapsulation material and SiN_y layer at the illuminated side. The deviation in P_{mpp} of both test modules with PERT cells is 3%, which is equal to the measured bifacial factor of 0.97 for the cells.

6.1.5 Discussion of optical and current-voltage measurement results

The encapsulation materials with enhanced UV transparency result in higher test module power outputs due to an increase in I_{sc} of 2% to 4%. Applying EVA or silicone with similar λ_c as for the test modules M-Ref and M-SIL, the EVA outperforms the silicone due to the lower refractive index of the silicone. The refractive index of silicone at 633 nm is 1.42 and the refractive index of EVA is 1.49 [198]. The larger deviation in n between silicone and glass ($n \approx 1.51$) increases the reflection at the glass/polymer interface, which reduces the I_{sc} of the solar module (see section 2.2.1, pp. 6).

For the modules with cells of varying SiN_y passivation layer the P_{mpp} also decreases with increasing refractive index from 2.07 to 2.53, although according to the theory the optimal n should be around 2.42 for the Si/EVA interface (see section 2.2.1, pp. 6). This has two reasons: (i) When increasing the refractive index the fraction of silicon in the SiN_y increases [53], which increases the absorption of the SiN_y layer (see Fig 6.1 (b)). (ii) The surface texture of the solar cells increases the light trapping compared to a solar cell with a planar surface. However, this also increases the surface area of the solar cell, which increases the surface recombination and deteriorates the cell's $I(V)$ characteristics. Hence, for textured solar cells the passivation quality of the SiN_y layer is of greater importance than the anti-reflection properties. Both effects shift the optimum refractive index to a SiN_y layer with $n = 2.07$.

For the two test modules with PERT cells the deviation in P_{mpp} is only 3%, although in test module M-PERT_{SiN} the SiN_y/n^+ -type emitter interface and in M-PERT_{AlO} the AlO_x/p^+ -type emitter interface faces the module's illuminated side. This is due to the high bifacial factor of this cell type of up to 0.99 as reported by Kiefer et al. [158]. Thus, they are well suited for investigations of the UV radiation hardness of the SiN_y and AlO_x surface passivation.

The increase in I_{sc} by 6% for the test modules with PERT cells compared to the test modules with PERC we ascribe to the better collection efficiency of the PERT cells compared to PERC and the improved optics of the PERT cell's rear side. Here, the SiN_y/EVA interface of the PERT cells reflects light more efficiently than the SiN_y/Al interface of the PERC [214]. Light reflected at the interface of the cell's rear side is reflected back into the cell and contributes to the current generation.

6.2 UV degradation of solar modules featuring passivated emitter and rear cells

6.2.1 Results of UV degradation of PERC test modules with varying encapsulation material

Figure 6.4 shows the relative change of the initial P_{mpp} , I_{sc} , and V_{oc} during UV exposure for the test modules with varying encapsulation material and with PERC employing the reference SiN_y with $n = 2.07$. For the accelerated UV aging test we utilize the UVASpot lamps (see section 3.5, pp. 42). We measure a power loss of 6% for the test module M-SIL_{UV} and 4% for the test module M-EVA_{UV} after a UV dose of 497 kW h m⁻². Both test modules employ the encapsulation polymers with

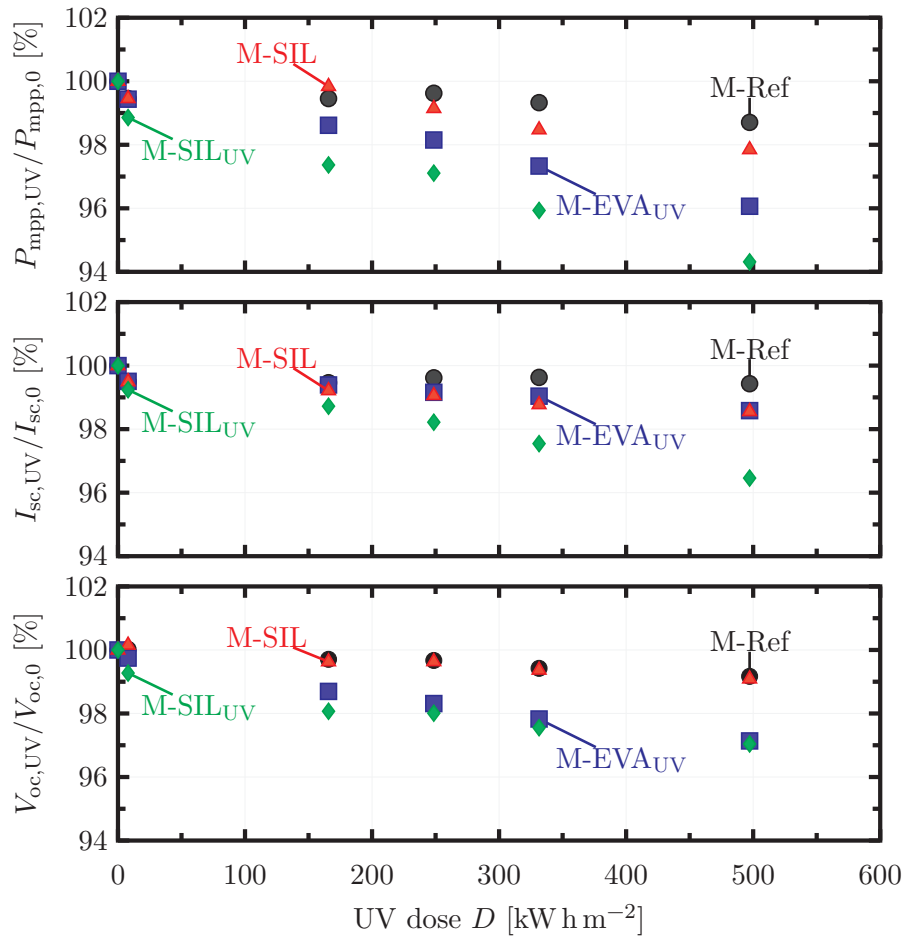


Figure 6.4: Relative change in module power P_{mpp} , short circuit current I_{sc} and open circuit voltage V_{oc} for the four test modules with PERCs and varying encapsulation polymer during UV exposure. All PERC have the reference SiN_y with a refractive index of 2.07.

enhanced UV transparency. In contrast, the two test modules with the UV absorbing polymers show a smaller degradation of 2% for the test module M-SIL and 1% for the test module M-Ref.

We observe a reduction of less than 0.6% in I_{sc} for the test module M-Ref within the full test period of the UV aging experiment. The test modules M-SIL and M-EVA_{UV} show a similar degradation in I_{sc} of 1.4%. For test module M-SIL_{UV} we observe the highest current loss with a decrease in I_{sc} of 4%

We also measure a loss in V_{oc} for all test modules after the UV aging experiment. The lowest degradation in V_{oc} of 0.8% we measure for the test modules M-Ref and M-SIL with the UV absorbing encapsulation. The highest loss of 2% we observe for the test modules M-EVA_{UV} and M-SIL_{UV}, employing the encapsulation materials with enhanced UV transparency.

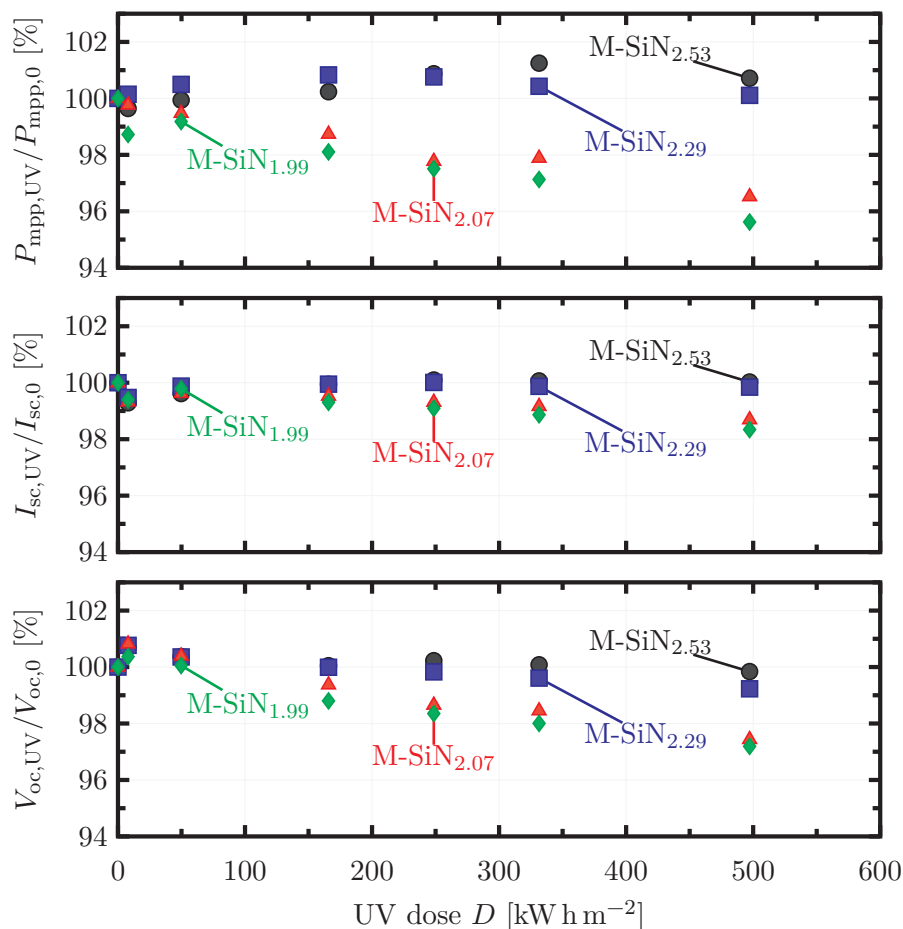


Figure 6.5: Relative change in module power P_{mpp} , short circuit current I_{sc} and open circuit voltage V_{oc} for the four test modules with PERCs and varying SiN_y coatings during UV exposure. All test modules have the EVA_{UV} with enhanced UV transparency

6.2.2 Results of UV degradation of PERC test modules with varying SiN_y refractive index

Figure 6.5 shows the relative degradation of P_{mpp} , I_{sc} , and V_{oc} during UV exposure for the test modules comprising of PERCs with varying SiN_y passivation layer. For the accelerated UV aging test we utilize the UVASpot lamps (see section 3.5, pp. 42). Similarly to the test modules with varying encapsulation materials, the test module featuring a PERC with a SiN_y layer with $n = 2.07$ and the EVA_{UV} with enhanced UV transparency degrades by 4% in P_{mpp} after a UV dose of 497 kW h m^{-2} . With decreasing SiN_y refractive index, the degradation in module power increases. The highest degradation in P_{mpp} we measure for the test module M-SiN_{1.99} with a SiN_y layer of $n = 1.99$, which degrades by 6% in P_{mpp} . In contrast, for the test modules M-SiN_{2.29} and M-SiN_{2.53} with a SiN_y layer of $n \geq 2.29$, we observe a deterioration in P_{mpp} of less than 1% within the full test period of the UV aging experiment.

We measure a similar change after the UV aging experiment for the test module's I_{sc} and V_{oc} . For both, the loss due to UV degradation increases with decreasing n . The test modules with a SiN_y of $n \leq 2.29$ show a degradation of up to 1.6% in I_{sc}

and up to 3% in V_{oc} . In contrast, we observe a degradation of less than 0.8% for the test modules with $n \geq 2.29$.

6.2.3 Discussion of UV aging experiments of PERC test modules

Regarding the UV aging experiments, we observe a correlation between the absorption of high energetic photons and the degradation of the cell's $I(V)$ parameters. The test modules with PERC and encapsulation polymers with $\lambda_c \geq 364$ nm degrade less in the module power than the test modules with the UV transparent encapsulation materials with $\lambda_c \leq 320$ nm. Similarly, increasing the refractive index of the PERC's SiN_y layer increases the absorption in the short wavelength range, which also improves the UV stability. The higher the absorption of the UV light in the encapsulation material and SiN_y passivation layer, the less the test modules degrade in P_{mpp} .

Thus, the initial advantage in transmittance of the UV transparent encapsulation polymers vanishes during the UV aging. According to the measurement results in Table 6.1 the test module M-EVA_{UV} has a 1.7% higher I_{sc} than the test module M-Ref under standard testing conditions (STC). Considering a spectral irradiance for a location in Potsdam (Germany), this advantage even increases to 1.9% due to a higher fraction of UV light compared to the illumination spectrum for the $I(V)$ measurement according to the STC [131]. We determine the break-even point, when the module power of the test module M-EVA_{UV} is equal to the module power of the test module M-Ref due to UV aging. After a UV dose of 342 kW h m^{-2} the module power of both test modules is equal, which corresponds to about 10 years of outdoor exposure in Potsdam [185].

In the literature, we find two possible reasons for the degradation under UV light: (i) due to a yellowing of the encapsulation polymer [132] and (ii) a degradation of the surface passivation [148]. There are various types of UV blocking agents mixed into the encapsulation polymer and some are known to decompose during UV exposure. For the EVA this decomposition induces the formation of chromophores, which results in a yellowing or browning effect [132, 215]. This yellowing reduces the transparency of the polymer and hence, primarily affects the I_{sc} of the test modules. However, we observe no reduction in the transmittance of the glass-polymer-glass samples and the loss in I_{sc} for the test modules explains only partly their degradation in P_{mpp} . Recalling the Shockley equation [96], the V_{oc} is given by

$$V_{oc} = \frac{kT}{q} \ln \left(\frac{J_{sc}}{J_0} + 1 \right), \quad (6.1)$$

where J_0 is the saturation current density of the test module. A loss of 1.4% in I_{sc} for the test module M-EVA_{UV} results in a V_{oc} reduction of 0.05% considering that J_0 is constant. Consequently, we explain the measured loss of 2.9% in V_{oc} by an increase in charge carrier recombination that manifests in an increase in J_0 . Applying Eq. 6.1 we find an increase in J_0 by a factor of 2 for the test module M-EVA_{UV}.

6.3 Analytical modeling of UV degradation

We assume that the V_{oc} reduction and the increased J_0 of the test modules with PERC is related to an increased surface recombination, since most of the UV light is absorbed close to the cell's front surface. Bulk effects due to light induced degradation are excluded by stabilizing the cells prior UV exposure [180]. We assume that a passivation by a fixed surface charge can be neglected for an emitter with such a high surface doping concentration [216]. Blumenstock et al. [147] proposed the hypotheses that light with a wavelength smaller than a critical value may reach the SiN_y/Si interface and affect the surface passivation, e.g. by bond breaking.

We employ the ray tracer *Daidalos* to simulate a complete test module with the standard EVA as well as the EVA_{UV} and determine the number of photons $N_{ph}(\lambda)$ that reach the SiN_y/Si interface for the various SiN_y coatings. For the simulation we employ the complex refractive index of the various SiN_y coatings from Fig. 6.1. The optical parameters for the glass ARC, glass, encapsulation material and backsheets we take from Ref. [198]. We weight the simulated number of photons with the spectral irradiance of the UV light source and integrate the bond breaking photon flux Φ_b reaching the SiN_y/Si interface as

$$\Phi_b = \int_{290}^{\lambda_b} \frac{N_{ph}(\lambda)}{N_{total}} \frac{E_{uv}(\lambda)}{\frac{hc}{\lambda}} d\lambda. \quad (6.2)$$

Here, N_{total} is the total number of ray-traced photons and the upper integration boundary λ_b is the wavelength of photons with energy $E > E_b$, where E_b is a threshold bond energy to break Si-H bonds.

When a photon with energy $E > E_b$ reaches the interface the number of interactions N_R with the Si-H bonds is related to

$$N_R = \sigma_{uv} N_P \Phi_b. \quad (6.3)$$

Here, N_P denotes the number of passivated bonds that could break and cause an interface state and σ_{uv} is the capture cross section area coefficient of a passivated bond for energies $E > E_b$. Thus, for an infinitesimal time step dt the number of interface states changes with

$$-\frac{dN_P}{dt} = \sigma_{uv} N_P \Phi_b(t). \quad (6.4)$$

Solving the differential equation we obtain

$$N_P = N_{P0} \exp[-\sigma_{uv} \Phi_b t], \quad (6.5)$$

where the integration constant N_{P0} represents the number of passivated and breakable bonds at $t_{uv} = 0$. Assuming that not all bonds are initially passivated, the total number of bonds is

$$N_T = N_P + N_{NP}, \quad (6.6)$$

where N_{NP} denotes the number of not passivated or dangling bonds prior UV exposure. During the UV exposure the number of dangling bonds increases with

$$N_{\text{NP}} = N_{\text{T}} - N_{\text{P0}} \exp[-\sigma_{\text{uv}}\Phi_{\text{b}}t]. \quad (6.7)$$

We suppose that a single dangling bond acts like a single defect state in the midgap and hence, can be described in terms of the SRH recombination theory (see section 2.2.2, pp. 9). When integrating the density of defect states D_{it} over the band gap energy E_{g} we obtain the number of defects N_{it} , which we consider to correspond to N_{NP} . Recalling the expression for the surface saturation current density $J_{0\text{s}}$ (see 2.2.2 pp. 9) we obtain

$$J_{0\text{s}} = \int_0^{E_{\text{g}}} q \frac{n_{\text{i}}^2}{n_{\text{s}}} D_{\text{it}} v_{\text{th}} \sigma_{\text{p}} dE = q \frac{n_{\text{i}}^2}{n_{\text{s}}} N_{\text{NP}} v_{\text{th}} \sigma_{\text{p}} = q \frac{n_{\text{i}}^2}{n_{\text{s}}} S_0, \quad (6.8)$$

where S_0 is the surface recombination velocity (SRV) (see Eq. 2.14, p. 10).

On substitution of Eq. 6.7 and Eq. 6.8 in Eq. 6.1, we find a relation for the V_{oc} and the bond breaking photon flux Φ_{b}

$$V_{\text{oc}} = \frac{kT}{q} \ln \left(\frac{J_{\text{sc}}}{J_{0\text{i}} + q \frac{n_{\text{i}}^2}{n_{\text{s}}} v_{\text{th}} \sigma_{\text{p}} (N_{\text{T}} - N_{\text{P0}} \exp[-\sigma_{\text{uv}}\Phi_{\text{b}}t])} + 1 \right), \quad (6.9)$$

where $J_{0\text{i}}$ is the initial diode saturation current density prior UV degradation. J_{sc} and $J_{0\text{i}}$ we extract from the $I(V)$ measurements prior UV exposure. This $J_{0\text{i}}$ consists of a contribution of the surface $J_{0\text{s}}$ and all remaining saturation current densities $J_{0\text{rem}}$ of the cell

$$J_{0\text{i}} = J_{0\text{rem}} + J_{0\text{s}}. \quad (6.10)$$

We assume that the UV light does not affect $J_{0\text{rem}}$, since the emitter absorbs all photons in the UV wavelength range. The $J_{0\text{s}}$ increases according to Eq. 6.8.

We utilize Eq. 6.9 to model the V_{oc} during the UV aging experiments. We extract n_{s} from the emitter doping profiles. For σ_{p} we employ $7.5 \times 10^{-18} \text{ cm}^2$ from Refs. [76, 77], who achieved a good agreement between simulated and measured $J_{0\text{s}}$ values for various surface recombination velocities. For the determination of the bond breaking photon flux Φ_{b} we employ the ray tracing results and Eq. 6.2, where the upper bound for the integral λ_{b} is a free fit parameter. The parameters σ_{uv} and N_{P0} are constrained fit parameters in Eq. 6.9.

For $t=0$ we rewrite the denominator of Eq. 6.9 to:

$$J_{0\text{i}} + q \frac{n_{\text{i}}^2}{n_{\text{s}}} v_{\text{th}} \sigma_{\text{p}} (N_{\text{T}} - N_{\text{P0}}) = J_{0\text{i}} + \Delta J_{0\text{i}}. \quad (6.11)$$

During the fit we constrain N_{P0} such that $3 \text{ fA cm}^{-2} > \Delta J_{0\text{i}} > 0 \text{ fA cm}^{-2}$.

In the limit of t , as t approaches infinity and considering a bond breaking photon flux Φ_{b} the number of not passivated bonds is equal to the number of total bonds in Eq. 6.7

$$\lim_{t \rightarrow \infty} N_{\text{NP}} = N_{\text{T}} \quad (6.12)$$

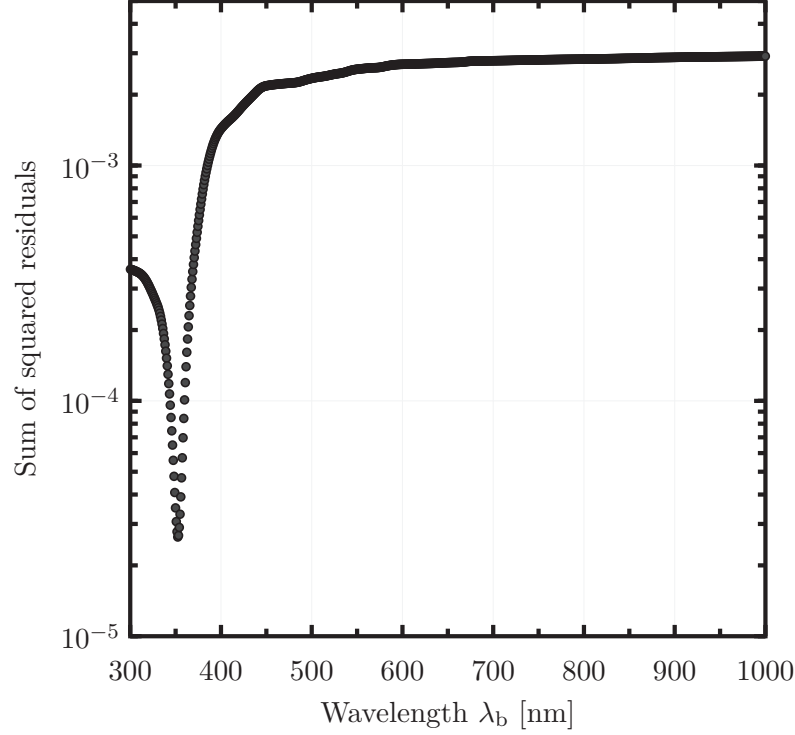


Figure 6.6: Sum of squared residuals of a least-square fit with Equation 6.9 with $\sigma_{\text{uv}} = 1 \times 10^{-23} \text{ cm}^2$ to the data of the M-SiN_{2.07} for various λ_b . The best fit is achieved when the sum of squared residuals has a minimum.

and the surface saturation current density approaches a maximum surface recombination velocity $S_{0\text{max}}$ in Eq. 6.8

$$\lim_{t \rightarrow \infty} J_{0s} = q \frac{n_i^2}{n_s} N_T v_{\text{th}} \sigma_p = q \frac{n_i^2}{n_s} S_{0\text{max}}. \quad (6.13)$$

The recombination of charge carriers is limited by the thermal velocity. Hence, S_0 in Eq. 6.8 approaches a maximum SRV $S_{0,\text{max}}$, which we set equal to the thermal velocity v_{th} . This also limits N_{NP} and thus, N_T in Eq. 6.9.

We fit Eq. 6.9 to the measured open circuit voltages in two steps. In the first step, we constrain σ_{uv} , since in Eq. 6.9 σ_{uv} and Φ_b may countervail. According to Barbé et al. [217] σ_{uv} varies for the considered wavelength range between $1 \times 10^{-20} \text{ cm}^2$ and $1 \times 10^{-25} \text{ cm}^2$. We create a list with σ_{uv} varying from $1 \times 10^{-20} \text{ cm}^2$ and $1 \times 10^{-25} \text{ cm}^2$ to fit Eq. 6.9 with a fixed σ_{uv} from this list.

The second step is to find a λ_b , where Eq. 6.9 fits best to the experimental data of each test module. We perform a least-square fit with a fixed σ_{uv} and vary λ_b from 300 nm to 1000 nm in each fit.

For the evaluation of the goodness of the fit we assess the sum of squared residuals (SSR). Figure 6.6 shows the SSR of a least-square fit with Eq. 6.9 and $\sigma_{\text{uv}} = 1 \times 10^{-23} \text{ cm}^2$ to the measurement data of test module M-SiN_{2.07}. The best fit is achieved when the SSR has a minimum, which is at $\lambda_b = 352 \text{ nm}$ for the data in Fig. 6.6. In the same manner we fit Eq. 6.9 to the experimental data of all samples and determine the corresponding λ_b .

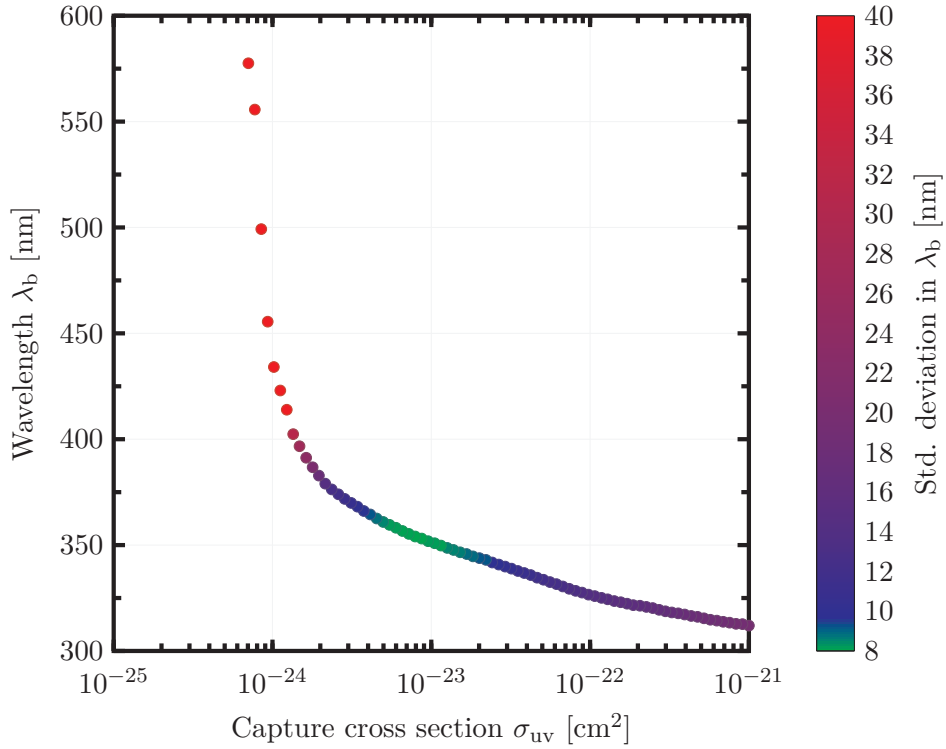


Figure 6.7: Obtained λ_b by fitting all measurement data with Equation 6.9 for various σ_{uv} . The colorbar indicates the standard deviation in λ_b for the various experimental data (e.g. fitting experimental data with $\sigma_{uv} = 1 \times 10^{-22} \text{ cm}^2$ results in $\lambda_b = 323 \text{ nm}$ for the module with SiN_y $n = 2.07$ and $\lambda_b = 319 \text{ nm}$ for the module with SiN_y $n = 2.29$). The smallest deviation in λ_b is obtained for $\sigma_{uv} = 9 \times 10^{-24} \text{ cm}^2$.

Further, we perform this fit procedure for all σ_{uv} in the list. Thus, we obtain different λ_b for each test module and σ_{uv} . For instance, choosing $\sigma_{uv} = 1 \times 10^{-22} \text{ cm}^2$ results in $\lambda_b = 323 \text{ nm}$ for the test module with a SiN_y of $n = 2.07$ and $\lambda_b = 319 \text{ nm}$ for the test module with a SiN_y of $n = 2.29$.

We expect that a certain energy is necessary to affect the surface passivation and thus, λ_b is similar for all samples. Further, we consider σ_{uv} to be equal for all samples. For the evaluation of the best λ_b , we determine an average λ_b and the corresponding standard deviation, for all σ_{uv} in the list. Figure 6.7 shows the average λ_b for the fit of Eq. 6.9 to the experimental data of all test modules for the elements in the σ_{uv} list. The color bar indicates the standard deviation of λ_b .

Our model fits best to the experimental data for $\sigma_{uv} = 9 \times 10^{-24} \text{ cm}^2$ and $\lambda_b = (353 \pm 8) \text{ nm}$.

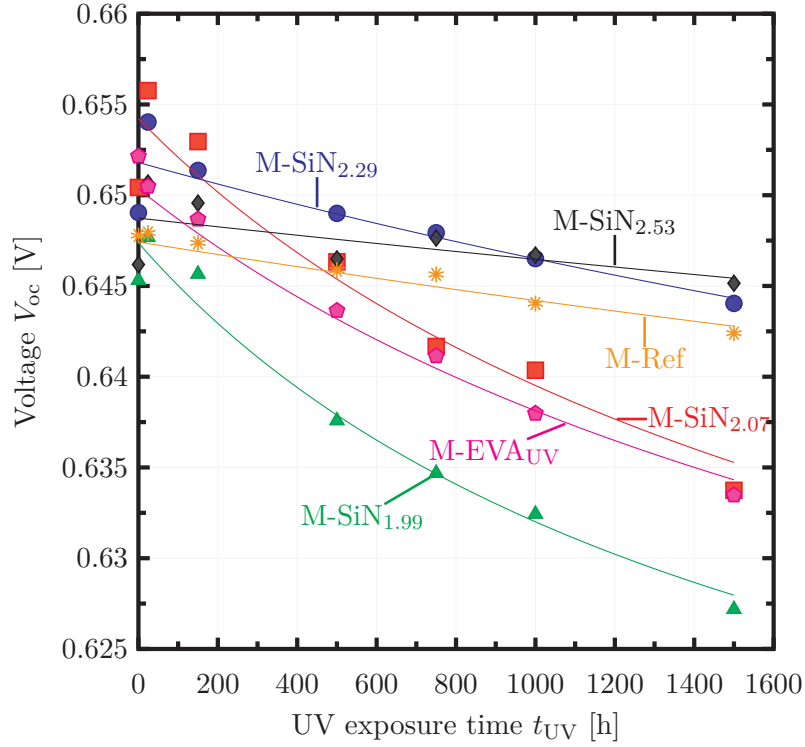


Figure 6.8: Measured V_{oc} during UV exposure for the various SiN_y coatings and UV transparent EVA. Additionally, the sample with UV absorbing EVA M-Ref is shown. The lines indicate the fit according to Equation 6.9

Figure 6.8 shows the measured and modeled V_{oc} data for the various EVA and SiN_y samples. The symbols indicate the measurement data denoted as $V_{oc,m}$ and lines indicate the corresponding fits according to Eq. 6.9. For all fits we utilize a capture cross section coefficient of $\sigma_{uv} = 9 \times 10^{-24} \text{ cm}^2$ and $\lambda_b = 353 \text{ nm}$. Measurement and model are in good agreement and the maximum relative deviation ($\Delta V_{oc}/V_{oc,m}$) is less than 0.5 %.

The λ_b of 353 nm is equivalent to a photon energy of 3.5 eV, which is in accordance with the bond energy of Si-H that is in the range from 3.34 eV to 3.5 eV [143, 217, 218, 219, 220]. Hence, we suppose that the UV radiation induces the breaking of Si-H bonds, which results in dangling bonds at the SiN_y/n^+ -type emitter interface. These dangling bonds increase the cell's surface recombination, which consequently results in a degradation of the open circuit voltage and eventually reduces the maximum power output of the solar module.

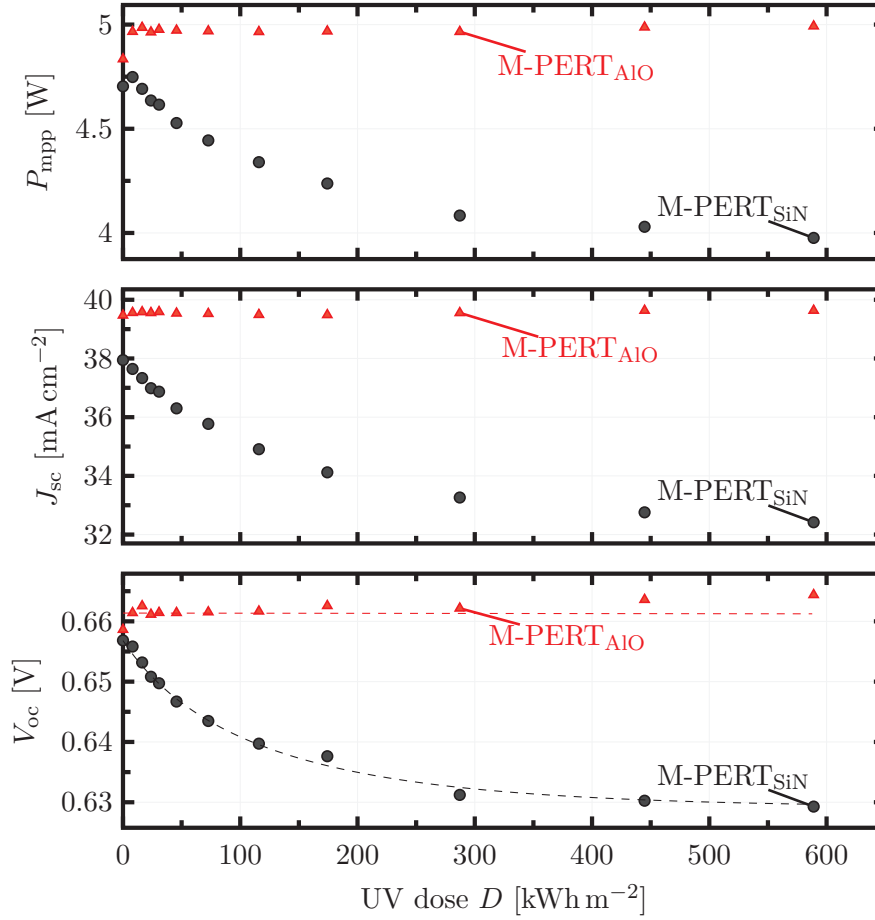


Figure 6.9: Module power P_{mpp} , short circuit current density J_{sc} and open circuit voltage V_{oc} for the two test modules with PERT cells during UV illumination. In test module M-PERT_{AlO} the p⁺-type emitter side with the AlO_x passivation and in test module M-PERT_{SiN} the n⁺-type BSF side with the SiN_y passivation faces the UV light. The dashed lines indicate a fit according to Eq. 6.9.

6.4 UV aging of test modules featuring PERT cells

The high bifacial factor of 0.97 of the PERT cells enables to compare the effect of UV radiation on solar modules with equal $I(V)$ characteristics and different passivation layers facing the UV lamps in the accelerated aging test. In M-PERT_{SiN} the SiN_y/n⁺-type Si interface and in M-PERT_{AlO} the AlO_x/p⁺-type Si interface faces the UV lamps.

6.4.1 Results of UV aging experiments

Figure 6.9 shows the module power output P_{mpp} of the test modules M-PERT_{SiN} and M-PERT_{AlO} as function of the UV dose D_{uv} . For the accelerated UV aging test we utilize the UVASpot lamps (see section 3.5, pp. 42). Test module M-PERT_{AlO} shows no significant degradation within the measurement accuracy after a UV dose D_{uv} of 598 kWh m⁻². In contrast, the test module M-PERT_{SiN} degrades during the UV illumination and we measure a decrease in P_{mpp} of 15%. Note that the module

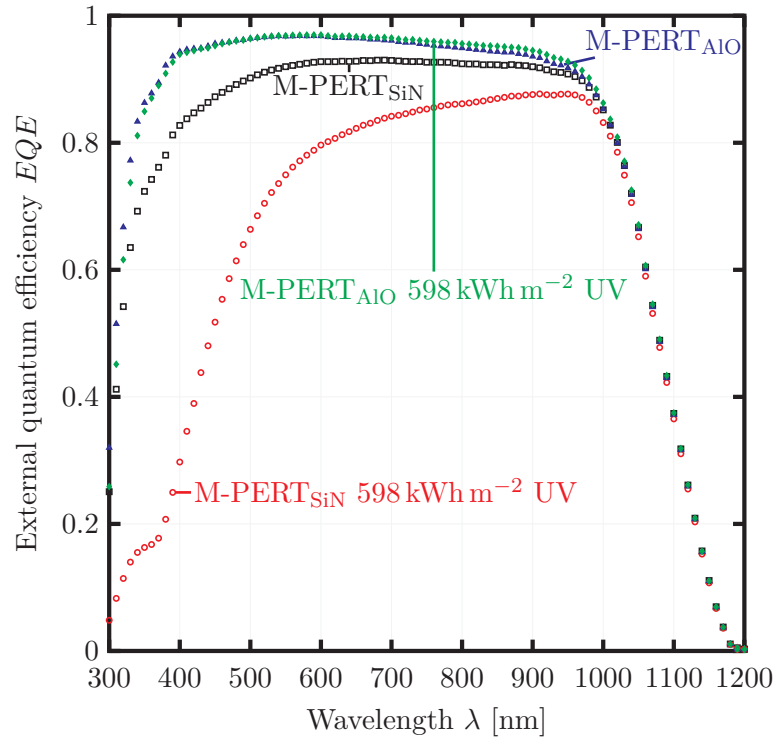


Figure 6.10: External quantum efficiency for the two test modules with PERT cells before and after 598 kWh m^{-2} UV exposure.

power of both test modules increases for a D_{uv} from 0 kWh m^{-2} to 8 kWh m^{-2} . For test module M-PERT_{AIO} we observe a gain in module power of 0.15 W , while for test module M-PERT_{SiN} the gain is only 0.04 W .

Figure 6.9 also shows the short circuit current density J_{sc} and the open circuit voltage V_{oc} as function of the UV dose for both test modules. Test module M-PERT_{AIO} shows no degradation in J_{sc} . For test module M-PERT_{SiN} we observe a loss in J_{sc} of 15% after the full test period.

The V_{oc} of test module M-PERT_{AIO} increases by 6 mV (1%), while the V_{oc} of test module M-PERT_{SiN} decreases by 28 mV (4%) within the full test period. The initial increase in V_{oc} of test module M-PERT_{AIO} for a D_{uv} from 0 kWh m^{-2} to 8 kWh m^{-2} correlates with the measured increase in P_{mpp} . The dashed lines indicate a fit according to Eq. 6.9.

Figure 6.10 shows the measured external quantum efficiency (EQE) for both test modules before and after UV exposure. We observe that the EQE degradation of test module M-PERT_{SiN} is particularly strong in the spectral range from 300 nm to 400 nm . The degradation of the EQE corresponds to the degradation in J_{sc} in Fig. 6.9. We exclude a degradation of the encapsulant, since the EQE of test module M-PERT_{AIO} employing the same encapsulation material shows no reduction after 598 kWh m^{-2} UV radiance.

6.4.2 Discussion of UV aging experiments

Due to their high bifacial factor, the PERT cells enable to compare the UV aging of AlO_x and SiN_y passivation layers for cells from the same production process and with similar $I(V)$ characteristics. Exposing test modules with PERT cells to UV light reveals that the AlO_x/p^+ -type emitter interface is stable, while the SiN_y/n^+ -type BSF interface degrades by 15 % in P_{mpp} . The EQE of test module M-PERT_{AlO} has not significantly changed indicating that the cell and the passivation is not affected by UV light. This further endorses that the degradation of test module M-PERT_{SiN} is not due to a yellowing effect of the encapsulant, since both test modules employ the same encapsulation materials. For test module M-PERT_{AlO} we measure a gain in V_{oc} of 4 mV at a D_{uv} of 16 kWh m⁻² increasing to 6 mV at a D_{uv} of 598 kWh m⁻². This might be related to an increase in fixed charge Q_f of the AlO_x layer under illumination as it was observed in several studies [221, 222, 223, 224, 225, 226].

We find that the EQE degradation of test module M-PERT_{SiN} is particularly strong in the spectral range from 300 nm to 400 nm. This supports the hypotheses of an increased surface recombination for test module M-PERT_{SiN} due to UV degradation. The penetration depth of light below 400 nm is only a few nanometers in silicon. For instance more than 99 % of the light with wavelengths below 400 nm are absorbed within the first 500 nm of silicon [227]. Further, about 40 % of the light with wavelengths below 400 nm are absorbed in a 100 nm SiN_y layer with $n = 2.53$ and will not reach the SiN_y/Si interface (see Fig. 6.1, pp. 86). Our hypotheses is that the UV aging manifests as a reduction of collected charge carriers close to the cell's surface due to a deterioration of the SiN_y surface passivation. This also reduces the EQE, which depends on the collection efficiency according to Eq. 3.11 [191].

6.5 Numerical modeling the UV degradation of the external quantum efficiency

We perform numerical simulations to further support the hypotheses of an increasing surface recombination due to UV radiation. We simulate the external quantum efficiency (EQE) of test module M-PERT_{SiN} prior and after UV exposure with *Sentaurus Device* [228] using the most recent device models and silicon parameters [229, 230, 231]. For the charge carrier mobility we apply the model of Klaassen [232], for the radiative recombination the model of Nguyen et al. [233], for the Auger recombination the model of Richter et al. [234], and for the band gap narrowing the model of Schenk [235]. We employ our ray tracer *Daidalos* including all optical effects of the glass, EVA, SiN_y and front metal fingers [127] to simulate the carrier generation profiles. We include the optical constants of the SiN_y from the VASE measurements and the optical parameters for the test module materials from Ref. [198]. The simulation considers a monochromatic illumination and a bias light for an area of $2 \times 2 \text{ cm}^2$ as in the EQE measurement.

In the transport simulation we employ the doping profiles from the ECV measurements of Kiefer [157] for the p^+ -type emitter and the n^+ -type BSF (see Fig. 6.3). We assume a fixed charge of $-4 \times 10^{12} \text{ cm}^{-2}$ [236] for the p^+ -type emitter with $\text{AlO}_x/\text{SiN}_y$ passivation and $2.5 \times 10^{12} \text{ cm}^{-2}$ for the n^+ -type BSF with SiN_y passivation [237]. Note that all charges are given in elementary charges per cm^2 . For the base we consider

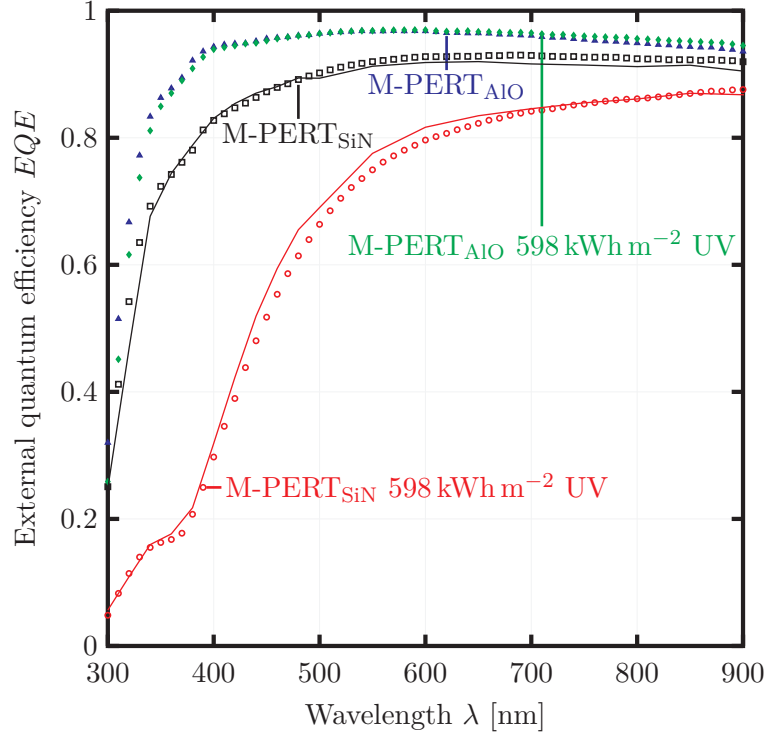


Figure 6.11: External quantum efficiency for the two investigated modules before and after 598 kWh m^{-2} UV exposure. The lines indicate results of numerical device simulations with *Sentaurus Device*.

a doping concentration of $7.5 \times 10^{14} \text{ cm}^{-3}$. We vary the surface recombination velocity (SRV) S_{p0} to fit the simulated to the measured EQE before and after UV degradation.

Figure 6.11 shows the measured and simulated external quantum efficiency for the module $\text{M-PERT}_{\text{SiN}}$ prior and after UV exposure. The lines represent the simulated EQE results. For a comparison we also include the EQEs of $\text{M-PERT}_{\text{AlO}}$ prior and after UV exposure. We find $S_{p0} = 5 \times 10^3 \text{ cm s}^{-1}$ for the initial EQE and $S_{p0} = 1.1 \times 10^6 \text{ cm s}^{-1}$ for the EQE after UV degradation. This corresponds to an increase in J_{0s} by a factor of 18 from 31 fA cm^{-2} to 559 fA cm^{-2} . This is in good agreement with the increase in J_{0s} determined with the analytical model. Here, we employ an initial J_{0s} of 35 fA cm^{-2} from Kiefer [157] in Eq. 6.10 for the n^+ -type BSF layer with SiN_y passivation. Due to the UV aging this J_{0s} increases to 585 fA cm^{-2} at a D_{UV} of 598 kWh m^{-2} , which is a factor of 17.

6.6 Modeling variations of the fixed charge

Our previous results show that a p^+ -type emitter with AlO_x passivation is stable, while an n^+ -type emitter with SiN_y passivation degrades within the accelerated UV aging tests. The theory of the passivation layer in section 2.2.2 shows that there are two possibilities to reduce the recombination at the silicon surface: (i) by a chemical passivation, reducing the dangling bonds at the surface, which reduces the interface states and thus, the surface recombination velocity (SRV). (ii) by a fixed charge

density Q_f in the passivation layer, which reduces the number of minority charge carriers at the silicon surface and thus, the effective SRV. In the analytical model for the UV degradation we neglect charge effects and assume that the recombination increases due to the deterioration of the chemical passivation by UV radiation. We perform numerical device simulations employing the EDNA 2 simulation tool [238] to test whether a change of the charge density explains the increase in J_{0s} due to UV light.

In the simulation we utilize the most recent device models and silicon parameters [229, 230, 231]. For the charge carrier mobility we apply the model of Klaassen [232], for the radiative recombination the model of Nguyen et al. [233], for the Auger recombination the model of Richter et al. [234], and for the band gap narrowing the model of Schenk [235].

We model the SiN_y/n^+ -type emitter interface with the parameters of the PERC with a base doping concentration of $5.7 \times 10^{15} \text{ cm}^{-3}$ and the emitter profile of the POCl_3 diffusion in Fig. 6.3. For the AlO_x/p^+ -type emitter interface we utilize the parameters of the PERT cell, with a base doping concentration of $7.5 \times 10^{14} \text{ cm}^{-3}$ and the emitter profile of the BF_2 ion implantation in Fig. 6.3 [157].

In the simulations for the n^+ -type emitter with SiN_y passivation layer we simulate a positive fixed charge density Q_f of $2.5 \times 10^{12} \text{ cm}^{-2}$ as reported in Ref. [237]. Additionally, we assume a reduction of the charge density and simulate a charge density of 0 cm^{-2} and $-2.5 \times 10^{12} \text{ cm}^{-2}$. For the p^+ -type emitter with AlO_x passivation layer we simulate a negative Q_f of $-4 \times 10^{12} \text{ cm}^{-2}$ as reported in Ref. [236]. In Ref. [239] we showed that UV light increases the Q_f at the AlO_x interface to $-1 \times 10^{13} \text{ cm}^{-2}$. Thus, we also simulate a fixed charge density of $-1 \times 10^{13} \text{ cm}^{-2}$. Additionally, we consider a reduction of the charge density to 0 cm^{-2} for the p^+ -type emitter with AlO_x passivation layer. Note that all charge densities are given in elementary charges per cm^2 .

Figure 6.12 shows the surface saturation current density J_{0s} as a function of the surface recombination velocity (SRV). In Fig. 6.12 (a) the black horizontal dashed lines indicate the J_{0s} of the n^+ -type emitter with a SiN_y passivation layer prior and after UV exposure. For the J_{0s} prior UV exposure we assume 80 fA cm^{-2} (see Table 4.3). For the J_{0s} after UV exposure we assume that J_{0i} in Eq. 6.10 equals 80 fA cm^{-2} , which increases to 361 fA cm^{-2} after a UV dose of 497 kW h m^{-2} for a SiN_y layer with $n = 2.07$. In Fig. 6.12 (b) the black horizontal dashed line indicates the J_{0s} of 42 fA cm^{-2} for the p^+ -type emitter with an AlO_x passivation layer for the PERT cell according to Kiefer [157].

For the heavily doped n^+ -type emitter with SiN_y passivation layer in Fig. 6.12 (a) a variation of the fixed charge density has only a minor effect on J_{0s} , which is in agreement with results reported in Ref. [216]. Even if the fixed charge vanishes or becomes negative, this can not account for the increase in J_{0s} due to the UV degradation. This further endorses the hypotheses that the increase in surface saturation current density during the UV aging experiments is due to a deterioration of the chemical passivation and the formation of dangling bonds, which is proportional to S_{p0} according to Eq. 6.8.

For the p^+ -type emitter with AlO_x passivation in Fig. 6.12 (b) the change in Q_f can compensate a deterioration of the chemical passivation. In Ref. [226] we reported that UV light also increases the density of defect states D_{it} by a factor of 7 at the

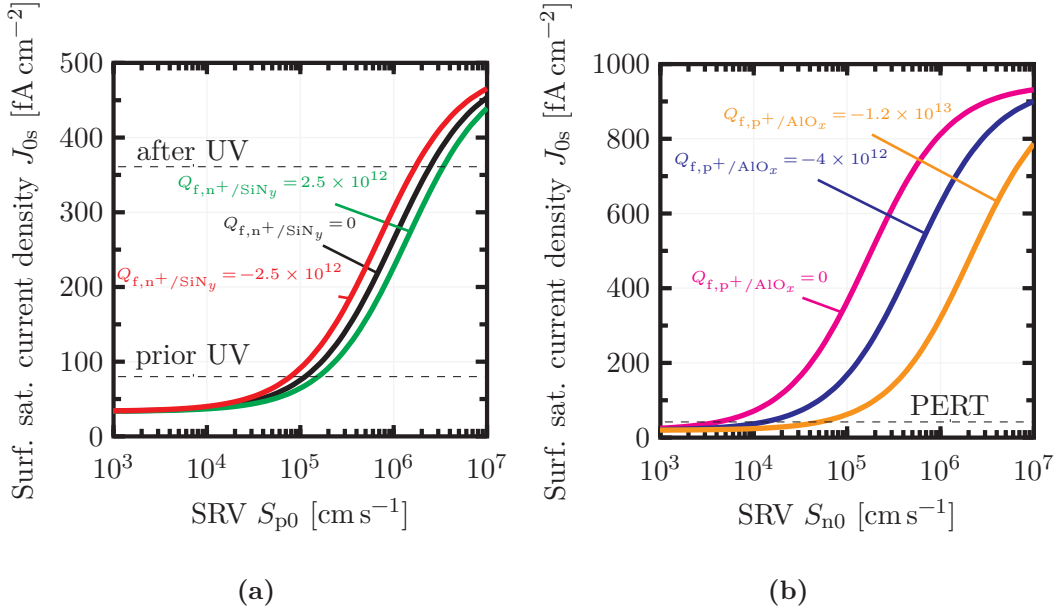


Figure 6.12: Surface saturation current density J_{0s} as a function of the surface recombination velocity (SRV) for: (a) an n^+ -type emitter with SiN_y passivation interface and (b) a p^+ -type emitter with AlO_x passivation interface. For each simulation we vary the fixed charge density Q_f . The dashed lines in (a) indicate a J_{0s} of 80 fA cm^{-2} [197] prior and 361 fA cm^{-2} after UV exposure for the n^+ -type emitter assuming a SiN_y passivation layer with $n = 2.07$. The black horizontal dashed line in (b) indicates a J_{0s} of 42 fA cm^{-2} for a p^+ -type emitter of a PERT cell [157].

AlO_x/p -type Si interface. However, we also observed an increase of the fixed charge density to $-1 \times 10^{13} \text{ cm}^{-2}$, which is in accordance with other studies [221, 240]. This may partly compensate the increased D_{it} . For instance, in our simulations an increase in SRV from $1 \times 10^4 \text{ cm s}^{-1}$ to $5 \times 10^4 \text{ cm s}^{-1}$ does not change the surface saturation current density of 42 fA cm^{-2} due to the increase in Q_f from $-4 \times 10^{12} \text{ cm}^{-2}$ to $-1 \times 10^{13} \text{ cm}^{-2}$.

6.7 Improved UV stability of silicon nitride passivation layers

The results of the accelerated UV aging tests with AlO_x passivation layers indicate that an $\text{AlO}_x/\text{SiN}_y$ stack is stable for UV radiation. However, AlO_x is commonly applied for p-type Si surfaces due to the negative fixed charge. A conceivable passivation for n-type Si surfaces are silicon oxide (SiO_x)/ SiN_y stacks [241]. Thus, we also test the UV radiation hardness of $\text{SiO}_x/\text{SiN}_y$ passivation stacks.

6.7.1 Results of quasi-steady state measurements on silicon oxide and silicon nitride passivation stacks

We process a batch similar to the PERC process flow in section 3.1 for QSSPC measurements. The bulk material is phosphorous doped n-type silicon with a sheet resistance of $4 \Omega/\square$. We create the phosphorous-doped regions with a POCl_3 diffusion

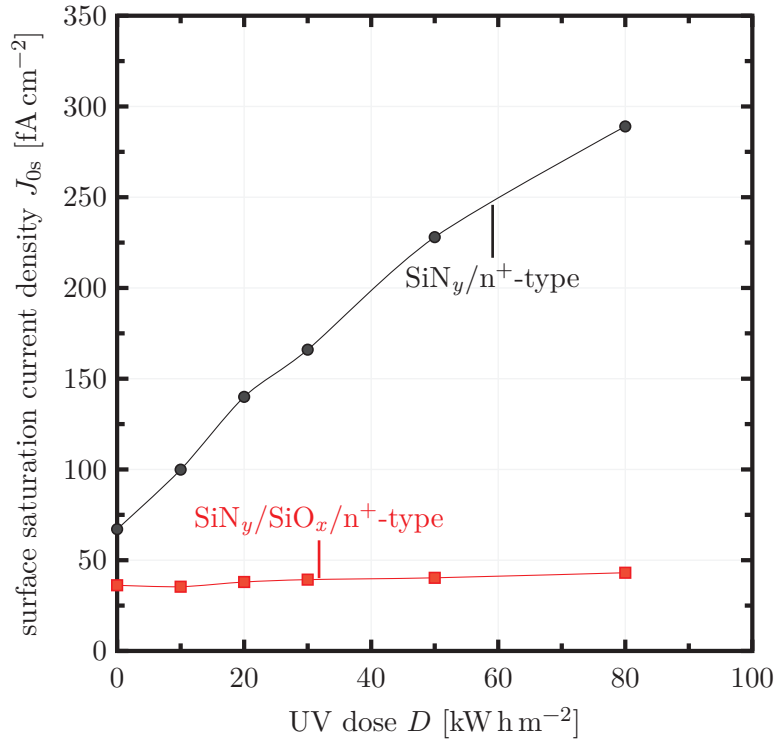


Figure 6.13: Surface saturation current density J_{0s} as a function of the UV dose for a SiN_y/n^+ -type and a $\text{SiN}_y/\text{SiO}_x/\text{n}^+$ -type sample.

process and apply a texture on both sides of the samples. For group I we apply a thermal SiO_x with a thickness of 6 nm and subsequently deposit the SiN_y layer as in the reference PERC process. For group II we only deposit the SiN_y layer as in the reference PERC process. After the deposition of the passivation layer we fire the samples in a conveyor belt furnace according to the reference PERC process.

For the accelerated UV aging test we utilize the UVB313 lamps (see section 3.5, pp. 42). We illuminate a sample of group I and group II with a UV dose of 80 kW h m^{-2} and measure J_{0s} . We determine J_{0s} from QSSPC measurements (see section 3.4.3, pp. 36) prior and after accelerated UV aging.

Figure 6.13 shows J_{0s} as a function of the UV dose. The J_{0s} for the sample of group II with the SiN_y/n^+ -type emitter interface increases from 67 fA cm^{-2} to 289 fA cm^{-2} . In contrast, for the samples of group I with the SiO_x/n^+ -type emitter interface, J_{0s} only increases from 36 fA cm^{-2} to 43 fA cm^{-2} .

6.7.2 Discussion of the quasi-steady state measurements

In the literature various authors reported that a single SiO_x layer degrades under UV exposure [144, 147, 242, 145]. However, the application of a $\text{SiO}_x/\text{SiN}_y$ stack on n^+ -type Si significantly improves the UV radiation hardness of the passivation for our test samples. Hence, the application of a $\text{SiO}_x/\text{SiN}_y$ stack could significantly improve the UV stability of PERC solar modules.

Lauinger [152] assumed that the ion bombardment during the plasma enhanced chemical vapour deposition (PECVD) of the SiN_y layer, damages the silicon surface

and increases the number of dangling bonds, which are initially passivated by hydrogen. This is also indicated in transmission electron microscope (TEM) images published by Kamioka et al. [150]. One hypothesis is that the thermal SiO_x layer protects the silicon surface during the subsequent PECVD process. The same effect might explain the enhanced UV stability of the PERT cells with the AlO_x/p^+ -type emitter interface, where the spatial atomic layer deposition (SALD) of an AlO_x layer protects the silicon surface during the subsequent PECVD process for the SiN_y deposition.

Another hypothesis is that the oxide decreases the number of dangling bonds at the silicon surface [243]. The bond energy of Si-O is 4.8 eV. This energy is beyond the energy of photons from the employed light source for the accelerated UV aging. Thus, N_{it} is not affected at the SiO_x/n^+ -type emitter interface. Several studies reported a thin 1 nm to 2 nm SiO_x layer between the AlO_x passivation layer and the silicon surface that is crucial for the passivation quality [44, 236]. However, TEM investigations of SiN_y interfaces also indicate the formation of a thin 1 nm to 2 nm SiO_x layer during the cleaning process before the PECVD deposition [244]. Hence, the thickness and deposition technique of the SiO_x layer may be important.

CHAPTER 7

Summary

The goal of this work was to analyse and reduce the cell to module (CTM) losses for solar modules featuring passivated emitter and rear cells (PERCs) and to improve their long-term reliability. In terms of reliability, we specifically examined the ultraviolet (UV) radiation hardness of PERC modules.

7.1 Analysis and reduction of cell to module losses

We developed an analytical model for the analysis of CTM losses of PERC solar modules, which considers the optical, recombination, and resistive losses. The analytical model enables to predict the power output of the solar module from the cell parameters. Further, the model allows to reduce the cell to modules losses by optimizing the cell and the module. For the model parameters, we measured the optical, recombination, and resistive characteristics of cell and module test samples. When an experimental determination was not possible or out of the scope of this work, we derived the parameters with the support of simulation tools or took them from the literature.

In the model we account for the optical losses by employing optical factors. We presented a method to derive the effective optical width of the front metalization and the cell interconnection in a photovoltaic module. For the front metal fingers we combined reflection measurements with ray tracing simulations and for the cell interconnection we applied light beam induced current measurements to determine the effective optical width.

The effective optical width of single screen-printed front metal fingers is reduced by 48 % for a cell in a module compared to a cell in air. We demonstrated that a specular reflecting front metal finger is beneficial within a module due to its parabola like shape, which enables a further optimization of future cell metalizations.

We determined the effective optical width for cell interconnection ribbons with different reflective surfaces and cell interconnection wires. A typical industrial cell interconnection ribbon has an effective optical width of 90 % of the geometrical width. In contrast, a diffuse reflecting cell interconnection ribbon surface reduces the geometrical width by 50 %. The geometrical width of cell interconnection wires is reduced by 33 % due to their round shape. For groove-structured cell interconnection ribbons we measured the highest optical reduction of 30 % of the geometrical width.

The optical factors for the current enhancement by internal backsheet reflections we determined with ray tracing simulations. We derived the optical factors for a typical industrial backsheet and an intermediate reflector for a solar module employing full cells and half cells. Half cells result in higher current enhancement factors within a module compared to full cells, which we attributed to an increased fraction of the backsheet area within the module.

For the modeling of series resistance losses we adopted the analytical model of Deb et al. We extended their model by the cell interconnection considering cell interconnection ribbons and cell interconnection wires. The comparison of the extended analytical model to finite element simulations revealed a maximum deviation of 8%. We successfully validated the analytical model by simulating the $I(V)$ -parameters of experimental test modules. The simulated and the measured power output of the modules agreed within the uncertainty of our measurement equipment.

After the verification, we applied the analytical model to investigate six state of the art cell interconnection configurations. The simulation results revealed that the combination of half cells with cell interconnection wires or groove-structured cell interconnections ribbons are the most promising approaches for a reduction of the cell to module losses and an improvement of the module power output. Both result in a power gain of 15 W for a module with 2 mm cell spacing compared to the reference cell interconnection. The dense mesh of cell interconnection wires reduces series resistance losses and allows to reduce the number of front metal fingers, which reduces the cell's front metal recombination. A groove-structure improves the optics of the cell interconnection ribbon and allows to increase the number and the application of wider cell interconnections ribbons, which reduces series resistance losses.

From the manufacturers point of view, the application of cell interconnection wires allow to omit the busbars and requires less front metal fingers, which reduces the Ag paste consumption and thus, the production costs. Though, this technology requires new manufacturing tools. In contrast, applying a groove-structured cell interconnection ribbon requires only an upgrade of the current stringer technology.

Enlarging the cell spacing enhances the module current due to an increased fraction of internal reflections within the module and results in the highest module power output of 323 W in our simulations. However, using a larger cell spacing reduces the module efficiency and the fill factor. For instance the efficiency for the simulated 323 W module is only 13% due to the enlarged module area, despite a cell efficiency of 20.8%. This increases the material consumption and has a negative impact on the system costs.

From the simulation results we derived the optimal parameters for the PERC front metalization and the cell interconnection to build a 60-cell sized high efficiency solar module. With this solar module we set a new world record for PERC modules in 2017 with an efficiency of 20.2% on the aperture area and an independently confirmed module power of 303 W.

7.2 Ultraviolet radiation hardness of solar modules

Besides a high power output or efficiency, the performance reliability is crucial for industrial photovoltaic modules. Hence, the application of UV transparent

encapsulation polymers requires to test the solar module's ultraviolet (UV) radiation hardness. We measured the effect of a UV radiation dose of 497 kW h m^{-2} on solar modules with passivated emitter and rear cells (PERCs) featuring various amorphous silicon nitride (SiN_y) passivation layers and encapsulated with different polymers. We showed that the power output of solar modules featuring encapsulation materials with an improved UV transmittance and solar cells with SiN_y passivation layer degrades after accelerated UV aging.

The initially enhanced power output due to an improved exploitation of the solar spectrum by photovoltaic modules employing UV transparent encapsulation polymers vanishes after approximately 10 years for a moderate climate location in Germany.

All test modules with a UV transparent encapsulation polymer and the cell's n^+ -type emitter featuring a SiN_y layer with varying refractive index facing to the UV lamps degraded in module power. We related this loss in module power to a decreased open circuit voltage V_{oc} . With increasing SiN_y refractive index the degradation rate of the PERC test modules decreased due to an increased absorption of UV light in the SiN_y layer. The module power of the test module with a typical industrial SiN_y passivation layer with a refractive index of 2.07 degraded by 4%.

We also examined the effect of UV radiation on test modules with ion-implanted bifacial n-type passivated emitter, rear totally-diffused (PERT) cells encapsulated in polymers with enhanced UV transmittance. The power of the module with the n^+ -type BSF featuring a SiN_y passivation layer at the illuminated side degraded by 15% after a UV dose of 598 kW h m^{-2} . We related this loss in module power to a decrease in V_{oc} and J_{sc} . Due to the back junction configuration the test module degraded by 15% in J_{sc} . External quantum efficiency (EQE) measurements prior and after UV degradation revealed a degradation in the spectral range from 300 nm to 400 nm. The degradation of the EQE corresponds to the degradation in J_{sc} .

We explain the UV induced degradation in module power with a degradation of the cell's SiN_y surface passivation. We assume that photons with sufficient energy to break the Si-H bond reach the interface between SiN_y and silicon. The breaking of Si-H bonds increases the number of dangling bonds at the silicon surface, which results in an increased surface recombination. We presented a novel physical model that connects the incident photon flux at the silicon surface with the recombination in the cell. The model was successfully tested for modules with varying SiN_y passivation layer and encapsulation materials with different UV transmittance. We found that photons with wavelengths below a critical wavelength of 353 nm result in a degradation of the module power. This critical wavelength is equivalent to the Si-H bond energy of 3.5 eV.

We also modeled the UV degradation of the external quantum efficiency of the PERT test modules with numerical simulations. A comparison of the simulated EQE prior and after a UV dose of 598 kW h m^{-2} revealed that the surface saturation current density $J_{0\text{s}}$ increased by a factor of 18 from 31 fA cm^{-2} to 599 fA cm^{-2} . This was in agreement with the analytical model, which revealed an increase in $J_{0\text{s}}$ by a factor of 15 from 40 fA cm^{-2} to 603 fA cm^{-2} .

In contrast, the module with the PERT cell's p^+ -type emitter with an $\text{AlO}_x/\text{SiN}_y$ passivation stack at the illuminated side was stable during accelerated UV aging for a UV dose of 598 kW h m^{-2} . We also observed no significant changes of the measured EQE before and after UV exposure. This implies, that the applied encapsulation

materials is stable under UV exposure and that the decrease in module performance of the test modules with SiN_y/n^+ -type Si interface facing the illuminated module side, resulted from the degradation of the surface passivation. We showed for the first time that solar modules containing cells with AlO_x/p^+ -type silicon interface facing the illuminated module side show no degradation after UV exposure and even observed an increase in module efficiency due to an enhanced V_{oc} . This effect we related to an increased fixed charge at the AlO_x/p^+ -type Si interface. Simulations with a varying fixed charge density for the SiN_y/n^+ -type Si interface showed that changes of the fixed charge by UV light can not explain the increased surface recombination after accelerated UV aging. This further endorsed our hypotheses that UV light deteriorates the chemical surface passivation.

We assume that the UV stability of the AlO_x passivation layer is due to a thin silicon oxide (SiO_x) layer at the $\text{AlO}_x/\text{silicon}$ interface. The application of a $\text{SiO}_x/\text{SiN}_y$ passivation stack to an n^+ -type emitter sample showed a significant reduction of the degradation of the surface recombination during accelerated UV aging.

The results in this work may help to reduce the CTM losses and improve the UV radiation hardness of solar modules with passivated emitter and rear cells and solar cells featuring SiN_y passivation layers. An extension of the presented analytical CTM model enables to reduce the CTM losses of the next generation bifacial PERC+ solar cells and modules or other cell interconnection techniques, e.g. shingling of the solar cells. Improved UV stable passivation layers are required to benefit of UV transparent encapsulation materials for solar modules and increase their annual yield and long-term stability. This requires additional studies of multi-layer passivation stacks on cell and module level and investigations of different deposition techniques for the SiO_x passivation layers. Moreover, the change of the charge density and microscopic analysis of the passivation interface require further examinations in future works.

APPENDIX A

Appendix A

A.1 Contact resistance

Figure 5.4 shows the current I flowing from the emitter into half a finger of width w_f and length l_f . Recalling that the current reduces below the finger in the x direction with

$$\frac{dI}{dx} = \frac{V(x)l_f}{\rho_c}. \quad (\text{A.1})$$

and the voltage drops due to emitter sheet resistance below the finger with

$$\frac{dV}{dx} = \frac{I(x)R_{\text{sh}}}{l_f}. \quad (\text{A.2})$$

Substituting Eq. A.1 in A.2 and rearranging results in

$$\frac{d^2I}{dx^2} = I(x)\frac{R_{\text{sh}}}{\rho_c}. \quad (\text{A.3})$$

For the sake of brevity we introduce

$$\alpha = \frac{1}{L_t} = \frac{R_{\text{sh}}}{\rho_c} \quad \text{and} \quad L = \frac{w_f}{2} \quad (\text{A.4})$$

where L_t is known as the transfer length. Solving the differential equation yields

$$I(x) = A \exp\left(\frac{x}{L_t}\right) + B \exp\left(\frac{-x}{L_t}\right), \quad (\text{A.5})$$

where A and B are unknown constants.

For the boundary conditions we assume that the current is at its maximum I_{max} , when it enters the metal finger and that the metal contact extracts all the current from the emitter, such that the current approaches zero at the end of the metal contact. With these boundary condition

$$I(x) = \begin{cases} 0 & , \quad \text{for } x = 0, \\ I_{\text{max}} & , \quad \text{for } x = \frac{w_f}{2} = L, \end{cases} \quad (\text{A.6})$$

we obtain

$$0 = A + B \Rightarrow A = -B \quad (\text{A.7})$$

and

$$I_{\max} = A \left(\exp\left(\frac{L}{L_t}\right) - \exp\left(\frac{L}{L_t}\right) \right) = 2A \sinh\left(\frac{L}{L_t}\right). \quad (\text{A.8})$$

This allows to determine the unknown constants as

$$\begin{aligned} A &= \frac{I_{\max}}{2 \sinh\left(\frac{L}{L_t}\right)}, \\ B &= \frac{-I_{\max}}{2 \sinh\left(\frac{L}{L_t}\right)}. \end{aligned} \quad (\text{A.9})$$

Substituting the solution for the constants in Eq. A.5 yields

$$I(x) = \frac{I_{\max}}{2 \sinh\left(\frac{L}{L_t}\right)} \exp\left(\frac{x}{L_t}\right) - \frac{I_{\max}}{2 \sinh\left(\frac{L}{L_t}\right)} \exp\left(\frac{-x}{L_t}\right) = I_{\max} \frac{\sinh\left(\frac{x}{L_t}\right)}{\sinh\left(\frac{L}{L_t}\right)}. \quad (\text{A.10})$$

Rearranging Eq. A.1 and taking the derivative of Eq. A.10 yields

$$\frac{dI}{dx} = \frac{V(x)l_f}{\rho_c} \Rightarrow V(x) = \frac{dI}{dx} \frac{\rho_c}{l_f} = I_{\max} \frac{\cosh\left(\frac{x}{L_t}\right)}{\sinh\left(\frac{L}{L_t}\right)} \frac{\rho_c}{l_f L_t}. \quad (\text{A.11})$$

Recalling Ohm's law and $I_{\max} = I(L)$ the contact resistance R_c for the full contact geometry of length L is

$$R_c = \frac{\rho_c}{l_f L_t} \coth\left(\frac{L}{L_t}\right). \quad (\text{A.12})$$

A.2 Half cell contact firing

In section 4.4 we show that the contact resistance increases for a specific region of the cells with a half cell metalization grid as in this work. We observe correlations between the increased contact resistance and the orientation of the solar cell within the conveyor belt furnace for the contact firing. Figure A.1 shows the electroluminescence images of four PERCs with a different orientation during contact firing process. The four vertical black lines are the cell's busbars. The red arrow indicates the orientation of the cell in the conveyor belt furnace. All cells are processed equally and the cell side labeled with "top" faces in the same direction in the other production processes. In the electroluminescence images we observe the formation of dark areas, which depend on the orientation of the cell during the contact firing. These dark areas correlate with the increased contact resistance. In the upper two images the busbars are parallel to the orientation in the belt furnace. Here the dark areas in the electroluminescence image form in the center of the cell, at the interruption of the half cell metalization grid on the cell side first entering the belt furnace. For the lower two images the busbars are perpendicular to the firing direction. Here, the formation of the dark areas also form at the cell side first entering the belt furnace

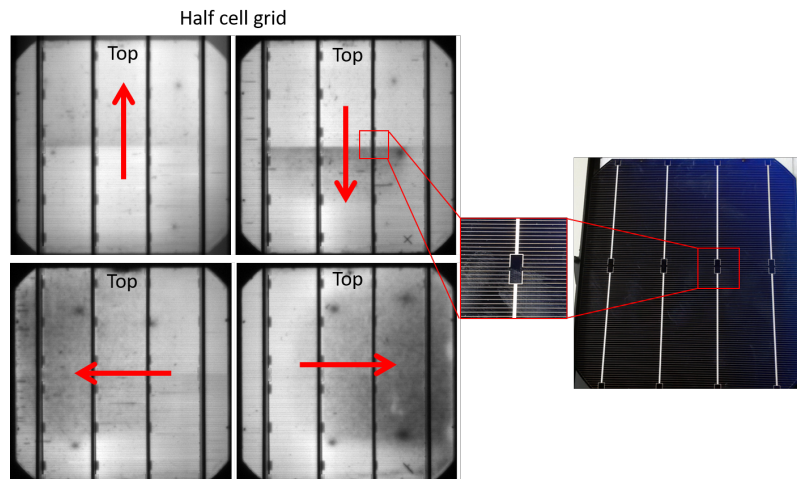


Figure A.1: Electroluminescence image of four PERCs. The photography on the right hand side show the front metalization of a PERC with a magnification of the half cell grid interruption. The arrow indicates the orientation of a cell during the contact firing.

and the dark areas are enlarged compared to the upper two images. For the lower two images the fingers are parallel to the firing direction. We assume that due to the small cross section of the fingers and the lower heat conductance this changes the local temperature of the cell, which deteriorates the contact firing process.

Applying a conductive connection to the half cell metal grid interruption by manually printing Ag paste with a tiny brush to the gap between the busbars in the center of the cell, shows no local increase in contact resistance at the metal grid interruption after the contact firing as shown in Fig. A.2.

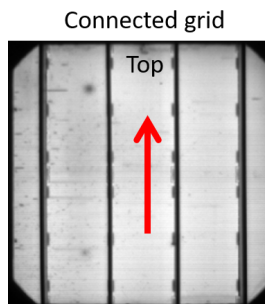


Figure A.2: Electroluminescence image of a PERC without interruption of the front metalization grid. The arrow indicates the orientation of a cell during the contact firing.

Bibliography

- [1] K. Yoshikawa, H. Kawasaki, W. Yoshida, T. Irie, K. Konishi, K. Nakano, T. Uto, D. Adachi, M. Kanematsu, H. Uzu, and K. Yamamoto. ‘Silicon heterojunction solar cell with interdigitated back contacts for a photoconversion efficiency over 26%’. In: *Nature Energy* 2.5 (2017). DOI: 10.1038/nenergy.2017.32.
- [2] A. Richter, M. Hermle, and S. W. Glunz. ‘Reassessment of the Limiting Efficiency for Crystalline Silicon Solar Cells’. In: *IEEE Journal of Photovoltaics* 3.4 (2013), pp. 1184–1191. DOI: 10.1109/jphotov.2013.2270351.
- [3] K. Yamamoto, D. Adachi, K. Yoshikawa, W. Yoshida, T. Irie, K. Konishi, T. Fujimoto, H. Kawasaki, M. Kanematsu, H. Ishibashi, T. Uto, Y. Takahashi, T. Terashita, G. Koizumi, N. Nakanishi, and M. Yoshimi. ‘Record-Breaking Efficiency Back-Contact Heterojunction Crystalline Si Solar Cell and Module’. eng. In: *33rd EUPVSEC*. WIP, 2017, pp. 201–204. DOI: 10.4229/eupvsec20172017-2bp.1.1.
- [4] D. DeGraaff. *SunPower Offers Customers the Most Efficient Solar Panels Commercially Available Today*. SunPower - United States. 2015. URL: <https://us.sunpower.com/blog/2015/10/08/sunpower-offers-customers-most-efficient-solar-panels-commercially-available-today/> (visited on 2017-08-23).
- [5] NREL. *The Open PV Project*. 2017. URL: <https://openpv.nrel.gov/> (visited on 2017-09-12).
- [6] ENFSolar. *Solar Companies and Products Database*. 2017. URL: <https://www.enfsolar.com/pv/panel> (visited on 2017-08-23).
- [7] R. Fu, D. Chung, T. Lowder, D. Feldman, K. Ardani, and R. Margolis. *US Solar Photovoltaic System Cost Benchmark: Q1 2016*. Tech. rep. NREL, 2016.
- [8] ITRPV. ‘International Technology Roadmap for Photovoltaic Results 2018’. In:
- [9] K. H. Kim, C. S. Park, J. D. Lee, J. Y. Lim, J. M. Yeon, I. H. Kim, E. J. Lee, and Y. H. Cho. ‘Record high efficiency of screen-printed silicon aluminum back surface field solar cell: 20.29%’. In: *Japanese Journal of Applied Physics* 56.8S2 (2017), 08MB25-1–08MB25-4. DOI: 10.7567/jjap.56.08mb25.
- [10] S. E&G. *Solar Module 5BB*. 2017. URL: https://www.shinsungeng.com/upload/brochure/attachment/14/Solar%20Module_ENG.pdf (visited on 2017-09-27).

- [11] P. Altermatt, S. Steingrube, Y. Yang, C. Sprodowski, T. Dezhdar, S. Koc, B. Veith, S. Herrman, R. Bock, K. Bothe, J. Schmidt, and R. Brendel. ‘Highly predictive modelling of entire Si solar cells for industrial applications’. In: *Proc. 24th Eur. Photovoltaic Solar Energy Conf.* 2009, pp. 901–906.
- [12] P. P. Altermatt, Z. Xiong, Q. He, W. Deng, F. Ye, Y. Yang, Y. Chen, Z. Feng, P. J. Verlinden, A. Liu, D. H. Macdonald, T. Luka, D. Lausch, M. Turek, C. Hagendorf, H. Wagner-Mohnsen, J. Schön, W. Kwapil, F. Frühauf, O. Breitenstein, E. E. Looney, T. Buonassisi, D. B. Needleman, C. M. Jackson, A. R. Arehart, S. A. Ringel, K. R. McIntosh, M. D. Abbott, B. A. Sudbury, A. Zuschlag, C. Winter, D. Skorka, G. Hahn, D. Chung, B. Mitchell, P. Geelan-Small, and T. Trupke. ‘High-performance p-type multicrystalline silicon (mc-Si): Its characterization and projected performance in PERC solar cells’. In: *Solar Energy* (2018). DOI: [10.1016/j.solener.2018.01.073](https://doi.org/10.1016/j.solener.2018.01.073).
- [13] B. Min, M. Muller, H. Wagner, G. Fischer, R. Brendel, P. P. Altermatt, and H. Neuhaus. ‘A Roadmap Toward 24% Efficient PERC Solar Cells in Industrial Mass Production’. In: *IEEE Journal of Photovoltaics* 7.6 (2017), pp. 1541–1550. DOI: [10.1109/jphotov.2017.2749007](https://doi.org/10.1109/jphotov.2017.2749007).
- [14] A. Metz, D. Adler, S. Bagus, H. Blanke, M. Bothar, E. Brouwer, S. Dauwe, K. Dressler, R. Droessler, T. Droste, M. Fiedler, Y. Gassenbauer, T. Grahl, N. Hermert, W. Kuzminski, A. Lachowicz, T. Lauinger, N. Lenck, M. Manole, M. Martini, R. Messmer, C. Meyer, J. Moschner, K. Ramspeck, P. Roth, R. Schönfelder, B. Schum, J. Sticksel, K. Vaas, M. Volk, and K. Wangemann. ‘Industrial high performance crystalline silicon solar cells and modules based on rear surface passivation technology’. In: *Solar Energy Materials and Solar Cells* 120 (2014), pp. 417–425. DOI: [10.1016/j.solmat.2013.06.025](https://doi.org/10.1016/j.solmat.2013.06.025).
- [15] International Electrotechnical Commission. *IEC60068:Electronic Equipment & Product Standards*. Tech. rep. International Electrotechnical Commission, Geneva, Switzerland, 2016.
- [16] International Electrotechnical Commission. *IEC61215:Terrestrial photovoltaic (PV) modules - Design qualification and type approval*. Tech. rep. International Electrotechnical Commission, Geneva, Switzerland, 2016.
- [17] International Electrotechnical Commission. *IEC 61646:Thin-film terrestrial photovoltaic (PV) modules - Design qualification and type approval*. Tech. rep. International Electrotechnical Commission, Geneva, Switzerland.
- [18] International Electrotechnical Commission. *IEC 61730-1:Photovoltaic (PV) module safety qualification - Part 1: Requirements for construction*. Tech. rep. International Electrotechnical Commission, Geneva, Switzerland, 2016.
- [19] International Electrotechnical Commission. *IEC 61345: UV test of photovoltaic (PV) modules*. Tech. rep. International Electrotechnical Commission, Geneva, Switzerland, 1998.
- [20] R. Hezel and R. Schörner. ‘Plasma Si nitride - A promising dielectric to achieve high-quality silicon MIS/IL solar cells’. In: *Journal of Applied Physics* 52.4 (1981), pp. 3076–3079. DOI: [10.1063/1.329058](https://doi.org/10.1063/1.329058).
- [21] J. Mandelkorn and J. H. Lamneck Jr. ‘Simplified fabrication of back surface electric field silicon cells and novel characteristics of such cells’. In: *9th IEEE PVSC*. 1972, pp. 121–130.

- [22] J. Fossum. ‘Physical operation of back-surface-field silicon solar cells’. In: *IEEE Transactions on Electron Devices* 24.4 (1977), pp. 322–325. DOI: 10.1109/T-ED.1977.18735.
- [23] A. Metz, D. Adler, S. Bagus, H. Blanke, M. Bothar, E. Brouwer, S. Dauwe, K. Dressler, R. Droessler, T. Droste, M. Fiedler, Y. Gassenbauer, T. Grahl, N. Hermert, W. Kuzminski, A. Lachowicz, T. Lauinger, N. Lenck, M. Manole, M. Martini, R. Messmer, C. Meyer, J. Moschner, K. Ramspeck, P. Roth, R. Schönfelder, B. Schum, J. Sticksel, K. Vaas, M. Volk, and K. Wangemann. ‘Industrial high performance crystalline silicon solar cells and modules based on rear surface passivation technology’. In: *Solar Energy Materials and Solar Cells* 120 (2014), pp. 417–425. DOI: 10.1016/j.solmat.2013.06.025.
- [24] A. W. Blakers, A. Wang, A. M. Milne, J. Zhao, and M. A. Green. ‘22.8% efficient silicon solar cell’. In: *Applied Physics Letters* 55.13 (1989), pp. 1363–1365. DOI: 10.1063/1.101596.
- [25] B. Rech, A. Bett, B. Burger, C. Brabec, R. Brendel, O. Führer, U. Möhrstedt, H. Neuhaus, M. Powalla, B. Utz, F. Wessendorf, S. Wieder, J. Binder, B. Dimmler, H.-J. Egelhaaf, D. Geyer, T. E. Kuhn, P. Lechner, L. Lucera, F. Machui, J. Mayer, P. Palinginis, S. Philipps, W. Wischmann, R. Witteck, B. Lunz, M. Merzkirch, and B. Erlach. *Photovoltaik - Technologiesteckbrief zur Analyse "Flexibilitätskonzepte für die Stromversorgung 2050"*. 2016. DOI: 10.13140/RG.2.1.2291.2885.
- [26] TrinaSolar. *Press Release - Trina Solar*. 2017. URL: <https://www.trinasolar.com/en-glb/resources/newsroom/20161219> (visited on 2017-04-25).
- [27] F. W. Sexton. ‘Plasma nitride AR coatings for silicon solar cells’. In: *Solar Energy Materials* 7.1 (1982), pp. 1–14. DOI: 10.1016/0165-1633(82)90091-0.
- [28] R. Sinton, Y. Kwark, J. Gan, and R. Swanson. ‘27.5-percent silicon concentrator solar cells’. In: *IEEE Electron Device Letters* 7.10 (1986), pp. 567–569. DOI: 10.1109/edl.1986.26476.
- [29] J. Zhao, A. Wang, P. Altermatt, and M. A. Green. ‘Twenty-four percent efficient silicon solar cells with double layer antireflection coatings and reduced resistance loss’. In: *Applied Physics Letters* 66.26 (1995), pp. 3636–3638. DOI: 10.1063/1.114124.
- [30] S. Glunz, A. Grohe, M. Hermle, M. Hofmann, S. Janz, T. Roth, O. Schultz, M. Vetter, I. Martin, R. Ferré, et al. ‘Comparison of different dielectric passivation layers for application in industrially feasible high-efficiency crystalline silicon solar cells in 20th EUPVSEC’. In: *Barcelona (Spain)* (2000), pp. 572–577.
- [31] S. D. Wolf, A. Descoedres, Z. C. Holman, and C. Ballif. ‘High-efficiency Silicon Heterojunction Solar Cells: A Review’. In: *green* 2.1 (2012). DOI: 10.1515/green-2011-0018.
- [32] D. Biro, S. Mack, A. Wolf, A. Lemke, U. Belledin, D. Erath, B. Holzinger, E. A. Wotke, M. Hofmann, L. Gautero, S. Nold, J. Rentsch, and R. Preu. ‘Thermal oxidation as a key technology for high efficiency screen printed industrial silicon solar cells’. In: *34th IEEE PVSC*. Institute of Electrical and Electronics Engineers (IEEE), 2009. DOI: 10.1109/pvsc.2009.5411381.
- [33] S. Gatz, F. Einsele, T. Dullweber, and R. Brendel. ‘Firing stability of SiNy/SiNx surface passivation stacks for crystalline silicon solar cells’. In: *26th EUPVSEC*. 2011.

- [34] E. P. Donovan, F. Spaepen, D. Turnbull, J. M. Poate, and D. C. Jacobson. ‘Calorimetric studies of crystallization and relaxation of amorphous Si and Ge prepared by ion implantation’. In: *Journal of Applied Physics* 57.6 (1985), pp. 1795–1804. DOI: 10.1063/1.334406.
- [35] S. Reiter, N. Koper, R. Reineke-Koch, Y. Larionova, M. Turcu, J. Krügener, D. Tetzlaff, T. Wietler, U. Höhne, J.-D. Kähler, R. Brendel, and R. Peibst. ‘Parasitic Absorption in Polycrystalline Si-layers for Carrier-selective Front Junctions’. In: *Energy Procedia* 92 (2016), pp. 199–204. DOI: 10.1016/j.egypro.2016.07.057.
- [36] R. Crabb and A. Atzei. ‘Environmental study of European silicon solar cells with improved antireflection coatings’. In: *8th IEEE PVSC*. 1970, pp. 78–83.
- [37] R. Gereth, H. Fischer, E. Link, S. Mattes, and W. Pschunder. ‘Silicon solar cell technology of the Seventies’. In: *8th IEEE PVSC*. 1970, pp. 353–359.
- [38] A. G. Aberle. ‘Surface passivation of crystalline silicon solar cells: a review’. In: *Progress in Photovoltaics: Research and Applications* 8.5 (2000), pp. 473–487. DOI: 10.1002/1099-159x(200009/10)8:5<473::aid-pip337>3.0.co;2-d.
- [39] B. Veith, F. Werner, D. Zielke, R. Brendel, and J. Schmidt. ‘Comparison of the thermal stability of single Al₂O₃ layers and Al₂O₃/SiN_x stacks for the surface passivation of silicon’. In: *Energy Procedia* 8 (2011), pp. 307–312. DOI: 10.1016/j.egypro.2011.06.141.
- [40] L. E. Black, T. Allen, A. Cuevas, K. R. McIntosh, B. Veith, and J. Schmidt. ‘Thermal stability of silicon surface passivation by APCVD Al₂O₃’. In: *Solar Energy Materials and Solar Cells* 120 (2014), pp. 339–345. DOI: 10.1016/j.solmat.2013.05.048.
- [41] S. D. Wolf, G. Agostinelli, G. Beaucarne, and P. Vitanov. ‘Influence of stoichiometry of direct plasma-enhanced chemical vapor deposited SiN_x films and silicon substrate surface roughness on surface passivation’. In: *Journal of Applied Physics* 97.6 (2005), p. 063303. DOI: 10.1063/1.1861138.
- [42] G. Agostinelli, P. Choulat, H. Dekkers, S. D. Wolf, and G. Beaucarne. ‘Screen Printed Large Area Crystalline Silicon Solar Cells On Thin Substrates’. In: *20th EUPVSEC*. 2005.
- [43] G. Agostinelli, A. Delabie, P. Vitanov, Z. Alexieva, H. Dekkers, S. D. Wolf, and G. Beaucarne. ‘Very low surface recombination velocities on p-type silicon wafers passivated with a dielectric with fixed negative charge’. In: *Solar Energy Materials and Solar Cells* 90.18-19 (2006), pp. 3438–3443. DOI: 10.1016/j.solmat.2006.04.014.
- [44] B. Hoex, S. B. S. Heil, E. Langereis, M. C. M. van de Sanden, and W. M. M. Kessels. ‘Ultralow surface recombination of c-Si substrates passivated by plasma-assisted atomic layer deposited Al₂O₃’. In: *Applied Physics Letters* 89.4 (2006), p. 042112. DOI: 10.1063/1.2240736.
- [45] A. Cuevas, M. J. Kerr, and J. Schmidt. ‘Passivation of crystalline silicon using silicon nitride’. In: *3rd WCPEC*. Vol. 1. IEEE. 2003, pp. 913–918.
- [46] T. Lauinger, J. Schmidt, A. G. Aberle, and R. Hezel. ‘Record low surface recombination velocities on 1 Ω cm p-silicon using remote plasma silicon nitride passivation’. In: *Applied Physics Letters* 68.9 (1996), pp. 1232–1234.

- [47] H. Nagel, A. G. Aberle, and R. Hezel. ‘Optimised antireflection coatings for planar silicon solar cells using remote PECVD silicon nitride and porous silicon dioxide’. In: *Progress in Photovoltaics: Research and Applications* 7.4 (1999), pp. 245–260.
- [48] E. Yablonovitch. ‘Statistical ray optics’. In: *Journal of the Optical Society of America* 72.7 (1982), p. 899. DOI: 10.1364/josa.72.000899.
- [49] M. H. Kang, K. Ryu, A. Upadhyaya, and A. Rohatgi. ‘Optimization of SiN AR coating for Si solar cells and modules through quantitative assessment of optical and efficiency loss mechanism’. In: *Prog. Photovolt: Res. Appl.* 19.8 (2011), pp. 983–990. DOI: 10.1002/pip.1095.
- [50] M. Born, E. Wolf, A. B. Bhatia, P. C. Clemmow, D. Gabor, A. R. Stokes, A. M. Taylor, P. A. Wayman, and W. L. Wilcock. *Principles of Optics*. Cambridge University Press, 1999. DOI: 10.1017/cbo9781139644181.
- [51] E. Hecht. *Optics*. Addison Wesley, 2007.
- [52] G. B. Airy. ‘VI. On the phaenomena of Newton’s rings when formed between two transparent substances of different refractive powers’. In: *The London, Edinburgh, and Dublin Philosophical Magazine and Journal of Science* 2.7 (1833), pp. 20–30.
- [53] B. Lenkeit. ‘Elektronische und strukturelle Eigenschaften von Plasma-Siliziumnitrid zur Oberflächenpassivierung von siebgedruckten, bifazialen Silizium-Solarzellen’. PhD thesis. Leibniz Universität Hannover, 2002.
- [54] W. Shockley and W. T. Read. ‘Statistics of the Recombinations of Holes and Electrons’. In: *Phys. Rev.* 87.5 (1952), pp. 835–842. DOI: 10.1103/physrev.87.835.
- [55] R. Hall. ‘Recombination processes in semiconductors’. In: *Proceedings of the IEEE - Part B: Electronic and Communication Engineering* 106.17S (1959), pp. 923–931. DOI: 10.1049/pi-b-2.1959.0171.
- [56] R. Hezel. ‘Low-Temperature Surface Passivation of Silicon for Solar Cells’. In: *Journal of The Electrochemical Society* 136.2 (1989), p. 518. DOI: 10.1149/1.2096673.
- [57] J. Schmidt and M. Kerr. ‘Highest-quality surface passivation of low-resistivity p-type silicon using stoichiometric PECVD silicon nitride’. In: *Solar Energy Materials and Solar Cells* 65.1 (2001), pp. 585–591.
- [58] K. Kimura. ‘Recent Developments in Polycrystalline Silicon Solar Cell’. In: *1st PVSEC*. 1984, pp. 37–42.
- [59] D. T. Krick, P. Lenahan, and J. Kanicki. ‘Nature of the dominant deep trap in amorphous silicon nitride’. In: *Physical Review B* 38.12 (1988), p. 8226.
- [60] D. T. Krick, P. M. Lenahan, and J. Kanicki. ‘Electrically active point defects in amorphous silicon nitride: An illumination and charge injection study’. In: *Journal of Applied Physics* 64.7 (1988), pp. 3558–3563. DOI: 10.1063/1.341499.
- [61] D. Jousse, J. Kanicki, D. T. Krick, and P. M. Lenahan. ‘Electron-spin-resonance study of defects in plasma-enhanced chemical vapor deposited silicon nitride’. In: *Applied Physics Letters* 52.6 (1988), pp. 445–447. DOI: 10.1063/1.99438.

- [62] C. H. Seager and J. Kanicki. ‘Photodarkening and bleaching in amorphous silicon nitride’. In: *Applied Physics Letters* 57.14 (1990), pp. 1378–1380. DOI: 10.1063/1.104089.
- [63] J. Robertson. ‘Defects and hydrogen in amorphous silicon nitride’. In: *Philosophical Magazine Part B* 69.2 (1994), pp. 307–326. DOI: 10.1080/01418639408240111.
- [64] J. Schmidt, A. Merkle, R. Bock, P. P. Altermatt, A. Cuevas, N.-P. Harder, B. Hoex, R. Van De Sanden, E. Kessels, and R. Brendel. ‘Progress in the surface passivation of silicon solar cells’. In: *23rd EUPVSEC*. 2008.
- [65] W. Shockley. *Electrons and holes in semiconductors*. van Nostrand New York, 1950.
- [66] J. Bardeen. ‘Surface states and rectification at a metal semi-conductor contact’. In: *Physical Review* 71.10 (1947), p. 717.
- [67] M. Tanenbaum and D. E. Thomas. ‘Diffused Emitter and Base Silicon Transistors’. In: *Bell System Technical Journal* 35.1 (1956), pp. 1–22. DOI: 10.1002/j.1538-7305.1956.tb02371.x.
- [68] W. V. Roosbroeck. ‘Theory of the Flow of Electrons and Holes in Germanium and Other Semiconductors’. In: *Bell System Technical Journal* 29.4 (1950), pp. 560–607. DOI: 10.1002/j.1538-7305.1950.tb03653.x.
- [69] A. Grove and D. Fitzgerald. ‘Surface effects on p-n junctions: Characteristics of surface space-charge regions under non-equilibrium conditions’. In: *Solid-State Electronics* 9.8 (1966), pp. 783–806. DOI: 10.1016/0038-1101(66)90118-3.
- [70] H. D. Man. ‘The influence of heavy doping on the emitter efficiency of a bipolar transistor’. In: *IEEE Transactions on Electron Devices* 18.10 (1971), pp. 833–835. DOI: 10.1109/t-ed.1971.17291.
- [71] H. de Graaff, J. Slotboom, and A. Schmitz. ‘The emitter efficiency of bipolar transistors’. In: *Solid-State Electronics* 20.6 (1977), pp. 515–521. DOI: 10.1016/s0038-1101(77)81008-3.
- [72] M. Shibib, F. Lindholm, and F. Therez. ‘Heavily doped transparent-emitter regions in junction solar cells, diodes, and transistors’. In: *IEEE Transactions on Electron Devices* 26.6 (1979), pp. 959–965. DOI: 10.1109/t-ed.1979.19525.
- [73] R. Girisch, R. Mertens, and R. de Keersmaecker. ‘A new method to determine Si/SiO₂ interface recombination parameters using a gate-controlled point-junction diode under illumination’. In: *Applied Surface Science* 30.1-4 (1987), pp. 127–133. DOI: 10.1016/0169-4332(87)90084-5.
- [74] P. P. Altermatt, J. O. Schumacher, A. Cuevas, M. J. Kerr, S. W. Glunz, R. R. King, G. Heiser, and A. Schenk. ‘Numerical modeling of highly doped Si:P emitters based on Fermi–Dirac statistics and self-consistent material parameters’. In: *Journal of Applied Physics* 92.6 (2002), pp. 3187–3197. DOI: 10.1063/1.1501743.
- [75] S. Steingrube, P. P. Altermatt, D. S. Steingrube, J. Schmidt, and R. Brendel. ‘Interpretation of recombination at c-Si/SiN_x interfaces by surface damage’. In: *Journal of Applied Physics* 108.1 (2010), p. 014506. DOI: 10.1063/1.3437643.
- [76] A. Kimmerle, A. Wolf, U. Belledin, and D. Biro. ‘Modelling carrier recombination in highly phosphorus-doped industrial emitters’. In: *Energy Procedia* 8 (2011), pp. 275–281. DOI: 10.1016/j.egypro.2011.06.136.

- [77] B. Min, H. Wagner, A. Dastgheib-Shirazi, A. Kimmerle, H. Kurz, and P. P. Altermatt. ‘Heavily doped Si: P emitters of crystalline Si solar cells: recombination due to phosphorus precipitation’. In: *physica status solidi (RRL)-Rapid Research Letters* 8.8 (2014), pp. 680–684. DOI: 10.1002/pssr.201409138.
- [78] R. N. Hall. ‘Electron-Hole Recombination in Germanium’. In: *Physical Review* 87.2 (1952), pp. 387–387. DOI: 10.1103/physrev.87.387.
- [79] W. H. Brattain and J. Bardeen. ‘Surface Properties of Germanium’. In: *Bell System Technical Journal* 32.1 (1953), pp. 1–41. DOI: 10.1002/j.1538-7305.1953.tb01420.x.
- [80] W. Fahrner and A. Goetzberger. ‘Energy Dependence Of Electrical Properties Of Interface States In Si-SiO₂ Interfaces’. In: *Applied Physics Letters* 17.1 (1970), pp. 16–18. DOI: 10.1063/1.1653234.
- [81] J. Schmidt, F. M. Schuurmans, W. C. Sinke, S. W. Glunz, and A. G. Aberle. ‘Observation of multiple defect states at silicon-silicon nitride interfaces fabricated by low-frequency plasma-enhanced chemical vapor deposition’. In: *Applied Physics Letters* 71.2 (1997), pp. 252–254. DOI: 10.1063/1.119512.
- [82] S. Steingrube. ‘Recombination models for defects in silicon solar cells’. PhD thesis. Leibniz Universität Hannover, 2011.
- [83] K. R. McIntosh and L. E. Black. ‘On effective surface recombination parameters’. In: *Journal of Applied Physics* 116.1 (2014), p. 014503. DOI: 10.1063/1.4886595.
- [84] L. E. Black. *New Perspectives on Surface Passivation: Understanding the Si-Al₂O₃ Interface*. Springer, 2016.
- [85] J. A. Del Alamo and R. M. Swanson. ‘The physics and modeling of heavily doped emitters’. In: *IEEE Transactions on Electron Devices* 31.12 (1984), pp. 1878–1888.
- [86] A. McEvoy, T. Markvart, L. Castañer, T. Markvart, and L. Castaner. *Practical Handbook of Photovoltaics*. Elsevier, 2012. DOI: 10.1016/c2011-0-05723-x.
- [87] A. Mette. ‘New Concepts for Front Side Metallization of Industrial Silicon Solar Cells’. PhD thesis. Albert-Ludwigs-Universität Freiburg, 2007.
- [88] H. Schulte-Huxel. ‘Laser Microspot Welding for Interconnection of Back-contacted Silicon Solar Cells’. PhD thesis. Leibniz Universität Hannover, 2015.
- [89] J. Müller. ‘Characterisation of local aluminum-alloyed contacts to silicon solar cells’. PhD thesis. Leibniz Universität Hannover, 2013.
- [90] J. Song, S. Park, S. Kwon, S. Kim, H. Kim, S. J. Tark, S. Yoon, and D. Kim. ‘A study on the aluminum fire-through to a-SiN_x:H thin film for crystalline solar cells’. In: *Current Applied Physics* 12.1 (2012), pp. 313–318. DOI: 10.1016/j.cap.2011.06.028.
- [91] G. Schubert, F. Huster, and P. Fath. ‘Physical understanding of printed thick-film front contacts of crystalline Si solar cells—Review of existing models and recent developments’. In: *Solar Energy Materials and Solar Cells* 90.18-19 (2006), pp. 3399–3406. DOI: 10.1016/j.solmat.2006.03.040.
- [92] A. Cuevas. *The Idea of J0*. Tech. rep. ANU, 2014.

- [93] T. Fellmeth, A. Born, A. Kimmerle, F. Clement, D. Biro, and R. Preu. ‘Recombination at Metal-Emitter Interfaces of Front Contact Technologies for Highly Efficient Silicon Solar Cells’. In: *Energy Procedia* 8 (2011), pp. 115–121. DOI: 10.1016/j.egypro.2011.06.111.
- [94] M. Müller. ‘Sensitivity of solar cells’. PhD thesis. Leibniz Universität Hannover, 2014.
- [95] ASTM. ‘G159, standard tables for references solar spectral irradiance at air mass 1.5: Direct normal and hemispherical for a 37 tilted surface’. In: *Society for Testing Matls* (1998).
- [96] W. Shockley. ‘The Theory of p-n Junctions in Semiconductors and p-n Junction Transistors’. In: *Bell System Technical Journal* 28.3 (1949), pp. 435–489. DOI: 10.1002/j.1538-7305.1949.tb03645.x.
- [97] M. Wolf, G. Noel, and R. J. Stirn. ‘Investigation of the double exponential in the current-voltage characteristics of silicon solar cells’. In: *IEEE Transactions on electron Devices* 24.4 (1977), pp. 419–428.
- [98] S. M. Sze and K. K. Ng. *Physics of semiconductor devices*. John wiley & sons, 2006. DOI: 10.1007/b117561.
- [99] O. Breitenstein. ‘Understanding the current-voltage characteristics of industrial crystalline silicon solar cells by considering inhomogeneous current distributions’. In: *Opto-Electronics Review* 21.3 (2013). DOI: 10.2478/s11772-013-0095-5.
- [100] Wolf and Rauschenbach. ‘Series resistance effects on solar cell measurements’. In: *Advanced energy conversion* 3.2 (1963), pp. 455–479.
- [101] K. R. McIntosh, J. N. Cotsell, J. S. Cumpston, A. W. Norris, N. E. Powell, and B. M. Ketola. ‘An optical comparison of silicone and EVA encapsulants for conventional silicon PV modules: A ray-tracing study’. In: *34th IEEE PVSC*. IEEE, 2009, pp. 000544–000549.
- [102] J. Fan, D. Ju, X. Yao, Z. Pan, M. Terry, W. Gambogi, K. Stika, J. Liu, W. Tao, Z. Liu, Y. Liu, M. Wang, Q. Wu, and T. J. Trout. ‘Study on snail trail formation in PV module through modeling and accelerated aging tests’. In: *Solar Energy Materials and Solar Cells* 164 (2017), pp. 80–86. DOI: 10.1016/j.solmat.2017.02.013.
- [103] W. Stark and M. Jaunich. ‘Investigation of Ethylene/Vinyl Acetate Copolymer (EVA) by thermal analysis DSC and DMA’. In: *Polymer Testing* 30.2 (2011), pp. 236–242. DOI: 10.1016/j.polymertesting.2010.12.003.
- [104] R. Julius. *Solar cell array*. US Patent 3,375,141. 1968.
- [105] A. Schneider, L. Rubin, and G. Rubin. ‘Solar Cell Efficiency Improvement by New Metallization Techniques - the Day4 Electrode Concept’. In: *4th WCPEC*. 2006, pp. 1095–1098. DOI: 10.1109/WCPEC.2006.279333.
- [106] S. Braun, G. Micard, and G. Hahn. ‘Solar Cell Improvement by using a Multi Busbar Design as Front Electrode’. In: *Energy Procedia* 27 (2012), pp. 227–233. DOI: 10.1016/j.egypro.2012.07.056.
- [107] J. Walter, M. Tranitz, M. Volk, C. Ebert, and U. Eitner. ‘Multi-wire Interconnection of Busbar-free Solar Cells’. In: *Energy Procedia* 55 (2014), pp. 380–388. DOI: 10.1016/j.egypro.2014.08.109.

- [108] L. Rubin and G. Rubin. ‘Electrode for photovoltaic cells, photovoltaic cell and photovoltaic module’. US Patent 7,432,438. 2008.
- [109] B. Sadlik, L. Rubin, and V. Nebusov. ‘Day4 Technology For Conceptually New PV Module Production’. In: *25th EUPVSEC*. 2010, pp. 4144–4147. DOI: 10.4229/25thEUPVSEC2010-4AV.3.56.
- [110] R. Grischke, R. Efinger, and L. Rubin. ‘Day4 Technology Allows Enhanced Fine-Line Front Metallization for Low Cost Mass Production’. In: *25th EUPVSEC*. 2010, pp. 2399–2402.
- [111] A. W. Blakers. ‘Shading losses of solar-cell metal grids’. In: *Journal of Applied Physics* 71.10 (1992), p. 5237. DOI: 10.1063/1.350580.
- [112] S. Krauter, R. Hanitsch, P. Campbell, and S. Wenham. ‘Optical modeling, simulation and improvement of PV module encapsulation’. In: *21st EUPVSEC*. 1994, pp. 11–15.
- [113] J. Schneider, M. Turek, M. Dyrba, I. Baumann, B. Koll, and T. Booz. ‘Combined effect of light harvesting strings, anti-reflective coating, thin glass, and high ultraviolet transmission encapsulant to reduce optical losses in solar modules’. In: *Progress in Photovoltaics: Research and Applications* 22.7 (2014), pp. 830–837. DOI: 10.1002/pip.2470.
- [114] I. Peters, Y. S. Khoo, and T. M. Walsh. ‘Detailed Current Loss Analysis for a PV Module Made With Textured Multicrystalline Silicon Wafer Solar Cells’. In: *IEEE Journal of Photovoltaics* 4.2 (2014), pp. 585–593. DOI: 10.1109/jphotov.2013.2295736.
- [115] L. J. Caballero, P. Sanchez-Friera, B. Lalaguna, J. Alonso, and M. A. Vazquez. ‘Series Resistance Modelling of Industrial Screen-Printed Monocrystalline Silicon Solar Cells and Modules Including the Effect of Spot Soldering’. In: *4th WCPEC*. 2006, pp. 1388–1391. DOI: 10.1109/WCPEC.2006.279710.
- [116] S. Guo, J. P. Singh, I. M. Peters, A. G. Aberle, and T. M. Walsh. ‘A Quantitative Analysis of Photovoltaic Modules Using Halved Cells’. In: *International Journal of Photoenergy* 2013 (2013), pp. 1–8. DOI: 10.1155/2013/739374.
- [117] T. Jung, H. Song, H. Ahn, and G. Kang. ‘A mathematical model for cell-to-module conversion considering mismatching solar cells and the resistance of the interconnection ribbon’. In: *Solar Energy* 103 (2014), pp. 253–262. DOI: 10.1016/j.solener.2014.01.032.
- [118] I. Haedrich, U. Eitner, M. Wiese, and H. Wirth. ‘Unified methodology for determining CTM ratios: Systematic prediction of module power’. In: *Solar Energy Materials and Solar Cells* 131 (2014), pp. 14–23. DOI: 10.1016/j.solmat.2014.06.025.
- [119] N. C. Wyeth. ‘Sheet resistance component of series resistance in a solar cell as a function of grid geometry’. In: *Solid-State Electronics* 20.7 (1977), pp. 629–634.
- [120] R. Handy. ‘Theoretical analysis of the series resistance of a solar cell’. In: *Solid-State Electronics* 10.8 (1967), pp. 765–775.
- [121] R. Sahai and A. G. Milnes. ‘Heterojunction solar cell calculations’. In: *Solid-State Electronics* 13.9 (1970), pp. 1289–1299. DOI: 10.1016/0038-1101(70)90026-2.

- [122] H. Serreze. ‘Optimizing solar cell performance by simultaneous consideration of grid pattern design and interconnect configuration’. In: *13th IEEE PVSC*. Vol. 1. 1978, pp. 609–614.
- [123] S. Deb and B. Ghosh. ‘Series resistance and optimum grid design for a thin film solar cell of rectangular shape’. In: *Solar cells* 13.2 (1984), pp. 145–162.
- [124] A. Burgers. ‘How to design optimal metallization patterns for solar cells’. In: *Progress in Photovoltaics Research and Applications* 7.6 (1999), pp. 457–461.
- [125] H. Mäckel, G. Micard, and K. Varner. ‘Analytical models for the series resistance of selective emitters in silicon solar cells including the effect of busbars’. In: *Prog. Photovolt: Res. Appl.* 23.2 (2013), pp. 135–149. DOI: 10.1002/pip.2403.
- [126] T. Yamada, H. Nakamura, T. Sugiura, K. Sakuta, and K. Kurokawa. ‘Reflection loss analysis by optical modeling of PV module’. In: *Solar Energy Materials and Solar Cells* 67.1-4 (2001), pp. 405–413. DOI: 10.1016/S0927-0248(00)00309-3.
- [127] H. Holst, M. Winter, M. R. Vogt, K. Bothe, M. Köntges, R. Brendel, and P. P. Altermatt. ‘Application of a New Ray Tracing Framework to the Analysis of Extended Regions in Si Solar Cell Modules’. In: *Energy Procedia* 38 (2013), pp. 86–93. DOI: 10.1016/j.egypro.2013.07.253.
- [128] H. Holst. ‘Development and application of a modular ray tracing framework to multi-scale simulations in photovoltaics’. PhD thesis. Leibniz Universität Hannover, 2015.
- [129] M. Winter, M. R. Vogt, H. Holst, and P. P. Altermatt. ‘Combining structures on different length scales in ray tracing: analysis of optical losses in solar cell modules’. In: *Optical and Quantum Electronics* 47.6 (2014), pp. 1373–1379. DOI: 10.1007/s11082-014-0078-x.
- [130] H. Holst, H. Schulte-Huxel, M. Winter, S. Blankemeyer, R. Witteck, M. R. Vogt, T. Booz, F. Distelrath, M. Köntges, K. Bothe, and R. Brendel. ‘Increased Light Harvesting by Structured Cell Interconnection Ribbons: An Optical Ray Tracing Study Using a Realistic Daylight Model’. In: *Energy Procedia* 92 (2016), pp. 505–514. DOI: 10.1016/j.egypro.2016.07.134.
- [131] M. R. Vogt, H. Holst, H. Schulte-Huxel, S. Blankemeyer, R. Witteck, D. Hinken, M. Winter, B. Min, C. Schinke, I. Ahrens, M. Köntges, K. Bothe, and R. Brendel. ‘Optical Constants of UV Transparent EVA and the Impact on the PV Module Output Power under Realistic Irradiation’. In: *Energy Procedia* 92 (2016), pp. 523–530. DOI: 10.1016/j.egypro.2016.07.136.
- [132] F. Pern. ‘Factors that affect the EVA encapsulant discoloration rate upon accelerated exposure’. In: *24 IEEE PVSC*. 1994, pp. 897–900.
- [133] F.-J. Pern and S. H. Glick. ‘Improved photostability of NREL-developed EVA pottant formulations for PV module encapsulation’. In: *26th IEEE PVSC*. IEEE. 1997, pp. 1089–1092.
- [134] F. Pern and S. Glick. ‘Photothermal stability of encapsulated Si solar cells and encapsulation materials upon accelerated exposures’. In: *Solar energy materials and solar cells* 61.2 (2000), pp. 153–188.

- [135] W. Holley, S. Agro, J. Galica, and R. Yorgensen. ‘UV stability and module testing of nonbrowning experimental PV encapsulants’. In: *25th IEEE PVSC*. 1996, pp. 1259–1262. DOI: [10.1109/pvsc.1996.564361](https://doi.org/10.1109/pvsc.1996.564361).
- [136] G. Barber, G. Jorgensen, K. Terwilliger, S. Glick, J. Pern, and T. McMahon. ‘New barrier coating materials for PV module backsheets’. In: *29th IEEE PVSC*. Institute of Electrical and Electronics Engineers (IEEE), 2002, pp. 1541–1544. DOI: [10.1109/pvsc.2002.1190906](https://doi.org/10.1109/pvsc.2002.1190906).
- [137] W. Gambogi, Y. Heta, K. Hashimoto, J. Kopchick, T. Felder, S. MacMaster, A. Bradley, B. Hamzavytehrany, L. Garreau-Iles, T. Aoki, K. Stika, T. J. Trout, and T. Sample. ‘A Comparison of Key PV Backsheet and Module Performance from Fielded Module Exposures and Accelerated Tests’. In: *IEEE Journal of Photovoltaics* 4.3 (2014), pp. 935–941. DOI: [10.1109/jphotov.2014.2305472](https://doi.org/10.1109/jphotov.2014.2305472).
- [138] L. Dunn, M. Gostein, and B. Stueve. ‘Literature Review of the Effects of UV Exposure on PV Modules’. In: *NREL PV Module Reliability Workshop*. NREL, 2013.
- [139] G. Griffini and S. Turri. ‘Polymeric materials for long-term durability of photovoltaic systems’. In: *J. Appl. Polym. Sci.* 133.11 (2015). DOI: [10.1002/app.43080](https://doi.org/10.1002/app.43080).
- [140] A. Jentsch, K.-J. Eichhorn, and B. Voit. ‘Influence of typical stabilizers on the aging behavior of EVA foils for photovoltaic applications during artificial UV-weathering’. In: *Polymer Testing* 44 (2015), pp. 242–247. DOI: [10.1016/j.polymertesting.2015.03.022](https://doi.org/10.1016/j.polymertesting.2015.03.022).
- [141] J. Kanicki, M. Sankaran, A. Gelatos, M. S. Crowder, and E. D. Tober. ‘Stretched exponential illumination time dependence of positive charge and spin generation in amorphous silicon nitride’. In: *Applied Physics Letters* 57.7 (1990), pp. 698–700. DOI: [10.1063/1.104255](https://doi.org/10.1063/1.104255).
- [142] V. Sharma. ‘Study of charges present in silicon nitride thin films and their effect on silicon solar cell efficiencies’. PhD thesis. Arizona State University, 2013.
- [143] R. L. Cicero, M. R. Linford, and C. E. D. Chidsey. ‘Photoreactivity of Unsaturated Compounds with Hydrogen-Terminated Silicon(111)’. In: *Langmuir* 16.13 (2000), pp. 5688–5695. DOI: [10.1021/1a9911990](https://doi.org/10.1021/1a9911990).
- [144] P. Gruenbaum, R. Sinton, and R. Swanson. ‘Stability problems in point contact solar cells’. In: *20th IEEE PVSC*. Institute of Electrical and Electronics Engineers (IEEE), 1988. DOI: [10.1109/pvsc.1988.105736](https://doi.org/10.1109/pvsc.1988.105736).
- [145] L. E. Black and K. R. McIntosh. ‘Defect Generation at Charge-Passivated Si-SiO Interfaces by Ultraviolet Light Interfaces by Ultraviolet Light’. In: *IEEE Transactions on Electron Devices* 57.8 (2010), pp. 1996–2004. DOI: [10.1109/ted.2010.2051199](https://doi.org/10.1109/ted.2010.2051199).
- [146] K. Jager and R. Hezel. ‘Optical stability of silicon nitride MIS inversion layer solar cells’. In: *IEEE Transactions on Electron Devices* 32.9 (1985), pp. 1824–1829. DOI: [10.1109/t-ed.1985.22204](https://doi.org/10.1109/t-ed.1985.22204).
- [147] K. Blumenstock and R. Hezel. ‘Interface State Generation in the Si-SiO₂ System by Non-Ionizing UV Irradiation’. In: *Insulating films on semiconductors* (1985), p. 221.

- [148] R. Hezel. 'UV Radiation Hardness Of Silicon Inversion Laye R Solar Cells'. In: *21st IEEE PVSC*. IEEE, 1990.
- [149] T. Lauinger, J. Moschner, A. G. Aberle, and R. Hezel. 'Optimization and characterization of remote plasma-enhanced chemical vapor deposition silicon nitride for the passivation of p-type crystalline silicon surfaces'. In: *Journal of Vacuum Science & Technology A* 16.2 (1998), pp. 530–543.
- [150] T. Kamioka, D. Takai, T. Tachibana, T. Kojima, and Y. Ohshita. 'Plasma damage effect on ultraviolet-induced degradation of PECVD SiNx:H passivation'. In: *42nd IEEE PVSC*. 2015, pp. 1–3. DOI: 10.1109/PVSC.2015.7356326.
- [151] T. Tachibana, D. Takai, Y. Yamashita, N. Ikeno, H. Tokutake, K. Nagata, A. Ogura, Y. Ohshita, I. T. T. Institute, Nagoya, and 4.-8. Japan. 'Effects of texture structure on crystalline damage induced by SiNx plasma CVD'. In: *29th EUPVSEC*. 2016, pp. 1090–1091.
- [152] T. Lauinger. 'Untersuchung und Optimierung neuartiger Plasmaverfahren zur Siliciumnitrid-Beschichtung von Silicium-Solarzellen'. PhD thesis. Leibniz Universität Hannover, 2001.
- [153] S. Gatz, H. Hannebauer, R. Hesse, F. Werner, A. Schmidt, T. Dullweber, J. Schmidt, K. Bothe, and R. Brendel. '19.4%-efficient large-area fully screen-printed silicon solar cells'. In: *physica status solidi (RRL)-Rapid Research Letters* 5.4 (2011), pp. 147–149.
- [154] J.-F. Lelièvre, E. Fourmond, A. Kaminski, O. Palais, D. Ballutaud, and M. Lemiti. 'Study of the composition of hydrogenated silicon nitride SiNx:H for efficient surface and bulk passivation of silicon'. In: *Solar Energy Materials and Solar Cells* 93.8 (2009), pp. 1281–1289. DOI: 10.1016/j.solmat.2009.01.023.
- [155] T. Dullweber, S. Gatz, H. Hannebauer, T. Falcon, R. Hesse, J. Schmidt, and R. Brendel. 'Towards 20% efficient large-area screen-printed rear-passivated silicon solar cells'. In: *Prog. Photovolt: Res. Appl.* 20.6 (2011), pp. 630–638. DOI: 10.1002/pip.1198.
- [156] W. Kern. 'Cleaning solutions based on hydrogen peroxide for use in silicon semiconductor technology'. In: *RCA review* 31 (1970), pp. 187–206.
- [157] F. Kiefer. 'Kontaktierung Ionen-implantierter Boremitter in n-Typ Silizium-Solarzellen mittels Silber/Aluminium-Pasten'. PhD thesis. Leibniz Universität Hannover, 2016.
- [158] F. Kiefer, J. Krügener, F. Heinemeyer, M. Jestremski, H. J. Osten, R. Brendel, and R. Peibst. 'Bifacial, fully screen-printed n-PERT solar cells with BF₂ and B implanted emitters'. In: *Solar Energy Materials and Solar Cells* 157 (2016), pp. 326–330. DOI: 10.1016/j.solmat.2016.05.028.
- [159] A. M. Gabor, M. Ralli, S. Montminy, L. Alegria, C. Bordonaro, J. Woods, L. Felton, E. Solar, and Inc. 'Soldering Induced Damage To Thin Si Solar Cells And Detection Of Cracked Cells In Modules'. In: *21st EUPVSEC*. 2006, pp. 4–8.
- [160] L. C. Rendler, J. Walter, T. Geipel, M. Volk, C. Ebert, and U. Eitner. 'Modelling And Verification Of Mechanical Stress Induced By Soldering Of Wires For Multi Busbar Interconnection'. In: *31st EUPVSEC*. 2015.

- [161] S. Suppiah, N. R. Ong, Z. Sauli, K. Sarukunaselan, J. B. Alcain, S. M. Visvanathan, and V. Retnasamy. ‘A review on solder reflow and flux application for flip chip’. In: *AIP Conference Proceedings*. Vol. 1885. 1. 2017, p. 020264. DOI: 10.1063/1.5002458.
- [162] A. Gabor, R. Janoch, A. Anselmo, and H. Field. ‘Solar panel design factors to reduce the impact of cracked cells and the tendency for crack propagation’. In: *NREL PV Module Reliability Workshop*. 2015.
- [163] International Electrotechnical Commission. *Measurement procedures for materials used in photovoltaic modules-Part 1-4: Encapsulants - Measurement of optical transmittance and calculation of the solar-weighted photon transmittance, yellowness index, and UV cut-off wavelength*. Tech. rep. International Electrotechnical Commission, Geneva, Switzerland, 2016.
- [164] H. Tompkins and E. A. Irene. *Handbook of ellipsometry*. William Andrew, 2005.
- [165] J. Woollam. ‘Guide To Using WVASE32’. In: *J.A. Woollam Co., Inc.* 2008.
- [166] J. A. Woollam, B. D. Johs, C. M. Herzinger, J. N. Hilfiker, R. A. Synowicki, and C. L. Bungay. ‘Overview of variable-angle spectroscopic ellipsometry (VASE): I. Basic theory and typical applications’. In: *Optical Metrology*. 1999, pp. 3–28.
- [167] B. D. Johs, J. A. Woollam, C. M. Herzinger, J. N. Hilfiker, R. A. Synowicki, and C. L. Bungay. ‘Overview of variable-angle spectroscopic ellipsometry (VASE): II. Advanced applications’. In: *Optical Metrology*. 1999, pp. 29–58.
- [168] Agilent Technologies. *Cary 100/300/4000/5000/6000i /7000 Spectrophotometers*. Tenth edition. Agilent Technologies. 2016.
- [169] C. Peest. ‘Bestimmung der Messunsicherheit eines Photospektrometers für Reflexions- und Transmissionsmessungen an planaren und Siliziumwafern’. MA thesis. Gottfried Wilhelm Leibniz Universität Hannover, 2014.
- [170] D. K. Schroder. *Semiconductor Material and Device Characterization*. Wiley-Blackwell, 2005. DOI: 10.1002/0471749095.
- [171] R. A. Sinton and A. Cuevas. ‘Contactless determination of current–voltage characteristics and minority-carrier lifetimes in semiconductors from quasi-steady-state photoconductance data’. In: *Applied Physics Letters* 69.17 (1996), pp. 2510–2512.
- [172] D. Kane and R. Swanson. ‘Measurement of the emitter saturation current by a contactless photoconductivity decay method’. In: *18th IEEE PVSC*. 1985, pp. 578–583.
- [173] H. Murrmann and D. Widmann. ‘Messung des Übergangswiderstandes zwischen Metall und Diffusionsschicht in Si-Planarelementen’. In: *Solid-State Electronics* 12.11 (1969), pp. 879–886. DOI: 10.1016/0038-1101(69)90045-8.
- [174] H. Berger. ‘Contact resistance on diffused resistors’. In: *1969 IEEE International Solid-State Circuits Conference*. Vol. XII. 1969, pp. 160–161. DOI: 10.1109/ISSCC.1969.1154702.
- [175] D. K. Schroder and D. L. Meier. ‘Solar cell contact resistance—A review’. In: *IEEE Transactions on Electron Devices* 31.5 (1984), pp. 637–647.
- [176] pv-tools. *LOANA solar cell analysis system manual*.

- [177] International Electrotechnical Commission. *IEC60904-3 - Photovoltaic devices Part 3: Measurement principles for terrestrial photovoltaic (PV) solar devices with reference spectral irradiance data (STC)*. Tech. rep. International Electrotechnical Commission, Geneva, Switzerland, 2016.
- [178] J. Metzdorf, A. Meier, S. Winter, and T. Wittchen. ‘Analysis and correction of errors in current-voltage characteristics of solar cells due to transient measurements’. In: *Proceedings of the 12th EC PVSEC*. 1994, pp. 496–499.
- [179] J. Metzdorf. ‘Calibration of solar cells. 1: The differential spectral responsivity method’. In: *Applied Optics* 26.9 (1987), pp. 1701–1708.
- [180] A. Herguth, G. Schubert, M. Kaes, and G. Hahn. ‘Investigations on the long time behavior of the metastable boron–oxygen complex in crystalline silicon’. In: *Progress in Photovoltaics: Research and Applications* 16.2 (2008), pp. 135–140. DOI: 10.1002/pip.779.
- [181] Avantes. *AvaSpec-ULS2048 StarLine Versatile Fiber-optic Spectrometer*. 2017.
- [182] ISO21348. *Definitions of Solar Irradiance Spectral Categories*. International Standard, 2007.
- [183] KippundZonen. *CUV3 - broadband scientific radiometer*. Roentgenweg 3, 2004.
- [184] Opsytec Dr. Goebel. *Opsytec Dr. Goebel Radiometer*. Am Hardtwald 6-8, 76275 Ettlingen, 2017.
- [185] U. Feister and K.-H. Grasnick. ‘Solar UV radiation measurements at Potsdam’. In: *Solar Energy* 49.6 (1992), pp. 541–548.
- [186] Evonik. *Weathering of acrylic resins*. Tech. rep. Evonik, 2012.
- [187] L. Hamann, L. Proenneke, M. Reuter, and J. H. Werner. ‘Colored ribbons achieve +0.3% abs module efficiency gain’. In: *The 22nd International Photovoltaic Science and Engineering Conference*. 2012. DOI: 10.13140/2.1.5107.2327.
- [188] E. M. Sachs, J. Serdy, A. M. Gabor, and F. van Mierlo. ‘Light-capturing Interconnect Wire For 2% Module Power Gain’. In: *24th EUPVSEC*. 2009, pp. 3222–3225.
- [189] J. Jaus, H. Pantsar, J. Eckert, M. Duell, H. Herfurth, and D. Doble. ‘Light management for reduction of bus bar and gridline shadowing in photovoltaic modules’. In: *35th IEEE PVSC*. 2010, pp. 000979–000983. DOI: 10.1109/pvsc.2010.5614568.
- [190] J. Levrat, C. Allebé, N. Badel, L. Barraud, M. Bonnet-Eymard, J. Champiaud, F. Debrot, A. Descoeurdes, A. Faes, A. Lachowicz, et al. ‘High-performance hetero-junction crystalline silicon photovoltaic technology’. In: *2014 IEEE 40th Photovoltaic Specialist Conference*. IEEE. 2014, pp. 1218–1222.
- [191] B. Fischer. ‘Loss analysis of crystalline silicon solar cells using photoconductance and quantum efficiency measurements’. PhD thesis. Uni Konstanz, 2003.
- [192] B. Thaidigsmann, A. Wolf, and D. Biro. ‘Accurate determination of the IQE of screen printed silicon solar cells by accounting for the finite reflectance of metal contacts’. In: *24th EUPVSEC*. 2009, pp. 2056–2059.

- [193] Y. Yuan and T. R. Lee. ‘Contact Angle and Wetting Properties’. In: *Surface Science Techniques*. Springer Series in Surface Sciences. Springer Berlin Heidelberg, 2013, pp. 3–34. DOI: 10.1007/978-3-642-34243-1_1.
- [194] R. Woehl, M. Hörteis, and S. W. Glunz. ‘Analysis of the Optical Properties of Screen-Printed and Aerosol-Printed and Plated Fingers of Silicon Solar Cells’. In: *Advances in OptoElectronics 2008* (2008), pp. 1–7. DOI: 10.1155/2008/759340.
- [195] S. Guo, J. Schneider, F. Lu, H. Hanifi, M. Turek, M. Dyrba, and I. M. Peters. ‘Investigation of the short-circuit current increase for PV modules using halved silicon wafer solar cells’. In: *Solar Energy Materials and Solar Cells* 133 (2015), pp. 240–247. DOI: 10.1016/j.solmat.2014.11.012.
- [196] M. Müller and F. Lottspeich. ‘Evaluation of determination methods of the Si/Al contact resistance of screen-printed passivated emitter and rear solar cells’. In: *Journal of Applied Physics* 115.8 (2014), p. 084505. DOI: 10.1063/1.4867188.
- [197] H. Hannebauer, M. Sommerfeld, J. Müller, T. Dullweber, and R. Brendel. ‘Analysis of the emitter saturation current density of industrial type silver screen-printed front contacts’. In: *27th EUPVSEC* 1360 (2012).
- [198] M. R. Vogt. ‘Development of Physical Models for the Simulation of Optical Properties of Solar Cell Modules’. PhD thesis. Leibniz Universität Hannover, 2015.
- [199] M. R. Vogt, H. Schulte-Huxel, M. Offer, S. Blankemeyer, R. Witteck, M. Köntges, K. Bothe, and R. Brendel. ‘Reduced Module Operating Temperature and Increased Yield of Modules With PERC Instead of Al-BSF Solar Cells’. In: *IEEE JPV* 7.1 (2017), pp. 44–50. DOI: 10.1109/jphotov.2016.2616191.
- [200] M. A. Green. *Solar cells: operating principles, technology, and system applications*. Prentice-Hall, Inc., Englewood Cliffs, NJ, 1982.
- [201] I. N. Bronstein, K. A. Semendjajew, and G. Musiol. *Taschenbuch der Mathematik*. Deutsch (Harri), 2008.
- [202] A. R. Burgers. *New metallisation patterns and analysis of light trapping for silicon solar cells*. Energieonderzoek Centrum Nederland, 2005.
- [203] C. AB. *COMSOL Multiphysics v. 5.2*. 2017. URL: www.comsol.com.
- [204] T. Fellmeth, S. Mack, J. Bartsch, D. Erath, U. Jäger, R. Preu, F. Clement, and D. Biro. ‘20.1% Efficient Silicon Solar Cell With Aluminum Back Surface Field’. In: *IEEE Electron Device Lett.* 32.8 (2011), pp. 1101–1103. DOI: 10.1109/led.2011.2157656.
- [205] H. Stascheit. ‘Leistungsvergleich zwischen dem 5 Busbar und dem SmartWire Modulkonzept’. MA thesis. HTW Berlin, 2016.
- [206] M. Peters, S. Guo, and Z. Liu. ‘Full loss analysis for a multicrystalline silicon wafer solar cell PV module at short-circuit conditions’. In: *Prog. Photovolt: Res. Appl.* 24.4 (2015), pp. 560–569. DOI: 10.1002/pip.2593.
- [207] A. Schneider, M. Pander, T. Korvenkangas, S. Aulehla, R. Harney, and T. Horttana. ‘Cell to Module Loss Reduction and Module Reliability Enhancements by Solder Ribbon Optimization’. In: *Proceedings of the 29th EUPVSEC, Amsterdam, Netherlands* (2014), pp. 165–170.

- [208] S. Roberts, K. Heasman, and T. Bruton. ‘The reduction of module power losses by the optimisation of the tabbing ribbon’. In: *16th PVSEC, Glasgow*. 2000, p. 2378.
- [209] J. Müller, D. Hinken, S. Blankemeyer, H. Kohlenberg, U. Sonntag, K. Bothe, T. Dullweber, M. Köntges, and R. Brendel. ‘Resistive Power Loss Analysis of PV Modules Made From Halved $15.6 \times 15.6 \text{ cm}^2$ Silicon PERC Solar Cells With Efficiencies up to 20.0%’. In: *IEEE Journal of Photovoltaics* 5.1 (2015), pp. 189–194. DOI: 10.1109/JPHOTOV.2014.2367868.
- [210] P. Verlinden, Z. Yingbin, and F. Zhiqiang. ‘Cost analysis of current PV production and strategy for future silicon PV modules’. In: *28th EUPVSEC*. 2013.
- [211] J. H. Petermann. ‘Prozessentwicklung und Verlustanalysen für dünne monokristalline Siliziumsolarzellen und deren Prozessierung auf Modullevel’. PhD thesis. Leibniz Universität Hannover, 2014.
- [212] R. Brendel, T. Dullweber, R. Peibst, C. Kranz, A. Merkle, and D. Walter. ‘Breakdown of the efficiency gap to 29% based on experimental input data and modeling’. In: *Prog. Photovolt: Res. Appl.* 24.12 (2015), pp. 1475–1486. DOI: 10.1002/pip.2696.
- [213] G. Jellison Jr, F. Modine, P. Doshi, and A. Rohatgi. ‘Spectroscopic ellipsometry characterization of thin-film silicon nitride’. In: *Thin Solid Films* 313 (1998), pp. 193–197.
- [214] M. R. Vogt, H. Holst, H. Schulte-Huxel, S. Blankemeyer, R. Witteck, P. Bujard, J.-B. Kues, C. Schinke, K. Bothe, M. Köntges, et al. ‘PV module current gains due to structured backsheets’. In: vol. 124. Elsevier, 2017, pp. 495–503.
- [215] F. J. Pern, S. H. Glick, and A. W. Czanderna. ‘Review of the photothermal stability of EVA pottants: Effects of formulation on the discoloration rate and mitigation methods’. In: *AIP Conference Proceedings*. Vol. 462. 1. AIP Publishing, 1999, pp. 599–604. DOI: 10.1063/1.58004.
- [216] K. R. McIntosh, P. P. Altermatt, T. J. Ratcliff, K. C. Fong, L. E. Black, S. C. Baker-Finch, M. D. Abbott, et al. ‘An examination of three common assumptions used to simulate recombination in heavily doped silicon’. In: *28th EUPVSEC*. 2013, pp. 1672–1679.
- [217] M. Barbé, F. Bailly, J. Chevallier, S. Silvestre, D. Loridant-Bernard, L. Kurowski, E. Constant, and M. Constant. ‘Photo-induced Dissociation and Optical Cross Section of Si-H and S-H Complexes in GaAs and AlGaAs’. In: *Symposium F – Defect- and Impurity-Engineered Semiconductors and Devices III*. Vol. 719. Cambridge Univ Press. 2002. DOI: 10.1557/PROC-719-F8.8.
- [218] Z. Yin and F. W. Smith. ‘Free energy model for the analysis of bonding in a-SixNyHz alloys’. In: *Journal of Vacuum Science & Technology A: Vacuum, Surfaces, and Films* 9.3 (1991), pp. 972–977. DOI: 10.1116/1.577558.
- [219] A. Mayne, D. Riedel, G. Comtet, and G. Dujardin. ‘Atomic-scale studies of hydrogenated semiconductor surfaces’. In: *Progress in Surface Science* 81.1 (2006), pp. 1–51. DOI: 10.1016/j.progsurf.2006.01.001.

- [220] J. Chevallier, M. Barbé, E. Constant, D. Loridant-Bernard, and M. Constant. ‘Strong isotope effects in the dissociation kinetics of Si–H and Si–D complexes in GaAs under ultraviolet illumination’. In: *Applied physics letters* 75.1 (1999), pp. 112–114.
- [221] D. A. Mehta, S. R. Butler, and F. J. Feigl. ‘Electronic charge trapping in chemical vapor-deposited thin films of Al₂O₃ on silicon’. In: *Journal of Applied Physics* 43.11 (1972), pp. 4631–4638. DOI: 10.1063/1.1660979.
- [222] J. J. H. Gielis, B. Hoex, M. C. M. van de Sanden, and W. M. M. Kessels. ‘Negative charge and charging dynamics in Al₂O₃ films on Si characterized by second-harmonic generation’. In: *Journal of Applied Physics* 104.7 (2008), p. 073701. DOI: 10.1063/1.2985906.
- [223] G. Dingemans, P. Engelhart, R. Seguin, F. Einsele, B. Hoex, M. C. M. van de Sanden, and W. M. M. Kessels. ‘Stability of Al₂O₃ and Al₂O₃/a-SiN_x:H stacks for surface passivation of crystalline silicon’. In: *J. Appl. Phys.* 106.11 (2009), p. 114907. DOI: 10.1063/1.3264572.
- [224] S. De Wolf, B. Demareux, A. Descoeurdes, and C. Ballif. ‘Very fast light-induced degradation of a-Si:H/c-Si(100) interfaces’. In: *Phys. Rev. B* 83 (23 2011), p. 233301. DOI: 10.1103/PhysRevB.83.233301.
- [225] B. Liao, R. Stangl, T. Mueller, F. Lin, C. S. Bhatia, and B. Hoex. ‘The effect of light soaking on crystalline silicon surface passivation by atomic layer deposited Al₂O₃’. In: *J. Appl. Phys.* 113.2 (2013), p. 024509. DOI: 10.1063/1.4775595.
- [226] B. Veith-Wolf, R. Witteck, A. Morlier, H. Schulte-Huxel, and J. Schmidt. ‘Effect of UV illumination on the passivation quality of AlO_x/c-Si interfaces’. In: *43rd IEEE PVSC*. IEEE. 2016, pp. 1173–1178.
- [227] C. Schinke, P. Christian Peest, J. Schmidt, R. Brendel, K. Bothe, M. R. Vogt, I. Kröger, S. Winter, A. Schirmacher, S. Lim, H. T. Nguyen, and D. MacDonald. ‘Uncertainty analysis for the coefficient of band-to-band absorption of crystalline silicon’. In: *AIP Advances* 5.6 (2015), p. 067168. DOI: 10.1063/1.4923379.
- [228] *Sentaurus user manual, Synopsys Inc. Mountain View, 2016.*
- [229] P. P. Altermatt. ‘Models for numerical device simulations of crystalline silicon solar cells—a review’. In: *Journal of Computational Electronics* 10.3 (2011), pp. 314–330. DOI: 10.1007/s10825-011-0367-6.
- [230] H. Steinkemper, M. Rauer, P. Altermatt, F. D. Heinz, C. Schmiga, and M. Hermle. ‘Adapted parameterization of incomplete ionization in aluminum-doped silicon and impact on numerical device simulation’. In: *Journal of Applied Physics* 117.7 (2015), p. 074504. DOI: 10.1063/1.4913255.
- [231] A. Fell, K. R. McIntosh, P. P. Altermatt, G. J. M. Janssen, R. Stangl, A. Ho-Baillie, H. Steinkemper, J. Greulich, M. Muller, B. Min, K. C. Fong, M. Hermle, I. G. Romijn, and M. D. Abbott. ‘Input Parameters for the Simulation of Silicon Solar Cells in 2014’. In: *IEEE JPV* 5.4 (2015), pp. 1250–1263. DOI: 10.1109/jphotov.2015.2430016.
- [232] D. Klaassen. ‘A unified mobility model for device simulation - I. Model equations and concentration dependence’. In: *Solid-State Electronics* 35.7 (1992), pp. 953–959. DOI: 10.1016/0038-1101(92)90325-7.

- [233] H. T. Nguyen, S. C. Baker-Finch, and D. Macdonald. ‘Temperature dependence of the radiative recombination coefficient in crystalline silicon from spectral photoluminescence’. In: *Applied Physics Letters* 104.11 (2014), p. 112105. DOI: 10.1063/1.4869295.
- [234] A. Richter, S. W. Glunz, F. Werner, J. Schmidt, and A. Cuevas. ‘Improved quantitative description of Auger recombination in crystalline silicon’. In: *Physical Review B* 86.16 (2012), p. 165202. DOI: 10.1103/physrevb.86.165202.
- [235] A. Schenk. ‘Finite-temperature full random-phase approximation model of band gap narrowing for silicon device simulation’. In: *Journal of Applied Physics* 84.7 (1998), pp. 3684–3695. DOI: 10.1063/1.368545.
- [236] F. Werner, B. Veith, D. Zielke, L. Kuehnemund, C. Tegenkamp, M. Seibt, R. Brendel, and J. Schmidt. ‘Electronic and chemical properties of the c-Si/Al₂O₃ interface’. In: *J. Appl. Phys.* 109.11 (2011), p. 113701. DOI: <http://dx.doi.org/10.1063/1.3587227>.
- [237] S. Dauwe, J. Schmidt, A. Metz, and R. Hezel. ‘Fixed charge density in silicon nitride films on crystalline silicon surfaces under illumination’. In: *29th IEEE PVSC*. Institute of Electrical and Electronics Engineers (IEEE), 2002, pp. 162–165. DOI: 10.1109/pvsc.2002.1190481.
- [238] K. R. McIntosh and P. P. Altermatt. ‘A freeware 1D emitter model for silicon solar cells’. In: *35th IEEE PVSC*. IEEE, 2010, pp. 002188–002193.
- [239] B. Veith-Wolf, R. Witteck, A. Morlier, H. Schulte-Huxel, M. R. Vogt, and J. Schmidt. ‘Spectra-Dependent Stability of the Passivation Quality of Al₂O₃/c-Si Interfaces’. In: *IEEE Journal of Photovoltaics* 8.1 (2017), pp. 96–102. DOI: 10.1109/jphotov.2017.2775147.
- [240] D. A. Mehta, S. R. Butler, and F. J. Feigl. ‘Effects of Postdeposition Annealing Treatments on Charge Trapping in Al₂O₃ Films on Si’. In: *Journal of The Electrochemical Society* 120.12 (1973), p. 1707. DOI: 10.1149/1.2403349.
- [241] J. Schmidt, M. Kerr, and A. Cuevas. ‘Surface passivation of silicon solar cells using plasma-enhanced chemical-vapour-deposited SiN films and thin thermal SiO₂/plasma SiN stacks’. In: *Semiconductor Science and Technology* 16.3 (2001), p. 164.
- [242] W. Lee, Y. Khong, M. R. Muhamad, and T. Tou. ‘The effect of ultraviolet irradiation on the minority carrier recombination lifetime of oxidized silicon wafers’. In: *Journal of The Electrochemical Society* 144.5 (1997), pp. L103–L105.
- [243] H. K. Asuha, O. Maida, M. Takahashi, and H. Iwasa. ‘Nitric acid oxidation of Si to form ultrathin silicon dioxide layers with a low leakage current density’. In: *Journal of Applied Physics* 94.11 (2003), pp. 7328–7335. DOI: 10.1063/1.1621720.
- [244] H. Ali, A. Moldovan, S. Mack, W. V. Schoenfeld, and K. O. Davis. ‘Transmission electron microscopy based interface analysis of the origin of the variation in surface recombination of silicon for different surface preparation methods and passivation materials’. In: *physica status solidi (a)* 214.10 (2017), p. 1700286. DOI: 10.1002/pssa.201700286.

List of publications

Peer reviewed journal papers

- R. Witteck, B. Min, H. Schulte-Huxel, H. Holst, B. Veith-Wolf, F. Kiefer, M. R. Vogt, M. Köntges, R. Peibst, and R. Brendel. ‘UV radiation hardness of photovoltaic modules featuring crystalline Si solar cells with AlO_x/p+-type Si and SiNy/n+-type Si interfaces’. In: *physica status solidi (RRL) – Rapid Research Letters* 11.8 (2017), pp. 1700178-1–1700178-6. DOI: 10.1002/pssr.201700178.
- R. Witteck, B. Veith-Wolf, H. Schulte-Huxel, A. Morlier, M. R. Vogt, M. Köntges, and R. Brendel. ‘UV-induced degradation of PERC solar modules with UV-transparent encapsulation materials’. In: *Progress in Photovoltaics: Research and Applications* (2017). DOI: 10.1002/pip.2861.
- R. Witteck, D. Hinken, H. Schulte-Huxel, M. R. Vogt, J. Müller, S. Blankemeyer, M. Köntges, K. Bothe, and R. Brendel. ‘Optimized Interconnection of Passivated Emitter and Rear Cells by Experimentally Verified Modeling’. In: *IEEE Journal of Photovoltaics* 6.2 (2016), pp. 432–439. DOI: 10.1109/jphotov.2016.2514706.

Conference proceedings papers

- R. Witteck, H. Schulte-Huxel, B. Veith-Wolf, M. R. Vogt, F. Kiefer, M. Köntges, R. Peibst, and R. Brendel. ‘Reducing UV induced degradation losses of solar modules with c-Si solar cells featuring dielectric passivation layers’. In: *44th IEEE PVSC*. 2017.
- R. Witteck, H. Schulte-Huxel, H. Holst, D. Hinken, M. Vogt, S. Blankemeyer, M. Köntges, K. Bothe, and R. Brendel. ‘Optimizing the Solar Cell Front Side Metallization and the Cell Interconnection for High Module Power Output’. In: *6th SiliconPV*. Vol. 92. Elsevier BV, 2016, pp. 531–539. DOI: 10.1016/j.egypro.2016.07.137.
- R. Witteck, D. Hinken, J. Müller, S. Blankemeyer, K. Bothe, H. Schulte-Huxel, M. Köntges, and R. Brendel. ‘Simulation of optimized cell interconnection for PERC modules exceeding 300 W’. In: *6th WCPEC*. 2015, pp. 515–516.
- R. Witteck, C. Schultz, M. Schüle, M. Weizman, B. Rau, R. Schlatmann, V. Quaschnig, K. Stelmaszczyk, B. Stegemann, and F. Fink. ‘Modified Series Connection Design for Thin Film Solar Modules’. In: *27th EUPVSEC*. 2012.

Co-authored peer reviewed journal papers

- T. Dullweber, H. Schulte-Huxel, S. Blankemeyer, H. Hannebauer, S. Schimanke, U. Baumann, R. Witteck, R. Peibst, M. Köntges, R. Brendel, and Y. Yao. 'Present status and future perspectives of bifacial PERC+ solar cells and modules'. In: *Japanese Journal of Applied Physics* 57.8S3 (2018), 08RA01. DOI: 10.7567/jjap.57.08ra01.
- B. Veith-Wolf, R. Witteck, A. Morlier, H. Schulte-Huxel, M. R. Vogt, and J. Schmidt. 'Spectra-dependent Stability of the Passivation Quality of Al₂O₃/c-Si Interfaces'. In: *IEEE Journal of Photovoltaics* 8.1 (2017), pp. 1–7. DOI: 10.1109/jphotov.2017.2775147.
- M. R. Vogt, H. Schulte-Huxel, M. Offer, S. Blankemeyer, R. Witteck, M. Köntges, K. Bothe, and R. Brendel. 'Reduced Module Operating Temperature and Increased Yield of Modules With PERC Instead of Al-BSF Solar Cells'. In: *IEEE Journal of Photovoltaics* 7.1 (2017), pp. 44–50. DOI: 10.1109/jphotov.2016.2616191.
- H. Schulte-Huxel, R. Witteck, H. Holst, M. R. Vogt, S. Blankemeyer, D. Hinken, T. Brendemühl, T. Dullweber, K. Bothe, M. Köntges, and R. Brendel. 'High-Efficiency Modules With Passivated Emitter and Rear Solar Cells - An Analysis of Electrical and Optical Losses'. In: *IEEE Journal of Photovoltaics* 7.1 (2017), pp. 25–31. DOI: 10.1109/jphotov.2016.2614121.

Co-authored conference Proceedings

- T. Dullweber, H. Schulte-Huxel, C. Kranz, S. Blankemeyer, U. Baumann, R. Witteck, R. Peibst, M. Köntges, and R. Brendel. 'Bifacial PERC+ solar cells and modules: an overview'. In: *33rd EUPVSEC*. 2017.
- M. R. Vogt, H. Holst, H. Schulte-Huxel, S. Blankemeyer, R. Witteck, P. Bujard, J.-B. Kues, C. Schinke, K. Bothe, M. Köntges, and R. Brendel. 'PV module current gains due to structured backsheets'. In: *7th SiliconPV*. Vol. 124. 7th International Conference on Silicon Photovoltaics, SiliconPV 2017, 3-5 April 2017, Freiburg, Germany. 2017, pp. 495–503. DOI: 10.1016/j.egypro.2017.09.286.
- H. Schulte-Huxel, R. Witteck, S. Blankemeyer, S. Spätlich, M. R. Vogt, D. Hinken, H. Holst, U. Sonntag, T. Brendemühl, I. Ahrens, T. Neubert, H. Hannebauer, U. Baumann, T. Dullweber, M. Köntges, K. Bothe, and R. Brendel. '20.2% module efficiency on large area with passivated emitter and rear solar cells'. In: *43rd IEEE PVSC*. 2016.
- M. R. Vogt, H. Schulte-Huxel, M. Offer, S. Blankemeyer, R. Witteck, P. P. Altermatt, M. Köntges, K. Bothe, and R. Brendel. 'Increased yield of PERC compared to Al-BSF cells due to inherently lower module operating temperatures'. In: *43rd IEEE PVSC*. 2016.
- B. Veith-Wolf, R. Witteck, A. Morlier, H. Schulte-Huxel, and J. Schmidt. 'Effect of UV Illumination on the Passivation Quality of AlO_x/c-Si Interfaces'. In: *43rd IEEE PVSC*. 2016.

- H. Schulte-Huxel, F. Kiefer, S. Blankemeyer, R. Witteck, M. R. Vogt, M. Köntges, RolfBrendel, J. Krügener, and R. Peibst. ‘Flip-flop Cell Interconnection Enabled By An Extremely High Bifaciality Of Screen-printed Ion Implanted N-pert Si Solar Cells’. In: *32nd EUPVSEC*. 2016, pp. 407–412.
- M. Köntges, H. Schulte-Huxel, S. Blankemeyer, M. R. Vogt, H. Holst, R. Reineke-Koch, R. Witteck, K. Bothe, and R. Brendel. ‘Method to Measure Light Recovery Probability of PV Module Backsheets Enabling 20.2% Module Efficiency with Passivated Emitter and Rear Solar Cells’. In: *32nd EUPVSEC*. 2016.
- M. R. Vogt, H. Holst, H. Schulte-Huxel, S. Blankemeyer, R. Witteck, D. Hinken, M. Winter, B. Min, C. Schinke, I. Ahrens, M. Köntges, K. Bothe, and R. Brendel. ‘Optical Constants of UV Transparent EVA and the Impact on the PV Module Output Power under Realistic Irradiation’. In: *6th SiliconPV*. Vol. 92. Elsevier BV, 2016, pp. 523–530. DOI: 10.1016/j.egypro.2016.07.136.
- H. Schulte-Huxel, R. Witteck, P. van Laak, T. Brendemühl, D. Hinken, K. Bothe, and R. Brendel. ‘Impact of Ag Pads on the Series Resistance of PERC Solar Cells’. In: *6th SiliconPV*. Vol. 92. Elsevier BV, 2016, pp. 743–749. DOI: 10.1016/j.egypro.2016.07.053.
- H. Holst, H. Schulte-Huxel, M. Winter, S. Blankemeyer, R. Witteck, M. R. Vogt, T. Booz, F. Distelrath, M. Köntges, K. Bothe, and R. Brendel. ‘Increased Light Harvesting by Structured Cell Interconnection Ribbons: An Optical Ray Tracing Study Using a Realistic Daylight Model’. In: *6th SiliconPV*. Vol. 92. Elsevier BV, 2016, pp. 505–514. DOI: 10.1016/j.egypro.2016.07.134.
- T. Dullweber, S.-H. H., C. Kranz, S. Blankemeier, U. Baumann, R. Witteck, M. Köntges, and R. Brendel. ‘Screen-printed rear Al finger grids enabling bifacial PERC+ solar cells and modules’. In: *26th International PVSEC*. 2016.
- K. Stelmaszczyk, C. Schultz, M. Schüle, M. Weizman, R. Witteck, B. Stegemann, and F. U. Fink. ‘In-line Inspection of P1-P3 Scribes in CIGS Solar Cell Substrates by using Laser Plasma Spectroscopy’. In: *Optical Society of America*. 2013.
- K. Stelmaszczyk, C. Schultz, M. Schüle, M. Weizman, R. Witteck, B. Stegemann, and F.-U. Fink. ‘Laser Scribing of Thin-Film CIGS Solar Cells Based on Depth Resolved LIBS Feedback’. In: *28th EUPVSEC*. 2013.
- C. Schultz, M. Schüle, K. Stelmaszczyk, J. Bonse, R. Witteck, M. Weizman, H. Rhein, B. Rau, R. Schlattmann, V. Quaschnig, B. Stegemann, and F.-U. Fink. ‘Film Side Laser Patterning of Molybdenum Thin Films Sputter-Deposited onto Glass’. In: *27th EUPVSEC*. 2012.

Others

- H. Schulte-Huxel, R. Witteck, M. R. Vogt, H. Holst, S. Blankemeyer, D. Hinken, T. Brendemühl, T. Dullweber, K. Bothe, M. Köntges, and R. Brendel. *Reducing the electrical and optical losses of PV modules incorporating PERC solar cells*. Tech. rep. Photovoltaics International, 2016.
- H. Schulte-Huxel, R. Witteck, S. Blankemeyer, K. Bothe, R. Peibst, T. Dullweber, and M. K. und R. Brendel. *From PERC and BJBC solar cells to modules - electrical and optical gains and losses*. Tech. rep. Seminar at National Renewable Energy Laboratory (NREL), 2016.

- M. R. Vogt, H. Holst, D. Hinken, H. Schulte-Huxel, S. Blankemeyer, R. Witteck, B. Min, I. Ahrens, C. Schinke, M. Köntges, K. Bothe, and R. Brendel. 'External quantum efficiencies of PV modules and their power output under realistic irradiation'. In: *TüV Rheinland PV workshop*. 2016.
- B. Rech, A. Bett, B. Burger, C. Brabec, R. Brendel, O. Führer, U. Möhrstedt, H. Neuhaus, M. Powalla, B. Utz, F. Wessendorf, S. Wieder, J. Binder, B. Dimmler, H.-J. Egelhaaf, D. Geyer, T. E. Kuhn, P. Lechner, L. Lucera, F. Machui, J. Mayer, P. Palinginis, S. Philipps, W. Wischmann, R. Witteck, B. Lunz, M. Merzkirch, and B. Erlach. *Photovoltaik - Technologiesteckbrief zur Analyse „Flexibilitätskonzepte für die Stromversorgung 2050“*. Tech. rep. acatech - Deutsche Akademie der Technikwissenschaften, Nationale Akademie der Wissenschaften Leopoldina, Union der deutschen Akademien der Wissenschaften, 2016. DOI: [10.13140/RG.2.1.2291.2885](https://doi.org/10.13140/RG.2.1.2291.2885).

Acknowledgments

Abschließend möchte ich mich ganz herzlich bei allen bedanken, die zum Gelingen dieser Arbeit beigetragen haben:

- Mein besonderer Dank gilt Prof. Dr. Rolf Brendel für die Betreuung meiner Dissertation, die Aufnahme als Doktorand am ISFH und für die wertvollen Anregungen, Diskussionen und den Freiraum bei der Erstellung dieser Arbeit.
- Prof. Dr. Giso Hahn und Prof. Dr. Friedrich Dinkelacker für die freundliche Übernahme des Korreferats.
- Prof. Dr. Holger Frahm für die Übernahme des Prüfungsvorsitzes.
- Henning Schulte-Huxel für die hervorragende wissenschaftliche Begleitung, fruchtbaren Diskussionen und Anregungen.
- Susanne Blankemeyer für die ausgezeichnete experimentelle Unterstützung und wertvolle Diskussionen zu den experimentellen Ergebnissen.
- Marc Köntges für wertvolle Diskussionen zu Solarmodulen und Alterungstests.
- Iris Kunze für die Unterstützung bei Alterungstests und Messungen am Flasher
- Sarah Spätlich und Ulrike Sonntag für die ECV Messungen und die Unterstützung bei der Herstellung der Zellchargen.
- Boris Veith-Wolf für seine Expertise und Diskussionen über Passivierschichten
- Byungsul Min für die Hilfe bei den Sentaurus Simulationen
- Malte Vogt für die Unterstützung bei der Auswertung der Ellipsometer Messungen und den Raytracing Simulationen
- Hendrik Holst für die Unterstützung bei den Raytracing Simulationen und dem Ausheilen von Zellen.
- Martin Rudolph für die Herstelleung der J0 Proben.
- Fabian Kiefer für die Bereitstellung der PERT Zellen.
- David Hinken für die wertvollen Diskussionen zu IV, QE und LBIC Messungen.
- Arnaud Morlier für die Hilfestellung beim Betrieb der UV Kammer und wissenswerte Gespräche zur UV Alterung von Polymeren.
- Marting Wolf und Till Brendemühl für den Support an der LOANA.

- Karsten Bothe, Carsten Schinke und Ingo Ahrens für Diskussionen zu Messtechnik.
- Tobias Neubert und David Sylla für das einrichten und betreuen der Laserarbeiten.
- Jens Müller für die anfängliche Betreuung als Doktorand.
- Allen Mitarbeitern des ISFH für die tolle Atmosphäre am Institut und die große Hilfsbereitschaft.
- Susanne Blankemeyer und Sascha Wolter für die gute Stimmung in Büro 429 und die vielen Kekse.
- Boris Veith-Wolf, Henning Schulte-Huxel, Malte Vogt, Sul Min, Tobias Ohrdes, Dimitri Zielke für die schönen Stunden an der Uni.
- Meinen Eltern für Ihre Unterstützung während des Studium und der Doktorarbeit.
- Jule für ihre Geduld, die Unterstützung und Motivation beim Schreiben dieser Arbeit und die Ablenkungen vom Doktorandenalltag.